

Solid-state NMR study of nitric oxide adsorption in carboxylate based MOFs

Der Fakultät für Physik und Geowissenschaften
der Universität Leipzig eingereichte

D I S S E R T A T I O N

zur Erlangung des akademischen Grades

doctor rerum naturalium

(Dr. rer. nat.)

vorgelegt von

M.Sc. Arafat Hossain Khan

geboren am 20.12.1985 in Chittagong, Bangladesh

Tag der Verleihung
Leipzig, den 21.10.2019

Bibliographische Beschreibung

Khan, Arafat Hossain

Solid-state NMR study of nitric oxide adsorption in carboxylate based MOFs

Universität Leipzig, Dissertation, 2019

139 S.*, 154 Lit.*, 21 Abb.

This dissertation is a compilation of six publications. It deals with the solid state NMR investigation of the biologically important molecule, nitric oxide (NO) adsorbed on Cu_3btc_2 , amine functionalized Cu_3btc_2 and MIL-100(Al) metal-organic frameworks (MOFs). At first, ^1H MAS NMR studies of NO loaded Cu_3btc_2 and $\text{Cu}_3(\text{NH}_2\text{btc})_2$ demonstrate the changed electronic properties of the antiferromagnetically coupled Cu-Cu ions due to addition of paramagnetic NO by changes of chemical shift, spin-lattice relaxation time T_1 and hyperfine coupling constant. However, the fairly constant values of those in $\text{Cu}_3(\text{NH}_2\text{btc})_2$ hint at the indirect detection of *N,N*-diazoniumdiolates (NONOate) by chemisorption. A multi-nuclear approach on ^{15}NO loaded $\text{Cu}_3(\text{NH}_2\text{btc})_2$ indicates NONOate as the primary mode of adsorption including NO adsorption at Cu sites. The direct detection of NONOate is confirmed by ^{15}N NMR studies. Multi-nuclear NMR studies on MIL-100(Al) illustrate presence of the extraframework $\text{Al}(\text{OH})_3$ and the adsorption of NO at unsaturated Al sites. Finally, a temperature dependent ^{15}N NMR studies of bulk ^{15}NO is carried out that reveals the fast dynamic equilibrium between NO monomers and dimerized $(\text{NO})_2$.

Die vorliegende Dissertation ist eine Zusammenstellung von sechs Publikationen. Sie handelt von Festkörper-NMR-Studien des biologisch wichtigen Botenstoffs Stickstoffmonoxid (NO) adsorbiert in Cu_3btc_2 , amin-funktionalisiertem Cu_3btc_2 und MIL-100(Al) metallorganischen Gerüstverbindungen (MOFs). Zunächst zeigen ^1H MAS-NMR-Studien an NO-beladenem Cu_3btc_2 und $\text{Cu}_3(\text{NH}_2\text{btc})_2$ die veränderten elektronischen Eigenschaften der antiferromagnetisch gekoppelten Cu-Cu-Paare aufgrund der Zugabe von paramagnetischem NO durch Änderungen der chemischen Verschiebung, der Spin-Gitter-Relaxationszeit T_1 und der Hyperfeinkopplungskonstante. Die nahezu unveränderten Werte dieser Parameter für $\text{Cu}_3(\text{NH}_2\text{btc})_2$ sind dabei der indirekte Nachweis der Bildung von *N,N*-Diazoniumdiolat (NONOate) durch Chemisorption. Ein multinuklearer Ansatz mit ^{15}NO beladenem $\text{Cu}_3(\text{NH}_2\text{btc})_2$ zeigt NONOate als primären Adsorptionsmodus an, einschließlich NO-Adsorption an den Cu-Positionen. Dazu bestätigt ^{15}N NMR den direkten Nachweis von NONOat. Die multinukleare NMR-Untersuchung an MIL-100(Al) veranschaulicht das Vorhandensein von Extraframework $\text{Al}(\text{OH})_3$ und die Adsorption von NO an ungesättigten Al-Positionen. Schließlich wurden temperaturabhängige NMR-Studien von ^{15}NO durchgeführt, die das schnelle dynamische Gleichgewicht zwischen NO Monomeren und dimerisiertem $(\text{NO})_2$ aufdeckt.

* ...S. (Seitenzahl insgesamt)

...Lit. (Anzahl der im Literaturverzeichnis ausgewiesenen Literaturangaben)

Acknowledgements

First and foremost, I would like to thank my supervisor, PD Marko Bertmer, for all I have learned from him and for his continuous help and support in all the stages to carry out this research. His knowledge, support and enthusiasm has been exceptional and the major factor in the success of this work. One could not ask for more from a supervisor.

I am much indebted to Prof. Jürgen Haase for giving me the opportunity to work in his group and providing access to the well-equipped NMR lab for the experiments. His attitude to research inspired me all time, his captivating personality has already made a lifelong impact on me.

I would like to thank all the collaborators with whom I have worked throughout this project, in particular Katharina Peikert, Frank Hoffmann and Prof. Michel Fröba at the University of Hamburg and Benjamin Barth and Prof. Martin Hartmann at the Friedrich Alexander University of Erlangen–Nürnberg.

I thank Prof. Dieter Michel and Prof. Dieter Freude for their guidance, help and friendship. I am grateful to Prof. Andreas Pöpl for his positive encouragement and guidelines. I am further indebted to Prof. Harald Krautscheid for allowing to use his glovebox and chemistry lab for certain samples activation and preparation.

My thanks also go to all my coworkers, PhD fellows, technicians and students for a very pleasant and cooperative working atmosphere, specially Alex, Michael, Daniel, Matthias, Robin, Nataliya and Seungtaik for their help and good friendship. I would like to thank Dr. Winfred Böhlmann for gas loading and glass blower Stephan Eckert for the sealed samples preparation. Furthermore, I am thankful to Gert Klotzsche for resolving all the technical issues, and to Sophie Kirchner for making my stay in Leipzig easier.

I greatly acknowledge the financial support by the Deutsche Forschungsgemeinschaft (DFG) in the frames of the priority program “Porous Metal-Organic Frameworks (MOFs) (SPP1362)”, project Be 2434/4-2.

Nonetheless, the most special thanks go to my parents and my wife Marufa, who give me unconditional mental support and love through all this long process. Finally, I wish one day my daughter Safiya will read this work.

Contents

Contents	v
List of Figures	vii
Abbreviations	ix
1 Motivation	1
2 Introduction	3
2.1 Nitric oxide (NO): A Potent Gasotransmitter	3
2.1.1 Biological action in human biology:	3
2.1.2 Structure and chemistry of NO	4
2.2 NO storage in porous materials	6
2.2.1 Physisorption	6
2.2.2 Chemisorption	6
2.3 Current NO storage materials	7
2.4 Metal-organic frameworks (MOFs)	8
2.4.1 Cu ₃ btc ₂	11
2.4.2 MIL-100(Al)	13
3 Experimental techniques	15
3.1 Nuclear spin interactions in solid-state NMR	15
3.2 NMR Techniques and Pulse Sequences	19
3.3 NMR sample tube preparation	24
3.4 Gas adsorption procedure	26

CONTENTS

4 Overview and enclosed papers	29
References	121
5 Contribution	137

List of Figures

2.1	Diagrammatic illustration of the biological functions of NO.	4
2.2	Schematic presentation of MO diagram for NO.	5
2.3	The vector coupling of NO according to Hund's coupling case (a) is presented.	5
2.4	The physisorption and regeneration of NO at OMS is schematically represented.	6
2.5	NONOate formation and NO regeneration in diethylamine at pH 7.4 is demonstrated.	7
2.6	Generic scheme for the preparation of a MOF from metal ion and ligand by using direct solvothermal synthesis.	8
2.7	Classification of the three classes of MOFs based on the flexibility.	9
2.8	The storage and release of guest molecules from MOF is illustrated.	10
2.9	The structure and building of 3D paddle wheel structure of Cu_3btc_2 from Cu ion and carboxylate ligand is demonstrated.	11
2.10	Schematic presentation of the building of $\text{Cu}_3(\text{RNHbtc})_2$ from the mixture of btc and the four types of (RNH_2btc) ligands.	12
2.11	A representation of NONOate formation and regeneration in UHM-37.	13
2.12	Schematic illustration of MIL-100(Al); hydrated (left) and dehydrated (right).	14
3.1	Schematic diagram of the MAS experiment where the sample is being spun at ($\theta_m = 54.74^\circ$) and its tensor are orientated to the B_0 at θ angle.	19
3.2	Graphical representation of depth pulse sequence.	20
3.3	Schematic diagram of CPMAS technique.	21
3.4	Representation of 3Q MAS pulse program for half-integer spin nuclei.	22
3.5	Schematic illustration of FSLG homonuclear H-H decoupling, with HETCOR pulse sequence.	23

3.6	The pulse sequence for the dipolar INEPT experiment.	24
3.7	Glass tube preparation for NO loading; adapter for sample tube, 4 mm MAS rotor and MOFs loaded sealed sample tube.	25
3.8	Glass tube preparation for NO loading; (a) large special glass tube and (b) small glass tube for ^{15}NO detection.	25
3.9	Pictorial diagram of the vacuum apparatus for gas loading is shown and the green area indicates the total volume of 50 ml.	26

Abbreviations

1D	One-dimensional
2D	Two-dimensional
3D	Three-dimensional
btc	1,3,5-benzene tricarboxylate
CP	Cross polarization
CUS	Coordinatively unsaturated metal site
DMAZn	Di-methyl-ammonium zinc
EPR	Electron paramagnetic resonance
FSLG	Frequency Switched Lee-Goldburg
FTIR	Fourier-transform infrared
HETCOR	Heteronuclear correlation
HKUST	Hong Kong University of Science and Technology
INEPT	Insensitive nuclei enhanced by polarization transfer
MAS	Magic angle spinning
MIL	M aterials I nstitute L avoisier

MOF	M etal O rganic F ramework
MQMAS	Multi-quantum magic angle spinning
NMR	Nuclear magnetic resonance
NO	Nitric oxide
NONOate	<i>N,N</i> diazonium diolate
OMS	Open metal site
PAF	Principle axis frame
PXRD	Powder X-ray diffraction
RSNO	N-nitrosothiol
SPINAL	Small phase incremental alternation decoupling
SQUID	Super conducting quantum interference device
SSB	Spinning side band
SSNMR	Solid-state NMR
TPPM	Two-pulse phase-modulated
UHM	University of H amburg M aterials

Chapter 1

Motivation

Gas storage in solids is becoming more important as a technology, with applications ranging in fields such as energy, the environment, and more importantly in biology and medicine. [1, 2, 3] Porous solid storage materials are also increasingly important to advancements in science, as seen through their use in emergent gas-delivery technologies.[4, 5, 6, 7] For the signaling molecule nitric oxide (NO) adsorption and delivery technologies using porous solid storage materials are gradually more significant for certain biomedical applications as therapeutic agents.[8, 9, 10, 11, 12] The deficiencies of NO biosynthesis have been interconnected to a number of diseases, such as cardiovascular dysfunction, thrombosis and cancer.[7, 9, 13] There are remarkable possibilities for the use of exogenous NO in anti-thrombogenic medical devices, therapeutic and prophylactic processes.[14, 15, 16, 17] A noteworthy proportion of the NO therapy market has therefore necessarily advanced on the targeted delivery of NO to specific sites of the body. Development of medical devices, such as stents and catheters, which use porous materials have received incredible interest in NO delivery.[15, 18, 19, 20] An exemplary gas-storage porous solid should have high adsorption capacity and fast NO kinetics at practical temperature. The reasonably new class of porous materials called metal-organic frameworks (MOFs) which possess chemical tunability and high porosities, is one of the best candidates for delivering NO. This is due to its ability to store significant quantities and then deliver it to specific sites in the body.[13, 18, 21, 22] Furthermore, one of the important features of some MOFs is the presence of an open metal site (OMS), which make room for the non-covalent interaction of NO at OMS [18, 22, 23] and an amine functionality that can store NO covalently as *N,N*-diazoniumdiolates (NONOate).[24, 25, 26, 27, 28]

NO storage technologies using MOFs have been studied by different techniques such as

FTIR,[14, 18] EPR,[29, 29] TGA[14] and XRD.[22] A fundamental understanding of NO interaction with MOFs is still lacking the knowledge of electronic behavior, physio-chemical changes at the atomic scale and the favorable adsorption sites. Interestingly, there is no report for studying NO interaction with MOFs by SSNMR. In this thesis, an approach to study NO interaction with one of the highly studied MOFs Cu_3btc_2 , its amine functionalized derivative and the aluminum based MOF MIL-100(Al), is accomplished by NMR. Recently, SSNMR has been successfully employed for adsorbed small molecules, such as CO_2 , H_2O and CO in Cu_3btc_2 . [30, 31, 32] NMR has advantages over other experimental techniques because it is non-invasive and element-specific, elucidates electronic information at the very atomic scale, exhibits changes after interaction with guest molecules and is suited to non-stoichiometric disordered guest loading.

Therefore, SSNMR is a powerful analytical tool that can elucidate paramagnetic NO adsorption and probe the electronic and chemical properties of MOFs. For this purpose, different relative amounts of NO are loaded in Cu_3btc_2 and its derivatives MOFs, and studied by ^1H , ^{13}C and ^{15}N NMR. Chemical shift, hyperfine interaction and relaxation analysis provide the rich particulars of NONOate formation and NO interaction at OMS. Multi-nuclear NMR study on MIL-100(Al) provided the information on the extraframework site, the quadrupolar parameters and NO adsorption in Al sites. Even the exchange dynamics between NO and $(\text{NO})_2$ with variable temperature is also characterized by ^{15}N NMR.

Chapter 2

Introduction

In this thesis the interaction of NO with MOFs is examined. In the following, a short description relating to the importance of NO and the current ‘know-hows’ for implementing its usage in medicine is presented. In due course, the field of MOFs is presented with the contemplation, why these materials can exhibit promise as a technology for storing and delivering NO.

2.1 Nitric oxide (NO): A Potent Gasotransmitter

Gasotransmitters are a group of small gaseous molecules such as NO, carbon monoxide and hydrogen sulfide that exhibit a signaling function in the body similar to neurotransmitters. However, despite the reputation given to the biological role of these agents, they can be detrimental, even lethal, to an individual’s health and wellbeing in high concentrations. NO is best known for being an atmospheric pollutant as part of NO_X, however, since the late 90’s the scenario has changed and this suspected carcinogen has gained a good reputation as NO has been considered to be a messenger molecule and a fundamental player in human biology. In 1992, NO was recognized as molecule of the year. Six years later, Furchgott, Ignarro, and Murad were awarded the noble prize in medicine, for independently identifying NO as the endothelium-derived relaxation factor (EDRF).[33, 34, 35]

2.1.1 Biological action in human biology:

NO is endogenously produced in a small but biologically significant amount in the body, that is known to modulate cellular functions. NO works as a potent antibacterial agent, which is a key to the cellular basis of memory and a mediator of ischemia injury or cardiovascular

dysfunction.[9, 36, 37] The influence of NO in human biology is shown in figure 2.1. Interestingly, NO translates sexual excitement, maintains proper blood flow without causing systemic vasodilation and hypotension, and inhibits angiogenesis and tumor growth.[38, 39, 40] In addition, NO has immense beneficial effects in wound healing such as modulating inflammation, cell proliferation, matrix deposition and remodeling.[41]

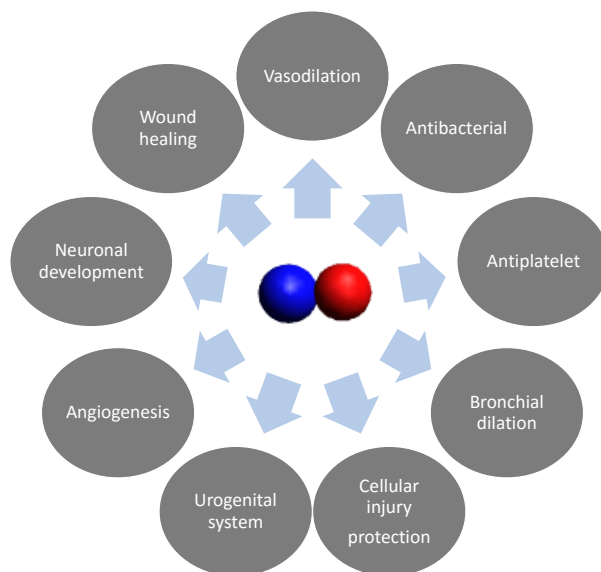


Figure 2.1: Diagrammatic illustration of the biological functions of NO.

2.1.2 Structure and chemistry of NO

Apart from the indispensable biological properties of NO, it also possesses interesting physical characteristics. NO is a diatomic free radical, having 11 valence electrons and possesses a bond length of 1.15 Å and the formal bond order of 2.5. The molecular orbital (MO) diagram for NO is presented in figure 2.2. NO possesses an unpaired electron at the anti-bonding $2\pi^*$ orbital.[42] In accordance with Hund's coupling case (a), the electronic angular momentum L and the spin angular momenta S of NO are assumed to be coupled with the internuclear axis.[43, 44] The components Σ and Λ of the momenta S and L along the intra-molecular axis of the ${}^2\Pi_{1/2}$ state are anti-parallel, creating zero total magnetic moment, ${}^J\mu_r = 0$. Therefore, the ${}^2\Pi_{1/2}$ ground state of free NO is not paramagnetic. However, the lowest rotational level of the first excited ${}^2\Pi_{3/2}$ state of NO is paramagnetic, since the parallel orientation of S and L causes ${}^J\mu_r \neq 0$. Vector coupling of the momenta is presented in figure 2.3, where Ω defines a vector of magnitude $\Omega = \Lambda + \Sigma$ pointing along the internuclear axis. ${}^2\Pi_{3/2}$ state an electron

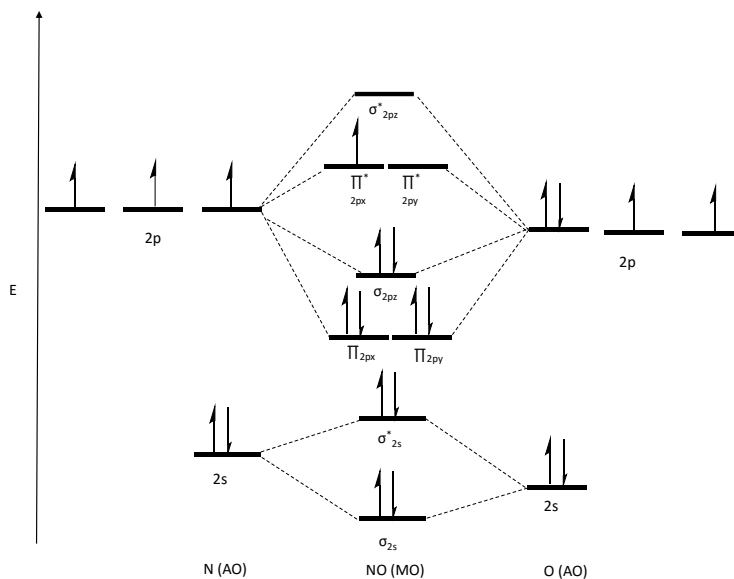


Figure 2.2: Schematic presentation of MO diagram for NO.

Zeeman-splitting constant $g = 0.7776$ is obtained at low temperature by EPR. Upon the adsorption of NO into porous materials, the coupling scheme changes completely because S and L are decoupled. This results in a paramagnetic complex with $S = 1/2$ and a g factor close

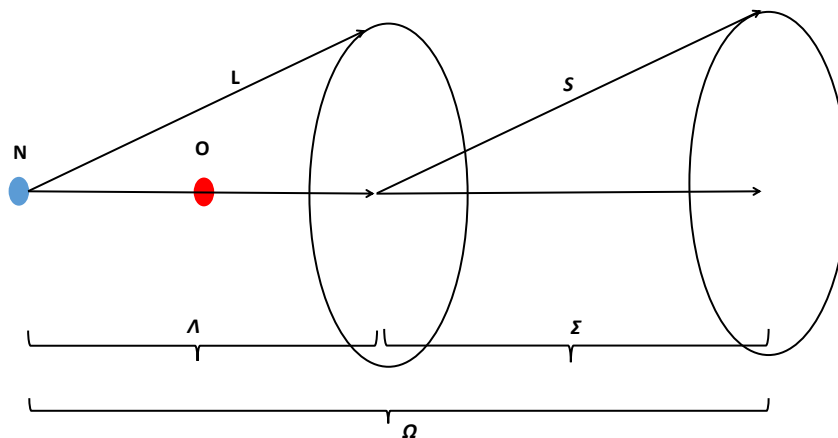


Figure 2.3: The vector coupling of NO according to Hund's coupling case (a) is presented.

to that of a free electron, $g_e \approx 2$ which generates a quite conventional EPR spectrum.[29, 45] Interestingly, the presence of the unpaired electron of NO within the MOF would exert a significant change in the electronic property of the surrounding nuclei. Furthermore, NO dimerizes into diamagnetic $(NO)_2$ under its melting point that is non-observable by EPR. The detection of $(NO)_2$ signal has been reported in a few earlier reports by IR spectroscopy[46], molecu-

lar beam spectroscopy[47] and magnetic susceptibility.[48] The presence of NO and (NO)₂ within variable temperatures (108 K-121 K) has been reported by heat of dissociation,[49] IR intensity,[46] magnetic susceptibility[48] and second virial coefficient.[50] The exceptional magnetic behaviors of NO and (NO)₂ have gained attention for characterization by different experimental techniques.[45, 46, 47, 51] Therefore it is worthy and interesting to understand magnetic behavior of NO by NMR.

2.2 NO storage in porous materials

In recent decades, much research has been done to develop suitable NO storage and release systems. There are mainly two ways of storing NO in a porous material: physisorption and chemisorption. Both modes of NO storage can deliver NO on exposure to water. In the following these two ways of adsorption are briefly discussed.

2.2.1 Physisorption

Generally, NO is weakly bound into the narrow pore wall surface of porous materials. However, some of the porous materials contain OMS, i.e., ion exchanged zeolites and MOFs. That could facilitate the interaction of NO with OMS, viz. Zeolites and MOFs. NO interaction with the OMS is portrayed in figure 2.4. Furthermore, an exchange of water with NO at

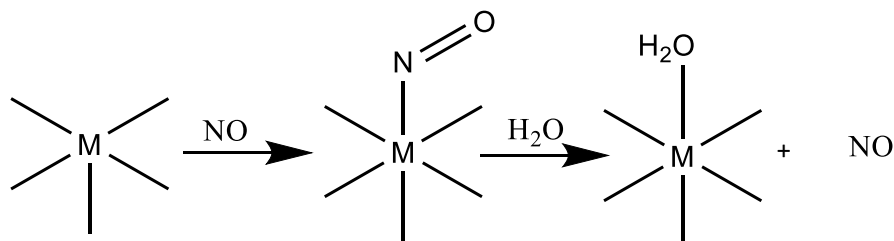


Figure 2.4: The physisorption and regeneration of NO at OMS is schematically represented.

the occupied OMS results the delivery of NO. Morris *et al.* reported the first studies of NO adsorption in porous materials such as, cobalt exchanged zeolite A[7] by FTIR and Gravimetric measurements.

2.2.2 Chemisorption

NO could be adsorbed in the porous material by creating a covalent bond, for example, NONOate or nitrosothiol (RSNO). Over the last few decades, NONOates compounds have been investigated due to their capability of releasing NO. Typically, NONOates can be formed

by the reaction of a primary or secondary amine with 2 moles of NO as shown in figure 2.5. The first report of N-bound NONOate was on diethylamine (DEA/NO) by Drago *et al.*[52] NONOate decomposes at pH 7.4 in body temperature, generating up to 2 moles of NO. Additionally, NONOate possesses a wide range of half-lives for example, diethylenetriamine (DETA/NO) and amino acid proline (PROLI/NO) feature an NO release half-life ($t_{1/2}$) of 20 h and 1.8 s, respectively.[25]

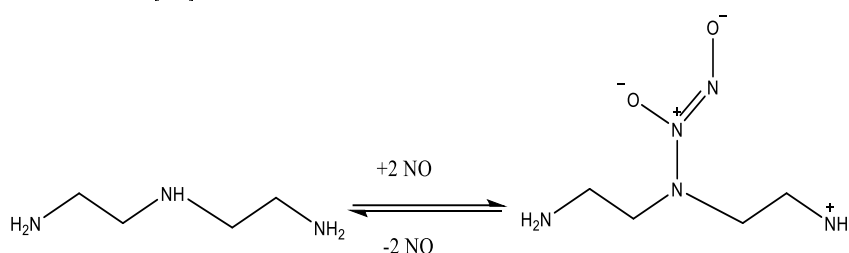


Figure 2.5: NONOate formation and NO regeneration in diethylamine at pH 7.4 is demonstrated.

2.3 Current NO storage materials

Complications arise with the dosage of NO - because it is gaseous at room temperature, and fatal in high dosage, meaning that the NO delivery from a gas cylinder would have to be very tightly controlled and the small amount dosing would be reasonably difficult. In case of NO, any exposure to oxygen causes immediate conversion into extremely toxic NO₂. In addition, the short lifetime of NO hinders systemic delivery to the precise parts of the body. Furthermore, the important parameters for the specific biological actions of NO are site, concentration and duration. For instance, therapeutic agents such as the vasodilator, anti-atherogenic and anti-thrombotic required a very low (picomolar - nanomolar) concentrations of NO, while the antibacterial need relatively higher (micromolar) local concentrations. Therefore, an appropriate material as a NO delivery agent is essential. That could release NO by simulating the concentration and duration of NO delivery, as well as emulating endogenous NO production at the body sites. NO-delivery agents could be manufactured based on NONOate, organic nitrate and RSNO compounds. Such organic moieties can also be assimilated into polymer matrices to form a coating on the device.[11] Furthermore, zeolites have been developed as storage and delivery agents for NO by binding it to the extra-framework transition metal cation.[7] In more recent years, MOFs have been considered for the NO storage application through NO incorporation at OMS and functional groups.[18, 22, 24] The design of MOFs incorporates both features; OMS and NO functionality, that may hold greater therapeutic

potential. They also offer the promise to help deliver the NO exactly when and where necessitated, at the correct dosage level and for the particular length of time necessary to generate that specific response.

2.4 Metal-organic frameworks (MOFs)

MOFs have attracted enormous attention during the last two decades due to the possibility of obtaining a large variety of interesting structures, ultrahigh porosity, enormous internal surface areas and uniform pore size. [2, 3, 53, 54] MOFs can be designed through metal ions or clusters, which act as polyhedral nodes and multi dentate ligand molecules as linkers (see in figure 2.6).

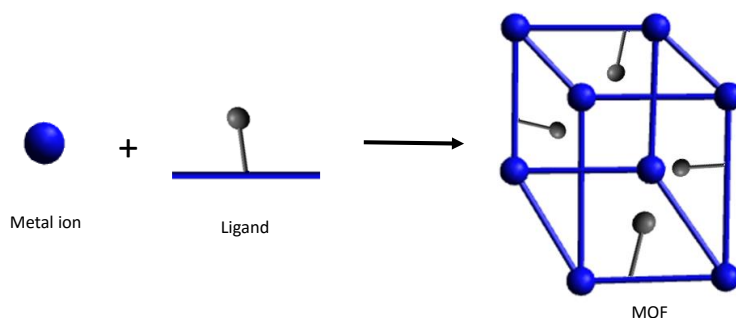


Figure 2.6: Generic scheme for the preparation of a MOF from metal ion and ligand by using direct solvothermal synthesis.

In MOFs, the interactions of the metal ions and the linker molecules vary widely, and could be ionic, covalent, coordinate interaction, as well as hydrogen bonding and $\pi - \pi$ interaction.[55] Most of the transition elements and even the main group elements (e.g., Al^{3+} , Ga^{3+} , Mg^{2+}) can be used as metal nodes in MOFs. Aromatic carboxylates or N-donor ligands are frequently chosen as rigid multi-dentate linkers [56, 57]. These multi-dentate ligands chelate metal ions and lock them into rigid and directional clusters, with a defined geometrical shapes referred to as secondary building units (SBUs). Consideration of the geometric and chemical attributes of the SBUs and linkers lead to the prediction of framework topology, robust structure and high porosity. In addition to the directly synthesized framework, it is also possible to amend the framework after the primary synthesis. This tactic known as post synthetic modification is commonly used to introduce functionality into the pores and channels of the material, required for specific purposes.[27, 58]

The tailoring of these materials for specific applications is one of the major advantages of MOFs over more traditional porous materials. The incorporation of functionality into the MOFs has been attained by modifying ligands with a specific substituent or pendant groups,

for example, $-\text{Br}$, $-\text{NH}_2$ and $-\text{CH}_3$. Another advantage of MOFs over other porous materials, is that OMS can be generated by the eviction of the coordinated water by activation.[59] Nevertheless, the stability of MOFs is still a matter of concern in comparison to zeolites. The relatively weak metal-ligand interaction that exists in MOFs, that makes them less thermally stable compared to zeolites.

Classification of MOFs

Regarding the spatial dimensions, the SBUs can consist of inorganic chains leading to four types of MOFs structures, illustrated as cavities (0D), channels (1D), layers (2D) and intersecting channels (3D).[4] Based on the dynamic structural transformation, Kitagawa *et al.*[4] distinguished the following three classes of flexible porous framework as shown in figure 2.7; type (I) the framework of ‘1st generation’ collapses irreversibly on the removal of the guest, type (II) the framework of ‘2nd generation’ shows the structural shift of the network due to the exchange of guest molecules, and type (III) the framework of ‘3rd generation’ refers to the flexible framework which change most of the time in response to external stimuli. MIL-53

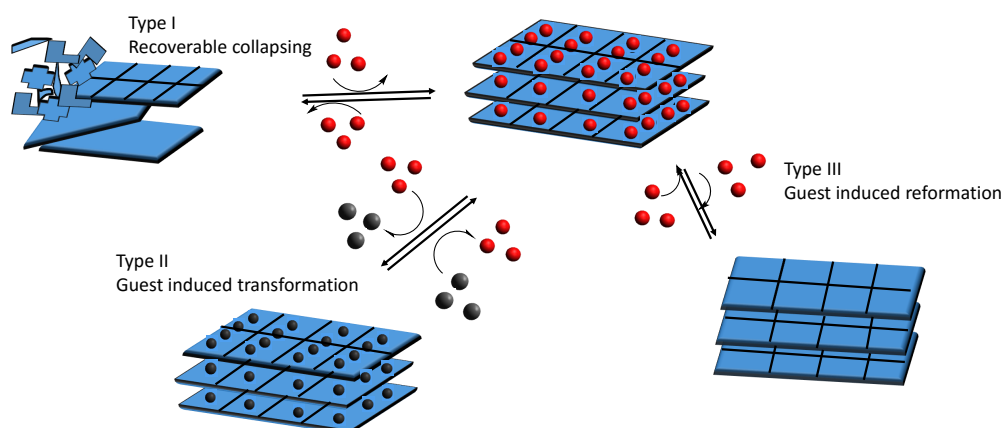


Figure 2.7: Classification of the three classes of MOFs based on the flexibility.

is one of the typical archetypal of the 3rd generation framework, which displays a ‘breathing effect’ upon the adsorption of CO_2 , H_2O or in the presence of external stimuli such as temperature.[2, 60, 61] Similar to the breathing effect, another interesting distinctive singularity of flexible framework is the ‘gate-pressure effect’ which is reported for DUT-8(Ni).[62]

Application of MOFs:

One of the hallmarks of MOFs are its topologically diverse structures with larger pores for specific applications. A larger pore in the MOFs is usually generated by the replacing

carboxylate linker with other longer aromatic carboxylates ligands, e.g., biphenyl and terphenyl. In iso-recticular MOFs (IRMOFs) pore sizes up to 18 nm are achieved by adopting a linker labilization method.[63, 64] High porosity, large pore sizes and enormous specific surface area of MOFs provide endless possibilities; such as gas storage, cost-effective gas separation, gas purification etc.[65, 66, 67, 68, 69] Studies pertaining to hydrogen storage, the selective separation of gas mixtures (N_2/CO_2), and the separation of environment pollutants, CO_2 using MOFs have been demonstrated well in the various works.[70, 71, 72, 73] Figure 2.8 presents gas adsorption and delivery from MOFs. Technological developments such as labs-

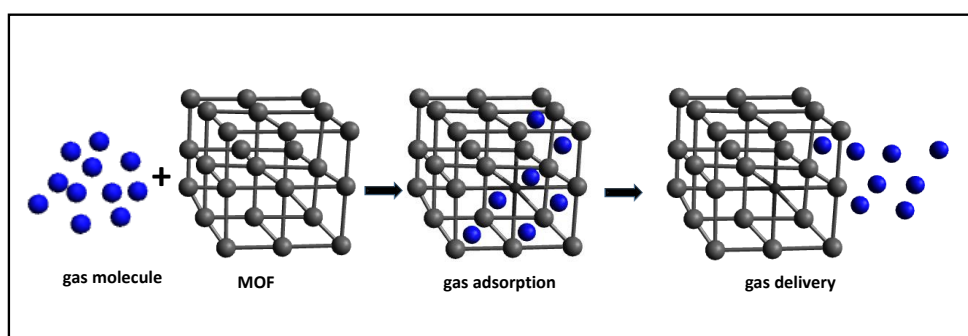


Figure 2.8: The storage and release of guest molecules from MOF is illustrated.

on-a-chip, microfluidic devices, solar cells, sensors and light emitters are attainable by the microfabrication of MOFs.[74, 75, 76, 77, 78, 79] The sequestration of heavy metal palladium, environmental hazard PAH and peptides from biomolecules have been achieved by combining magnetic nano species to MOFs.[80, 81, 82] MOFs with homogeneous thin films have opened up several avenues of research into electrical and electronic applications, for instance new types of semiconductor[83], electrochemical sensors and electrodes.[84] The perovskite type MOFs have attracted interest over the years due to the coexistence of electric and magnetic orders within certain compositions.[85, 86] The advantages of MOFs as heterogeneous catalysts are seen as easy separation, high yield, shape and size selectivity.[87, 88, 89, 90] MOFs have been recently used as potential nanocarrier platforms in biomedical applications such as MRI contrast agents, bioactive MOFs and drug storage.[91, 92, 93] Petroleum refinement and even the upgrades of biogas is attainable by using iron(III)-pyrazolate MOF and MOF-508.[94, 95, 96]

Certainly, the intelligent architecture and topology of MOFs make them prospective for unique applications. Coming back to the discussion on the construction units of MOFs, the aromatic carboxylates are the most extensively studied poly-functional ligands for the successful synthesis of MOFs. Among the various MOFs, the following thesis will investigate some of the most highly studied aromatic carboxylates-based MOFs, which are Cu_3btc_2 and

its amine derivatives, as well as MIL-100(Al) for NO adsorption. Furthermore, toxicity of copper containing MOFs is also considered in accompanying to the bio-medical applications. That may be viewed as a usual disadvantage of Cu-based MOFs. In recent times, iron (Fe) containing MOFs e.g., MIL-127(Fe), MIL-100(Fe) and MIL-53(Fe)[97, 98] highlight great potential to work as bio-active MOFs. Unfortunately, NMR studies on Fe containing MOFs have proven difficult, due to the strong ferromagnetic nature of Fe. Therefore, an aluminum based MIL-100(Al), which is analogous to Fe containing MOFs, could be used in its place to understand NO adsorption behavior by NMR. A short description of these MOFs is provided in the following section.

2.4.1 Cu_3btc_2

Cu_3btc_2 also known as HKUST-1, has a high surface area and large pore volume.[59] This cubic 3D MOF possesses a space group of $Fm\bar{3}m$ and large interconnecting square channel which are surrounded by small tetrahedral side pockets. Cu_3btc_2 and all its amine functionalized derivatives were obtained from professor Fröba's group at the University of Hamburg. The framework of Cu_3btc_2 is based on a dimeric copper carboxylate unit, the so-called paddle wheel unit, that is connected via btc to give a three-dimensional framework. This is presented in figure 2.9. The two copper ions in the paddlewheel are coordinated to two water molecules to

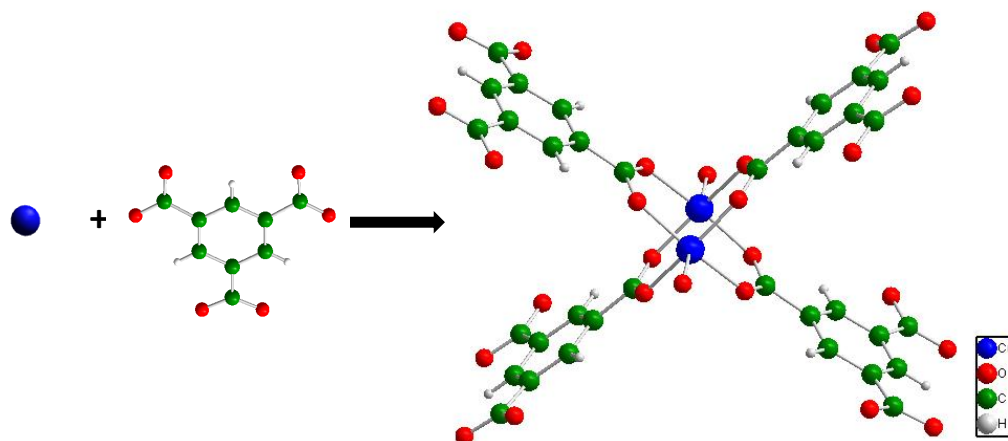


Figure 2.9: The structure and building of 3D paddle wheel structure of Cu_3btc_2 from Cu ion and carboxylate ligand is demonstrated.

create a double square pyramidal geometry in the hydrated form. Interestingly, in Cu_3btc_2 , two copper ions are antiferromagnetically coupled resulting in $S=0$ ground electronic state and $S=1$ excited electronic state above 90 K.[99, 100] In NMR observation, these materials perform as a paramagnet due to the presence of $S=1$. Moreover, the paramagnetic behavior strongly

2. Introduction

influences the magnetic properties of the surrounding nuclei of the metal sites.[101, 102, 103] Additionally, for each copper atom a weakly bound water molecule is present at the axial coordination site, which can be detached easily by its activation in vacuum. This will make the copper site affordable for other small molecules.[104, 105] Thus, the rigid porous structure of the Cu_3btc_2 combined with the accessibility of OMS upon dehydration has led to a lot of interest in adsorption, separation, humidity sensor and catalysis applications.[78, 82, 106, 107, 108, 108] SSNMR has proven well-suited for demonstrating the paramagnetic behavior of Cu_3btc_2 , in spite of the difficulty arising from line broadening.[30, 31, 32] NMR studies of Cu_3btc_2 presented the strong paramagnetic shift and the dynamic adsorption process of small molecules e.g., H_2O , CO , CO_2 , and NH_3 at variable temperatures.[30, 32, 109] NO adsorption in Cu_3btc_2 , which was first reported by Morris *et al.*, by FTIR and gravimetric analysis showed a seven fold increase in adsorption capacity compared to zeolite A.[14, 18]

$\text{Cu}_3(\text{NH}_2\text{btc})_2$ is a primary amine functionalized Cu_3btc_2 ,[110] also known as UHM-30 (UHM = University of Hamburg Materials). Apart from this, four other secondary amine functionalized mixed-linker MOFs, ($\text{Cu}_3(\text{NHRbtc})_2$), known as UHM-36, UHM-37, UHM-38 and UHM-39 were also studied in this thesis. These MOFs were synthesized by mixing of H_3btc with either $\text{H}_3\text{MeNHbtc}$, $\text{H}_3\text{EtNHbtc}$, $\text{H}_3^n\text{PrNHbtc}$ or $\text{H}_3^i\text{PrNHbtc}$. [111] The illustration of the formation of these mixed linker MOFs is presented in figure 2.10.

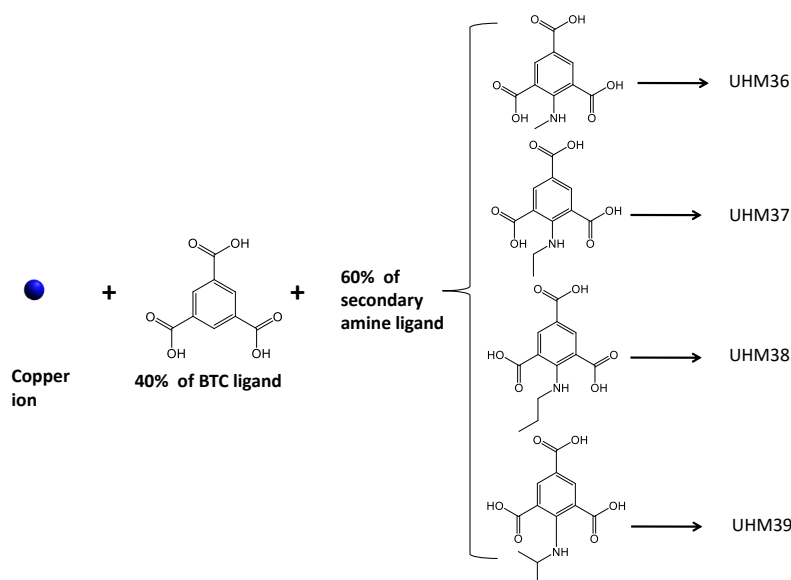


Figure 2.10: Schematic presentation of the building of $\text{Cu}_3(\text{RNHbtc})_2$ from the mixture of btc and the four types of (RNH_2btc) ligands.

The solvo-thermal method is primarily applied for the synthesis of these MOFs.[110, 111]

Interestingly, all of these amine functionalized Cu_3btc_2 are isostructural to Cu_3btc_2 . In this context, amine functionalized Cu_3btc_2 can be covalently bonded to NO and formed NONOate functional groups which are attractive for NO release. Some other MOFs such as Cu-TDPAT, UMCM-1, IRMOF-3 and 4-(methylamino)-pyridine(4-Map) possessing amine groups have been reported for forming NONOate as identified by FTIR.[24, 27, 112] FTIR study also revealed NONOate formation in UHM-37,[111] which is represented in figure 2.11.

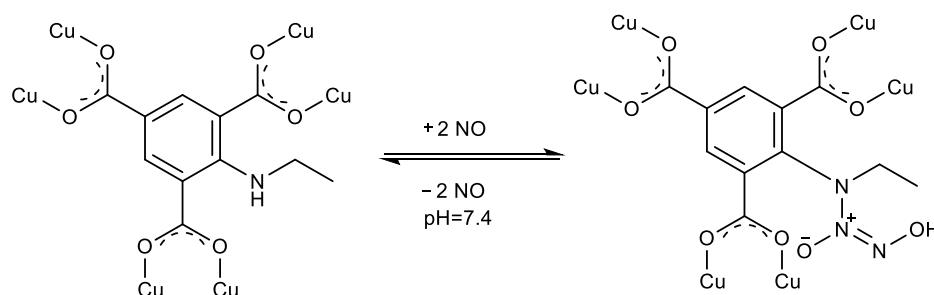


Figure 2.11: A representation of NONOate formation and regeneration in UHM-37.

2.4.2 MIL-100(Al)

MIL has gained recognition for gas delivery technology and a few of them such as, MIL-53(Fe), MIL-100(Fe) are promising candidates for drug delivery.[97, 113, 114, 115] In this work, aluminum trimesate MIL-100(Al), which is similar to biocompatible MIL-100(Fe), has been elaborately examined. MIL-100(Al) is synthesized by solvo-thermal method with the reaction of $\text{Al}(\text{NO}_3)_3 \cdot 9\text{H}_2\text{O}$ and btc under ambient pressure (see figure 2.12).[116] As synthesized MIL-100(Al) is received from professor Hartmann's group at the Friedrich–Alexander University of Erlangen–Nürnberg. In MIL-100(Al), μ_3 -oxo-centered metal trimers are connected to btc ligands forming a tetrahedral cage. Two water molecules and one hydroxide are bonded to the three aluminum atoms in the μ_3 -oxo trimer. Later water molecules can be removed by heating, which generates OMS. This MOF demonstrated a remarkable stability towards water adsorption.[117] The presence of OMS in MIL-100(Al) showed its potential in water and CO adsorption, and as a heterogenous catalyst.[118, 119, 120] Adsorption and release of the NO was evaluated in MIL-88(Fe) type MOFs by XRD and in situ IR spectroscopy.[121] NO coordination on metal sites of (MIL)-100(Fe or Cr) and MIL-127(Fe) has been revealed by situ IR spectroscopy studies, and that studies also demonstrated the dependence of NO adsorption on the nature of the metal cation, the structure and the presence of additional iron(II).[97] Recently, NO adsorption in MIL-100(Al) at low temperatures have been demonstrated by EPR studies.[29, 122]

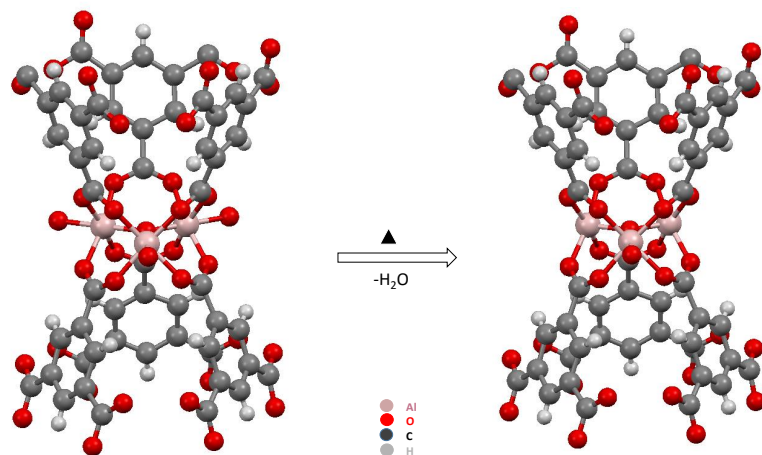


Figure 2.12: Schematic illustration of MIL-100(Al); hydrated (left) and dehydrated (right).

Chapter 3

Experimental techniques

3.1 Nuclear spin interactions in solid-state NMR

This section covers the nuclear spin interactions, which are relevant for the NMR experiments executed throughout this work. Unless stated otherwise, the information presented here is based on standard NMR textbooks.[123, 124, 125, 126, 127] Nuclear spin interactions can be separated in two contributions; external interaction and internal interaction. The total Hamiltonian for a nuclear spin is the sum of these two terms:

$$\hat{\mathcal{H}} = \hat{\mathcal{H}}_{ext} + \hat{\mathcal{H}}_{int} \quad (3.1)$$

The external part of the spin Hamiltonian, $\hat{\mathcal{H}}_{ext}$, comprises of the interaction of spins with the static field, B_0 , and RF field, B_{RF} , which is represented as follows:

$$\hat{\mathcal{H}}_{ext} = \hat{\mathcal{H}}_{static} + \hat{\mathcal{H}}_{RF} \quad (3.2)$$

The internal spin Hamiltonian, $\hat{\mathcal{H}}_{int}$, expresses the interactions of spins with magnetic and electric fields that are generated within the sample's environment. The internal spin Hamiltonian, $\hat{\mathcal{H}}_{int}$, can be written as,

$$\hat{\mathcal{H}}_{int} = \hat{\mathcal{H}}_{CS} + \hat{\mathcal{H}}_{DD} + \hat{\mathcal{H}}_Q + \hat{\mathcal{H}}_J + \hat{\mathcal{H}}_{HF} \quad (3.3)$$

where, $\hat{\mathcal{H}}_{CS}$, $\hat{\mathcal{H}}_{DD}$, $\hat{\mathcal{H}}_Q$, $\hat{\mathcal{H}}_{HF}$ and $\hat{\mathcal{H}}_J$ represents Hamiltonian of chemical shift, dipolar coupling, quadrupole coupling, hyperfine coupling and J-coupling respectively.

Chemical shift:

Chemical shift of an atom in a molecule emerges from the nuclear shielding effect of the applied magnetic field, caused by the induced magnetic field owing to the circulation of the surrounding electrons. The corresponding chemical shielding Hamiltonian, which acts on spin I can be written as:[123, 124]

$$\hat{\mathcal{H}}_{cs} = -\gamma\hat{\mathbf{I}} \cdot \boldsymbol{\sigma} \cdot \mathbf{B}_0 \quad (3.4)$$

where \mathbf{B}_0 is the applied magnetic field, $\boldsymbol{\sigma}$ is the second-rank Cartesian tensor of nuclear shielding and γ is the gyromagnetic ratio. Shielding tensor defines the alignment of chemical shielding with respect to the Cartesian axis of the molecule. The symmetric shielding tensor which contributes to the frequency shift in NMR spectra, can be diagonalized to its own principal axis frame (PAF) as: [128]

$$\boldsymbol{\sigma}_s = \begin{pmatrix} \sigma_{11} & 0 & 0 \\ 0 & \sigma_{22} & 0 \\ 0 & 0 & \sigma_{33} \end{pmatrix} \quad (3.5)$$

where σ_{11} , σ_{22} and σ_{33} are the principal components of the shielding tensor and defined as $\sigma_{33} \leq \sigma_{22} \leq \sigma_{11}$. The principal value is can be expressed as the isotropic value (σ_{iso}) the span (Ω) and the skew (κ). They are defined as follows:

$$\begin{aligned} \sigma_{iso} &= \frac{\sigma_{11} + \sigma_{22} + \sigma_{33}}{3} \\ \Omega &= \sigma_{11} - \sigma_{33} \\ \kappa &= \frac{3(\sigma_{22} - \sigma_{iso})}{\Omega} \end{aligned} \quad (3.6)$$

The orientation of the principal axes is determined by the electronic structure of the molecule. Practically, the chemical shielding is not measured directly in NMR experiments; instead, it is reported in ppm scale as:

$$\delta = \frac{\nu - \nu_{ref}}{\nu_{ref}} \times 10^6 \quad (3.7)$$

with the frequency of the sample, ν and the reference, ν_{ref} .

Dipolar coupling:

The magnetic moments of nuclear spins interact through space; this is known as dipole–dipole

or dipolar coupling. The corresponding Hamiltonian for dipolar coupling between spins I and S is given by :[124, 126, 127]

$$\hat{\mathcal{H}}_{dd} = - \left(\frac{\mu_0}{4\pi} \right) \gamma_I \gamma_S \hbar \left(\frac{\hat{\mathbf{I}} \cdot \hat{\mathbf{S}}}{r^3} - 3 \frac{(\hat{\mathbf{I}} \cdot \mathbf{r})(\hat{\mathbf{S}} \cdot \mathbf{r})}{r^5} \right) \quad (3.8)$$

In Eq. (3.8), \hbar ($\hbar = h/2\pi$) is Planck's constant, γ_I and γ_S are gyromagnetic ratio of I and S spins, μ_0 is vacuum permittivity and r is the inter-nuclear distance between spins. There are two possible cases of dipolar coupling; homonuclear and heteronuclear dipolar coupling. The secular part of dipolar coupling Hamiltonian for homonuclear coupled like spins I and S can be shown as: [124]

$$\hat{\mathcal{H}}_{dd}^{homo} = -D/2(3\cos^2\theta - 1) \left(3\hat{I}\hat{S} - \hat{\mathbf{I}} \cdot \hat{\mathbf{S}} \right) \quad (3.9)$$

The angle θ describes the orientation of the inter-nuclear vector with respect to the external magnetic field, and D is the dipolar coupling constant. In the case of heteronuclear dipolar coupling between different I and S spins,

$$\hat{\mathcal{H}}_{dd}^{hetero} = -D(3\cos^2\theta - 1) \left(\hat{I}\hat{S} \right) \quad (3.10)$$

Hyperfine Interaction:

The hyperfine interaction is generated from the interaction between the nuclear spin and the magnetic moment of an unpaired electron. The hyperfine interaction originates from the interaction between electron and nuclear spin where the Hamiltonian can be described as,

$$\hat{\mathcal{H}}_{HF} = \hat{\mathbf{I}} \cdot \mathbf{A} \cdot \hat{\mathbf{S}} \quad (3.11)$$

with \mathbf{A} being the hyperfine interaction tensor and \mathbf{I} and \mathbf{S} stand for the nuclear and electron spin, respectively. The total observed hyperfine shift, δ^{hyp} is represented as:

$$\delta^{hyp} = \delta^{contact} + \delta^{dipolar} \quad (3.12)$$

The Fermi contact shift, $\delta^{contact}$ is directly proportional to the amount of unpaired electron spin density at the nucleus. The Fermi contact interaction is isotropic in nature.[129, 130, 131, 132] This effect can be calculated by,

$$\delta^{contact} = A_{iso} \frac{(g_{\parallel} + 2g_{\perp}) \mu_B S(S+1)}{9\gamma_I \hbar kT} \quad (3.13)$$

where μ_B is the Bohr magneton, k is the Boltzmann constant, g_{\parallel} and g_{\perp} are parallel and the perpendicular components of the electron g-tensor, T is temperature and S is the effective electron spin quantum number.

The pseudo contact shift, $\delta^{dipolar}$, is a magnetic dipole-dipole interaction between the observed nuclei and the unpaired electron. The electron-nuclear dipolar coupling arises through space and it is anisotropic. This contribution can be expressed as: [129, 133]

$$\delta^{dipolar} = \left(\frac{\mu_0}{4\pi}\right) \frac{\mu_B^2 S(S+1)}{9\kappa T} \frac{3(\cos^2\theta - 1)}{r^3} (g_{\parallel}^2 - g_{\perp}^2) \quad (3.14)$$

where μ_0 is the vacuum permeability, r is the electron-nuclear distance, θ is the angle between the vector r and the molecular z axis. As can be seen, both the contact and the dipolar part of the hyperfine interaction are temperature dependent, thereby, the reported shift values have to be specified with the measurement temperature. The anisotropic hyperfine coupling is determined from the simulation of sideband patterns by assuming an isotropic g-tensor and a point electron dipole at the metal center.[134]

Quadrupole coupling:

Nuclei with spin $I > 1/2$ possess a quadrupole moment Q which interacts with the electric field gradient (EFG) generated by the surrounding of the nucleus, and this interaction is known as quadrupole coupling. EFG of the quadrupolar nucleus can be defined by a symmetric traceless tensor, i.e., $V_{xx} + V_{yy} + V_{zz} = 0$ in the principal axis system (PAF). The PAF components of the EFG tensor are defined as $|V_{xx}| \leq |V_{yy}| \leq |V_{zz}|$. In the PAF frame, the quadrupole hamiltonian is given by:[126, 127]

$$\hat{\mathcal{H}}_Q = \frac{e^2qQ}{4I(2I-1)} \left(3\hat{I}_{z^{PAF}}^2 - \hat{I}(\hat{I}+1) + \eta[\hat{I}_{x^{PAF}}^2 - \hat{I}_{y^{PAF}}^2] \right) \quad (3.15)$$

In this equation, electric quadrupole moment, eq is V_{zz}^{PAF} and η is the asymmetry parameter having a value from $0 \leq \eta \leq 1$ and is defined as:

$$\eta = \frac{V_{xx} - V_{yy}}{V_{zz}} \quad (3.16)$$

The constant e^2qQ/h is known as the quadrupole coupling constant, C_Q . The quadrupole coupling constant can also be expressed in terms of the quadrupole frequency, ν_Q :

$$\nu_Q = \frac{3e^2qQ}{h2I(2I-1)} = \frac{3C_Q}{2I(2I-1)} \quad (3.17)$$

3.2 NMR Techniques and Pulse Sequences

Magic Angle Spinning (MAS) is primarily applied in this work. In addition, some other important pulse sequences are employed throughout this thesis. This section presents a short description of the MAS technique, and used pulse sequences are briefly discussed.

Magic Angle Spinning (MAS)

MAS is used frequently in the mainstream of solid-state NMR experiments. One of its principal task is to remove the effects of CSA and the hetero and homonuclear dipolar coupling as well as 1st order quadrupolar effect. MAS provides a line-narrowing effect on the central transition lineshape of half-integer quadrupolar nuclei; however, a complete removal of the 2nd order quadrupolar effect by this technique is impossible. The demand of MAS for the removal of homonuclear dipolar coupling effects is rapidly increasing, that can be achieved by using ultra high spinning speed. In solution, the rapid tumbling of the molecules means that the angle θ describing the orientation of the shielding/dipolar tensor with respect to the applied field B_0 , is rapidly averaged over all possible values. The molecular spatial orientation dependence is of the form $(3\cos^2\theta-1)$. In the MAS NMR experiment, the sample is rotated rapidly in a cylindrical rotor along a spinning axis, which is oriented at the magic angle, ($\theta_m = 54.74^\circ$), as shown in figure 3.1. Therefore, the averaging of the orientation dependence of

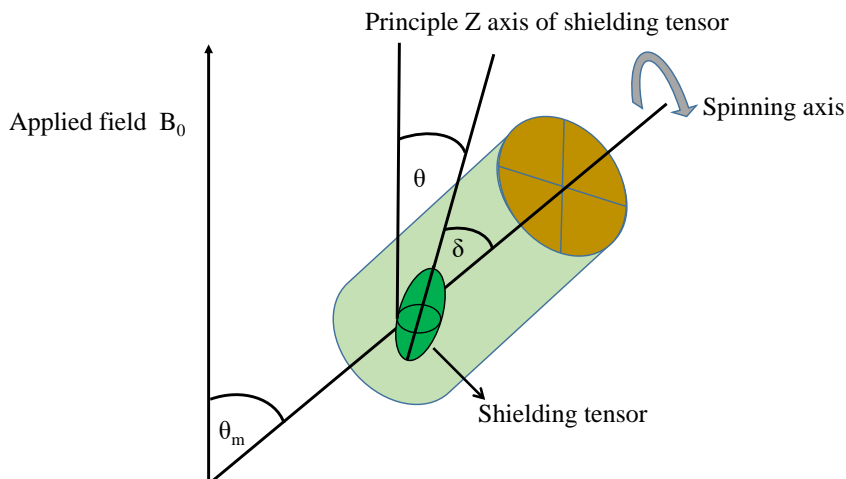


Figure 3.1: Schematic diagram of the MAS experiment where the sample is being spun at ($\theta_m = 54.74^\circ$) and its tensor are orientated to the B_0 at θ angle.

the nuclear spin interaction, $(3\cos^2\theta-1)$ can be written as:[124, 135]

$$3\cos^2\theta - 1 = 1/2(3\cos^2\theta_m - 1)(3\cos^2\delta - 1) \quad (3.18)$$

where, δ is the angle between the principle z-axis of the shielding tensor and the spinning axis. If θ_m is set to 54.74° , then $(3\cos^2\theta_m-1) = 0$ which averages out $(3\cos^2\theta-1)$ to zero. In order to average out the anisotropic interactions effectively to zero, the sample must be spun faster than the anisotropy of the sample. Slower spinning produces a set of spinning sidebands, which radiate out from the isotropic shift.

DEPTH

The DEPTH sequence is a method to eliminate probe background resonances due to instrumental hardware materials; e.g., probe stator and rotor tips, glues and markers.[136, 137] The DEPTH sequence is composed of one $\pi/2$ initial pulse and two consecutive π pulses without delay in between them, (see figure 3.2) and embedded with 16 step EXORCYCLE [138] phase cycles. The initial and two consecutive π pulses function complementarily and prove most effective in removing background signals from both strong and weak B_{RF} fields. The phase cycling functions to abolish the coherent components those are a consequence of the imperfect π pulses and the efficiency of background suppression is determined by the relative strength of B_{RF} field experienced by sample versus background spins.[139]

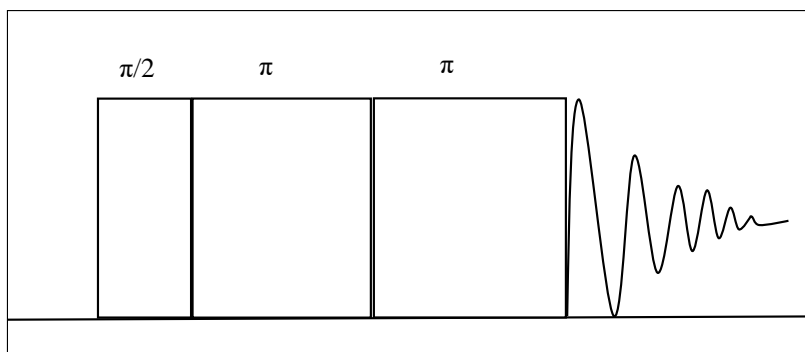


Figure 3.2: Graphical representation of depth pulse sequence.

Inversion recovery

Relaxation times or rates provide an important measurable quantity to gain an understanding into structural and dynamic features of a material. Longitudinal relaxation T_1 is associated with an energy transfer to a lattice. In general, T_1 is usually determined using the inversion recovery sequence $\pi - t - \pi/2$. [140, 141] The main idea behind the sequence is to invert the bulk magnetization using a π pulse. Immediately after the inversion, the system is then left to relax for the delay time (t) before the signal is recorded with the $\pi/2$ pulse. During the experiment, delay time (t) between the two pulses is varied, and the recovery of

the corresponding magnetization is recorded. Finally, the return of the magnetization to the equilibrium is expressed as the following equation:

$$M_z(t) = M_0 \left(1 - 2\exp^{-\frac{t}{T_1}}\right) \quad (3.19)$$

where $M_z(t)$ is the bulk magnetization at time t and M_0 is the equilibrium magnetization.

Dipolar decoupling

High resolution in the NMR spectra can be attained by the high power decoupling to remove heteronuclear dipolar coupling, as a source of line broadening. In the case of I-S system, generally S spin is measured while I spin is decoupled. The decoupling of I-S is removed by irradiating the I spin with a continuous RF field.[124] Several decoupling sequences, e.g., TPPM, XiX (X inverse -X) and SPINAL are used in this work.[124, 142, 143, 144, 145] All of these sequences infer high power irradiation during the acquisition.

CPMAS

Cross polarization is one of the most important pulse sequence techniques in SSNMR.[146, 147] It works via dipolar coupling and can collect direct information on the structural, motional and conformational characteristics of the compounds. By the application of the CP technique, the signal to noise ratio for the dilute spin S can be increased by a maximum factor of $\frac{\gamma_I}{\gamma_S}$. Furthermore, the relaxation delays of the CP experiments typically are reduced due to the faster I spins relaxations time, I and S spins are excited together with a matching spin-lock. In the CP experiment, $\pi/2$ pulse (see figure 3.3) is applied on I spin, which creates

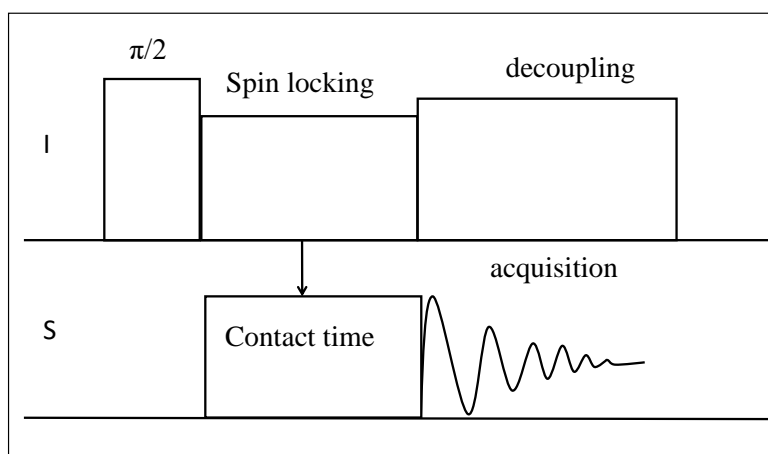


Figure 3.3: Schematic diagram of CPMAS technique.

transverse magnetization. Then a spin locking pulse is applied to lock the transverse magneti-

zation. Another long pulse is applied to the S spins, and this time period is known as contact time. During the contact time, I magnetization is transferred to S magnetization.[147] For the CPMAS experiment, the contact pulse power is adjusted in order to achieve the Hartmann-Hahn condition ($\gamma_I B_I = \gamma_S B_S$ or $\omega_I = \omega_S$) by changing power on each of the channels. However, Hartmann-Hahn matching profile in CPMAS NMR shows a mismatch, if the MAS frequency is on the order of the dipolar coupling of the samples. In general, to overcome mismatching for fast rotor spinning rates, a ramped-amplitude (RAMP) CP pulse sequence is employed. Finally, the S spin magnetization is observed during the decoupling on the I channel.

MQMAS

MQMAS is a 2D experiment by which the multiple-quantum transitions are combined with MAS to remove the anisotropy of the quadrupole interaction of half integer nuclei. Highly resolved NMR lines, isotropic chemical shifts and quadrupolar parameters are obtained for quadrupolar nuclei by applying this pulse sequence.[148] The first pulse excites multiple-quantum coherences (pQ), and that evolves at the time t_1 , as seen in figure 3.4. Generally, coherence can be associated with the transitions between the different spin states. The second pulse converts pQ back to zero-quantum coherence. An additional selective $\pi/2$ pulse for the

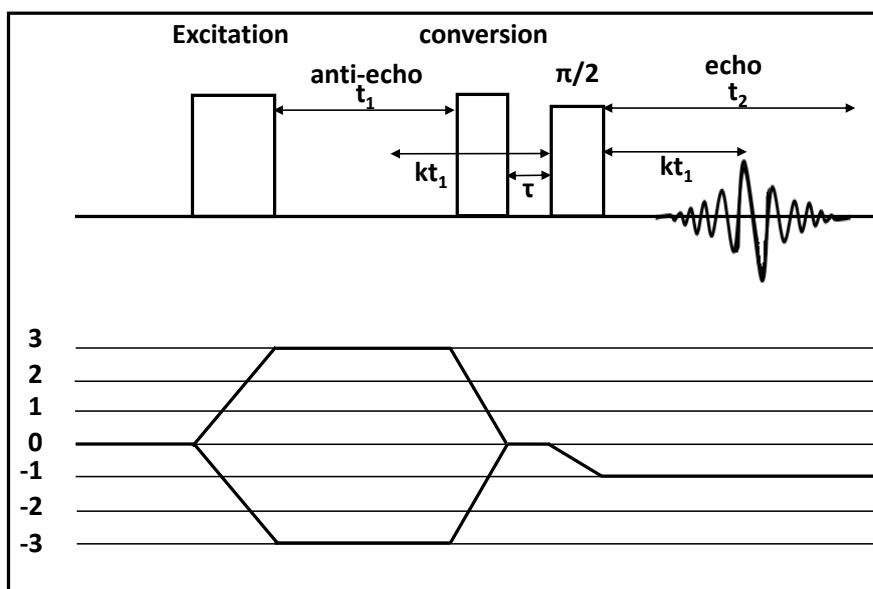


Figure 3.4: Representation of 3Q MAS pulse program for half-integer spin nuclei.

central transition is added at the end of the two-pulse by which non-observable zero-quantum

coherences converts into observable single-quantum (-1) Q coherence. After evolution time, kt_1 the fourth-rank quadrupolar terms at t_1 is refocused. Subsequently, an FID is recorded in t_2 , as displayed in figure 3.4.[149, 150] The value of k is set according to different spin quantum numbers and pQ coherences. Fourier transformation results in a 2D spectrum by which f_1 and f_2 exhibits isotropic and the anisotropic shift, respectively.

Heteronuclear correlation (HETCOR)

Hetcor experiment is important for achieving high resolution of the abundant spins I by a correlation with dilute S spins. In the 2D HETCOR experiments, a spatial correlation between two heteronuclei is accomplished by dipolar coupling and chemical shift.[151] In HETCOR, a $\pi/2$ pulse is applied on the I spins and allowed the magnetization to evolve at its characteristic frequency in t_1 time, as represented in figure 3.5. During the evolution time t_1 another pulse is aligned with the I spins, then the magnetization is subjected to frequency-switched Lee-Goldburg (FSLG) homonuclear decoupling.[151, 152] At that time, the heteronuclear dipolar coupling is averaged by MAS, while the homonuclear dipolar coupling is averaged by both the MAS and FSLG pulse train. Finally, I magnetization is transferred to S spins by a contact pulse, and an FID of S spins is acquired with the decoupling of I spins. By adjusting different CP time, one could establish intra-/ internuclear connectivities in 2D spectrum, which in turn provide insights into the local structures of the materials.

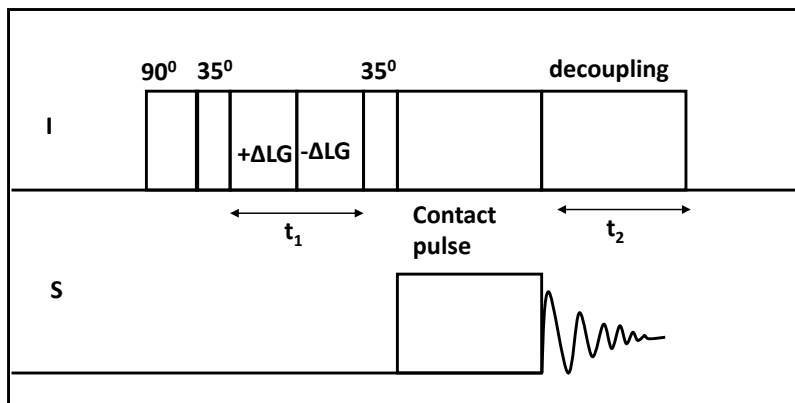


Figure 3.5: Schematic illustration of FSLG homonuclear H-H decoupling, with HETCOR pulse sequence.

Dipolar INEPT

Insensitive nucleus enhancement by polarization transfer (INEPT) is another useful pulse sequence for transferring spin population from one spin to another by which the intensity

of low gyromagnetic nuclei enhances. A modified INEPT sequence [153, 154] is applied for paramagnetic solid samples, to differentiate different carbon moieties, e.g., CH, CH₂, CH₃ and C_q by the τ -dependence of signal intensities in dipolar INEPT experiments. That can be achieved by the application of re-coupling based polarization transfer of I to S spins. Therefore, a rotor synchronous echo sequence is applied to I and S spins through the initial two rotor cycles ($2\tau_R$), as shown in figure 3.6. That reintroduces I-S dipolar interaction by

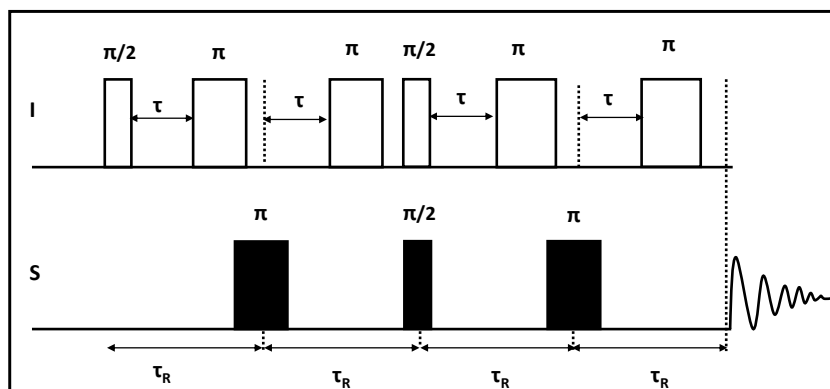


Figure 3.6: The pulse sequence for the dipolar INEPT experiment.

cancelling I spins anisotropic shift. The concurrent applications of $\pi/2$ pulses to I and S spins convert anti-phase transverse magnetization of I to S spins. After the completion of the polarization-transfer by the second echo, the enhanced S signal is acquired.[153]

3.3 NMR sample tube preparation

MAS NMR sample preparation

A special glass tube (Wilmad) of 3 mm diameter and 10-12 mm length is prepared to be well-suited for the MAS rotor and 10-12 kHz spinning speed. Figure 3.7 presents the adapter for glass tube, the MAS NMR glass tube and the rotor. In general, the desired amount the MOFs sample was loaded in the glass tube. After accomplishing the NO adsorption procedure in the MOFs (mentioned below), at first the middle part of the adapter with the glass tube is sealed off so that all of the gas settles in the MOFs containing 10-12 mm long glass tube. Finally, glass tube is further sealed very symmetrically from the lower part at 77 K by immersing it into liquid nitrogen, thereby, it can be spun at high spinning speed without problem.

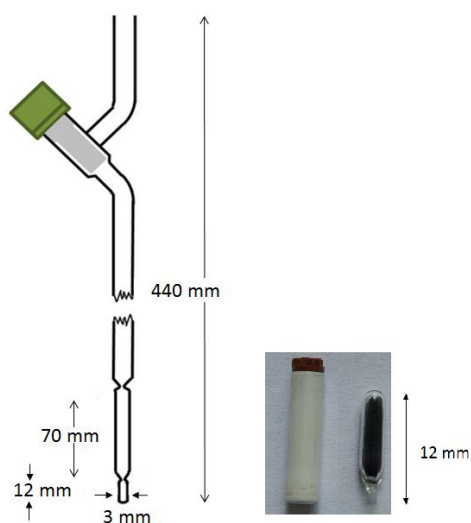


Figure 3.7: Glass tube preparation for NO loading; adapter for sample tube, 4 mm MAS rotor and MOFs loaded sealed sample tube.

Sample preparation for bulk NO detection

In case of only NO detection, the specially prepared larger glass container is mounted with a holder inside a home-built probe. Figure 3.8 shows a (a) special large and (b) small glass container for ^{15}NO detection.

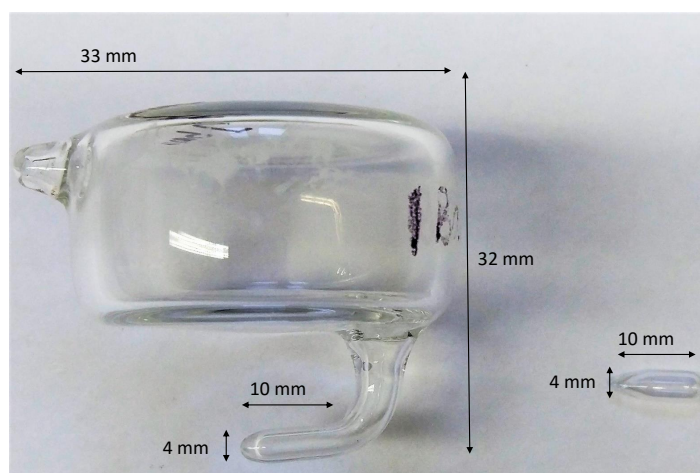


Figure 3.8: Glass tube preparation for NO loading; (a) large special glass tube and (b) small glass tube for ^{15}NO detection.

The diameter and height of the large glass container is about 32 mm, i.e., those are adapted for the NMR probehead. In the larger container, the part with the larger diameter is outside

of the NMR coil and serves as an NO reservoir, while the smaller part with a diameter of 4 mm fits well within the NMR coil. The relatively high amount of NO (about 10^{21} spins) contained now in the larger glass container, assists to detect the ^{15}N NMR signal as the chemical shift range is unknown. With decreasing temperature, the amount of NO molecules within the small part of the container increases, which facilitates the better signal-to-noise ratio. A drawback of this setup is that, no all spins are measurable all the time because the bigger part of the glass container is outside of the NMR coil. Even the condensation of NO at lower temperatures in the smaller part of the container, that is lying inside the NMR coil, does not guarantee to detect all spins within the coil. However, the use of the larger container assisted to find the signal and optimize the measuring conditions. Afterwards, that setup is used for subsequent measurements of the small 4 mm quartz glass container, which completely fits in the NMR coil and contains ca. 10^{18} spins (loading pressure ca. 40 mbar at room temperature).

3.4 Gas adsorption procedure

The NO loading procedure has been conducted in the controlled vacuum apparatus, as seen in figure 3.9. Prior to the NO adsorption, the MOF containing tube or empty glass container was connected to the vacuum apparatus and evacuated at a high temperature (383-423 K) under low vacuum (10^{-6} mbar) overnight. The ^{15}NO gas is supplied by Icon Service Inc. (USA) with a ^{15}N enrichment of 98 %. Before opening the valve of the sample cell, it was

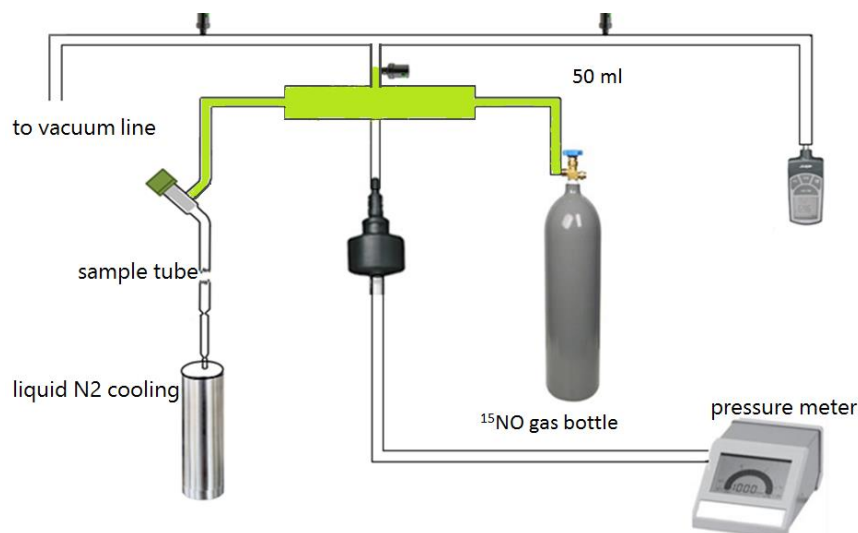


Figure 3.9: Pictorial diagram of the vacuum apparatus for gas loading is shown and the green area indicates the total volume of 50 ml.

immersed in a bath containing liquid nitrogen to keep the sample temperature at 77 K. This ensured that all NO is moved to the sample tube from the vessel. The pressure dropped down to zero due to adsorption. Finally, the sample tube was isolated from the system, after closing the sample isolation valve and sealing it immediately at liquid nitrogen temperatures (77 K), to prevent further modification.

Chapter 4

Overview and enclosed papers

The results obtained in this dissertation are summary of five published and one accepted papers, which are enclosed below in chronological order.

Paper I: NO adsorption in amino-modified Cu_3btc_2 - type MOFs studied by solid-state NMR [*Microporous Mesoporous Mater.*, 216: 111–117, 2015.]

In the previous chapter, it has been already mentioned that NO loaded Cu_3btc_2 was studied by different techniques e.g., FTIR, EPR and TGA. However, the precise information on the electronic effect, binding sites and the binding nature of NO in Cu_3btc_2 are still inadequate. To shed light on this problem, SSNMR could play an important role. A significant insight into the understanding of NO interaction, the changing of electronic properties of NO loaded Cu_3btc_2 , and the formation of NONOate in $\text{Cu}_3(\text{NH}_2\text{btc})_2$ has been achieved by MAS NMR. The outcome of this work is presented in the paper I.

In this paper the effects of NO adsorption on the Cu_3btc_2 and UHM-30 have been studied by adsorbing different amounts of NO/Cu via the gas phase. ^1H NMR spectra of NO loaded Cu_3btc_2 and UHM-30 have revealed NO interaction at Cu sites as well indirect suggestions of NONOate formation. The relevant NMR parameters of NO loaded MOFs have displayed the change of electron density in Cu sites due to NO adsorption. For the higher NO loaded samples, the decomposition of the MOFs framework is also noticeable. Additionally, XRD measurement has been done to check the phase purity of the starting material and the decomposition of the NO loaded MOFs.



NO adsorption in amino-modified $\text{Cu}_3(\text{btc})_2$ -type MOFs studied by solid-state NMR



Arafat Hossain Khan ^a, Katharina Peikert ^b, Michael Fröba ^b, Marko Bertmer ^{a,*}

^a Leipzig University, Physics and Earth Sciences, Linnéstr. 5, 04103 Leipzig, Germany

^b Department of Chemistry, Institute of Inorganic and Applied Chemistry, University of Hamburg, Martin-Luther-King Platz 6, 20146 Hamburg, Germany

ARTICLE INFO

Article history:

Received 3 December 2014

Received in revised form

23 January 2015

Accepted 11 February 2015

Available online 24 February 2015

Keywords:

MOF

Metal-organic framework

Solid-state NMR

Nitric oxide

NONOate

ABSTRACT

Adsorption of nitric oxide – NO – in the MOFs $\text{Cu}_3(\text{btc})_2$ (HKUST-1) and $\text{Cu}_3(\text{NH}_2\text{btc})_2$ (UHM-30) was studied via ^1H solid-state NMR. Changes to the electronic properties by adding paramagnetic molecules to antiferromagnetically coupled copper ions is evident in ^1H NMR shift, hyperfine coupling, and spin-lattice relaxation times (T_1). Furthermore, in the case of $\text{Cu}_3(\text{NH}_2\text{btc})_2$, the results indicate the formation of NONOates.

© 2015 Elsevier Inc. All rights reserved.

1. Introduction

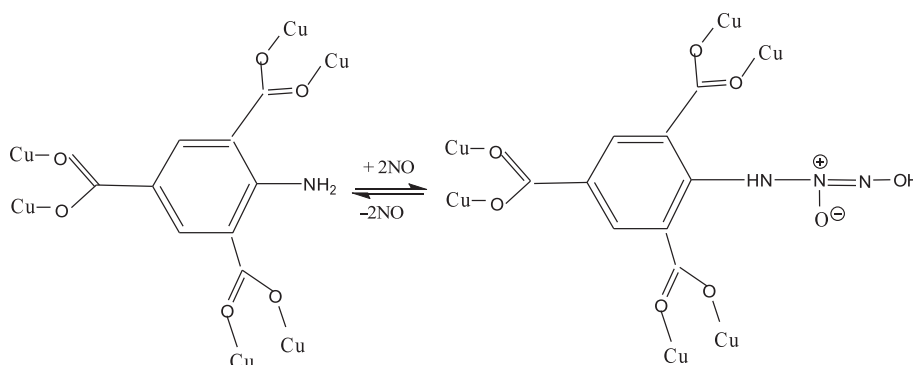
The potential applications of various porous materials continue to be at the forefront of research, for instance in gas adsorption. The properties of porous materials are at present receiving great attraction in many areas of science [1–5]. For the biological signaling molecule nitric oxide (NO) adsorption and delivery technologies using porous solid storage materials are increasingly significant [6–8]. NO delivery from a storage material is attractive for many *in vitro* and *in vivo* antibacterial, antithrombotic, and wound healing applications [9–13]. There is currently particular interest in using NO delivery materials to prevent life-threatening complications associated with thrombosis formation at the surface of medical devices such as stents and catheters [7]. One of the most promising candidates for NO delivery is currently the use of porous materials, especially metal organic frameworks (MOFs). Metal organic frameworks are materials with extremely high porosities, some of them have coordinatively unsaturated metal sites (CUSs) on the walls of the pores that are available for binding of small molecules [14,15]. The presence of CUSs in a coordination polymer has a particularly pronounced effect on the NO adsorption

and release characteristics of the material [16]. Moreover, incorporating an $-\text{NH}_2$ functionality into the MOF is particularly interesting for NO adsorption as here covalent bonds can be formed in the type of N-diazeniumdiolates (NONOates) (Scheme 1). This offers an additional method to CUSs for storing NO within the MOF [17] and therefore increases storage capacity. Furthermore, the release of NO from NONOates happens at physiological pH (7) and body temperature (37°), generating two molecules of NO per amino function. The presence of NONOates in MOFs can also facilitate the targeting of NO to specific sites of interest [17,18].

Among other MOFs, $\text{Cu}_3(\text{btc})_2$ – also named HKUST-1 – [19] is one of the highly studied standard MOFs with coordinatively unsaturated metal sites. The rigid porous structure combined with the accessibility of the activated metal sites upon dehydration has led to a lot of interest in adsorption, separation, and catalysis applications [20,21]. Wu et al. identified the main adsorption sites of CO_2 and D_2 in $\text{Cu}_3(\text{btc})_2$ by neutron diffraction studies and observed that the open metal sites are the most favorable ones [22]. Morris and coworkers reported NO interaction at the metal sites of $\text{Cu}_3(\text{btc})_2$ at room temperature identified by the FTIR stretching frequency and also determined a high adsorption capacity of NO [23]. Rosseinsky and coworkers conducted an FTIR study on 4-(methylamino)-pyridine (4-map) functionalized $\text{Cu}_3(\text{btc})_2$ to identify NONOate formation [24]. Recently, the amino functionalized MOF, $\text{Cu}_3(\text{NH}_2\text{btc})_2$ (UHM-30) [25] was presented which should be

* Corresponding author.

E-mail address: bertmer@physik.uni-leipzig.de (M. Bertmer).



Scheme 1. Covalent binding of nitric oxide in amino-functionalized $\text{Cu}_3(\text{btc})_2$ to form NONOates.

a good candidate to show NONOate formation upon exposure to NO additional to the coordination of NO to unsaturated copper centers.

In the case of $\text{Cu}_3(\text{btc})_2$ and $\text{Cu}_3(\text{NH}_2\text{btc})_2$, the two copper ions are arranged in a paddle-wheel and are antiferromagnetically coupled which results in an $S = 1$ excited and an $S = 0$ ground electronic state. The latter is populated at low temperature, whereas at higher temperature (above 90 K) the $S = 1$ state becomes more and more populated. For NMR measurements at higher temperatures the effect of the electronic state is similar to paramagnetic behavior that strongly influences the magnetic properties of the surrounding nuclei [26]. Additionally in the case studied here, NO itself is a paramagnetic molecule at room temperature, containing an unpaired electron. Although analysis of paramagnetic systems by NMR is typically complicated, we have recently shown that important information about the framework and its interaction with small molecules like H_2O , CO or CO_2 can be obtained from both ^1H and ^{13}C NMR [27–32]. Dawson et al. reported on the high-resolution ^{13}C NMR of HKUST-1 and STAM-1 [33]. Solid-state NMR is sensitive to the local atomic environment and ideally suited to probe disordered gas loaded systems. Information on interaction of guest molecules with the host material, adsorption sites as well as the dynamics of NO within the pore can be obtained.

In this paper, we studied the adsorption of defined amounts of NO on $\text{Cu}_3(\text{btc})_2$ and $\text{Cu}_3(\text{NH}_2\text{btc})_2$. Analysis is performed by ^1H MAS NMR measurements as well as ^1H spin-lattice relaxation studies. Further experiments follow the aging behavior of NO-loaded $\text{Cu}_3(\text{btc})_2$ to get information about decomposition of the MOF structure.

2. Experimental

2.1. Synthesis of $\text{Cu}_3(\text{btc})_2$ -type MOFs

$\text{Cu}_3(\text{btc})_2$ and $\text{Cu}_3(\text{NH}_2\text{btc})_2$ samples were synthesized based on published procedures [19,25]. Here, $\text{Cu}_3(\text{btc})_2$ was synthesized by a slightly modified solvo-thermal method under ambient pressure in the reaction between $\text{Cu}(\text{NO}_3)_2 \cdot 3\text{H}_2\text{O}$ and trimesic acid (H_3btc) with refluxing ethanol [21]. In addition, isostructural $\text{Cu}_3(\text{NH}_2\text{btc})_2$ was synthesized by the reaction between 2-amino-1,3,5-benzenetricarboxylic acid and $\text{Cu}(\text{NO}_3)_2 \cdot 3\text{H}_2\text{O}$ under solvo-thermal conditions. Purification of the MOFs was done via soxhlet extraction with ethanol.

2.2. Preparation of NO-loaded samples

MOF samples were activated (dehydrated) under vacuum of 10^{-3} bar at a temperature of 383 K for 24 h to remove water

coordinated to the copper sites. Samples were kept under nitrogen environment before gas loading. The color of the $\text{Cu}_3(\text{btc})_2$ samples turned from light blue into dark violet immediately after activation, whereas for $\text{Cu}_3(\text{NH}_2\text{btc})_2$ the color changed from bright green to dark green. Before NO loading, the samples were placed in 3 mm glass tubes (Wilmad), which are tightly fitting in the MAS rotors. NO was adsorbed via the gas phase at rather low pressures (less than 50 mbar) in a pressure controlled vacuum apparatus under nitrogen cooling at 77 K. For $\text{Cu}_3(\text{btc})_2$, the amount of NO (for details see SI) is given with respect to the number of copper atoms in the MOF, corresponding to 0.2, 0.5, 0.8, 1.0, 1.5 and 2.0 equivalents of NO/Cu (labeled b to g). In case of $\text{Cu}_3(\text{NH}_2\text{btc})_2$, NO loaded samples with 0.5, 1.0 and 2.0 equivalents of NO (labeled k, l, and m, respectively) with respect to copper were prepared. Additional samples labeled a and h were prepared containing just the dehydrated $\text{Cu}_3(\text{btc})_2$ and $\text{Cu}_3(\text{NH}_2\text{btc})_2$, respectively. Finally, the glass tubes were sealed to prevent further alteration of the samples. NMR measurements were conducted directly after completion of the sealing process. For the time dependent study the relevant time after sealing is indicated.

2.3. X-ray diffraction

To verify sample quality after activation, PXRD measurements of both MOFs were carried out after sample activation on a STOE STADI-P X-ray diffractometer in Debye–Scherrer mode equipped with a linear PSD and Ge(111) monochromator using $\text{Cu-K}\alpha_1$ ($\lambda = 154.060$ pm) radiation (40 kV, 40 mA), and scanned within a 2θ range from 1° to 60° with a step size of 0.015° with a Mythen1K detector. Samples were mounted on glass capillaries of outer diameter 0.3 mm. The results are shown in Figs. S1 and S2 in the supplementary information. For both $\text{Cu}_3(\text{btc})_2$ and $\text{Cu}_3(\text{NH}_2\text{btc})_2$ the PXRD pattern is in good agreement with the calculated pattern from the published crystal structures [19,25] indicating no destruction during the activation process. Additionally, $\text{Cu}_3(\text{btc})_2$ loaded with 1.5 NO/Cu was checked after NO loading to get information about the sample integrity (results discussed below). For this, the sealed glass tube was broken immediately before taking the XRD.

2.4. Solid-state NMR measurements

^1H solid-state NMR experiments of dehydrated and NO adsorbed samples were executed on a Bruker Avance 400 spectrometer at a frequency of 400.167 MHz (magnetic field strength 9.4 T). A 4 mm MAS probe was used at a MAS rotation frequency of 10 kHz. Spectra were recorded by using the DEPTH [34] sequence to

suppress signals from the probe background. Recycle delays were set to 50 ms, which is more than five times the longitudinal relaxation time (T_1). The 90° pulse length was 2.4 μ s. All spectra were referenced to TMS using PDMS (poly(dimethylsiloxane)) as secondary reference for ^1H , resonating at 0.07 ppm. Spin-lattice relaxation times were obtained with the inversion-recovery sequence modified with DEPTH-detection. Spectrum deconvolution was done using the dmfit-software [35] and analysis of the hyperfine coupling via the spinning sideband intensities with the HBA program [36]. For the ^1H – ^1H correlation spectrum, a standard NOESY sequence from solution NMR was used which was rotor-synchronized with the MAS frequency of 10 kHz.

3. Results and discussions

3.1. ^1H MAS NMR of NO-loaded $\text{Cu}_3(\text{btc})_2$

The isotropic region of the ^1H MAS spectra of all NO loaded samples is shown as a stack plot in Fig. 1. The sample containing 0.2 NO/Cu shows one resonance at 8.3 ppm, similar to that of unloaded $\text{Cu}_3(\text{btc})_2$ assigned to the aromatic proton signal [28]. With increasing NO content a gradual decrease of isotropic shift down to 7.6 ppm for sample g is observed. Besides this one resonance, small signals in the range between 13 and 21 ppm, visible from sample 0.5 NO/Cu and higher NO content are present. The intensity of these additional signals is increasing with increasing NO content. For sample g already four additional signals at around 14.9, 16.5, 18.5, and 21.2 ppm can be distinguished. We assign these peaks to indicate decomposition of the MOF framework at high NO loadings (see below). Table S1 in the supplementary information summarizes the relative intensity of these additional signals with respect to the aromatic proton signal.

3.2. ^1H MAS NMR of NO-loaded $\text{Cu}_3(\text{NH}_2\text{btc})_2$

Included in Fig. 1 are also the ^1H MAS spectra of NO-loaded $\text{Cu}_3(\text{NH}_2\text{btc})_2$. The aromatic proton signal of the dehydrated sample appears at 8.4 ppm similar to $\text{Cu}_3(\text{btc})_2$ and the chemical shift also decreases with increasing NO content. The signal for the amino protons we assign to the broad underlying signal in the spectra with an isotropic shift of 9.1 ppm. The higher linewidth compared to the aromatic proton we describe to the disorder of the amino group in the crystal structure [25]. The position of the amine function relative to other ligands varies statistically. This leads to different ^1H – ^1H distances as well as ^1H – $^{63,65}\text{Cu}$ distances that gives rise to heterogenous broadening.

Fig. 2 represents the correlation of the aromatic proton shift for both sample series as a function of NO content. For $\text{Cu}_3(\text{btc})_2$, we observe a linear decreasing shift with increasing NO content, while for $\text{Cu}_3(\text{NH}_2\text{btc})_2$ above 0.5 NO/Cu the shift remains practically constant.

For $\text{Cu}_3(\text{btc})_2$, the observed shift is the result of the mobility of NO in the MOF framework and its interaction with the uncoordinated copper site. Due to weak NO adsorption at room temperature, as indicated by theoretical calculations [16], the time NO spends at the Cu site is rather short. For higher NO loading, the probability of finding NO at the copper sites increases. NO – containing an unpaired electron – adsorbed at the copper site will change the electron spin density which influences the ^1H shift of the aromatic protons of the btc linker due to hyperfine interaction [28]. This leads to a linear decreasing chemical shift as a function of NO content. The observed chemical shift then represents the result of the dynamic average of NO adsorbed and desorbed from the copper site. A similar observation of decreasing shift with reduced electron spin density was also found for $\text{Cu}_3(\text{btc})_2$ where part of the copper was replaced by diamagnetic zinc ions [29]. We note that FTIR

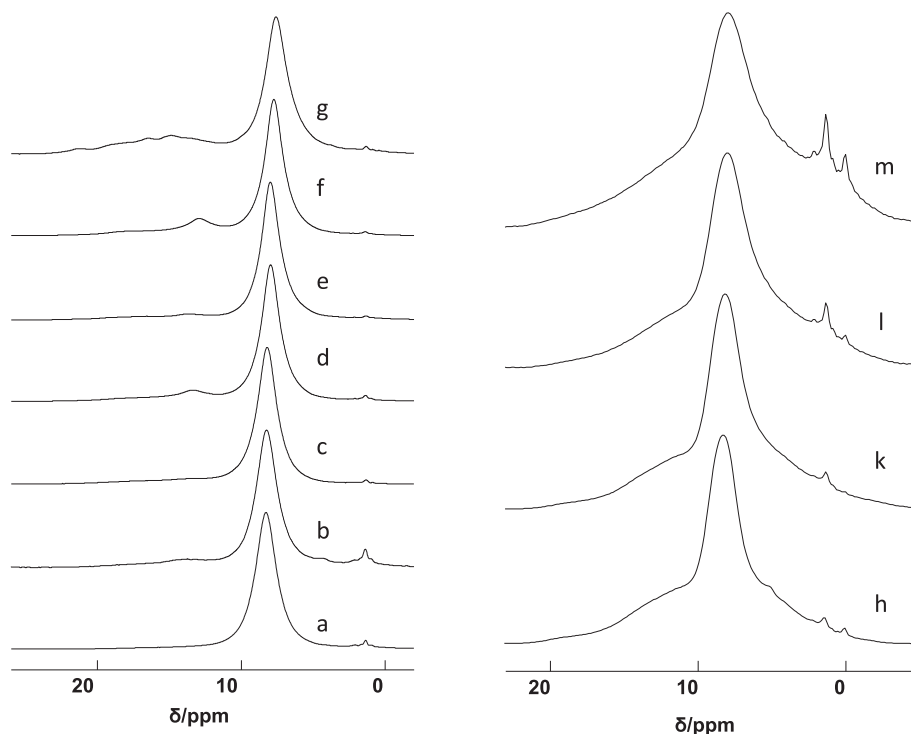


Fig. 1. Isotropic region of ^1H MAS spectra of NO loaded $\text{Cu}_3(\text{btc})_2$ of samples a–g (left). The narrow signal around 1 ppm results from the sealing procedure of the glass tubes, probably due to enclosed natural gas used for sealing. Right: Isotropic region of ^1H MAS spectra of NO loaded $\text{Cu}_3(\text{NH}_2\text{btc})_2$ samples h to m. Small signals near 0 and 1 ppm are due to the sealing procedure.

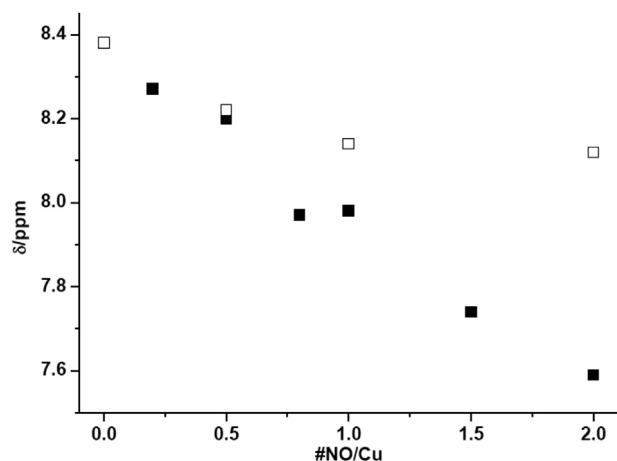


Fig. 2. Dependence of aromatic ¹H shift with NO content for Cu₃(btc)₂ (solid squares) and Cu₃(NH₂btc)₂ (open squares).

measurements [23] indicated ‘strong’ binding of NO at the copper site. However, IR is sensitive to shorter timescales than NMR so that a short-time adsorption at the copper site can be identified. NMR being a slower observation technique compared to IR will only see the time average of NO being adsorbed at the copper site or moving freely within the pores, indicating the dynamic nature of NO being studied by NMR.

In case of Cu₃(NH₂btc)₂, in general the same effect would be expected which is also found for low NO contents. The fact that the chemical shift does not change for larger NO contents could in principle be due either to a fixed adsorption of NO at the copper site or the unchanged electronic structure for higher NO contents. The former, however, is quite unexpected because in the case of Cu₃(btc)₂ the shift decrease with NO content is even larger. Due to the similar structures of the two MOFs we would expect that the aromatic ¹H shift of strongly adsorbed NO at the copper site will be at even smaller shift values. The latter case – unchanged electronic structure – can be understood if we assume the creation of N-diazonium diolates (NONOates) (see Scheme 1) by reaction of NO with the amino functionality of the organic ligand. This will not change the amount of unpaired electrons with increasing NO content and therefore lead to a constant chemical shift, which is observed.

We note that for the Cu₃(NH₂btc)₂ samples we prepared there is no indication of decomposition from additional signals in the ¹H spectrum. This is in opposition to our results where it was observed that at high pressures of NO (1 bar and higher) reduction of Cu²⁺ to elementary copper takes place as seen by XRD measurements [37]. We explain this difference by the much lower NO pressure in the samples studied here.

3.3. Analysis of ¹H hyperfine couplings

The ¹H MAS spectra of the two series contain a manifold of spinning sidebands as can be seen for example in Fig. S3 in the supplementary information. For ¹H NMR of diamagnetic samples, spinning sidebands mainly arise due to dipole–dipole interaction. However, in the btc ligand the dipole–dipole interaction is rather small due to the small amount of protons and the rather large distance between them (minimum distance 4.03 Å) leading to a second moment [38] of 190 kHz², which would give rise to a static linewidth of about 14 kHz. However, in the studied systems the static linewidth ranges up to 90 kHz representing the large anisotropic part of the hyperfine shift or more precisely the anisotropic

part of the electron–nucleus dipolar interaction [28,39,40] between the proton and the unpaired electrons that dominates in our case over the dipole–dipole interaction. The contribution of dipole–dipole coupling is therefore neglected in the analysis of the size of the hyperfine interaction. Further on, we will refer to this interaction simply as hyperfine coupling. The hyperfine interaction can be analyzed in the same way as a chemical shift anisotropy (CSA) pattern [28,39–42]. An increase in the second moment due to interaction with paramagnetic molecules was also observed in the interaction of oxygen with the surface protons of porous materials [43,44]. Fig. 3 shows the results for the hyperfine coupling of the different samples as a function of NO content. For Cu₃(btc)₂, a linear decrease of hyperfine coupling with increasing NO content is observed reducing from 28 kHz down to 16 kHz. The sample with 2 NO/Cu does not follow this linear decrease, probably because of partial decomposition concluded from the high amounts of additional signals in the ¹H NMR spectrum (see above). The linear dependence can be understood in the same way as the variation of isotropic chemical shift: An increasing amount of NO with increasing interaction at the copper site reduces the amount of unpaired electrons thereby reducing the interaction strength of electrons and protons and with that reduce the size of the hyperfine coupling.

In opposition to this, the hyperfine coupling for Cu₃(NH₂btc)₂ remains constant with increasing NO content, showing even a slight increase from 28 kHz to 30 kHz. If we assume NONOate formation, we would not expect a change of hyperfine coupling since the amount of unpaired electron density is constant, which is also observed. Small variations might be explained by the slightly changing structure due to NONOate formation.

3.4. Analysis of spin-lattice relaxation times

Relaxation processes in paramagnetic systems are typically much faster than in diamagnetic systems due to the presence of unpaired electrons that can act as relaxation sinks. T₁ relaxation times therefore can be used to get information about the electronic structure of the MOFs. Fig. 4 shows the dependence of ¹H T₁ as a function of NO content. For all samples, single exponential fits were possible with high accuracy (R ≥ 98%) indicating that the samples represent homogenous systems. The determined T₁ values confirm the results of the chemical shift variation and the strength of the hyperfine coupling discussed above. The T₁ values of NO loaded

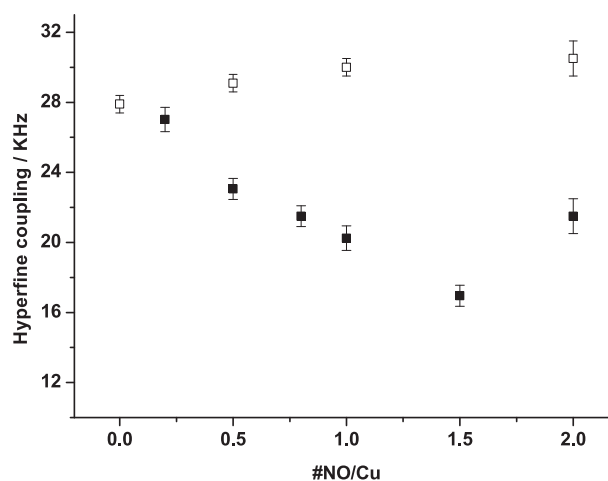


Fig. 3. Dependence of hyperfine coupling with NO content for Cu₃(btc)₂ (black squares) and Cu₃(NH₂btc)₂ (open squares).

$\text{Cu}_3(\text{btc})_2$ increase with increasing NO content due to reduced number of unpaired electrons. The effect is quite large, increasing T_1 by a factor of more than three. In contrast to this, T_1 of the NO-loaded $\text{Cu}_3(\text{NH}_2\text{btc})_2$ remains practically constant for different NO loadings. Formation of NONOates will not change the unpaired electron density due to the copper atoms as dominating source of relaxation and therefore no change in spin-lattice relaxation is expected.

3.5. ^1H MAS NMR linewidth

Fig. S4 depicts the linewidth (FWHM) of the isotropic signal as a function of NO loading for $\text{Cu}_3(\text{btc})_2$ and $\text{Cu}_3(\text{NH}_2\text{btc})_2$ samples. In case of $\text{Cu}_3(\text{btc})_2$, the linewidth increases only slightly with NO content, whereas for $\text{Cu}_3(\text{NH}_2\text{btc})_2$ a significant increase in linewidth with increasing NO content is observed. The different behavior of the two systems is not fully understood. Nayeem et al. [40] reported that the anisotropic bulk magnetic susceptibility tensor of randomly oriented crystallites produces slightly different frequencies, leading to inhomogeneous line broadening. The anisotropic hyperfine coupling will influence the intensity of spinning sidebands but not the linewidth of centerband and sideband. For $\text{Cu}_3(\text{btc})_2$ a practically constant linewidth indicates that there are no significant changes with NO loading. In the case of $\text{Cu}_3(\text{NH}_2\text{btc})_2$, an increasing linewidth with increasing NO content and therefore increasing formation of NONOates might hint at the fact that a higher disorder is created in the system since not all amino groups react. Therefore, this increases isotropic shift distributions and adds to the broadening of the line.

3.6. Additional signals in NO-loaded $\text{Cu}_3(\text{btc})_2$

In order to get some more insight into the additional signals present in the range from 13 to 21 ppm, we performed time dependent measurements on the sealed samples. For sample f, this is shown in Fig. 5 for a time span of more than five months. The intensity of the additional signals increases with time which hints at a continued reaction. Since samples are within sealed ampules this can only be due to the presence of NO in the pores. Furthermore, the shift of these signals varies, for instance directly after sample loading there is an additional signal at 13 ppm and a slight

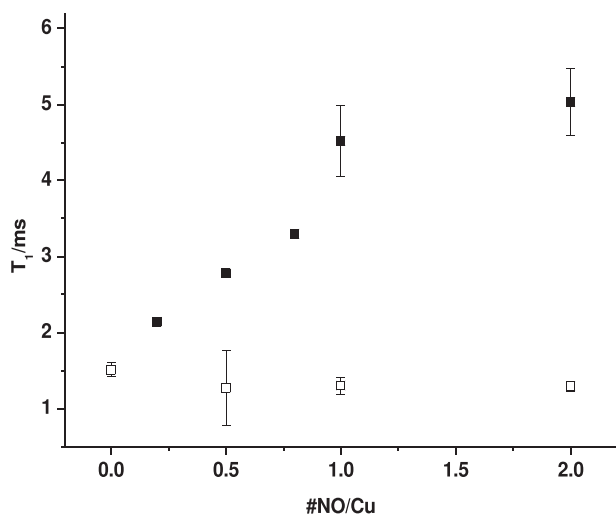


Fig. 4. Correlation of spin-lattice relaxation time with NO loading. Filled squares represent data for $\text{Cu}_3(\text{btc})_2$, open squares those for $\text{Cu}_3(\text{NH}_2\text{btc})_2$. If no error bars are seen, the uncertainty is on the size of the symbols.

shoulder at 18 ppm. With increasing time more signals arise and after five months signals at 14 ppm, 16 ppm, and 21 ppm are visible. This could mean that different reaction products are formed or that there are several reaction steps of decomposition involved. After more than five months, no more changes to the ^1H spectrum are observed.

The ^1H shift range of the additional signals is rather unusual and for diamagnetic systems typically indicates strongly hydrogen bonded systems. However, for (para)magnetic systems the isotropic chemical shift can be severely influenced by the unpaired electron density. Therefore, no clear conclusions can be drawn from the chemical shift. As the spin-lattice relaxation time is in the same range to that of the main signal at 8 ppm, we can conclude that there also exists an interaction with copper. We were therefore interested if there is close connection of the protons in this shift range with those of the main aromatic protons. We performed 2D NOESY measurements that have been successfully used in paramagnetic systems [45]. One example is shown in Fig. S5 in the Supplementary information. The aromatic proton signal and two strong signals at higher ppm values are seen together with the broadened signal between 0 and 5 ppm that reflects signals from the sealing procedure that are enhanced in the NOESY spectrum due to long spin–spin relaxation time. Several experiments with different mixing times between 100 μs and 1 ms were run. However, in none of these spectra a correlation peak between the signals was found indicating that the species responsible for the signals are not close to each other. Due to the short T_1 of the sample the maximum mixing time is, however, limited. Therefore it might be possible that we are unable to see correlations because of relaxation effects. Finally, we ran a PXRD of the sample to see if the MOF structure is maintained and if other crystalline phases have evolved that can document decomposition. The results are shown in Fig. S6. Although the major diffractions for $\text{Cu}_3(\text{btc})_2$ are present, the high linewidth of those indicates loss of crystallinity probably indicating breaking up of the framework leaving over smaller units.

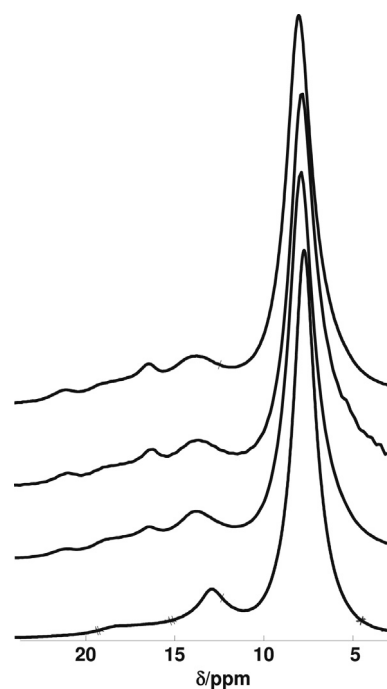


Fig. 5. Isotropic region of the ^1H NMR spectra of sample f as a function of aging time. From bottom to top: directly after sealing, after three months, after four months and after five months, respectively.

No additional diffractions are visible. On the local scale, which is probed by NMR, the aromatic proton signal is unchanged indicating intact ligands between copper junctions. The additional signals are coming preferably from the end points of these small units where breaking of, e. g., Cu–O bonds has occurred.

4. Conclusion

We have shown that significant information on Cu₃(btc)₂-type MOFs interacting with nitric oxide can be obtained from ¹H solid-state NMR. NO interaction with Cu₃(btc)₂ follows a linear trend for ¹H shift, hyperfine coupling, and spin-lattice relaxation time that can be explained by a decrease of unpaired electron density by interaction of the unpaired electron at the copper sites with that of nitric oxide. This also indicates the copper site as the primary adsorption site for NO. Especially for higher NO contents, additional signals in the ¹H NMR spectra hint at a decomposition of the framework. From NOESY measurements no correlation peaks of the additional signals with the main aromatic signal were found. However, PXRD data indicate significant loss of crystallinity. For Cu₃(NH₂btc)₂, clear evidence is found that NONOate formation occurs, as the ¹H shift, the hyperfine coupling, and the ¹H T₁ remain fairly constant with NO loading. No additional signals are visible that could indicate decomposition in opposition to related results obtained at high NO loading pressures.

One limitation of this approach is that the effects of nitric oxide in interaction with the MOF could only be detected indirectly. Therefore, ¹⁵N NMR experiments are underway using ¹⁵N enriched nitric oxide to get some direct information from the adsorbed guest molecule and to search for NONOate signals. Information from ¹³C NMR and temperature dependent measurements to study the NO adsorption strength are also in progress.

Finally, we want to mention that obviously the presence of copper ions in the studied MOFs would – because of its toxicity – prevent these types of MOFs for application in drug-delivery. Nevertheless, the research undertaken here serves as a basis for further studies backing on our knowledge of this system. In the future, measurements on more applicable MOF systems such as MIL100(Fe) are planned.

Acknowledgements

The authors thank the German Research Foundation (DFG) for financial support within the priority program 'porous metal-organic frameworks (MOFs)' (SPP1362), projects Be 2434/4-2 and Fr 1372/18-2. We thank M. Sc. Karolin Stein for performing the XRD measurements.

Appendix A. Supplementary data

Supplementary data related to this article can be found at <http://dx.doi.org/10.1016/j.micromeso.2015.02.022>.

References

- [1] O.M. Yaghi, C.E. Davis, G.M. Li, H.L. Li, *J. Am. Chem. Soc.* 119 (1997) 2861–2868.
- [2] C. Janiak, *Dalton Trans.* (2003) 2781–2804.
- [3] S. Kitagawa, R. Kitaura, S. Noro, *Angew. Chem. Int. Ed. Engl.* 43 (2004) 2334–2375.
- [4] P. Horcajada, C. Serre, M. Vallet-Regi, M. Sebba, F. Taulelle, G. Férey, *Angew. Chem. Int. Ed. Engl.* 45 (2006) 5974–5978.
- [5] A. Schneemann, V. Bon, I. Schwedler, I. Senkovska, S. Kaskel, R.A. Fischer, *Chem. Soc. Rev.* 43 (2014) 6062–6096.
- [6] P.S. Wheatley, A.R. Butler, M.S. Crane, S. Fox, B. Xiao, A.G. Rossi, I.L. Megson, R.E. Morris, *J. Am. Chem. Soc.* 128 (2006) 502.
- [7] L.K. Keefer, *Nat. Mater.* 2 (2003) 357–358.
- [8] A.C. McKinlay, R.E. Morris, P. Horcajada, G. Férey, R. Gref, P. Couvreur, C. Serre, *Angew. Chem. Int. Ed. Engl.* 49 (2010) 6260–6266.
- [9] H.F. Zhu, B. Ka, F. Murad, *World J. Surg.* 31 (2007) 624–631.
- [10] S. Moncada, E.A. Higgs, *Brit. J. Pharm.* 147 (2006) S193–S201.
- [11] M.C. Frost, M.M. Reynolds, M.E. Meyerhoff, *Biomaterials* 26 (2005) 1685–1693.
- [12] E.M. Hetrick, J.H. Shin, N.A. Stasko, C.B. Johnson, D.A. Wespe, E. Holmuhamedov, M. Schoenfish, *ACS Nano* 2 (2008) 235–246.
- [13] M.R. Miller, I.L. Megson, *Brit. J. Pharm.* 151 (2007) 305–321.
- [14] B. Chen, M. Eddaoudi, T.M. Reineke, J.W. Kampf, M. O'Keeffe, O.M. Yaghi, *J. Am. Chem. Soc.* 122 (2000) 11559–11560.
- [15] M. Dinca, A.F. Yu, J.R. Long, *J. Am. Chem. Soc.* 128 (2006) 8904–8913.
- [16] B. Supronowicz, A. Mavrandonakis, T. Heine, *J. Phys. Chem. C* 117 (2013) 14570–14578.
- [17] A. Hrabie, L.K. Keefer, *Chem. Rev.* 102 (2002) 1135–1154.
- [18] P.G. Parzuchowski, M.C. Frost, M.E. Meyerhoff, *J. Am. Chem. Soc.* 124 (2002) 12182–12191.
- [19] S.S.-Y. Chui, S.M.-F. Lo, J.P.H. Charmant, A.G. Orpen, I.D. Williams, *Science* 283 (1999) 1148–1150.
- [20] B. Panella, M. Hirscher, H. Putter, U. Müller, *Adv. Funct. Mater.* 16 (2006) 520–524.
- [21] M. Hartmann, S. Kunz, D. Himsel, O. Tangermann, S. Ernst, A. Wagener, *Langmuir* 24 (2008) 8634–8642.
- [22] H. Wu, J.M. Simmons, G. Srinivas, W. Zhou, T. Yildirim, *J. Phys. Chem. Lett.* 1 (2010) 1946–1951.
- [23] B. Xiao, P.S. Wheatley, X. Zhao, A.J. Fletcher, S. Fox, A.G. Rossi, I.L. Megson, S. Bordiga, L. Regli, K.M. Thomas, R.E. Morris, *J. Am. Chem. Soc.* 129 (2007) 1203–1209.
- [24] M.J. Ingleson, R. Heck, J.A. Gould, M.J. Rosseinsky, *Inorg. Chem.* 48 (2009) 9986–9988.
- [25] K. Peikert, F. Hoffmann, M. Fröba, *Chem. Commun.* 48 (2012) 11196–11198.
- [26] K. Liu, D. Ryan, K. Nakanishi, A. McDermott, *J. Am. Chem. Soc.* 117 (1995) 6897–6906.
- [27] B. Jee, K. Eisinger, F. Gul-E-Noor, M. Bertmer, M. Hartmann, D. Himsel, A. Pöpl, *J. Phys. Chem. C* 114 (2010) 16630–16639.
- [28] F. Gul-E-Noor, B. Jee, A. Pöpl, M. Hartmann, D. Himsel, M. Bertmer, *Phys. Chem. Chem. Phys.* 13 (2011) 7783–7788.
- [29] F. Gul-E-Noor, B. Jee, M. Mendt, D. Himsel, A. Pöpl, M. Hartmann, J. Haase, H. Krautscheid, M. Bertmer, *J. Phys. Chem. C* 116 (2012) 20866–20873.
- [30] F. Gul-E-Noor, D. Michel, H. Krautscheid, J. Haase, M. Bertmer, *J. Chem. Phys.* 139 (2013a) 034202.
- [31] F. Gul-E-Noor, M. Mendt, D. Michel, A. Pöpl, H. Krautscheid, J. Haase, M. Bertmer, *J. Phys. Chem. C* 117 (2013b) 7703–7712.
- [32] F. Gul-E-Noor, D. Michel, H. Krautscheid, J. Haase, M. Bertmer, *Microporous Mesoporous Mater.* 180 (2013c) 8–13.
- [33] D.M. Dawson, L.E. Jamieson, M.I.H. Mohideen, A.C. McKinlay, I.A. Smellie, R. Cadou, N.S. Keddie, R.E. Morris, S.E. Ashbrook, *Phys. Chem. Chem. Phys.* 15 (2013) 919–929.
- [34] M.R. Bendall, R.E. Gordon, *J. Magn. Reson.* 53 (1983) 365–385.
- [35] D. Massiot, F. Fayon, M. Capron, I. King, S.L. Calvé, B. Alonso, J.-O. Durand, B. Bujoli, Z. Gan, G. Hoatson, *Magn. Reson. Chem.* 40 (2002) 70–76.
- [36] K. Eichele, Hba V1.7, Universität Tübingen, 2012.
- [37] K. Peikert, L.J. McCormick, D. Cattaneo, F. Hoffmann, A.H. Khan, M. Bertmer, R.E. Morris, M. Fröba, *Microporous Mesoporous Mater.* (2015) 118–126.
- [38] C.P. Slichter, *Principles of Magnetic Resonance*, third ed., Springer-Verlag, Berlin, Heidelberg, New York, 1990.
- [39] N.P. Wickramasinghe, M.A. Shaibat, C.R. Jones, L.B. Casabianca, A.C. de Dios, J.S. Harwood, Y. Ishii, *J. Chem. Phys.* 128 (2008), 052210–052211 – 052210–052216.
- [40] A. Nayeem, J.P. Yesinowski, *J. Chem. Phys.* 89 (1988) 4600–4608.
- [41] G. Kervern, A. D'Aléo, L. Toupet, O. Maury, L. Emsley, G. Pintacuda, *Angew. Chem. Int. Ed. Engl.* 48 (2009) 3082–3086.
- [42] H. Heise, F.H. Köhler, X. Xie, *J. Magn. Reson.* 150 (2001) 198–206.
- [43] D. Zscherpel, E. Brunner, M. Koch, *Z. Phys. Chem.* 190 (1995) 123–127.
- [44] H. Liu, H.-M. Kao, C.P. Grey, *J. Phys. Chem. B* 103 (1999) 4786–4796.
- [45] S.K.K. Swamy, A. Karczmarzka, M. Makoska-Janusik, A. Kassiba, J. Dittmer, *ChemPhysChem* 14 (2013) 1864–1870.



Arafat Hossain Khan earned Bachelor and Master degree in Applied Chemistry and Chemical Engineering from Dhaka University, Bangladesh. He achieved a second Master degree in Structural Chemistry and Spectroscopy from Leipzig University in 2014. His research interests focus on Solid State NMR characterization of metal-organic frameworks, particularly the interaction with NO.

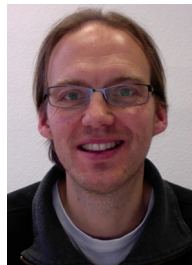


Katharina Peikert studied chemistry at the University of Hamburg and received her diploma in 2011. She is currently working on her PhD at the University of Hamburg under the guidance of Prof. Michael Fröba. Her research focus is on the synthesis of metal-organic frameworks as NO storage and delivery systems.



Michael Fröba studied chemistry in Würzburg and Hamburg and received his doctorate in 1993 from the Institute of Physical Chemistry, where he worked with Prof. W. Metz on graphite intercalation compounds. From 1994 to 1996, he was a Feodor Lynen research fellow in the group of Dr J. Wong at the Lawrence Livermore National Laboratory. After his habilitation at the University of Hamburg in 2000, he was appointed as an Associate

Professor for Inorganic Chemistry at the University of Erlangen-Nuremberg. From 2001 to 2007 he was Full Professor for Inorganic Chemistry at the University of Giessen, and since 2007 he holds a chair for Inorganic Chemistry at the University of Hamburg, with a strong focus on solid-state and materials chemistry.



Marko Bertmer studied Chemistry at the Westfälische-Wilhelms-Universität Münster, where he received a Ph.D. Degree in 1999 in Physical Chemistry, working with Prof. Hellmut Eckert on solid-state NMR of alumoborate glasses. At RWTH Aachen University he finished his habilitation in 2006. He was a Feodor-Lynen stipend from the Alexander-von-Humboldt Society working with Dr. S. Hayes at Washington University, St. Louis, MO, USA from 2002 to 2003. Currently, he is working as staff scientist and lecturer at Leipzig University in the group of Prof. J. Haase. His research interest is focussing on solid-state NMR of materials.

Supplementary information

Calculation of NO amount

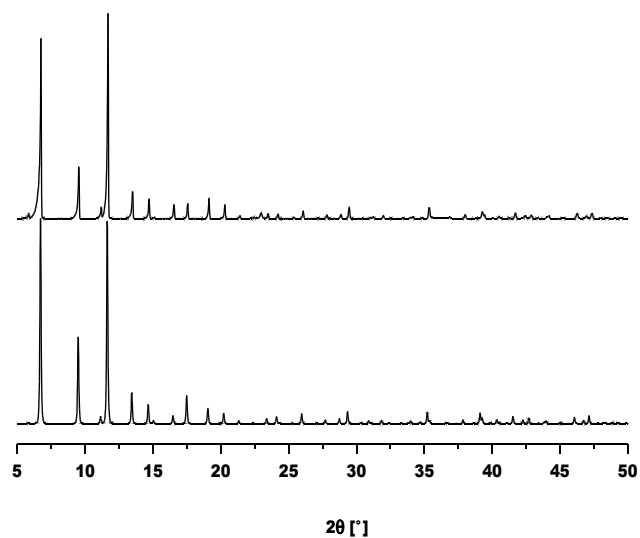
For the loading with NO, for a given weight of HKUST-1 or UHM-30, the
455 number of copper atoms was calculated and with that the number of desired NO
molecules. For a given volume of 50 ml, the gas pressure of NO was calculated
according to the ideal gas law. After filling the 50 ml reservoir with this pressure,
it was connected to the sample tube. The pressure then dropped down to zero,
so all NO molecules ended up in the MOF.

460

Table S1: Relative amount from signal integration of additional signals with
respect to the aromatic proton signal as a function of NO content for

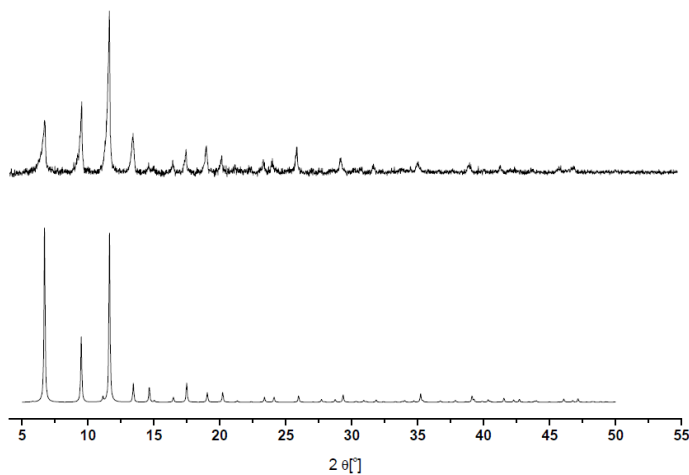
$\text{Cu}_3(\text{btc})_2$.

NO/Cu	amount of additional signals [%]
0.2	0.0
0.5	3.4
0.8	5.1
1.0	4.1
1.5	11.4
2.0	16.1



465

Figure S1: XRD powder pattern of activated $\text{Cu}_3(\text{btc})_2$ (top) compared to the calculated powder pattern according to the published structure.[19]



470

Figure S2: XRD powder pattern of activated $\text{Cu}_3(\text{NH}_2\text{btc})_2$ (top) compared to the calculated powder pattern according to the published structure.[25]

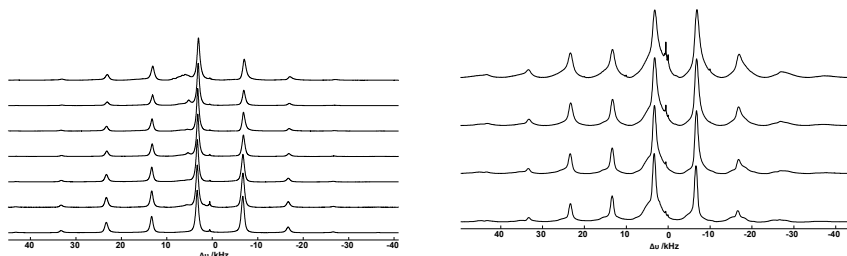
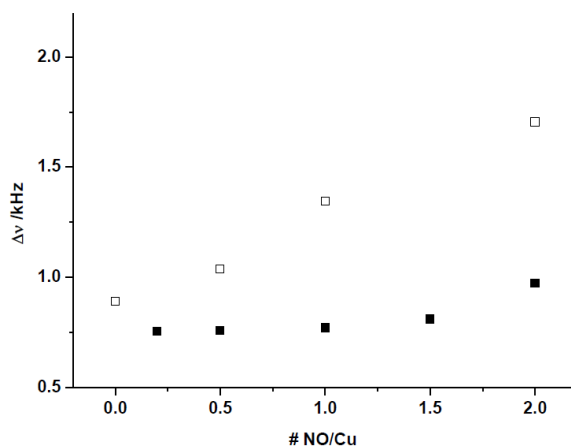
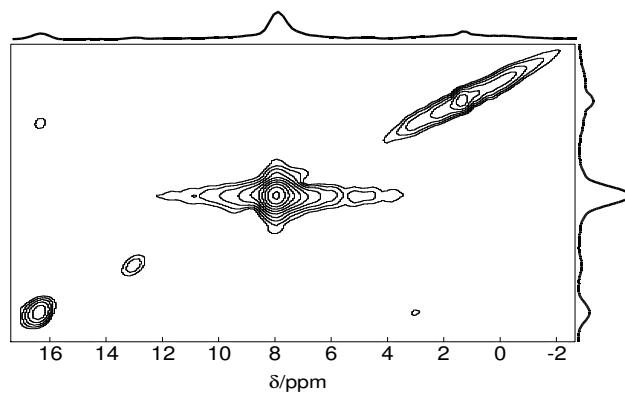


Figure S3: Full ^1H MAS spectra showing all spinning sidebands of NO-loaded $\text{Cu}_3(\text{btc})_2$ (left, samples a-g from bottom to top) and $\text{Cu}_3(\text{NH}_2\text{btc})_2$ (right, samples h-m from bottom to top).



475

Figure S4: ^1H linewidth as a function of NO content for $\text{Cu}_3(\text{btc})_2$ (solid squares) and $\text{Cu}_3(\text{NH}_2\text{btc})_2$ (open squares). The uncertainty of the linewidth is on the order of 100 Hz.



480 **Figure S5:** 2D NOESY spectrum of sample f recorded with a mixing time of 500 μ s.

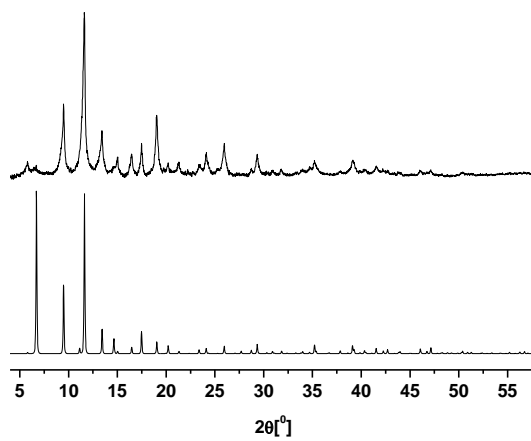


Figure S6: PXRD of sample f after NO loading.

Paper II: Tuning the nitric oxide release behavior of amino functionalized HKUST-1
[*Microporous Mesoporous Mater.*, 216: 118-126, 2015.]

Secondary amine functionalized MOFs, $\text{Cu}_3(\text{NHRbtc})_2$ have exposed greater potentiality for NONOate formation in comparison with its primary derivative, due to the stability of NONOate in the former one. On account of this, four different sets of $\text{Cu}_3(\text{NHRbtc})_2$ are synthesized and scrutinized with different techniques by professor Fröba's group. Complement to their work, MAS NMR is also applied to characterize the MOFs. In paper II presents our contribution for the structural characterization of $\text{Cu}_3(\text{NHRbtc})_2$ by MAS NMR. It is evident that ^1H alkyl signals merged together and appeared as a broad resonance. In spite of their overlap, the alkyl protons' signals shifted to a smaller value with increasing alkyl chain length. This observation is in good agreement with the results from the solution NMR experiment.



Tuning the nitric oxide release behavior of amino functionalized HKUST-1



Katharina Peikert^{a, b}, Laura J. McCormick^b, Damiano Cattaneo^b, Morven J. Duncan^b, Frank Hoffmann^a, Arafat H. Khan^c, Marko Bertmer^c, Russell E. Morris^b, Michael Fröba^{a, *}

^a Department of Chemistry, Institute of Inorganic and Applied Chemistry, University of Hamburg, Martin-Luther-King Platz 6, D-20146 Hamburg, Germany

^b EaSTChem School of Chemistry, University of St. Andrews, Purdie Building, St. Andrews KY16 9ST, United Kingdom

^c Physics and Earth Sciences, Institute of Experimental Physics II, Leipzig University, Linnéstraße 5, 04103 Leipzig, Germany

ARTICLE INFO

Article history:

Received 3 December 2014

Received in revised form

12 June 2015

Accepted 15 June 2015

Available online 25 June 2015

Keywords:

Metal-organic framework

HKUST-1

Amino functionalized HKUST-1

Nitric oxide release

NONOate

ABSTRACT

Four new secondary amino functionalized trimesic acid ligands (H_3RNHbc , $R = Me, Et, ^nPr, \text{ and } ^iPr$) were synthesized. When used in combination with H_3btc these ligands lead to four new mixed-linker metal-organic frameworks (MOFs) which we call UHM-36, UHM-37, UHM-38, and UHM-39. All MOFs are isostructural to HKUST-1. We tested these MOFs as nitric oxide storage and release materials and investigate the influence of the amine groups on the NO storage capacity of the MOFs. The results were compared to the unfunctionalized HKUST-1, *i.e.* $Cu_3(btc)_2$.

© 2015 Elsevier Inc. All rights reserved.

1. Introduction

Nitric oxide (NO) is a colorless, diatomic gas and a radical with one unpaired electron. For a long time this molecule had primarily been known as a toxic gas which contributes to acid rain, and is contained in smog and tobacco smoke [1]. However, since Furchgott, Ignarro, Murad, and Moncada investigated the crucial role of NO in the cardiovascular system in the late 1980s [2–4] the interest in this small compound has steadily grown. NO is now known as an extremely important biological protective, regulatory, and signaling molecule which plays a key role in many physiological processes, such as regulation of blood pressure and clotting, neurotransmission, vasodilation, inflammation, immune response, pulmonary hypertension, penile erection, anti-tumor activity, and wound healing [5–11].

The concentrations of NO that are needed for physiological processes are estimated to vary between 100 pM and 5 nM [12]. The required amount of NO is normally regulated and well balanced by the endothelial enzyme nitric oxide synthase (NOS). However,

excessive NO can lead to dangerously low blood pressure and interaction with transition metals, heme-containing proteins, and thiol groups, which results in the oxidation and damage of functional groups on proteins and DNA. On the other hand, a lack of NO will lead to serious health problems, such as unwanted clot formation, erectile dysfunction, and respiratory distress [1,13,14]. When using exogenous NO for therapeutic applications it is therefore important to develop compounds, which allow a controlled release and targeted delivery of NO to specific sites in the body [1].

During the last decades a lot of research has been done in developing appropriate NO storage and release systems: NO can be released from organic nitrates, nitrites, metal-NO complexes, nitrosamines, *N*-diazoniumdiolates (NONOates), and *S*-nitrosothiols (RSNOs) [15]. NO release systems based on these functionalities include amino functionalized polymers [16,17] and silica particles [18,19], in which the NO is stored as NONOates, as well as metal exchanged zeolites [20] and metal-organic frameworks (MOFs), in which the NO is bound directly to the metal centers [21].

MOFs are solid state inorganic-organic materials, which have attracted much attention during the past decade as they have shown excellent performance in applications like gas storage and separation [22,23], catalysis [24], sensing [25,26], and drug delivery [27].

* Corresponding author.

E-mail address: freeba@chemie.uni-hamburg.de (M. Fröba).

So far, two ways of using MOFs as NO release materials have been developed. On the one hand the NO can be adsorbed inside the pores and coordinate to so-called coordinatively unsaturated metal sites (CUS) or 'open' metal sites (OMS) [28–30]. On the other hand NONOates can be built inside the MOF if the ligands contain amino functionalities [31,32]. Two molecules of NO react with one primary or secondary amine group to form an ionic diazeniumdiolate. In both cases NO can be released again on contact with water (see Fig. 1).

Xiao et al. [28] were the first to report on NO storage in MOFs. They examined the NO adsorption and release behavior of HKUST-1. This MOF contains OMS and NO can be stored by coordination to these metal centers. At 1 bar, HKUST-1 adsorbs $\sim 9 \text{ mmol g}^{-1}$ at $-104 \text{ }^\circ\text{C}$ and $\sim 3 \text{ mmol g}^{-1}$ at $25 \text{ }^\circ\text{C}$. In both cases, 2.21 mmol g^{-1} remains inside the MOF even after the pressure is reduced to almost zero. However, the NO-loaded MOF releases only around $2 \text{ } \mu\text{mol NO per g}$ of HKUST-1 when exposed to a flow of humid nitrogen (11% relative humidity, RH). CPO-27-M (M = Co, Ni) shows improved delivery behavior over HKUST-1, storing $\sim 7 \text{ mmol NO per g}$ MOF at $25 \text{ }^\circ\text{C}$ and releasing almost the total amount under humid conditions [30,33].

Other groups concentrated on the storage of NO in form of NONOates. For example, Nguyen et al. [32] used IRMOF-3 and UMCM-1-NH₂, both zinc-containing MOFs without OMS but which have primary amine groups on the bridging ligand. These MOFs were loaded with NO dissolved in CHCl₃ at 8 bar and room temperature for 24 h. By FT-IR studies it was shown that under these conditions NONOates were formed. When placed in a phosphate buffer solution, IRMOF-3-NONO and UMCM-1-NONO release 0.51 mmol and $0.10 \text{ mmol NO per g}$ MOF, respectively.

Lowe et al. [34] used Cu-TDPAT (H₆TDPAT = 2,4,6-tris(3,5-dicarboxylphenylamino)-1,3,5-triazine) as an NO storage and release system, a MOF which offers both OMS as well as secondary amine groups. The NO release was tested at $37 \text{ }^\circ\text{C}/0\% \text{ RH}$ and $\text{RT}/85\% \text{ RH}$, respectively. The best results were achieved under the latter conditions to give a total release amount of $175 \text{ } \mu\text{mol NO per g}$ Cu-TDPAT.

In this work, we present the synthesis and characterization of the four mixed-linker MOFs – UHM-36, UHM-37, UHM-38, and UHM-39 (UHM = University of Hamburg Materials) – formed using a mixture of H₃btc with either H₃MeNHbtc, H₃EtNHbtc, (H₃¹³CPrNHbtc), or (H₃¹PrNHbtc) (Fig. 2). All MOFs are isostructural with HKUST-1 and UHM-30 [35] – the primary amino functionalized HKUST-1. We show how the amine groups influence the NO storage capacity and release performance of these MOFs. In contrast to HKUST-1, our MOFs store NO not only via sorption at the OMS but via NONOate formation as well.

2. Experimental

2.1. Materials

All starting materials and solvents were purchased and used without further purification from commercial suppliers (Sigma–Aldrich, Alfa Aesar, Grüssing, Merck, and others).

2.2. Methods

Solution NMR spectra were acquired using a Bruker Fourier 300, a Bruker AV 400, or a Varian Gemini-200BB spectrometer. For solid-state NMR measurements, the activated samples UHM-36, UHM-37, UHM-38, and UHM-39 were sealed into glass ampules that fit into MAS rotors to prevent further modification. ¹H measurements were performed on a Bruker Avance 400 spectrometer using a 4 mm MAS probe. The spinning frequency was set to 10 kHz. The DEPTH pulse sequence [36] was used to suppress probe background signal. Recycle delays were 50 ms and the 90° pulse length was set to 2.4 μs . Spectra were referenced externally to TMS using PDMS as secondary reference ($\delta = 0.07 \text{ ppm}$). Spectra deconvolution was done with the dmfit program [37].

Infrared spectra were acquired using a Bruker Vertex FT-IR spectrometer (as KBr pellet or in ATR mode). Powder X-ray diffraction (PXRD) patterns were recorded at room temperature with a PANalytical X'Pert Pro PW3040/60 reflexion powder diffractometer using Cu K α radiation (45 kV, 40 mA; counting time:

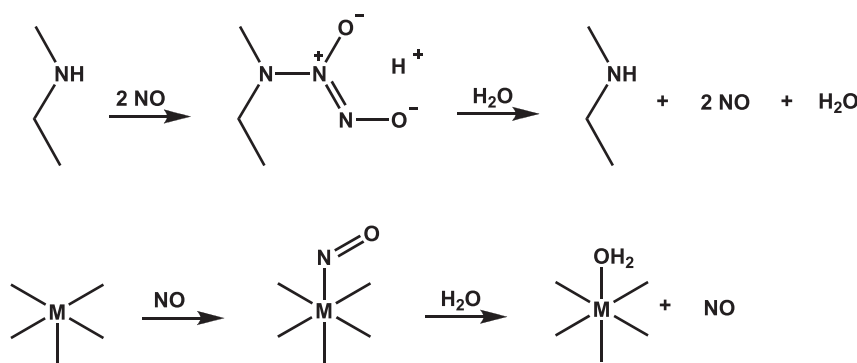


Fig. 1. NONOate formation and release mechanism (top), NO coordination to a metal center and release mechanism (bottom).

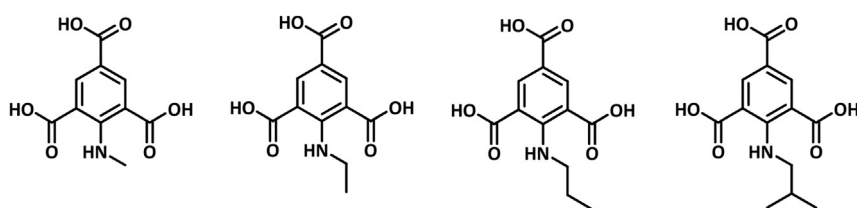


Fig. 2. New secondary amine H₃RNHbtc linkers used for the synthesis of UHM-36, UHM-37, UHM-38, and UHM-39.

74 s; steps: 0.013° (2 θ)). Thermal analysis (thermogravimetry (TG)/mass spectrometry (MS)) was conducted under argon flow (20 mL min⁻¹) with a NETZSCH STA 449 F3 Jupiter thermo-balance coupled by capillary with an Aëolos QMS 403 mass spectrometer. The heating rate was 5 °C min⁻¹ up to 800 °C. Nitrogen physisorption data were recorded with a Quantachrome QUADRASORB-SI-MP at -196.15 °C. The specific surface area was calculated from the adsorption branch in the relative pressure interval from 0.001 to 0.028 using the Brunauer–Emmett–Teller (BET) method. The micro pore volume was estimated from the quantity of gas adsorbed at a relative pressure of 0.18.

2.3. Linker synthesis

The synthesis of the four new secondary amino functionalized trimesic acid ligands (H₃RNHbtc, R = Me, Et, ⁿPr, and ⁱPr) were all carried out in a four step synthesis starting with 2-fluoro-1,3,5-trimethylbenzene. After oxidation of the methyl groups with potassium permanganate the resulting 2-fluoro-1,3,5-benzenetricarboxylic acid was esterified with methanol and sulfuric acid to give 2-fluoro-1,3,5-benzenetricarboxylic acid trimethyl ester. This compound was the starting compound for the amination. Either methylamine, ethylamine, *n*-propylamine, or *i*-propylamine was reacted with 2-fluoro-1,3,5-benzenetricarboxylic acid trimethyl ester in a mixture of methanol and dioxane. The resulting amines were each hydrolyzed in a mixture of methanol, tetrahydrofuran, and aqueous potassium hydroxide to give the final linkers *N*-methyl-2-amino-1,3,5-benzenetricarboxylic acid (H₃MeNHbtc), *N*-ethyl-2-amino-1,3,5-benzenetricarboxylic acid (H₃EtNHbtc), *N*-*n*-propyl-2-amino-1,3,5-benzenetricarboxylic acid (H₃ⁿPrNHbtc), and *N*-*i*-propyl-2-amino-1,3,5-benzenetricarboxylic acid (H₃ⁱPrNHbtc). Synthesis details for all compounds as well as the analytical data are given in the ESI.

2.4. MOF synthesis

2.4.1. HKUST-1

In a typical synthesis H₃btc (238 mg, 1.13 mmol) was dissolved in *N,N*-Dimethylacetamide (DMA) (20 mL), aqueous Cu(NO₃)₂·3H₂O (200 mg mL⁻¹, 2.25 mL, 1.86 mmol) was added and the mixture was heated to 85 °C for 46 h. The resulting blue crystalline powder was collected by filtration, washed with DMA and dried in air to yield 575 mg of HKUST-1. To remove the DMA the MOF powders were solvent exchanged with ethanol by continuous Soxhlet extraction for 20 h. After the solvent exchange the MOFs were thermally activated in vacuo for 20 h at 120 °C.

2.4.2. UHM-36, UHM-37, UHM-38, UHM-39 | Cu₃(RNHbtc)_x(btc)_{2-x} (x ≤ 1.2)

The amounts of the secondary amine linker were varied between 30 mol% and 70 mol%. The values for each synthesis are given in Table 1. In a typical synthesis the appropriate amount of H₃btc and H₃RNHbtc (R = Me, Et, ⁿPr, and ⁱPr) were dissolved in DMA (8 mL) with HNO₃ (20%, 0.56 mL). Afterwards aqueous Cu(NO₃)₂·3H₂O (200 mg mL⁻¹, 0.90 mL, 0.745 mmol) was added and the reaction mixture was heated to 80 °C for 46 h. The resulting

green powders were collected by filtration, washed with DMA, and dried in air to give the new MOFs UHM-36 (R = Me), UHM-37 (R = Et), UHM-38 (R = ⁿPr) and UHM-39 (R = ⁱPr). To remove the DMA the MOF powders were solvent exchanged with ethanol by continuous Soxhlet extraction for 20 h. After the solvent exchange the MOFs were thermally activated in vacuo for 20 h at 120 °C. For ¹H NMR studies approximately 20 mg MOF were digested in DMSO-*d*₆ and DCl.

2.5. Nitric oxide loading

The solvent exchanged MOF powders (~20 mg) were thermally activated under vacuum (10⁻⁸ bar) for 20 h at 120 °C. This temperature was chosen due to TGA data indicating a complete activation of the sample was achieved whilst maintaining the structural integrity of the MOF. After cooling to room temperature, the samples were exposed to nitric oxide (1 bar, 100%, BOC) for 1 h. Excess NO was removed by evacuation and flushing with argon. This process was repeated three times. NO-loaded samples were then flame-sealed under an argon atmosphere.

2.6. Nitric oxide release experiments

The quantification of NO release was carried out using a Sievers NOA 280i chemiluminescence NO analyzer. The instrument was calibrated by passing air through a zero filter (Sievers, < 1 ppb NO) and 87.6 ppm NO gas. The flow rate was set to 200 mL min⁻¹ with a cell pressure of 11.3 mbar and an oxygen pressure of 420 mbar. To measure the NO release of the MOFs approximately 20 mg of NO-loaded MOF powder was exposed to a nitrogen flow (11% RH), the resultant gas was directed into the analyzer, and the concentration of NO was recorded in ppm or ppb. Measurements were stopped when the sample release dropped below 20 ppb.

3. Results and discussion

3.1. Characterization of MOFs as-synthesized

In the first instance, attempts were made to generate single-linker MOFs containing the tri-anions of the four new H₃RNHbtc derivatives. This invariably led to fine crystalline powders – in the case of H₃MeNHbtc and H₃EtNHbtc even porous materials could be obtained – whose structures could not be solved and which are definitely not isostructural to HKUST-1. Therefore, an alternate synthetic approach was adopted, in which a mixture of H₃btc and H₃RNHbtc linkers was reacted with Cu(NO₃)₂. The amount of H₃RNHbtc was varied from 30 to 70 mol%, in order to find the maximum amount of the secondary amino linker component in the mixture that still lead to the formation of an HKUST-1 analogous phase. As NMR studies show (see below) the novel MOF materials have the composition Cu₃(RNHbtc)_x(btc)_{2-x} (x ≤ 1.2) and we have named them UHM-36 (R = Me), UHM-37 (R = Et), UHM-38 (R = ⁿPr) and UHM-39 (R = ⁱPr).

The PXRD patterns of the resulting MOFs show that, for mol fractions of up to 60% H₃RNHbtc, the resulting materials are composed of only one single phase, all unmistakable being isostructural to HKUST-1 (see Fig. 3 right). The use of 70 mol% H₃RNHbtc always leads to mixed-phase products. For the representative case of the linker mixture H₃btc/H₃MeNHbtc the PXRD patterns obtained in dependence of the varying molar ratios are shown in Fig. 3 (left). (For further details Fig. S1, ESI).

¹H NMR studies of the digested MOFs provide information on the ratio of the two linkers actually contained inside the MOF. In general, the results are in good agreement with the amount of linkers used in the synthesis, however, the mole fraction of

Table 1

Molar amounts which were used with all linkers for the syntheses of the mixed-linker MOFs Cu₃(RNHbtc)_x(btc)_{2-x} (x ≤ 1.2).

Percentage of RNH-H ₃ btc	30%	40%	50%	60%	70%
H ₃ btc	318 μmol	273 μmol	227 μmol	182 μmol	137 μmol
RNH-H ₃ btc	137 μmol	182 μmol	227 μmol	273 μmol	318 μmol

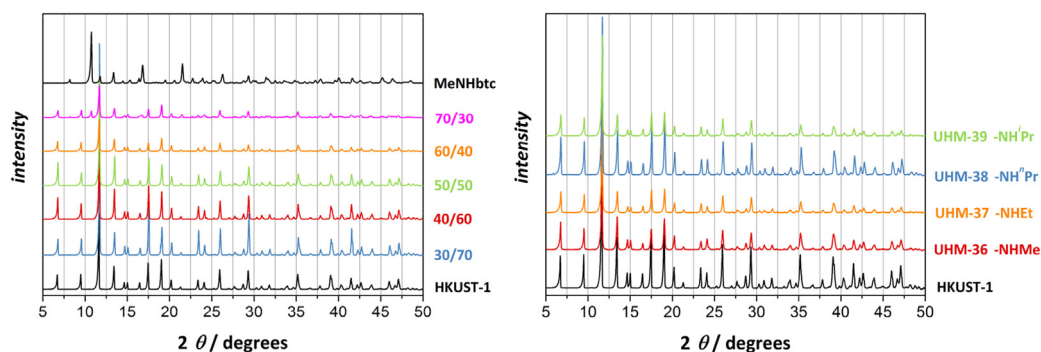


Fig. 3. Left: PXRD patterns of UHM-36 with different molar ratios of $\text{H}_3\text{MeNHbtc}$ used in the MOF synthesis. At mole fraction of 70% $\text{H}_3\text{MeNHbtc}$ the synthesis results in mixed phases. Concentrations between 30 and 60 mol% of the amine linker always lead to pure HKUST-1 analogous phases. (The diffraction patterns of UHM-37, UHM-38 and UHM-39 can be found in the ESI). Right: PXRD patterns of all mixed-linker MOFs with use of 60 mol% amine linker in the syntheses, compared to the PXRD pattern of HKUST-1.

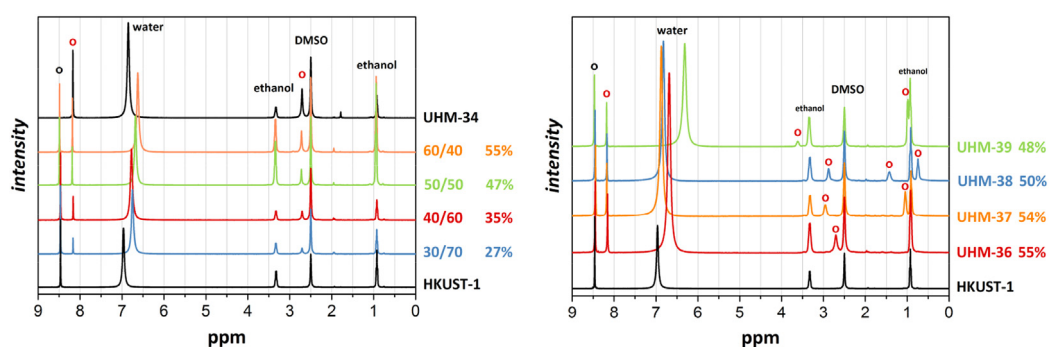


Fig. 4. Left: ^1H NMR spectra of digested UHM-36 samples with different molar ratios of $\text{H}_3\text{MeNHbtc}$ used in the MOF synthesis. Right: ^1H NMR spectra of all mixed-linker MOFs with use of 60 mol% amine linker in the syntheses, digested in DMSO and DCI. The shift of the water signal is due to variations of the pH value. The black circles mark the signal which belongs to H_3btc , the red ones mark the signals which belong to H_3RNHbtc . The signals are normalized to the peak at 8.5 ppm. The mole fraction of H_3RNHbtc is given as a percentage to the right of each diagram. (For interpretation of the references to color in this figure legend, the reader is referred to the web version of this article.)

RNHbtc^{3-} included in the final MOF is always slightly lower than that used in the synthesis (see Fig. 4, left), indicating that the incorporation of btc^{3-} is slightly more favored. This effect gets stronger with increasing length of the alkyl chain of the secondary amine group. But in all cases, the use of 60 mol% H_3RNHbtc in the synthesis lead to MOF structures in which approximately 50% of the linkers are amino functionalized (see Fig. 4, right). The final values are 55% MeNHbtc^{3-} for UHM-36, 54% EtNHbtc^{3-} for UHM-37, 50% $^n\text{PrNHbtc}^{3-}$ for UHM-38, and 48% $^i\text{PrNHbtc}^{3-}$ for UHM-39. Therefore, all further experiments were carried out on MOFs where the amount of amine-btc component used in the synthesis was 60 mol%.

In addition to solution NMR studies we did solid-state ^1H -NMR studies on all mixed-linker MOFs where 60 mol% H_3RNHbtc were used in the syntheses. Fig. 5 shows the isotropic region of the ^1H solid-state NMR spectra. In all cases only one signal at around 8.2 ppm is detected for aromatic protons, representing the protons from the btc^{3-} linker as well as from the RNHbtc^{3-} linkers. Similar to the results for UHM-30 [38], the amine proton signals show broad resonances due to structural disorder, the exact shift is hard to determine because of signal overlap. In spite of this overlap, we determine a shift of the alkyl proton signals to smaller values with increasing alkyl chain length. The signal maximum is moving roughly from 3 ppm (methyl group, UHM-36) to 1 ppm (ethyl group, UHM-37) and finally to -0.5 ppm (*n*-propyl group, UHM-38). For UHM-39 (*i*-propyl group) we detect a shift towards higher values again with a maximum at approximately 0.7 ppm. This observation is in good agreement with the results from the solution NMR experiments. Additionally, the intensity of the alkyl

proton signal is increasing with respect to the aromatic proton signal due to the higher number of protons with increasing alkyl chain length. The large line width, which is due to interaction with the unpaired electron at the copper site [39] prevents resolution of all signals for the individual functional groups. By signal deconvolution of the full spectrum including spinning sidebands, quantification of the final incorporation of the two linkers inside the MOFs was possible. The full spectra are shown in the ESI (Fig. S11). From

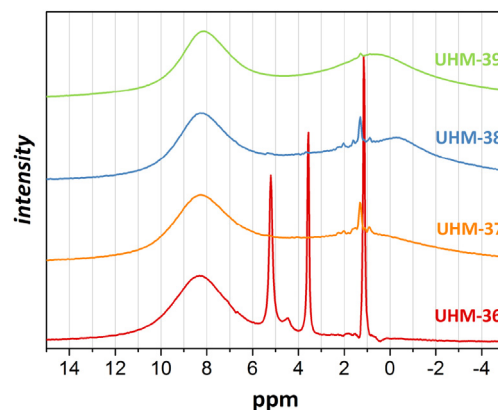


Fig. 5. Isotropic region of ^1H solid-state NMR spectra of UHM-36, UHM-37, UHM-38, and UHM-39. In UHM-36 three narrow signals are visible stemming from remaining ethanol molecules within the MOF. In all samples small narrow signals around 1 ppm are visible due to the sealing of the glass ampoules with natural gas. The signals are normalized to the peak at 8.2 ppm.

Table 2
BET surface areas and micropore volumes of all secondary amine functionalized mixed-linker MOFs.

	UHM-36	UHM-37	UHM-38	UHM-39
$S_{\text{BET}}/\text{m}^2 \text{g}^{-1}$	1390	1299	1264	1326
$V_{\text{micropore}}/\text{cm}^3 \text{g}^{-1}$	0.54	0.51	0.49	0.53

the relative area integration with respect to the contribution of the aromatic proton signal (by both btc^{3-} and RNHbtc^{3-}) and other signals belonging only to the RNHbtc^{3-} linker, the relative ratios of the two linkers can be calculated (for details see ESI). The final values are 57% MeNHbtc^{3-} for UHM-36, 56% EtNHbtc^{3-} for UHM-37, 46% PrNHbtc^{3-} for UHM-38, and 49% PrNHbtc^{3-} for UHM-39. This trend is similar to the one observed in the solution NMR analysis of the digested MOFs. Due to the strong overlap of the signals, there is a significant uncertainty associated with the integration. However, this method allows the quantification of the linker ratio inside the MOFs without destroying the MOF structure. In diamagnetic MOFs, having much lower line widths, a quantification would be more accurate.

To test the permanent porosity of the mixed-linker MOFs, the MOFs were activated via solvent exchange with ethanol and thermal treatment at 120 °C under vacuum, and nitrogen physisorption isotherms were measured at −196.15 °C. The isotherms show a typical type-I shape and analysis reveals specific surface areas between 1264 $\text{m}^2 \text{g}^{-1}$ and 1390 $\text{m}^2 \text{g}^{-1}$ (calculated from the adsorption branch and in the relative pressure interval from 0.001 to 0.028) and micropore volumes between 0.49 $\text{cm}^3 \text{g}^{-1}$ and 0.54 $\text{cm}^3 \text{g}^{-1}$ (calculated at $p/p_0 = 0.18$). These values are lower but still comparable to those known for HKUST-1 ($S_{\text{BET}} = 1239\text{--}1944 \text{m}^2 \text{g}^{-1}$, $V_{\text{micropore}} = 0.62 \text{cm}^3 \text{g}^{-1}$) [40–43] and UHM-30 ($S_{\text{BET}} = 1834 \text{m}^2 \text{g}^{-1}$, $V_{\text{micropore}} = 0.69 \text{cm}^3 \text{g}^{-1}$) [35]. The isotherms of all MOFs can be found in the ESI and Table 2 gives the details for each material.

3.2. Characterization of NO-loaded and NO-released MOFs

The NO-loaded MOFs were characterized by PXRD, ATR-FTIR and Raman spectroscopy as well as TG-DSC studies.

The PXRD patterns indicate that the structures remain intact after solvent exchange as well as after NO loading. Some intensity differences and missing diffraction peaks may reflect scatter from coordinated NO and NONOate groups inside the pores. After the NO release the MOFs loose crystallinity but the HKUST-1 analogous structure can still be recognized (see Fig. S10 ESI).

The ATR-FTIR spectrum of HKUST-1 shows only one significant difference for the NO-loaded MOF compared to the unloaded MOF: In the IR spectra of the NO-loaded MOF samples an additional weak band at 1700 cm^{-1} is detectable (see Fig. 6, top). A similar result has already been reported in the literature [32]. This additional band at 1700 cm^{-1} is also observed for all of the secondary amine mixed-linker MOFs after the NO loading procedure. However, in their NO-loaded status further changes in their respective IR spectra can be revealed. For UHM-36 ($R = \text{Me}$) the shoulder at 1421 cm^{-1} is slightly more pronounced in the NO-loaded MOF (see Fig. 6, bottom). This wavenumber is characteristic of an $-\text{N}=\text{N}-\text{O}$ group and therefore would indicate the formation of NONOate groups inside the MOF. However, this change is not significant for the other amino functionalized MOFs (UHM-37 to −39). Furthermore, the shoulder at 700 cm^{-1} disappears after NO loading – this signal is typical of $-\text{N}-\text{H}$ deformation vibrations in secondary amines and would also suggest NONOate formation. This effect is weaker for UHM-37, UHM-38, and UHM-39, but still detectable. We also observe a shift of the band at 1275 to 1282 cm^{-1} . In this region the $-\text{C}-\text{N}$ stretching vibrations of secondary amines are expected and a shift

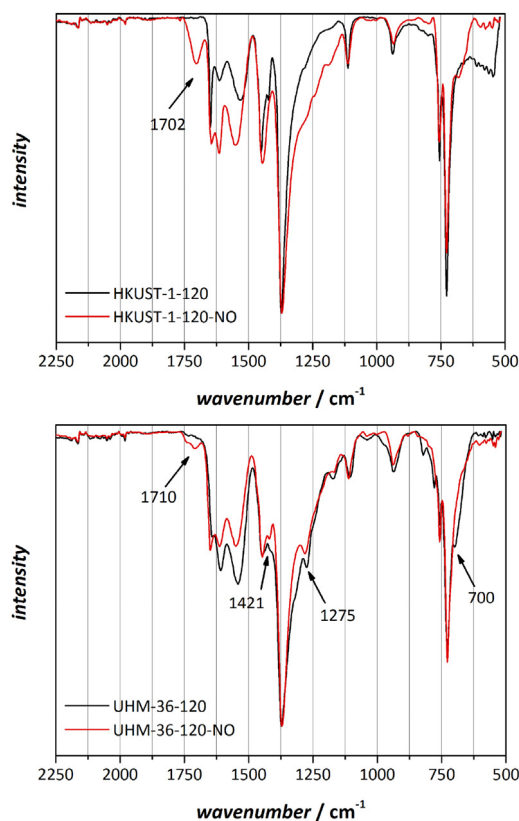


Fig. 6. ATR-FTIR spectra of HKUST-1 (top) and UHM-36 (bottom) after thermal activation at 120 °C in vacuo (black) and after thermal activation under the same conditions and NO loading at 1 bar (red). The spectra are normalized to the most intense band (1375 cm^{-1}). Analogous spectra for the other MOFs are shown in Figs. S3–S5, ESI. (For interpretation of the references to color in this figure legend, the reader is referred to the web version of this article.)

of this band could indicate a change of the chemical surrounding of the respective bond. Shifting of the peaks at 1542, 1609, and 1642 cm^{-1} to 1549, 1614, and 1650 cm^{-1} , respectively, is also observed. Even though the evidence is not conclusive, we assume the formation of NONOates took place. Possibly one bar loading pressure and a loading time of 1 h are insufficient to completely convert the amine groups into NONOate groups and as the expected bands for a NONOate group ($-\text{N}=\text{N}-\text{O}$, $-\text{N}=\text{N}$, $-\text{N}-\text{N}$, $-\text{N}-\text{O}$) occur in a region where the spectra of the unloaded MOFs contain a large number of non-characteristic and unrelated peaks, the successful conversion will not necessarily be evidently seen in the FT-IR spectra. This leads to the conclusion that NO is coordinated to the copper centers on the one side and reacts with the amine groups to form NONOate groups at the same time. Detailed information is given in Table S1 (ESI).

Raman spectroscopy investigations were conducted on both NO-loaded and unloaded MOFs, however, no conclusive evidence for NONOate formation could be obtained.

Fig. 7 shows TG-DSC studies in argon atmosphere coupled with mass spectrometry of both an unloaded and NO-loaded sample of HKUST-1 and UHM-38, respectively. HKUST-1 is stable up to 300 °C, and the decomposition of the NO-loaded HKUST-1 sample occurs at a slightly lower temperature. Both HKUST-1 samples show a loss of water up to 100 °C even though they were thermally activated. Most likely, the samples adsorbed some water during the preparation for the TG experiment. Between 100 °C and 300 °C the unloaded HKUST-1 sample shows a weight loss of 4.4%, whereas the NO-loaded HKUST-1 sample shows a significantly higher mass loss

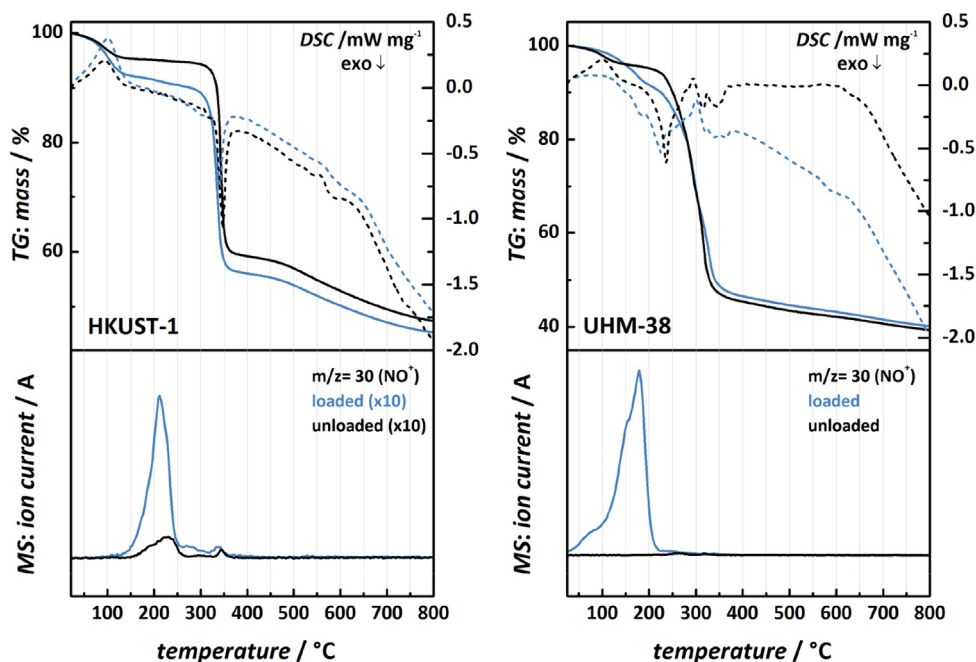


Fig. 7. Results of TG-DSC/MS studies of HKUST-1 (left) and UHM-38 (right) before (black) and after (blue) NO loading. All measurements were carried out in argon atmosphere. Analogous graphs of the other MOFs are shown in Fig. S6, ESI. The bottom part shows the ion current of the mass signal $m/z = 30$. In the top part, the solid lines represent the TG signal with the corresponding scale on the left side of the graph, the dotted lines represent the DSC signal with the corresponding scale on the right side of the graph. (For interpretation of the references to color in this figure legend, the reader is referred to the web version of this article.)

of around 8%. Similarly, the mass signal of $m/z = 30$ (NO^+) is significantly higher for the NO-loaded HKUST-1 and it can be detected in a temperature region between 140 °C and approximately 250 °C, which is in both cases below the temperature at which the main decomposition of the framework starts. The origin of the $m/z = 30$ signal of the unloaded HKUST-1 sample is unclear, but it can possibly be attributed to an incomplete activation procedure, in consequence of which decomposition of the remaining ethanol molecules leads, amongst others, to C_2H_6^+ fragments which also show a mass signal of $m/z = 30$. As the NO-loaded HKUST-1 sample also generates a signal of $m/z = 14$ (N^+) over the exact same temperature range as for the $m/z = 30$ signal, while this is absent for the unloaded HKUST-1, this leads to the assumption that the $m/z = 30$ signal for the unloaded HKUST-1 sample did not arise from (erroneous) contaminations with NO. For full TG/MS details with all m/z traces, see the ESI.

The secondary amino functionalized MOFs show a thermal stability up to around 250 °C. Between 100 °C and the start of the decomposition, the unloaded and NO-loaded UHM-38 samples show a mass loss of around 5% and 12%, respectively. Comparing the NO-loaded HKUST-1 with the NO-loaded UHM-38 sample, the most prominent difference is related to the temperature region, in which the $m/z = 30$ signal can be detected. While it starts only at 140 °C for NO@HKUST-1 it is already detectable at 25 °C for NO@UHM-38 and shows several steps with the maximum ion current at 175 °C. Interestingly, these steps can also be observed in the accompanying DSC curve as small exothermal peaks, which are not detectable for the NO-loaded HKUST-1 sample or any unloaded MOF. These results support the hypothesis that at least two differently bound NO species are present inside the NO-loaded amino functionalized MOFs – one being adsorbed by the copper OMS and one via NONOate formation. Furthermore, taking into account the considerably lower temperature at which the NO-loaded UHM-38 sample releases NO in comparison to the HKUST-1 sample, which only provides OMS, it is obvious that the NONOate-mediated delivery of NO demands lower thermal energy.

3.3. NO release studies

The NO release profiles of the NO-loaded mixed-linker MOFs were plotted, together with the respective profile of HKUST-1, in two different manners, in Fig. 8 as a cumulative total amount of NO released per gram of MOF versus time and in Fig. S8 (ESI) as the actual NO concentration in the gas stream at a given point in time. Measurements were carried out at least in triplicate and representative values are used for discussion and in Fig. 8 and S8. A full documentation of all measurement results is given in the ESI. The total amount of NO released for HKUST-1 is around 2 μmol NO per g MOF, which is in good agreement with the results obtained by earlier studies [28]. The duration until the NO concentration dropped below 20 ppb amounts to approx. 1 h. For all mixed-linker MOFs this time period was considerably longer and it takes up to 7 h in the case of UHM-39. The highest total amount of NO released is around 65 μmol NO per g of MOF for UHM-37, which is approximately 30 times more than for HKUST-1. In general, it is expected that a stronger nucleophile exhibits a higher reactivity towards the electrophilic NO. This means that secondary amine groups should react more easily with NO than primary amine groups. Furthermore, as the nucleophilicity of secondary amines increases with increasing electron density at the nitrogen atom and the electron donating effect (+I effect) of alkyl groups increases with increasing chain length and branching, we would have expected the highest release for UHM-39, as the *i*-propyl group gives the strongest +I effect. However, the reaction of the amine group with NO is not only controlled by the nucleophilicity of the amine. Probably, the accessibility of the nitrogen atom of the amine group plays a crucial role as well. Therefore, we assume that in UHM-37 the best balance between steric effects and the influence of the +I effect is given.

ATR-FTIR studies and TG-MS experiments indicate that NO sorption takes place via coordination to the OMS of copper as well as via NONOate formation. However, the NO release curves do not give any conclusive evidence that there are different release

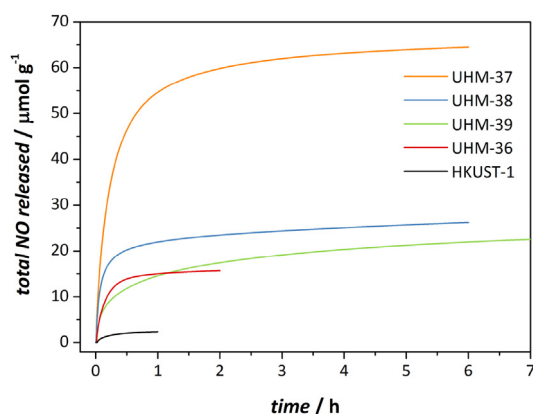


Fig. 8. Cumulative total amount of NO released by the mixed-linker MOFs versus time ($\mu\text{mol per g of MOF}$) compared to HKUST-1.

kinetics for the two differently bound NO species. The release of both NO species induced by a humid gas stream seems to be simultaneous and it is a continuous process. In contrast to this observation the thermally induced release (see TGA studies) starts at lower temperatures for the NONOate-mediated NO release. However, we observe different NO release kinetics for the different mixed-linker MOFs, which is also reflected in the initial slope of the release curves, which increase in the order $\text{UHM-39} < \text{UHM-36} < \text{UHM-38} \approx \text{UHM-37}$. The time it takes for half of the NO to be released (half-life period) is quite similar for UHM-36, UHM-37, and UHM-38 (values for all measurements are between 4.17 and 12.3 min, see Table S3, ESI), but significantly longer for UHM-39 (between 25.9 and 60.3 min). This effect could be related to the strongest +I effect for the *i*-propyl group, as it can be assumed that the easier the NONOate is formed the stronger it is bound, and *vice versa*, the slower the NO release. Interestingly, a first analysis of the time dependency of the NO release reveals that the kinetics for all mixed-linker MOFs does not follow a rate law of zero-, first-, or second-order. In order to find rate laws, which are coherent for all MOFs under investigation further studies on the release kinetics are needed and are already in progress.

The comparison of the total NO amounts released from the four different RNHbtc-MOFs does not reveal a conclusive pattern. However, the results demonstrate that the different alkyl groups at the amines have apparently a different influence on the NONOate formation. The results also manifest that the NO loading conditions (1 bar loading pressure and 1 h loading time) were insufficient to completely convert the amine into NONOate groups. If the NONOate formation was complete, we would expect comparable amounts of NO released from all the mixed-linker MOFs. However, we would still expect differences in the kinetics of the NO release with regard to an increasing binding strength of NO within the NONOate groups with increasing +I effect. It is necessary to further investigate the influence of the alkyl groups with respect to the NONOate formation and the release behavior. Investigations could for example include NO loading procedures with longer loading times and/or at higher pressures as well as studies with other secondary amino functionalized MOFs.

The exact release amounts and release times for all MOFs under consideration are gathered in Table 3.

Regarding the reported results on the NONOate formation and the NO release behavior of these secondary amino functionalized MOFs, we planned to investigate the NO release behavior of the corresponding primary amino functionalized MOF UHM-30 as well. First NO loading experiments with UHM-30 surprisingly showed that this MOF briefly ignites when exposed to an NO atmosphere.

Table 3

Values of total NO release, release times and half-life periods.

	HKUST-1	UHM-36	UHM-37	UHM-38	UHM-39
Total release/ $\mu\text{mol g}^{-1}$	2.36	15.69	64.45	26.21	22.54
Time of release/h	1	2	6	3	7
Half-life period/min	8.10	7.02	12.3	4.32	25.9

PXRD experiments reveal the MOF is reduced to Cu_2O and elemental copper.

Compared to other NO-releasing MOFs the total amount of NO released from our MOFs is significantly lower. IRMOF-3-NONO and UMCM-1-NONO (both MOFs containing primary amine groups) for instance release $510 \mu\text{mol}$ and $100 \mu\text{mol}$ NO per g of MOF, respectively [32]. Cu-TDPAT gives a total amount of release of $175 \mu\text{mol}$ NO per g of Cu-TDPAT [33]. However, it has to be mentioned, that the loading of these MOFs took place at higher pressures and the NO release experiments were conducted in a 0.01 M phosphate buffer for IRMOF-3-NONO and UMCM-1-NONO and under 85% relative humidity for Cu-TDPAT. In both cases the humidity was therefore significantly higher than for our release experiments. And we could possibly expect higher NO release amounts after loading at higher pressures and under more humid conditions as well. A direct comparison is therefore not possible. For a controlled NO release, the release time also plays a crucial role. Our MOFs release NO over a period between 2 and 7 h. Compared to Cu-TDPAT which releases NO over a period of seven days this is still not a very long period of time. However, we are able to show that incorporation of secondary amino functionalities inside the HKUST-1 structure leads to (a) a significant increase of the total amount of NO released from the MOFs and (b) an increase of the duration of the NO release as well.

3.4. Toxicology

An important question when thinking about the use of any new material to deliver an agent that may be therapeutic is the toxicology. While a full toxicology study is beyond the scope of this paper, it is valuable to at least ascertain any issues that might preclude the use of the basic HKUST-1 MOFs. Two of the most likely targets for any therapies using NO are the cardiovascular system and dermatology. Therefore for our initial screens we looked at the red blood cells and dermal fibroblasts were chosen as representative cells.

For toxicology testing, small pellets (5 mm diameter, total mass = 20 mg) were prepared using varying quantities of HKUST-1 blended with polytetrafluoroethylene (PTFE), some of these pellets were NO loaded using a similar procedure as previously outlined (see section 2.4). Known concentrations of both human red blood cells and dermal fibroblast cells were exposed to HKUST-1 and HKUST-1-NO for 3 h at 37°C . Hemolysis, the destruction of red blood cells, was determined by measuring the increase in absorbance at 575 nm relative to controls, sterile deionized water (100% hemolysis) and isotonic buffer (0% hemolysis), whereas the metabolic activity of the skin cells was monitored via a fluorescence technique using the cell viability indicator (10% v/v, Alamar blue) with sodium dodecyl sulfate (100% lysis) and isotonic buffer (0% lysis) as controls.

For all concentrations of HKUST-1 tested (up to ~ 5 mg) there was no hemolytic effect for either HKUST-1 or the material that was NO loaded. On exposure to this Cu based MOF the less robust skin cells, however, did show a toxicological effect, although there was no marked difference between the NO loaded material and as-synthesized. This would suggest that the cytotoxicity is triggered by the release of Cu ions from the MOF. It is widely known that HKUST-1 is unstable in aqueous conditions and dissolves significantly.

Indeed, high tens of ppm of Cu ions were released from the surface of a pellet containing ~5 mg of HKUST-1 during the first 24 h period, thereafter dropping to a constant release of <2 ppm over the next 10 days. For real application in, for example, medical devices one will need to avoid this solubility of HKUST-1. One could do this in two main ways. One method is to choose a more stable MOF that is not so soluble in aqueous solutions, applying the same concepts as described here to develop new MOFs that do not have the toxicity issues. However, another option is to formulate the materials in such a way as to prevent excessive dissolution. A good example of this is the coating of medical devices with NO delivering agents. More complex formulations than that utilized here, such as MOF-polymer composites, that will allow for the diffusion of the small molecule NO from the 3D framework whilst acting as a barrier to release of any MOF degradation products, in particular charged ones like metal ions, can be visualized. Such formulations to reduce the delivery of metal ions into physiological solutions are the subject of further ongoing research.

4. Conclusion

In conclusion, we have synthesized four new secondary amino functionalized H₃btc linkers. Usage in MOF syntheses in mixtures with H₃btc results in four new mixed-linker MOFs, UHM-36, UHM-37, UHM-38, and UHM-39 (R = Me, Et, ³Pr, and ⁴Pr, respectively), all being isostructural to HKUST-1. It was possible to incorporate up to approximately 50 mol% of amino functionalized linkers inside the MOFs. The mixed-linker MOFs were used for NO release studies and the results were compared to the release behavior of HKUST-1. AT-FTIR studies and TG-MS experiments indicate the formation of NONOate groups. For all H₃RNHbtc-MOFs a significant increase in the total NO release amount could be detected. UHM-37 shows the highest NO release with 65 μmol g⁻¹ which is approximately 30 times more than for HKUST-1. Furthermore, the duration of NO release is up to 7 times longer than for HKUST-1. Further NO loading studies at higher pressures and kinetic studies of the release behavior are already in progress.

Acknowledgments

We thank the Deutsche Forschungsgemeinschaft (DFG: Fr 1372/18-2) for supporting this work as part of the priority program 1362 (porous metal-organic framework).

Appendix A. Supplementary data

Supplementary data related to this article can be found at <http://dx.doi.org/10.1016/j.micromeso.2015.06.020>.

References

- [1] J.E. Saavedra, L.K. Keefer, *J. Chem. Educ.* 79 (12) (2002) 1427–1434.
- [2] L.J. Ignarro, G.M. Buga, K.S. Wood, R.E. Byrns, G. Chaudhuri, *Proc. Natl. Acad. Sci. U. S. A.* 84 (1987) 9265–9269.
- [3] R.M.J. Palmer, A.G. Ferrige, S. Moncada, *Nature* 327 (1987) 524–526.
- [4] R.M.J. Palmer, D.S. Ashton, S. Moncada, *Nature* 333 (1988) 664–666.
- [5] A.W. Carpenter, M.H. Schoenfish, *Chem. Soc. Rev.* 41 (2012) 3742–3752.
- [6] K. Thermos, *Mol. Cell. Endocrinol.* 286 (2008) 49–57.
- [7] M.T. Gladwin, J.H. Crawford, R.P. Patel, *Free Radic. Biol. Med.* 36 (2004) 707–717.
- [8] L.J. Hofseth, *Cancer Lett.* 268 (2008) 10–30.
- [9] K.D. Bloch, F. Ichinose Jr., J.D. Roberts, W.M. Zupl, *Cardiovasc. Res.* 75 (2007) 339–348.
- [10] M.R. Melis, A. Argiolas, *Eur. J. Pharmacol.* 264 (1995) 1–9.
- [11] P. Pacher, J.S. Beckmann, L. Liaudet, *Physiol. Rev.* 87 (2007) 315–424.
- [12] C.N. Hall, J. Garthwaite, *Nitric Oxide* 21 (2009) 92–103.
- [13] A.B. Seabra, N. Duran, *J. Mater. Chem.* 20 (2010) 1624–1637.
- [14] L.K. Folkes, P. O'Neill, *Nitric Oxide* 34 (2013) 47–55.
- [15] D.A. Riccio, M.H. Schoenfish, *Chem. Soc. Rev.* 41 (2012) 3731–3741.
- [16] P.G. Parzuchowski, M.C. Frost, M.E. Meyerhoff, *J. Am. Chem. Soc.* 124 (2002) 12182–12191.
- [17] M.M. Reynolds, J.A. Hrabie, B.K. Oh, J.K. Politis, M.L. Citro, L.K. Keefer, M.E. Meyerhoff, *Biomacromolecules* 7 (2006) 987–994.
- [18] H. Zhang, G.M. Annich, J. Miskulin, K. Stankiewicz, K. Osterholzer, S.I. Merz, R.H. Bartlett, M.E. Meyerhoff, *J. Am. Chem. Soc.* 125 (2003) 5015–5024.
- [19] J.H. Shin, S.K. Metzger, M.H. Schoenfish, *J. Am. Chem. Soc.* 129 (2007) 4612–4619.
- [20] P.S. Wheatley, A.R. Butler, M.S. Crane, S. Fox, B. Xiao, A.G. Rossi, I.L. Megson, R.E. Morris, *J. Am. Chem. Soc.* 128 (2006) 502–509.
- [21] A.C. McKinlay, R.E. Morris, P. Horcajada, G. Férey, P. Couvreur, C. Serre, *Angew. Chem. Int. Ed.* 49 (2010) 6260–6266.
- [22] R.E. Morris, P.S. Wheatley, *Angew. Chem. Int. Ed.* 47 (2008) 4966–4981.
- [23] J.-R. Li, R.J. Kuppler, H.-C. Zhou, *Chem. Soc. Rev.* 38 (2009) 1477–1504.
- [24] J. Lee, O.K. Farha, J. Roberts, K.A. Scheidt, S.T. Nguyen, J.T. Hupp, *Chem. Soc. Rev.* 38 (2009) 1450–1459.
- [25] M.D. Allendorf, R.J.T. Houk, L. Andruszkiewicz, A.A. Talin, J. Pikarsky, A. Choudhury, K.A. Gall, P.J.J. Hesketh, *J. Am. Chem. Soc.* 130 (2008) 14404–14405.
- [26] L.E. Kreno, K. Leong, O.K. Farha, M.D. Allendorf, R.P. van Duyne, J.T. Hupp, *Chem. Rev.* 112 (2011) 1105–1125.
- [27] P. Horcajada, R. Gref, T. Baati, P.K. Allan, G. Maurin, P. Couvreur, G. Férey, R.E. Morris, C. Serre, *Chem. Rev.* 112 (2012) 1232–1268.
- [28] B. Xiao, P.S. Wheatley, X. Zhao, A.J. Fletcher, S. Fox, A.G. Rossi, I.L. Megson, S. Bordiga, L. Regli, K.M. Thomas, R.E. Morris, *J. Am. Chem. Soc.* 129 (2007) 1203–1209.
- [29] N.J. Hinks, A.C. McKinlay, B. Xiao, P.S. Wheatley, R.E. Morris, *Microporous Mesoporous Mater.* 129 (2010) 330–334.
- [30] A.C. McKinlay, B. Xiao, D.S. Wragg, P.S. Wheatley, I.L. Megson, R.E. Morris, *J. Am. Chem. Soc.* 130 (2008) 10440–10444.
- [31] M.J. Ingleson, R. Heck, J.A. Gould, M. Rosseinsky, *Inorg. Chem.* 48 (2009) 9986–9988.
- [32] J.G. Nguyen, K.K. Tanabe, S.M. Cohen, *Cryst. Eng. Comm.* 12 (2010) 2335–2338.
- [33] F. Bonino, S. Chavan, J.G. Vitillo, E. Groppo, G. Agostini, C. Lamberti, P.D.C. Dietzel, C. Prestipino, S. Bordiga, *Chem. Mater.* 20 (2008) 4957–4968.
- [34] A. Lowe, P. Chittajallu, Q. Gong, J. Li, K.J. Balkus Jr., *Microporous Mesoporous Mater.* 181 (2013) 17–22.
- [35] K. Peikert, F. Hoffmann, M. Fröba, *Chem. Commun.* 48 (2012) 11196–11198.
- [36] M.R. Bendall, R.E. Gordon, *J. Magn. Reson.* 53 (1983) 365–385.
- [37] D. Massiot, F. Fayon, M. Capron, I. King, S.L. Calvé, B. Alonso, J.-O. Durand, B. Bujolli, Z. Gan, G. Hoatson, *Magn. Reson. Chem.* 40 (2002) 70–76.
- [38] A.H. Khan, K. Peikert, M. Fröba, M. Bertmer, same issue.
- [39] F. Gul-E-Noor, B. Jee, A. Pöpl, M. Hartmann, D. Hims, M. Bertmer, *Phys. Chem. Chem. Phys.* 13 (2011) 7783–7788.
- [40] J. Liu, J.T. Culp, S. Natesakhawat, B.C. Bockrath, B. Zande, S.G. Sankar, G. Garberoglio, J.K. Johnson, *J. Phys. Chem. C* 111 (2007) 9305–9313.
- [41] P. Krawiec, M. Kramer, M. Sabo, R. Kunschke, H. Frode, S. Kaskel, *Adv. Eng. Mater.* 8 (2006) 293–296.
- [42] A.G. Wong-Foy, A.J. Matzger, O.M. Yaghi, *J. Am. Chem. Soc.* 128 (2006) 3494–3495.
- [43] A.R. Millward, O.M. Yaghi, *J. Am. Chem. Soc.* 127 (2005) 17998–17999.



Katharina Peikert studied chemistry at the University of Hamburg and received her diploma in 2011. She is currently working on her PhD at the University of Hamburg under the guidance of Prof. Michael Fröba. Her research focus is on the synthesis of metal-organic frameworks as NO storage and delivery systems.



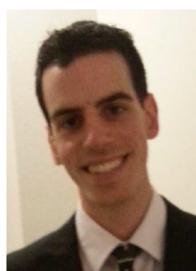
Dr. Frank Hoffmann After studying Chemistry at the University of Hamburg, Germany, he received a Ph.D. degree in 2002 and held a postdoctoral position at the University of Giessen until 2007. After returning to Hamburg he became the head of the X-ray crystallography division at the Institute of Inorganic Chemistry. He has worked for a long time on Langmuir monolayers – in particular studying chiral interactions – and Periodic Mesoporous Organosilicas (PMOs). His current research interests include crystal design, Metal-organic Frameworks (MOFs), network topology, gas storage, gas separation, molecular modeling in material science, chirality, fragrances and olfaction, and energy storage and conversion.



Michael Fröba studied chemistry in Würzburg and Hamburg and received his doctorate in 1993 from the Institute of Physical Chemistry, where he worked with Prof. W. Metz on graphite intercalation compounds. From 1994 to 1996, he was a Feodor Lynen research fellow in the group of Dr J. Wong at the Lawrence Livermore National Laboratory. After his habilitation at the University of Hamburg in 2000, he was appointed as an Associate Professor for Inorganic Chemistry at the University of Erlangen-Nuremberg. From 2001 to 2007 he was Full Professor for Inorganic Chemistry at the University of Giessen, and since 2007 he holds a chair for Inorganic Chemistry at the University of Hamburg, with a strong focus on solid-state and materials chemistry.



Russell Morris was born in St. Asaph, North Wales, and completed a D.Phil. at the University of Oxford. From 1991 to 1995 he was a postdoctoral researcher at the University of California Santa Barbara before returning to the UK to take up a position at the University of St. Andrews, where he is now Professor of Structural and Materials Chemistry. His research interests lie in the synthesis, characterization, and application of porous solids. Among his notable research successes are development of ionothermal synthesis, chiral induction of solids built from achiral precursors, characterization of solids by microcrystal X-ray diffraction, and application of porous solids in medicine and biology, particularly for the delivery of biologically active gases such as nitric oxide.



Damiano Cattaneo obtained his master's degree in Medicinal Chemistry at the Università degli Studi di Milano. He then moved to St Andrews, Scotland and began his PhD with the research group under the supervision of Professor Russell Morris. His research interests are mainly focused on using MOFs for biomedical application. Specifically, he investigates the development of porous materials as delivery systems. His research interests include the synthesizing of biocompatible metal organic frameworks using environmental friendly routes. These MOFs have the capacity to adsorb, store and release multiple entities such as drug molecules and biological relevant gases.



Arafat Hossain Khan earned Bachelor and Master degree in Applied Chemistry and Chemical Engineering from Dhaka University, Bangladesh. He achieved a second Master degree in Structural Chemistry and Spectroscopy from Leipzig University in 2014. His research interests focus on Solid State NMR characterization of metal-organic frameworks, particularly the interaction with NO.



Dr. Laura J. McCormick completed her undergraduate and PhD degrees at the University of Melbourne, Australia. This was followed by post-doctoral work at Monash University, Australia. She is currently a post-doctoral researcher at the University of St Andrews, where her research is focused on using known and novel coordination polymers and MOFs to store and deliver otherwise toxic gases for medical applications.



Marko Bertmer studied Chemistry at the Westfälische-Wilhelms-Universität Münster, where he received a Ph.D. Degree in 1999 in Physical Chemistry, working with Prof. Hellmut Eckert on solid-state NMR of aluminoborate glasses. At RWTH Aachen University he finished his habilitation in 2006. He was a Feodor-Lynen stipend from the Alexander-von-Humboldt Society working with Dr. S. Hayes at Washington University, St. Louis, MO, USA from 2002 to 2003. Currently, he is working as staff scientist and lecturer at Leipzig University in the group of Prof. J. Haase. His research interest is focusing on solid-state NMR of materials.

Paper III: Nitric oxide Adsorption in Cu₃btc₂-type MOFs - Physisorption and Chemisorption as NONOates [*J. Phys. Chem. C*, 123 (7): 4299-4307, 2019.]

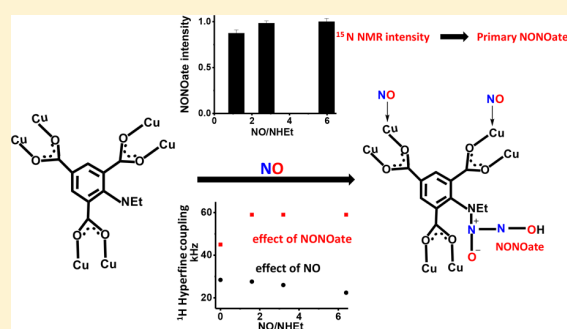
MAS NMR has been extensively investigated isotopically leveled ¹⁵NO loaded UHM-37 to understand the sorption priority, e.g., chemisorption or physisorption. The selection of UHM-37 out of other Cu₃(NHRbtc)₂ is imbued with the interest that the ethyl amine promotes UHM-37 more effectively than other secondary amine groups for NO adsorption and delivery. Ethyl amine achieves the best balance between the steric influences and the electron donating effects (+I effect) more than other amines. The multinuclear methodology together with the circumstance that the MOFs have antiferromagnetically coupled Cu-Cu pairs and NO being paramagnetic displays substantial effects on spectra that is in agreement with the inference of adsorption effects in these MOFs. Primary mode of NO adsorption as NONOate formation in UHM-37 is documented by the analysis of ¹H NMR spectra. ¹H spectra disclose that after the completion of NONOate formation, a surplus NO adsorption at the copper sites takes place. Furthermore, the observed ¹³C NMR shift is in accordance with ¹H NMR results upon NO adsorption in MOFs. ¹⁵N NMR studies of ¹⁵NO loaded in UHM-37 assigned directly NONOate signal, which is, to the best of our knowledge, the first report on ¹⁵N NMR results of NONOates in porous systems. In paper III the interactions of NO with UHM-37 and Cu₃btc₂ have been studied thoroughly by MAS NMR.

Nitric Oxide Adsorption in Cu_3btc_2 -Type MOFs—Physisorption and Chemisorption as NONOates

Arafat Hossain Khan,[†] Katharina Peikert,^{‡,¶} Frank Hoffmann,[‡] Michael Fröba,[‡] and Marko Bertmer^{*,†,§}[†]Felix Bloch Institute for Solid State Physics, Leipzig University, Linnéstraße 5, 04103 Leipzig, Germany[‡]Department of Chemistry, Institute of Inorganic and Applied Chemistry, University of Hamburg, Martin-Luther-King Platz 6, 20146 Hamburg, Germany[¶]Micromeritics GmbH, Rutherford 108, 52072 Aachen, Germany

Supporting Information

ABSTRACT: The adsorption of the biologically important signaling molecule nitric oxide (NO) on two metal–organic frameworks (MOFs), Cu_3btc_2 and $\text{Cu}_3(\text{NHetbtc})_2$, has been studied by multinuclear solid-state NMR. *N*-Diazenium diolate (NONOate) formation as primary mode of NO adsorption in the latter MOF is concluded from ^{15}N , ^1H , and ^{13}C NMR spectra together with analysis of the ^1H spin–lattice relaxation time (T_1). Furthermore, NO adsorption at the open metal site of Cu_3btc_2 as well as $\text{Cu}_3(\text{NHetbtc})_2$ is also evident, indicating both physisorption and chemisorption of nitric oxide.



INTRODUCTION

Metal organic frameworks (MOFs) represent a class of hybrid organic–inorganic porous materials that have attracted a lot of interest because of their chemical tunability, high porosities, and good thermal stability.^{1–5} The combination of these properties make these materials appealing for applications in gas adsorption, separation, and catalysis.^{6–8} Application of MOFs in the biomedical area has only recently been explored.⁹ Delivery and storage of exogenous nitric oxide (NO) from MOFs have come into focus.^{10–12} Nitric oxide is chemically a reactive-free radical. In the human body, it is endogenously produced and plays a central role with different functions such as preventing platelet activation and adhesion, inhibiting bacterial proliferation, enhancing endothelialization, signaling the response of the immune system, promoting angiogenesis, and contributing to the wound healing process.^{13–18} On the basis that NO holds promise as a potential therapeutic agent, a significant body of research has focused on strategies to deliver NO using synthetic donors, such as metal–NO complexes, *S*-nitrosothiols, and *N*-diazenium diolates (NONOates).^{11,12,17,19–21}

To date, one of the promising NO delivery materials is the MOF, which can store significant quantities of NO and then deliver it to specific sites in the body.^{22–24} The Ni-MOF

$[\text{Ni}_2(\text{C}_8\text{H}_2\text{O}_6)(\text{H}_2\text{O})_2] \cdot 8\text{H}_2\text{O}$ possesses at room temperature an adsorption capacity of ~ 7 mmol NO/g and releases almost all of the adsorbed NO upon exposure to moisture, an amount 7 times larger than released by metal-exchanged zeolite-A.^{10,24} An important feature of some MOFs is the presence of open metal sites (OMS) that are generated upon

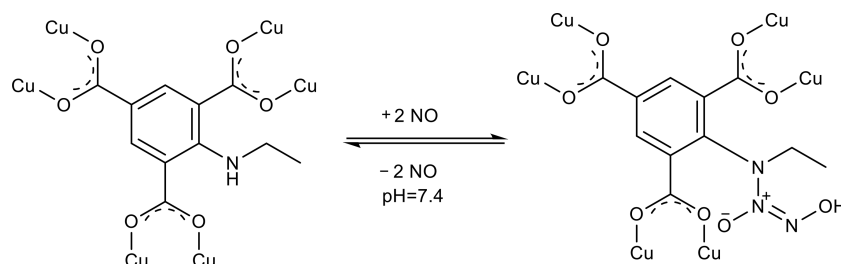
activation.^{25,26} Open metal sites are known to be preferred physisorption sites for guest molecules like NO, water, or other solvents, but physisorption might also take place at the pore walls, in particular at higher loadings. In addition, MOFs can be functionalized by amines that can chemisorb and covalently bind NO by forming *N*-diazenium diolates.^{27–29} NONOates (Scheme 1) are a particularly attractive vehicle for NO storage and delivery, because they undergo pH-dependent decomposition (faster release as the pH is lowered) to liberate NO.

Among the various MOFs, Cu_3btc_2 (also known as HKUST-1, commercially available as Basolite C300 from BASF) is one of the most prominent MOFs with OMS, for which applications in gas storage and gas separation have been demonstrated.³⁰ Morris and co-workers identified NO interaction at the OMS of Cu_3btc_2 at room temperature by changes via FTIR by detection of a characteristic shift of the NO stretching frequency.²² UMCM-1 and IRMOF-3, with pendant primary-amine groups, have been reported to form a NONOate as identified by FTIR, though NONOates derived from primary amines are not as stable as from secondary amines.³¹ Recently, Haikal et al. reported NONOate formation in the UiO-66-NH₂ MOF and physisorption of NO in different classes of microporous solids.³² Ingleson et al. reported NONOate formation in 4-(methylamino)-pyridine (4-map) by the reaction with NO where 4-map was coordinated to the Cu sites of Cu_3btc_2 .³³ In the Cu-TDPAT

Received: December 11, 2018

Revised: January 15, 2019

Published: January 23, 2019

Scheme 1. NONOate Formation at the NHEtbtC Linker in UHM-37^a

^aNONOates regenerate the secondary amine and 2 moles of NO per mole in physiological solution at pH 7.4 (and below).

MOF, NONOate formation with the secondary-amine linker was also shown by FTIR.³⁴

Recently, Peikert et al. presented a series of secondary-amine-functionalized mixed-linker Cu_3btc_2 -type MOFs.³⁵ $\text{Cu}_3(\text{NHEtbtC})_2$ (UHM-37, University of Hamburg Materials), synthesized using a mixture of H_3btc and $\text{H}_3\text{EtNHbtC}$ as linkers, is isostructural to Cu_3btc_2 and a good candidate for NONOate formation as well as NO coordination at copper sites. In addition, NONOate formation in UHM-37 upon NO adsorption has also been observed by FTIR.³⁵

Here, we report on the solid-state NMR study on NO adsorption for UHM-37 with varying loadings of NO. NMR is an element-specific technique and can provide various types of information on different nuclei that exhibit changes after interaction with paramagnetic NO. Solid-state NMR is sensitive to the local atomic environment and ideally suited to probe gas-loaded MOF systems. Moreover, in UHM-37, the antiferromagnetic coupling of two copper atoms in the paddle wheel results in an $S = 0$ electronic spin state at low temperatures where the excited $S = 1$ state is populated at elevated temperatures (above 90 K).³⁶ For NMR measurements at higher temperatures, the electronic state will have similar effects on spectra and relaxation as is known for paramagnetic materials that strongly influence the magnetic properties of the surrounding nuclei.³⁶ As NO is also paramagnetic, the system under investigation is quite challenging for solid-state NMR. Although analysis of paramagnetic systems by NMR is typically complicated, we have recently shown that important information about the NO interaction with Cu_3btc_2 and indirect detection of NONOate in UHM-30, a primary-amine-functionalized Cu_3btc_2 , is possible.³⁷

Recently, we studied NO adsorption in the aluminum-containing MOF MIL-100.³⁸ There we followed adsorption of NO at the unsaturated Al sites by ²⁷Al NMR, and further information was obtained from influences of the paramagnetic NO on, e.g., ¹H T_1 relaxation times. In this manuscript, we compare the adsorption of defined amounts of NO in UHM-37 and Cu_3btc_2 MOFs. From the NMR point of view, these samples are challenging because of the antiferromagnetic coupling of copper ions, and the metal ion can practically not be studied by NMR. The interaction with paramagnetic NO can have significant effects on the magnetic properties of the MOFs. Furthermore, in UHM-37, both physisorption and chemisorption as NONOates can take place and it is of special importance, if information on preference of one adsorption process can be identified. We used ¹H and ¹³C NMR and especially study ¹⁵N NMR data from isotopically labeled NO, which gives direct information on the adsorbed species that has

not been possible before. Relevant parameters are, in addition to isotropic chemical shifts, also ¹H spin–lattice relaxation times (T_1) and hyperfine coupling constants.

EXPERIMENTAL SECTION

Synthesis of Cu_3btc_2 and UHM-37. Cu_3btc_2 and UHM-37 were synthesized based on published procedures.^{30,35} The BET surface areas were 1572 and 1011 m^2g^{-1} , respectively, based on nitrogen adsorption. For UHM-37, a 40:60 molar ratio of btc to NHEtbtC linkers was used.

Preparation of NO-Loaded Samples. MOFs were thermally activated in vacuum for 20 h at 373 K and kept under nitrogen environment. The color of the Cu_3btc_2 samples turned from light blue into dark violet immediately after activation, whereas for UHM-37, the color changed from green to black. Before NO loading, the samples were placed in 3 mm glass tubes, which are specially prepared for MAS NMR experiments (Wilmad). ¹⁵N-labeled NO was supplied by Icon Service Inc. (USA) with a purity of 98%. Gas loading was done via the gas phase in a pressure controlled vacuum apparatus under nitrogen cooling at 77 K (details can be found in the Supporting Information, page S2). In the case of Cu_3btc_2 , ¹⁵NO-loaded samples with 0.5, 1, 1.5, and 2 NO equivalents with respect to Cu were adsorbed. For UHM-37, defined amounts of NO corresponding to 0.5, 1, and 2 molecules were adsorbed with respect to the number of copper atoms. These are equivalent to 1.6, 3.2, and 6.4 NO/NHEtbtC functional groups (calculated based on ¹H MAS spectrum deconvolution, see below). Afterward, the glass tubes were sealed to prevent further alteration of the samples. NMR measurements were conducted directly after the sealing process.

Solid-State NMR Measurements. Experiments were performed on a Bruker Avance 400 spectrometer (magnetic field = 9.4 T) with frequencies of 400.17 and 100.62 MHz for ¹H and ¹³C, respectively. ¹⁵N measurements were run on a Bruker Avance III HD 500 spectrometer (11.7 T) with a frequency of 50.67 MHz.

¹H experiments were carried out at MAS rotation frequencies of 10–12 kHz using a 4 mm MAS probe. Spectra were recorded using the DEPTH sequence to suppress signals from the probe background.³⁹ Recycle delays were set to 50 ms, which is more than 5 times the longitudinal relaxation time T_1 (see below). The 90° pulse length was 3 μs . Temperature-dependent measurements were carried out within the temperature range of 200 to 300 K and a spinning frequency of 7 kHz. Spin–lattice relaxation times were determined with the inversion–recovery sequence modified with DEPTH detection.

^{13}C MAS spectra (4 mm MAS probe) were measured using direct excitation without high-power ^1H decoupling but with a pulse length of 3 μs and a recycle delay of 100 ms. The spinning frequency was 10 kHz unless mentioned otherwise. For comparison, selected experiments were also carried out with high-power ^1H decoupling using the XiX decoupling sequence, which has proven to be successful for paramagnetic systems.⁴⁰

^{15}N NMR experiments were recorded under static conditions with a home-built probe. A single pulse experiment was carried out with a 90° pulse length of 10 μs . The recycle delay was 2 s.

All measurements were done at room temperature unless specified otherwise. ^1H and ^{13}C spectra were referenced to TMS using PDMS (polydimethylsiloxane) and tyrosine hydrochloride as secondary references, respectively. ^{15}N spectra are referenced to nitromethane using glycine as a secondary reference (-347 ppm). Spectrum deconvolution was done using dmfit.⁴¹

DFT Calculations. ^{13}C NMR chemical shift calculations were performed using Gaussian16.⁴² For this, the pure ligand with carboxylic acid functionalities and the corresponding molecule as a NONOate were used. Geometry optimization was done using the B3LYP functional^{43,44} and a 6-311G(d,p) basis set. Chemical shifts were calculated using the GIAO method^{45,46} with the B3LYP functional and a cc-PVDZ basis set. Chemical shifts were obtained from the shielding results by referencing with tetramethylsilane calculated at the same level of theory.

RESULTS AND DISCUSSION

^1H MAS NMR of UHM-37. The isotropic region of the ^1H MAS spectra of as-synthesized and activated UHM-37 is shown in Figure 1. The as-synthesized sample shows only one

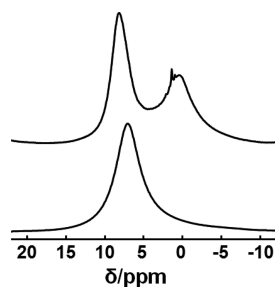


Figure 1. ^1H MAS spectrum of activated (top) and as-synthesized (bottom) UHM-37.

signal at 7 ppm, which is a result of signal overlap from aromatic and aliphatic protons with the strong signal from water protons as has also been seen for Cu_3btc_2 .⁴⁷ However, the activated sample shows two resolved signals at 8 and 0.4 ppm. Additional narrow spikes around 1 ppm originate from the sealing process. The signal at 8 ppm is from the btc protons as has also been seen in Cu_3btc_2 ⁴⁷ and UHM-30.³⁷ We assign a third signal at 8.1 ppm based on the deconvolution that is not resolved to the NH proton, which is similar to the value already reported in the solution NMR spectrum of the free ligand.³⁵ The broad signal at 0.4 ppm is then combined from the protons of the alkyl group that are not further resolved.

A full deconvoluted ^1H MAS spectrum of activated UHM-37 is shown in Figure S2 showing multiple spinning sidebands due

to the hyperfine coupling from the antiferromagnetically coupled Cu^{2+} pairs. Quantification of the final incorporation of the two linkers in the MOF by integration of isotropic signals and all spinning sidebands gave a ratio of btc/NHEtbtc of 47:53. On the basis of the 40:60 input of the two linkers in the synthesis, it indicates that incorporation of the pure btc ligand in the MOF is slightly favored. On the basis of the experimentally determined ratio of the two ligands, the composition of the MOF can be written as $\text{Cu}_3\text{btc}_{0.94}(\text{NHEtbtc})_{1.06}$.

^1H MAS NMR of NO-Loaded Samples. Figure 2 compares the ^1H NMR spectra of the activated UHM-37 and Cu_3btc_2 loaded with different amounts of NO.

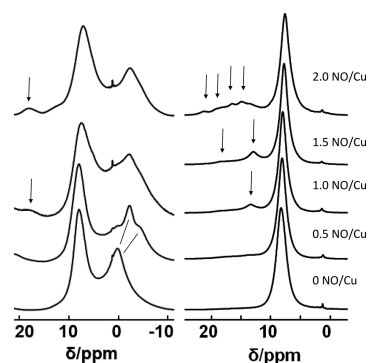


Figure 2. ^1H MAS spectra of UHM-37 (left) and Cu_3btc_2 (right) with 0 to 2 NO/Cu. For UHM-37, the NO content accounts to 0, 1.6, 3.2, and 6.4 NO/NHEt (from bottom to top). Lines indicate peaks that undergo changes upon loading. Arrows refer to additional signals indicating decomposition (see also text). The full spectra including spinning sidebands is given in Figures S4 and S5.

For 1.6 NO/NHEt loading for UHM-37, two new signals appear at -2.1 and -4.0 ppm. The appearance of new signals is the result of the reaction with NO that took place to lead to the formation of NONOate, thereby shifting the methylene and methyl signals to -2.1 and -4.0 ppm, respectively. The N–OH proton (see Scheme 1) is probably resonating around 9 ppm (see calculations below) and is hidden among the aromatic proton signals (see deconvolution in Figure S3). Exact assignment is difficult due to the paramagnetic shift, whose size is unknown. However, Nurhasni et al. reported in polyethylenimine (PEI) nanoparticles a methylene proton signal next to a secondary amine at 2.7 ppm that was shifted to approximately 3.1 ppm after PEI/NONOate formation.⁴⁸ Comparison between diamagnetic and paramagnetic systems is not straightforward, but the new signals indicate that some change has happened to the MOF, most probably to the alkyl protons.

For higher NO-loaded samples, these new signals broaden and finally merge into one signal only at 2.6 ppm (see Figure S3). Additionally, a signal around 18 ppm shows up, which we assign as a signal indicating MOF decomposition (see also below). Additional signals are also seen for NO-loaded Cu_3btc_2 .³⁷

Furthermore, a shift of the aromatic signal to lower ppm values is observed with increasing NO loading in UHM-37 (summarized in Figure S6). The same trend has been observed for the Cu_3btc_2 samples. It indicates interaction of NO at the copper site, as this is the expected adsorption site in Cu_3btc_2 . Basically, the observed shift is the result of the mobility of NO

in the Cu_3btc_2 framework and its interaction with the OMS. NO spends a short time at the Cu site because of weak adsorption at room temperature, which is also reported in theoretical calculations.⁴⁹ The electron spin density at the Cu site changes upon adsorption because of the unpaired electron of NO and thus affects the hyperfine interaction to nuclei from the btc linker.^{37,47} The change in peak position is the result of averaging the effects with and without adsorbed NO. With higher NO loading, there is a higher probability that NO is at the copper site, and therefore, there is a larger shift for higher NO loading. The unpaired electron of NO interacts with the d^9 system of copper and also formally leads to a partial quenching of electron spin density. A similar trend was also observed for the aromatic protons of $\text{Cu}_{3-x}\text{Zn}_x\text{btc}_2$, where the reduced electron spin density for a mixed-metal paddle wheel led to a decreasing ^1H shift with increasing zinc content.⁵⁰

For UHM-37, therefore, ^1H MAS data indicate both chemisorption as NONOate and physisorption at the OMS. The change of shift for the aromatic protons takes place just after the sample with 1.6 NO/NHET (see Figure S6). Although there is only a limited number of different loadings, it can be concluded that first NONOates are formed, and then, additional NO is interacting with the OMS.

^1H Line Width of UHM-37. Studying the dependence of the ^1H line width with NO loading can provide information on structural changes taking place that are spectroscopically not resolved. Figure 3 plots the line width of the aromatic and

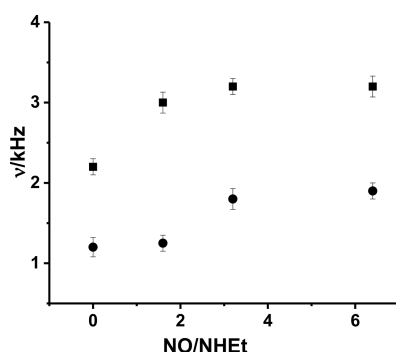


Figure 3. ^1H MAS line width of UHM-37 as a function of NO loading; squares refer to aliphatic protons, and circles refer to aromatic protons.

aliphatic signals of UHM-37 as a function of NO loading. The line width of the aromatic protons shows a jump between 1.6 NO/NHET and 3.2 NO/NHET loading (an increase by 30%) and remains constant afterward. For the alkyl signal, the line width increases by 40% for the 1.6 NO/NHET sample and then remains almost constant. We explain these observations as a result of two effects: First, NONOate formation generates new signals that lead to an increase in aliphatic line width because of chemical shift dispersion. We observed a similar result also in NO-loaded $\text{Cu}_3(\text{NH}_2\text{btc})_2$ (UHM-30).³⁷ Second, the increase in aromatic line width is a result of the paramagnetic nitric oxide leading to an increase in the anisotropic bulk magnetic susceptibility of protons near NO.⁵¹ Both effects together then explain that until 1.6 NO/NHET, diamagnetic NONOates form that affect the line width of the aliphatic protons because of the new signals. With higher NO content, coordination at the copper site or the presence of paramagnetic

NO near the aromatic ring takes place that leads to an increasing line width of the aromatic protons.

^1H T_1 (MAS) of UHM-37. As a result of the paramagnetic nature of nitric oxide, spin–lattice relaxation times T_1 are also varying with NO content. The effect of diamagnetic NONOate on the T_1 should be negligible, as the major source of relaxation is the presence of unpaired electrons at the copper site, together with additional NO carrying an unpaired electron. Cu_3btc_2 -type MOFs are already relaxing quite fast due to the unpaired electron at the copper atom.⁴⁷ Figure 4

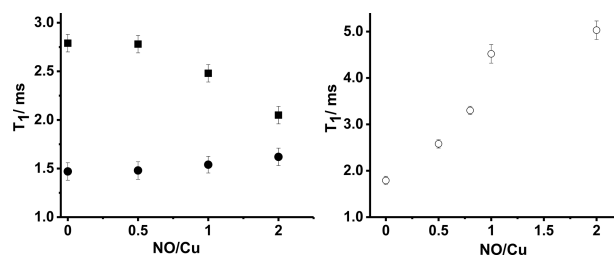


Figure 4. ^1H T_1 as a function of NO loading for UHM-37 (left) and Cu_3btc_2 (right). Circles represent aromatic protons, and squares represent aliphatic protons.

shows the ^1H T_1 dependence for differently NO-loaded UHM-37 samples. In all samples, the experimental data can be fit monoexponentially. For the aliphatic signal, T_1 decreases linearly with increasing NO content just after 0.5 NO/Cu (equivalent to 1.6 NO/NHET). In a related study, we reported NO influence on ^1H T_1 of the diamagnetic MOF MIL-100(Al) at room temperature, where ^1H T_1 is decreasing with increasing NO loading because of uniform distribution of NO within the MOF.³⁸ These decreasing ^1H T_1 values are in accordance with diamagnetic NONOate formation at first and the presence of additional NO in the surrounding of the aliphatic groups at higher loadings that lead to a decrease of the spin–lattice relaxation time. In contrast to this, for the aromatic signal, a slight increase in T_1 with increasing NO content is observed, also just starting after the 1.6 NO/NHET sample. A strong increase of T_1 , however, with increasing NO content is observed for Cu_3btc_2 .³⁷ The increase results from the interaction of NO with the copper site also carrying unpaired electrons leading to a—partial—quenching of unpaired electron density. In comparison to this, the smaller increase of T_1 for the aromatic protons in UHM-37 is clearly visible. The reason is not fully understood, but there is a similarity to the observation of line width on NO content (see above). Therefore, it would be a result of the changed electron spin density. To get more insight, one would need to calculate the electron spin density at the corresponding atoms and from that determine the influence on T_1 . However, this is out of the scope of this manuscript. Nevertheless, for both aliphatic and aromatic signals, there is no change in T_1 up to 1.6 NO/NHET, which is in agreement with preferred NONOate formation.

The influence of NO on the ^1H T_1 is also studied by temperature-dependent measurements. In Figure S7, the results for unloaded and 3.2 NO/NHET-loaded UHM-37 samples are summarized. The latter was chosen, since at this loading, there is some excess NO available after NONOate formation based on the previous results. For unloaded UHM-37, within the studied temperature range of 200 to 300 K, both the aromatic and aliphatic signals show no temperature

variation. This is also the case for the aromatic signal of the NO-loaded sample. This indicates that interaction with the paramagnetic NO is not significantly varying in the studied temperature range. The same observation was made for the aromatic signal of Cu_3btc_2 (data not shown). The aliphatic signal of the 3.2 NO/NHEt sample, however, shows a decrease of T_1 with decreasing temperature for the NO-loaded sample. At lower temperatures, excess NO seems to interact more strongly with the aliphatic side chain, and by that, its ^1H T_1 is affected.

Analysis of ^1H Hyperfine Couplings. In Cu_3btc_2 -type MOFs, the anisotropic part of the electron–nuclear dipolar interaction between the proton and the unpaired electrons dominates over the nuclear dipole–dipole interaction and is primarily responsible for the large number of spinning sidebands.^{37,47,51} The hyperfine interaction (or more precisely the anisotropic hyperfine shift⁵²) can be analyzed in the same way as a chemical shift anisotropy (CSA) pattern.^{37,53} Additional paramagnetic NO should therefore also have an effect on the hyperfine coupling. Figure S8 shows the results for the hyperfine coupling of both Cu_3btc_2 and UHM-37 samples as a function of NO loading. For the UHM-37 samples, the hyperfine coupling for the aliphatic signal increases significantly up to 1.6 NO/NHEt and then remains constant with further increasing NO content. This result is also somewhat comparable to that of primary-amine-functionalized $\text{Cu}_3(\text{NH}_2\text{btc})_2$, which should also form NONOates.³⁷ The initial increase indicates a change of electron density distribution after reaction to NONOates and therefore is derived from the structural change rather than the influence of paramagnetic NO. After NONOate formation, no further change is expected, which is also in accordance with the observation made here. For the aromatic signal of UHM-37, a slight decrease is observed with increasing NO content. This is similar to pure Cu_3btc_2 though on a smaller scale is similar to the T_1 data. Clearly, the amount of “available” NO is smaller in UHM-37 than in Cu_3btc_2 for the same NO/Cu loading due to NONOate formation. But even if one would include this lower amount (resulting in a horizontal shift of the curve by 0.5 NO/Cu), there is a deviation between the two curves for the aromatic signals. This might hint at a modification of electron density around the aromatic protons due to NONOate formation.

In summarizing the different types of information from ^1H NMR data, the results indicate that NO primarily reacts with the secondary amine of UHM-37 to form NONOates. On further increasing the NO content, interaction with the coordinatively unsaturated copper sites is taking place.

^{13}C MAS NMR of UHM-37 and Cu_3btc_2 . Figure 5 shows the ^{13}C MAS spectrum of activated UHM-37, showing a large shift range spanning more than 1000 ppm because of hyperfine interaction with Cu^{2+} , also resulting in large line widths. The paramagnetic-induced shifts for ^{13}C are much larger than for ^1H , because it is known from EPR studies on Cu_3btc_2 ⁵⁴ that electron spin density from the Cu–Cu paddle wheel is predominantly transferred to the carbon nuclei. The line widths are larger compared to Cu_3btc_2 , probably because of the larger dispersion of signals as a result of the chemical composition (multiple signals from the two linker molecules).

Assignment is done in accordance with previous results on Cu_3btc_2 ,^{47,55} aided by results from further experiments (see below). Table 1 summarizes the assignments.

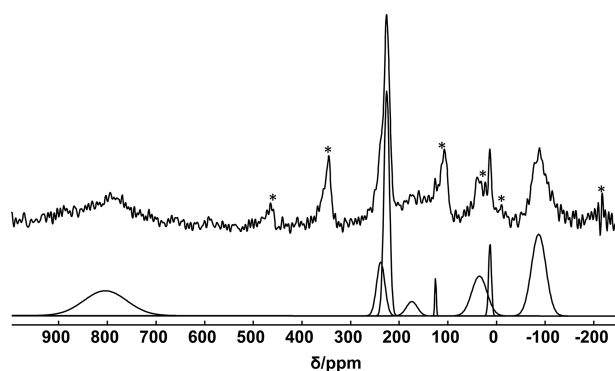


Figure 5. ^{13}C spectrum of activated UHM-37 measured with a spinning frequency of 12 kHz. Asterisks indicate spinning sidebands with 12 kHz spinning speed. The deconvolution (below) includes only isotropic signals.

Table 1. ^{13}C Signal Assignment for Cu_3btc_2 and UHM-37⁴⁷

	Cu_3btc_2	UHM-37
CH	228 ± 3	229 ± 3
C–N	-	240 ± 3
C_q	790 ± 20	780 ± 20
COO^-	-86 ± 10	-82 ± 10
CH_2	-	40 ± 3
CH_3	-	16 ± 1

^aValues are given in ppm. Uncertainties are based on the fitting procedure and the line width of signals.

Besides the aromatic CH signal at 229 ppm as also found in Cu_3btc_2 , an additional signal at 240 ppm appears for UHM-37, visible only as a shoulder, which we assign to the aromatic carbon next to the secondary amine. It becomes more evident in the ^1H decoupled spectrum shown in Figure 6.

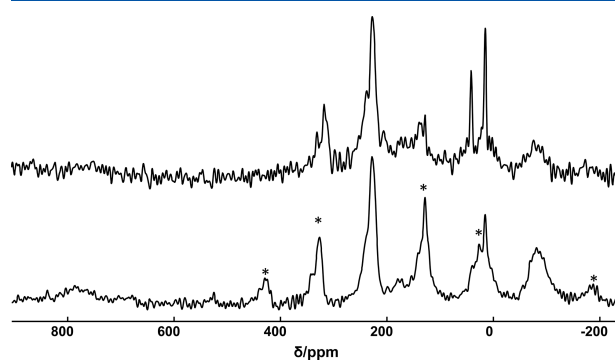


Figure 6. ^{13}C MAS spectra of activated UHM-37 without (bottom) and with ^1H decoupling (top). Asterisks mark spinning sidebands only in the bottom spectrum for clarity.

For further assignment verification, especially methyl and methylene signals, the rotor synchronized dipolar INEPT experiment⁵⁶ was performed to deduce CH_n multiplicities from the τ dependence (interpulse delay) of signal intensities. Figure S9 summarizes the results. The oscillation pattern of the experimental curves agrees reasonably well with the predicted behavior.⁵⁶ Therefore, the signals at 40 and 16 ppm are clearly assigned to methylene and methyl carbons, respectively. There are also signals with low intensity at 170, 145, and 124 ppm. We think these are diamagnetic signals indicating MOF

decomposition by bond breaking near the copper atom. They fall in the range of carboxylic and aromatic carbons. Furthermore, their intensities (together with those of the methyl and methylene carbons) increase with increasing recycle delay in contrast to the other signals (data not shown). This strengthens our hypothesis of assignment as diamagnetic signals.

The ^1H decoupled spectrum in Figure 6 shows that methylene and to a smaller degree also methyl signals are better resolved in the ^1H decoupled spectrum. Here, the contribution from the ^1H – ^{13}C dipolar coupling to the line width is larger than for the other carbons, predominantly because of the larger distance to the copper atoms. Because of rotation around the C_3 axis, the methyl signal is already significantly narrowed even without proton decoupling. The two signals at 240 and 229 ppm show an improved resolution with decoupling. This indicates that C–H dipolar coupling is non-negligible in these samples. For the other signals, no differences with or without decoupling are observed, as the main source of line width is the anisotropic bulk magnetic susceptibility. C–H dipolar couplings are also weaker, because there are no directly bound protons for these carbons. For this reason, typically spectra were recorded without ^1H decoupling, as they also allow for a shorter recycle delay.

The ^{13}C spectra of NO-loaded Cu_3btc_2 are summarized in Figure S10. The shifts of all three ^{13}C signals are linearly varying with NO content. For higher-loaded samples, additional signals between 120 and 170 ppm are appearing, and their intensities are also increasing further with loading, which we also assign to decomposition signals, similar to UHM-37. Figure 7 shows the ^{13}C spectra of UHM-37 loaded with

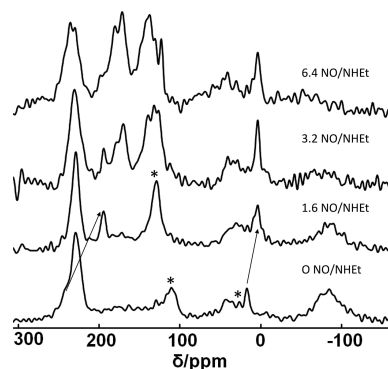


Figure 7. ^{13}C spectra of UHM-37 loaded with 0, 1.6, 3.2, and 6.4 NO/NHEt (bottom to top) in UHM-37. Only the range of 300 to -100 ppm is displayed, as the 800 ppm signal of the quaternary aromatic carbon is not detectable for higher loadings. Arrows indicate peaks that undergo changes upon loading. Asterisks mark spinning sidebands shown only for the unloaded spectrum.

different amounts of NO. At first, increasing NO loading leads to a broadening of lines. This is best seen for the carboxylate signal at -82 ppm but especially for the quaternary carbon that, at least at a spinning frequency of 10 kHz, is broadened so much that it cannot be differentiated anymore from the baseline. Additionally, new signals in the range of 124 to 170 ppm are detected, whose intensities increase with NO loading. These signals are not shifting with NO loading. Similar to Cu_3btc_2 , this hints at decomposition of the framework. Also, in water-adsorbed Cu_3btc_2 , similar signals were observed.⁴⁷ Peikert et al. concluded from TG-DSC measurements that

NO-loaded Cu_3btc_2 and UHM-37 samples show stronger decomposition than the unloaded samples.³⁵

^{13}C signals of UHM-37 are also shifted with NO loading. Most notably, the C–N signal is shifted from 240 to 194 ppm after NO interaction (sample with a loading of 1.6 NO/NHEt); however, the position of this signal stays constant for samples with higher NO loadings. Other than the “decomposition signals”, the 194 ppm signal intensity does not increase for longer recycle delays. Also, the methyl group signal shifts by 12 ppm to 4 ppm. Both changes could be due to NONOate formation. The methylene carbon might also show a shift, though it is not simple to verify this because of the larger broadening of this signal originating from C–H dipolar coupling as discussed above. Interestingly, a 5 ppm shift of the methylene carbon signal is also evident in the ^1H decoupled spectrum of NO-loaded UHM-37 (see Figure S11).

Results from DFT calculations for just the free linker $\text{H}_3\text{btcNHet}$ and the corresponding NONOate show a shift difference for the C–N aromatic carbon of about 14 ppm, while the other carbon signals remain fairly constant. Clearly, this is for a diamagnetic system without copper next to it and therefore only gives a hint that the assignment of the 240/194 ppm signal is probably correct. Hyperfine couplings could not be calculated at this level of theory. For comparison, in diazoketone, the signal of the carbon attached to nitrogen is shifted by 10 ppm because of formation of an alkylated NONOate.⁵⁷ Although shifts in paramagnetic systems are not straightforward to compare with diamagnetic systems, the similarity offers some hint for the assignment to NONOate signals. Figure 8 summarizes the ^{13}C isotropic shift changes for

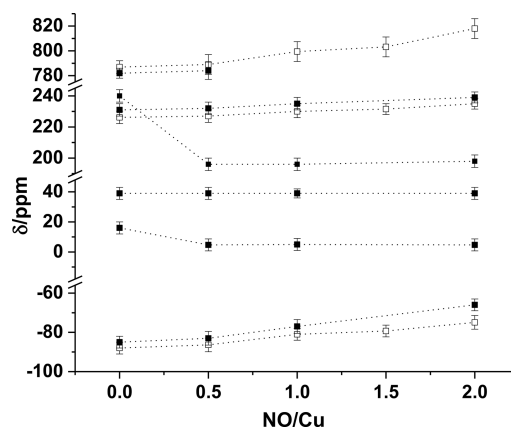


Figure 8. ^{13}C isotropic shift dependence of UHM-37 (solid symbols) and Cu_3btc_2 (open symbols) as a function of NO content.

both UHM-37 and Cu_3btc_2 samples as a function of NO loading. The aromatic CH and carboxylic carbon signals present in both samples show similar effects (for the quaternary carbon in UHM-37, this cannot be verified as it is not resolved with NO loading). The signals show an increase in shift with NO loading. The strongest effect can be observed for the quaternary carbon, the smallest for the aromatic CH signal.

^{15}N NMR Measurement of ^{15}NO -Loaded UHM-37. To get direct evidence of NONOate formation, we also studied ^{15}N NMR of UHM-37 loaded with isotopically enriched ^{15}NO . Figure 9 shows the ^{15}N NMR spectra measured under nonspinning conditions. In every spectrum, four resonances

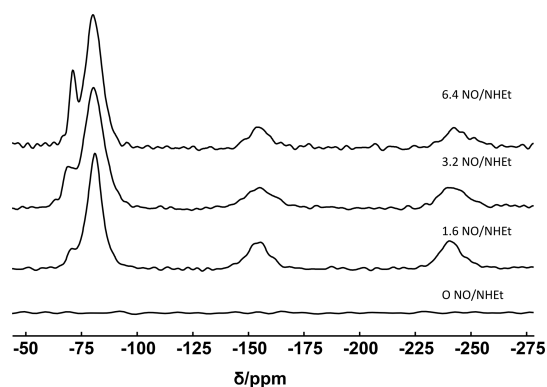


Figure 9. ^{15}N NMR spectra of UHM-37 samples loaded with 0, 1.6, 3.2, and 6.4 NO/NH₄Et (bottom to top).

are observed at -72 , -84 , -155 , and -240 ppm, and the intensity of -72 ppm signal increases with increasing NO loading. Signals at -155 and -240 ppm can be assigned to the terminal and center nitrogen atoms of N_2O , respectively.^{58,59} As we also found these signals in pure NO samples, we assume that these signals are due to an impurity in the NO bottle for sample preparation.

The paramagnetic NO should not be detectable at room temperature. Therefore, we assign the signal at -82 and -72 ppm to the two labeled nitrogens of the NONOate. These two signals appear in the typical ^{15}N chemical shift range of $\text{N}=\text{N}$ -type compounds.^{57,60} Therefore, this is the first report of NONOate signals by solid-state NMR in a porous system. On the basis of signal intensity, the signal at -72 ppm could also indicate a decomposition product. Luk'yanov et al. reported a single narrow ^{14}N signal around -70 ppm for alkyl-*N*-alkoxydiazene-*N*-oxides (an alkylated NONOate) generated from the reduction of diazoketone.⁵⁷ Fluck and Ekkehard report ^{15}N signals for NONOate at 12 and -159 ppm by the reaction between ethylamine and NO in the liquid state.⁶¹ However, for this compound, the IR frequency of 1133 cm^{-1} is different from the reported values of a NONOate of 1470 – 1510 , 1270 – 1315 , and a weak signal of 1000 – 1060 cm^{-1} ,²⁷ which were also observed for NO-loaded UHM-37.³⁵ Also in other MOFs, like a primary-amine-functionalized UCMC-1 (University of Michigan Crystalline Material-1) and in IRMOF-3 (isorecticular MOFs), these vibration frequencies have been detected.³¹ The DFT calculations of the linker (see above) reveal ^{15}N shifts of -14 and -35 ppm referred to glycine (-347 ppm, calculated at same level of theory), which are not helping in precisely assigning the ^{15}N NONOate shifts. The static NMR line width of the NONOate signals is quite narrow, about 550 Hz for 1.6 NO/NH₄Et and shows only a small increase by 30–40 Hz for higher NO loading. This small increase is probably due to interaction of NONOate with additional surrounding paramagnetic NO. Cross-polarization from ^1H to ^{15}N would be also helpful, but we could not detect any signal. However, in paramagnetic systems, cross-polarization is often difficult, partially because of short $T_{1\rho}$. Figure S12 displays the area intensity of the NONOate signals as a function of NO loading. The intensity of the -82 ppm signal is almost constant with NO loading, showing only a slight increase from 1.6 to 3.2 NO/NH₄Et. This would mean that at 1.6 NO/NH₄Et, almost all amine groups are converted to NONOate, which should happen only at loadings of at least 2 NO/NH₄Et, as two molecules of NO react with one secondary-

amine group. This result also supports our analysis of the ^1H and ^{13}C data above. Most strikingly, the ^{15}N data show direct evidence of NONOate formation, whereas ^1H and ^{13}C data hint at NONOate formation only indirectly by changes to the NMR spectra of the nearby nuclei.

CONCLUSIONS

Nitric oxide adsorption in UHM-37, an amine-functionalized MOF, and Cu_3btc_2 was studied by ^1H , ^{13}C , and ^{15}N solid-state NMR. This multinuclear approach together with the fact that the MOFs contain antiferromagnetically coupled Cu–Cu pairs and NO being paramagnetic shows significant effects on spectra that allow for the deduction of adsorption effects in these MOFs. Results from changes of the isotropic shifts, ^1H T_1 relaxation data, and ^1H hyperfine coupling upon NO adsorption reveal that in both MOFs, adsorption of NO takes place at the coordinatively unsaturated copper sites. However, in the amine-functionalized UHM-37, first chemisorption of NO takes place to form NONOates. When this reaction is completed, additional adsorption at the copper takes place. These conclusions are also in accordance with observed ^{13}C shift changes upon NO adsorption.

With ^{15}N -labeled NO, we were able to directly determine signals of NONOate formation in UHM-37. To the best of our knowledge, this is the first report on ^{15}N NMR data of NONOates in porous systems. The area intensity of the signals of the NONOate moiety stays constant with different NO contents, suggesting that almost all the amine groups have already reacted at 1.6 NO/NH₄Et loading. At higher loadings, diamagnetic signals in ^1H and ^{13}C spectra hint at decomposition of the MOF framework, which has been also observed by other techniques at high NO loadings.

ASSOCIATED CONTENT

Supporting Information

The Supporting Information is available free of charge on the ACS Publications website at DOI: 10.1021/acs.jpcc.8b11919.

Details on gas adsorption; sketch of ^{15}NO loading setup; assorted ^1H spectra; ^1H isotropic shift dependence of aromatic signals of Cu_3btc_2 and UHM-37 with NO loading; temperature dependence of ^1H T_1 for activated and 3.2 NO/NH₄Et (1 NO/Cu)-loaded UHM-37; dependence of hyperfine coupling on NO content; results of the dipolar INEPT experiment for UHM-37 at a spinning speed of 10 kHz; ^{13}C MAS spectra of Cu_3btc_2 loaded with different amounts of NO; ^1H decoupled ^{13}C MAS spectra of activated UHM-37 and 1.6 NO/NH₄Et-loaded UHM-37; normalized area intensity of ^{15}N signals at -82 and -72 ppm (PDF)

AUTHOR INFORMATION

Corresponding Author

*E-mail: bertmer@physik.uni-leipzig.de.

ORCID

Marko Bertmer: 0000-0002-3208-7927

Notes

The authors declare no competing financial interest.

ACKNOWLEDGMENTS

The authors thank the German Research Foundation (DFG) for financial support within the priority program “porous

metal-organic frameworks (MOFs) (SPP1362)", projects Be 2434/4-2 and Fr 1372/18-2. We thank Dr. W. Böhlmann (Leipzig University) for gas loading of the samples.

REFERENCES

- (1) Furukawa, H.; Cordova, K. E.; O'Keeffe, M.; Yaghi, O. M. The chemistry and applications of metal-organic frameworks. *Science* **2013**, *341*, 1230444.
- (2) Férey, G. Hybrid porous solids: past, present, future. *Chem. Soc. Rev.* **2008**, *37*, 191–214.
- (3) Tranchemontagne, D. J.; Mendoza-Cortés, J. L.; O'Keeffe, M.; Yaghi, O. M. Secondary building units, nets and bonding in the chemistry of metal-organic frameworks. *Chem. Soc. Rev.* **2009**, *38*, 1257–1283.
- (4) Morris, R. E.; Wheatley, P. S. Gas storage in nanoporous materials. *Angew. Chem., Int. Ed.* **2008**, *47*, 4966–4981.
- (5) Maurin, G.; Serre, C.; Cooper, A.; Férey, G. The new age of MOFs and of their porous-related solids. *Chem. Soc. Rev.* **2017**, *46*, 3104–3107.
- (6) Kitagawa, S.; Kitaura, R.; Noro, S. Functional porous coordination polymers. *Angew. Chem., Int. Ed.* **2004**, *43*, 2334–2375.
- (7) Yaghi, O. M.; Davis, C. E.; Li, G.; Li, H. Selective guest binding by tailored channels in a 3-D porous zinc(II)-benzenetricarboxylate network. *J. Am. Chem. Soc.* **1997**, *119*, 2861–2868.
- (8) Hoffmann, H. C.; Paasch, S.; Müller, P.; Senkovska, I.; Padmanaban, M.; Glorius, F.; Kaskel, S.; Brunner, E. Chiral recognition in metal organic frameworks studied by solid-state NMR spectroscopy using chiral solvating agents. *Chem. Commun.* **2012**, *48*, 10484–10486.
- (9) McKinlay, A. C.; Morris, R. E.; Horcajada, P.; Férey, G.; Gref, R.; Couvreur, P.; Serre, C. BioMOFs: metal-organic frameworks for biological and medical applications. *Angew. Chem., Int. Ed.* **2010**, *49*, 6260–6266.
- (10) Wheatley, P. S.; Butler, A. R.; Crane, M. S.; Fox, S.; Xiao, B.; Rossi, A. G.; Megson, I. L.; Morris, R. E. NO-releasing zeolites and their antithrombotic properties. *J. Am. Chem. Soc.* **2006**, *128*, 502–509.
- (11) Miller, M. R.; Megson, I. L. Recent developments in nitric oxide donor drugs. *Br. J. Pharmacol.* **2007**, *151*, 305–321.
- (12) Frost, M. C.; Reynolds, M. M.; Meyerhoff, M. E. Polymers incorporating nitric oxide releasing/generating substances for improved biocompatibility of blood-contacting medical devices. *Biomaterials* **2005**, *26*, 1685–1693.
- (13) Zhu, H.; Ka, B.; Murad, F. Nitric oxide accelerates the recovery from Burn Wounds. *World J. Surg.* **2007**, *31*, 624–631.
- (14) Moncada, S.; Higgs, E. A. The discovery of nitric oxide and its role in vascular biology. *Br. J. Pharmacol.* **2006**, *147*, S193–S201.
- (15) Hetrick, E. M.; Shin, J. H.; Stasko, N. A.; Johnson, C. B.; Wespe, D. A.; Holmuhamedov, E.; Schoenfish, M. H. Bactericidal efficacy of nitric oxide-releasing Silica nanoparticles. *ACS Nano* **2008**, *2*, 235–246.
- (16) Hetrick, E. M.; Schoenfish, M. H. Analytical chemistry of nitric oxide. *Annu. Rev. Anal. Chem.* **2009**, *2*, 409–433.
- (17) Carpenter, A. W.; Schoenfish, M. H. Nitric oxide release: Part II. Therapeutic applications. *Chem. Soc. Rev.* **2012**, *41*, 3742–3752.
- (18) Wo, Y.; Brisbois, E. J.; Bartlett, R. H.; Meyerhoff, M. E. Recent advances in thromboresistant and antimicrobial polymers for biomedical applications: just say yes to nitric oxide (NO). *Biomater. Sci.* **2016**, *4*, 1161–1183.
- (19) Wang, P. G.; Xian, M.; Tang, X.; Wu, X.; Wen, Z.; Cai, T.; Janczuk, A. J. Nitric oxide donors: chemical activities and biological applications. *Chem. Rev.* **2002**, *102*, 1091–1134.
- (20) Huerta, S.; Chilka, S.; Bonavida, B. Nitric oxide donors: Novel cancer therapeutics. *Int. J. Oncol.* **2008**, *33*, 909–927.
- (21) Hrabie, J. A.; Klose, J. R.; Wink, D. A.; Keefer, L. K. New nitric oxide-releasing zwitterions derived from polyamines. *J. Org. Chem.* **1993**, *58*, 1472–1476.
- (22) Xiao, B.; Wheatley, P. S.; Zhao, X.; Fletcher, A. J.; Fox, S.; Rossi, A. G.; Megson, I. L.; Bordiga, S.; Regli, L.; Thomas, K. M.; et al. High-capacity Hydrogen and Nitric Oxide adsorption and Storage in a metal organic framework. *J. Am. Chem. Soc.* **2007**, *129*, 1203–1209.
- (23) Huxford, R. C.; Della Rocca, J.; Lin, W. Metal-organic frameworks as potential drug carriers. *Curr. Opin. Chem. Biol.* **2010**, *14*, 262–268.
- (24) McKinlay, A. C.; Xiao, B.; Wragg, D. S.; Wheatley, P. S.; Megson, I. L.; Morris, R. E. Exceptional behavior over the wWhole adsorption storage delivery cycle for NO in porous metal organic frameworks. *J. Am. Chem. Soc.* **2008**, *130*, 10440–10444.
- (25) Chen, B.; Eddaoudi, M.; Reineke, T. M.; Kampf, J. W.; O'Keeffe, M.; Yaghi, O. M. Cu₂ (ATC) 6 H₂O design of open metal sites in porous metal-organic crystals (ATC: 1,3,5,7-Adamantane Tetracarboxylate). *J. Am. Chem. Soc.* **2000**, *122*, 11559–11560.
- (26) Ma, Z.; Moulton, B. Recent advances of discrete coordination complexes and coordination polymers in drug delivery. *Coord. Chem. Rev.* **2011**, *255*, 1623–1641.
- (27) Hrabie, J. A.; Keefer, L. K. Chemistry of the nitric oxide-releasing diazeniumdiolate (Nitrosohydroxylamine) functional group and its oxygen-substituted derivatives. *Chem. Rev.* **2002**, *102*, 1135–1154.
- (28) Parzuchowski, P. G.; Frost, M. C.; Meyerhoff, M. E. Synthesis and characterization of polymethacrylate-based nitric oxide donors. *J. Am. Chem. Soc.* **2002**, *124*, 12182–12191.
- (29) Tanabe, K. K.; Cohen, S. M. Postsynthetic modification of metal-organic frameworks—a progress report. *Chem. Soc. Rev.* **2011**, *40*, 498–519.
- (30) Chui, S. S.-Y.; Lo, S. M.-F.; Charmant, J. P. H.; Orpen, A. G.; Williams, I. D. A Chemically functionalizable nanoporous material [Cu₃(TMA)₂H₂O]_n. *Science* **1999**, *283*, 1148–1150.
- (31) Nguyen, J. G.; Tanabe, K. K.; Cohen, S. M. Postsynthetic diazeniumdiolate formation and NO release from MOFs. *CrystEngComm* **2010**, *12*, 2335–2338.
- (32) Haikal, R. R.; Hua, C.; Perry, J. J.; O'Nolan, D.; Syed, I.; Kumar, A.; Chester, A. H.; Zaworotko, M. J.; Yacoub, M. H.; Alkordi, M. H. Controlling the Uptake and Regulating the Release of Nitric Oxide in Microporous Solids. *ACS Appl. Mater. Interfaces* **2017**, *9*, 43520–43528.
- (33) Ingleson, M. J.; Heck, R.; Gould, J. A.; Rosseinsky, M. J. Nitric oxide chemisorption in a postsynthetically modified metal-organic framework. *Inorg. Chem.* **2009**, *48*, 9986–9988.
- (34) Lowe, A.; Chittajallu, P.; Gong, Q.; Li, J.; Balkus, K. J. Storage and delivery of nitric oxide via diazeniumdiolated metal organic framework. *Microporous Mesoporous Mater.* **2013**, *181*, 17–22.
- (35) Peikert, K.; McCormick, L. J.; Cattaneo, D.; Duncan, M. J.; Hoffmann, F.; Khan, A. H.; Bertmer, M.; Morris, R. E.; Fröba, M. Tuning the nitric oxide release behavior of amino functionalized HKUST-1. *Microporous Mesoporous Mater.* **2015**, *216*, 118–126.
- (36) Pöppel, A.; Kunz, S.; Himsl, D.; Hartmann, M. CW and pulsed ESR spectroscopy of cupric ions in the metal-organic framework compound Cu₃btc₂. *J. Phys. Chem. C* **2008**, *112*, 2678–2684.
- (37) Khan, A. H.; Peikert, K.; Fröba, M.; Bertmer, M. NO adsorption in amino-modified Cu₃btc₂-type MOFs studied by solid-state NMR. *Microporous Mesoporous Mater.* **2015**, *216*, 111–117.
- (38) Khan, A. H.; Barth, B.; Hartmann, M.; Haase, J.; Bertmer, M. Nitric Oxide adsorption in MIL-100(Al) MOF studied by Solid-State NMR. *J. Phys. Chem. C* **2018**, *122*, 12723–12730.
- (39) Bendall, M. R.; Gordon, R. E. Depth and refocusing pulses designed for multipulse NMR with surface coils. *J. Magn. Reson.* **1983**, *53*, 365–385.
- (40) Willans, M. J.; Sears, D. N.; Wasylishen, R. E. The effectiveness of ¹H decoupling in the ¹³C MAS NMR of paramagnetic solids: An experimental case study incorporating copper(II) amino acid complexes. *J. Magn. Reson.* **2008**, *191*, 31–46.
- (41) Massiot, D.; Fayon, F.; Capron, M.; King, I.; Le Calvé, S.; Alonso, B.; Durand, J.-O.; Bujoli, B.; Gan, Z.; Hoatson, G. Modelling one and two dimensional solid-state NMR spectra. *Magn. Reson. Chem.* **2002**, *40*, 70–76.

- (42) Frisch, M. J.; Trucks, G. W.; Schlegel, H. B.; Scuseria, G. E.; Robb, M. A.; Cheeseman, J. R.; Scalmani, G.; Barone, V.; Petersson, G. A.; Nakatsuji, H.; Li, X.; Caricato, M.; Marenich, A. V.; Blolino, J.; Janesko, B. G.; Gomperts, R.; Mennucci, B.; Hratchian, H. P.; Ortiz, J. V.; Izmaylov, A. F.; Sonnenberg, J. L.; Williams-Young, D.; Ding, F.; Lipparini, F.; Egidi, F.; Goings, J.; Peng, B.; Petrone, A.; Henderson, T.; Ranasinghe, D.; Zakrzewski, V. G.; Gao, J.; Rega, N.; Zheng, G.; Liang, W.; Hada, M.; Ehara, M.; Toyota, K.; Fukuda, R.; Hasegawa, J.; Ishida, M.; Nakajima, T.; Honda, Y.; Kitao, O.; Nakai, H.; Vreven, T.; Throssell, K.; Montgomery, J. A., Jr.; Peralta, J. E.; Oligaro, F.; Bearpark, M. J.; Heyd, J. J.; Brothers, E. N.; Kudin, K. N.; Staroverov, V. N.; Keith, T. A.; Kobayashi, R.; Normand, J.; Ragavachari, K.; Rendell, A. P.; Burant, J. C.; Iyengar, S. S.; Tomasi, J.; Cossi, M.; Millam, J. M.; Klene, M.; Adamo, C.; Cammi, R.; Ochterski, J. W.; Martin, R. L.; Morokuma, K.; Farkas, O.; Foresman, J. B.; Fox, D. J. *Gaussian 16*, revision A.03; Gaussian, Inc.: Wallingford, CT, 2016.
- (43) Becke, A. D. Density-functional thermochemistry. III. The role of exact exchange. *J. Chem. Phys.* **1993**, *98*, 5648–5652 pdf, B3LYP .
- (44) Lee, C.; Yang, W.; Parr, R. G. Development of the Colle-Salvetti correlation-energy formula into a functional of the electron density. *Phys. Rev. B: Condens. Matter Mater. Phys.* **1988**, *37*, 785–789 pdf, B3LYP .
- (45) Ditchfield, R. Self-consistent perturbation theory of diamagnetism. *Mol. Phys.* **1974**, *27*, 789–807 GIAO .
- (46) Wolinski, K.; Hinton, J. F.; Pulay, P. Efficient implementation of the gauge-independent atomic orbital method for NMR chemical shift calculations. *J. Am. Chem. Soc.* **1990**, *112*, 8251–8260 pdf, GIAO .
- (47) Gul-E-Noor, F.; Jee, B.; Pöpl, A.; Hartmann, M.; Himsl, D.; Bertmer, M. Effects of varying water adsorption on a Cu_3btc_2 metal organic framework (MOF) as studied by ^1H and ^{13}C solid-state NMR spectroscopy. *Phys. Chem. Chem. Phys.* **2011**, *13*, 7783–7788.
- (48) Nurhasni, H.; Cao, J.; Choi, M.; Kim, I.; Lee, B. L.; Jung, Y.; Yoo, J. W. Nitric oxide-releasing poly(lactic-co-glycolic acid)-polyethylenimine nanoparticles for prolonged nitric oxide release, antibacterial efficacy, and in vivo wound healing activity. *Int. J. Nanomed.* **2015**, *10*, 3065–3080.
- (49) Supronowicz, B.; Mavrandonakis, A.; Heine, T. Interaction of small gases with the unsaturated metal centers of the HKUST-1 metal organic framework. *J. Phys. Chem. C* **2013**, *117*, 14570–14578.
- (50) Gul-E-Noor, F.; Jee, B.; Mendt, M.; Himsl, D.; Pöpl, A.; Hartmann, M.; Haase, J.; Krautscheid, H.; Bertmer, M. Formation of mixed Metal $\text{Cu}_{3-x}\text{Zn}_x\text{btc}_2$ frameworks with different Zinc Contents: Incorporation of Zn^{2+} into the metal-organic framework structure as studied by Solid-State NMR. *J. Phys. Chem. C* **2012**, *116*, 20866–20873.
- (51) Nayeem, A.; Yesinowski, J. P. Calculation of magic angle spinning nuclear magnetic resonance spectra of paramagnetic solids. *J. Chem. Phys.* **1988**, *89*, 4600–4608.
- (52) Heise, H.; Köhler, F. H.; Xie, X. Solid-state NMR spectroscopy of paramagnetic Metallocenes. *J. Magn. Reson.* **2001**, *150*, 198–206.
- (53) Wickramasinghe, N. P.; Shaibat, M. A.; Jones, C. R.; Casabianca, L. B.; de Dios, A. C.; Harwood, J. S.; Ishii, Y. Progress in ^{13}C and ^1H solid-state nuclear magnetic resonance for paramagnetic systems under very fast magic angle spinning. *J. Chem. Phys.* **2008**, *128*, No. 052210.
- (54) Jee, B.; Eisinger, K.; Gul-E-Noor, F.; Bertmer, M.; Hartmann, M.; Himsl, D.; Pöpl, A. Continuous wave and pulsed electron spin resonance spectroscopy of paramagnetic framework cupric ions in the Zn(II) doped porous coordination polymer $\text{Cu}_{3-x}\text{Zn}_x\text{btc}_2$. *J. Phys. Chem. C* **2010**, *114*, 16630–16639.
- (55) Dawson, D. M.; Jamieson, L. E.; Mohideen, M. I. H.; McKinlay, A. C.; Smellie, I. a.; Cadou, R.; Keddie, N. S.; Morris, R. E.; Ashbrook, S. E. High-resolution solid-state ^{13}C NMR spectroscopy of the paramagnetic metal-organic frameworks, STAM-1 and HKUST-1. *Phys. Chem. Chem. Phys.* **2013**, *15*, 919–929.
- (56) Wickramasinghe, N. P.; Ishii, Y. Sensitivity enhancement, assignment, and distance measurement in ^{13}C solid-state NMR spectroscopy for paramagnetic systems under fast magic angle spinning. *J. Magn. Reson.* **2006**, *181*, 233–243.
- (57) Luk'yanov, O. A.; Smirnov, G. A.; Sevost'yanova, V. V. β , β - Dinitro derivatives of N-alkyl-N-alkoxydiazene-N-oxides. *Russ. Chem. Bull.* **1995**, *44*, 1474–1478.
- (58) Bhattacharyya, P. K.; Dailey, B. P. ^{15}N magnetic shielding anisotropies in $^{15}\text{N}^{15}\text{NO}$. *J. Chem. Phys.* **1973**, *59*, 5820–5823.
- (59) Carravetta, M.; Levitt, M. H. Long-lived nuclear spin states in high-field solution NMR. *J. Am. Chem. Soc.* **2004**, *126*, 6228–6229.
- (60) Machacek, V.; Lycka, A.; Simunek, P.; Weidlich, T. ^{15}N , ^{13}C and ^1H NMR study of azo coupling products from diazonium salts and enamines. *Magn. Reson. Chem.* **2000**, *38*, 293–300.
- (61) Schultheiss, H.; Fluck, E. ^{15}N NMR studies on compounds with direct N-N bonds. *Z. Naturforsch., B: J. Chem. Sci.* **1977**, *32*, 257–264.

Nitric Oxide Adsorption in Cu_3btc_2 -type MOFs - Chemisorption as NONOates besides Physisorption

Arafat Hossain Khan,[†] Katharina Peikert,^{‡,¶} Frank Hoffmann,[‡] Michael Fröba,[‡]
and Marko Bertmer^{*,†}

[†]*Felix Bloch Institute for Solid State Physics, Leipzig University, Linnéstraße 5, Leipzig,
Germany*

[‡]*Department of Chemistry, Institute of Inorganic and Applied Chemistry, University of
Hamburg, Martin-Luther-King Platz 6, Hamburg, Germany*

[¶]*Micromeritics GmbH, Rutherford 108, 52072 Aachen, Germany*

E-mail: bertmer@physik.uni-leipzig.de

Gas adsorption

For the loading with NO, for a given weight of Cu_3btc_2 or UHM-37, the number of copper atoms/ NHEt was calculated and with that the number of desired NO molecules. For a given volume of 50 ml, the gas pressure of NO was calculated according to the ideal gas law. After filling the 50 ml reservoir with this pressure, it was connected to the sample tube in a vacuum apparatus. The pressure then dropped down to zero with the help of liquid N_2 , so all NO molecules ended up in the MOF. Sample are prepared in a very controlled way in liquid N_2 temperature so that no water gets in.

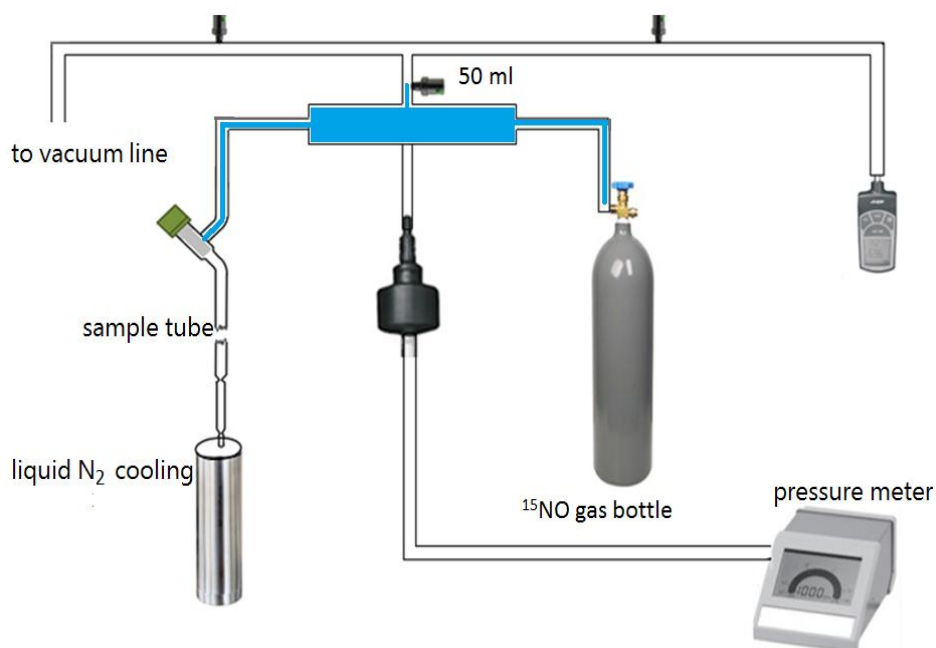


Figure S1: Sketch of ^{15}NO loading setup.

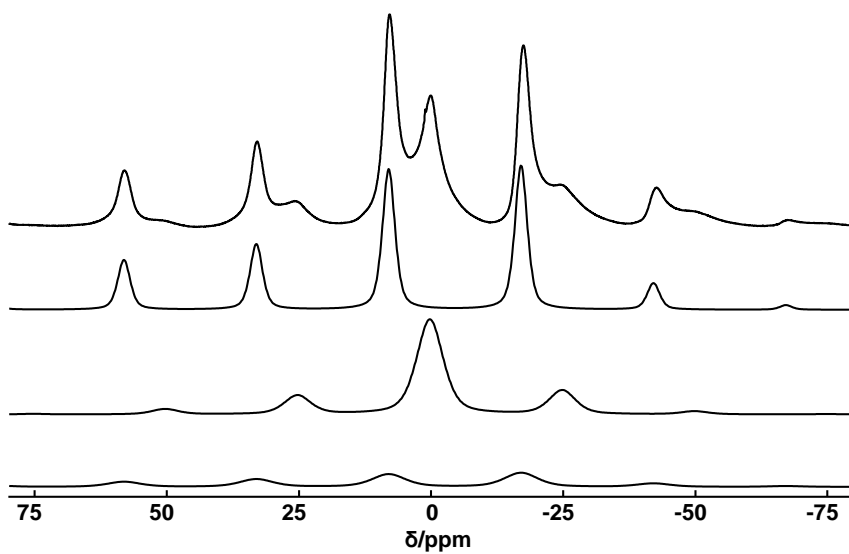


Figure S2: Full ^1H spectrum of activated UHM-37 together with the deconvolution of - from bottom to top - NH, alkyl, and aromatic protons, respectively.

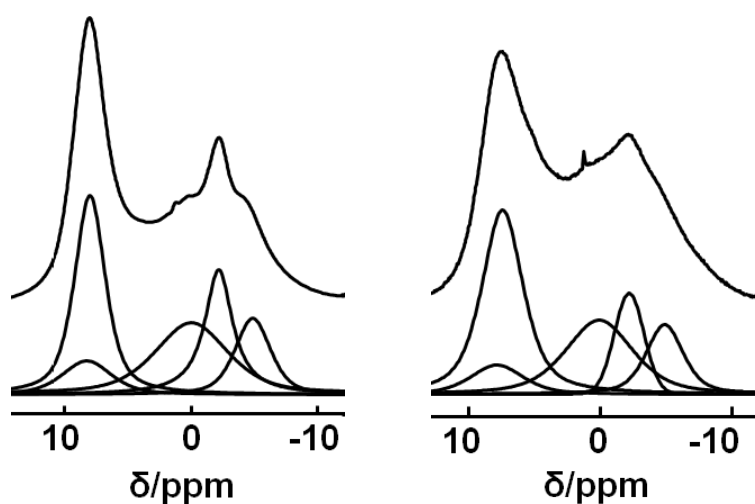


Figure S3: ^1H spectra of the isotropic region for 1.6 NO/NHEt (left) and 3.2 NO/NHEt (right) loaded UHM-37 together with the deconvolution.

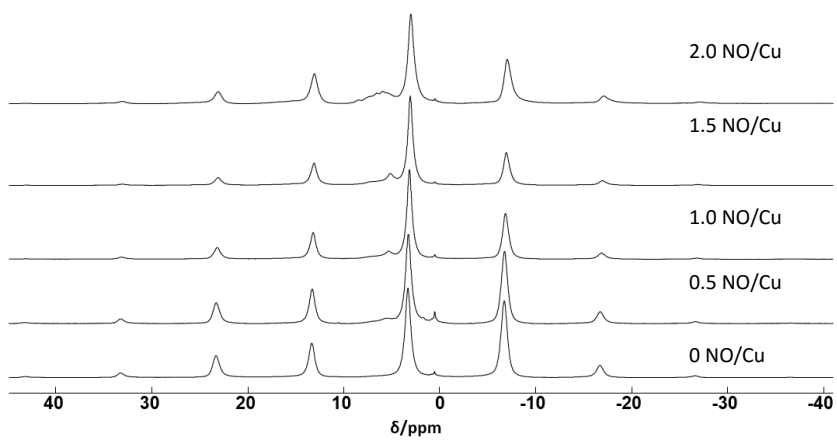


Figure S4: Full ^1H spectra of the Cu_3btc_2 .

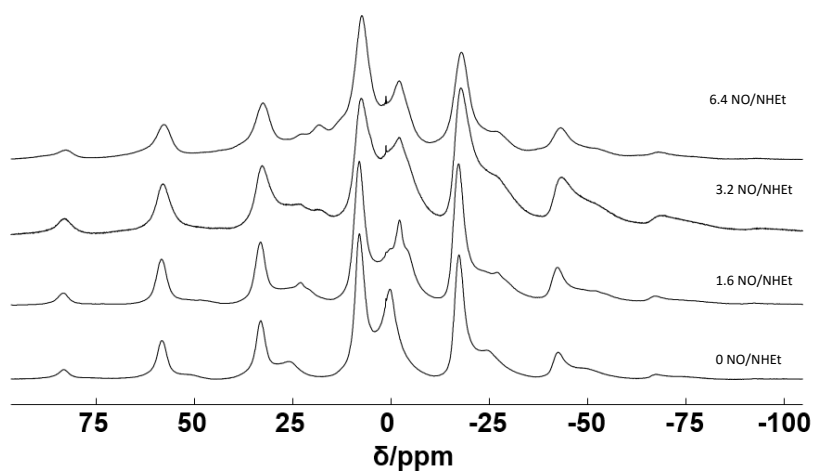


Figure S5: Full ^1H spectra of the UHM-37.

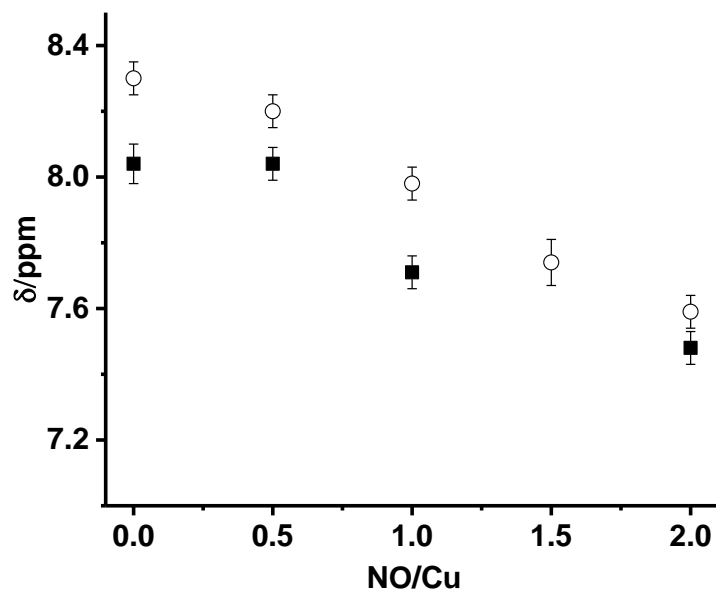


Figure S6: ^1H isotropic shift dependence of aromatic signals of Cu₃btc₂ (open circles) and UHM-37 (solid squares).

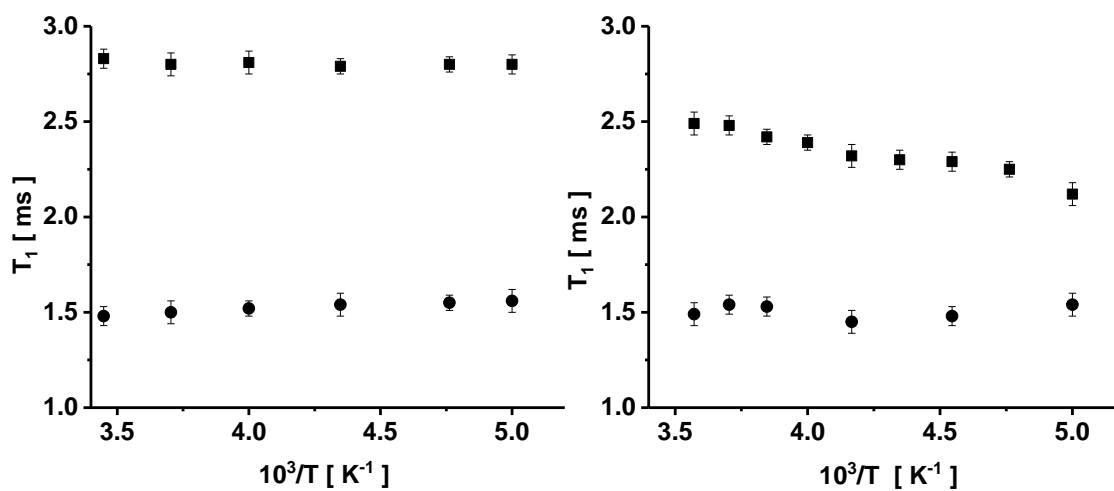


Figure S7: Temperature dependence of ^1H T_1 for activated (left) and 3.2 NO/NHEt (1 NO/Cu) loaded UHM-37 (right). Squares refer to aliphatic and circles to aromatic proton signals.

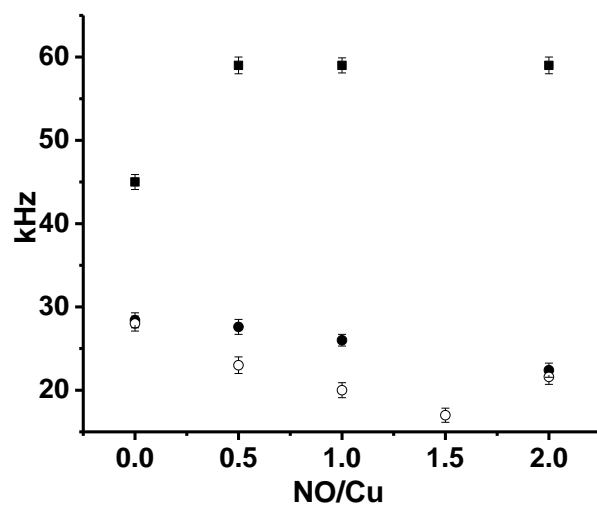


Figure S8: Dependence of hyperfine coupling on NO content; aromatic protons are represented as solid circles and aliphatic protons as solid squares for UHM-37. Open circles are for the aromatic protons of Cu₃btc₂.

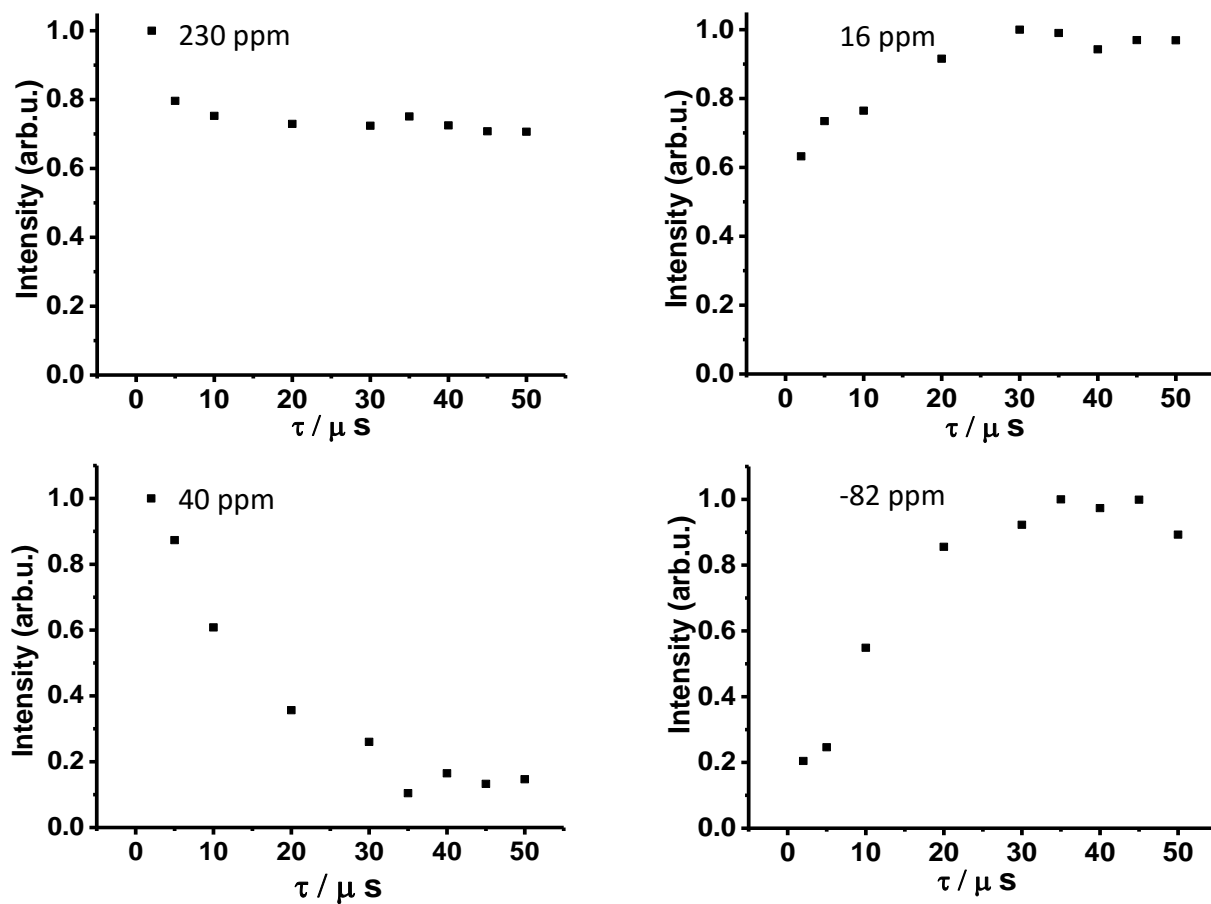


Figure S9: Results of the dipolar INEPT experiment for UHM-37 at a spinning speed of 10 kHz. Top left: aromatic CH signal, top right: CH₂ signal, bottom left: CH₃ signal, and bottom right: signal of COO⁻.

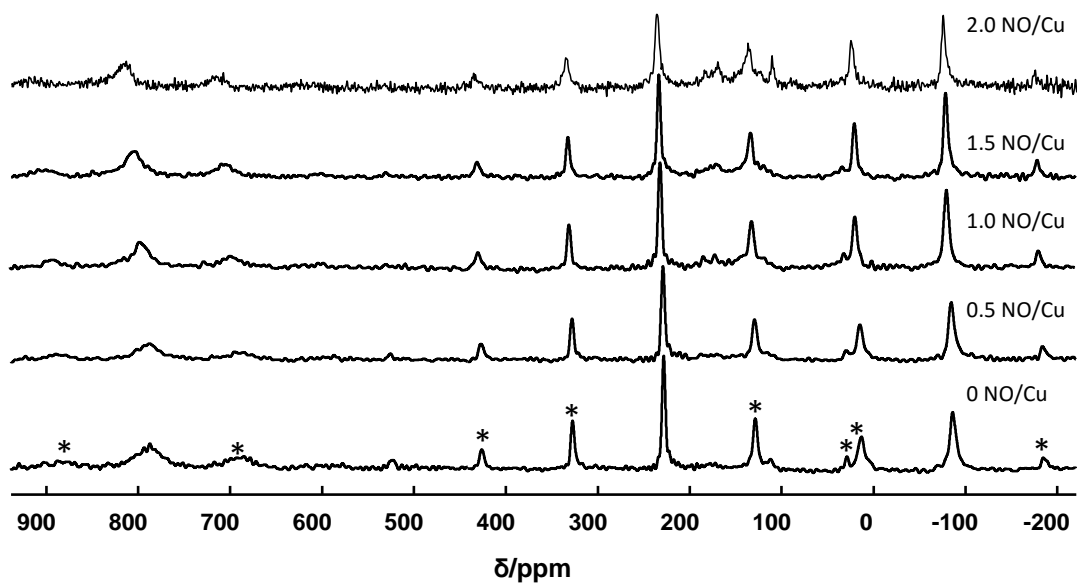


Figure S10: ^{13}C MAS spectra of Cu_3btc_2 loaded with different amounts of NO. Asterisks mark spinning sidebands only in the bottom spectrum for clarity.

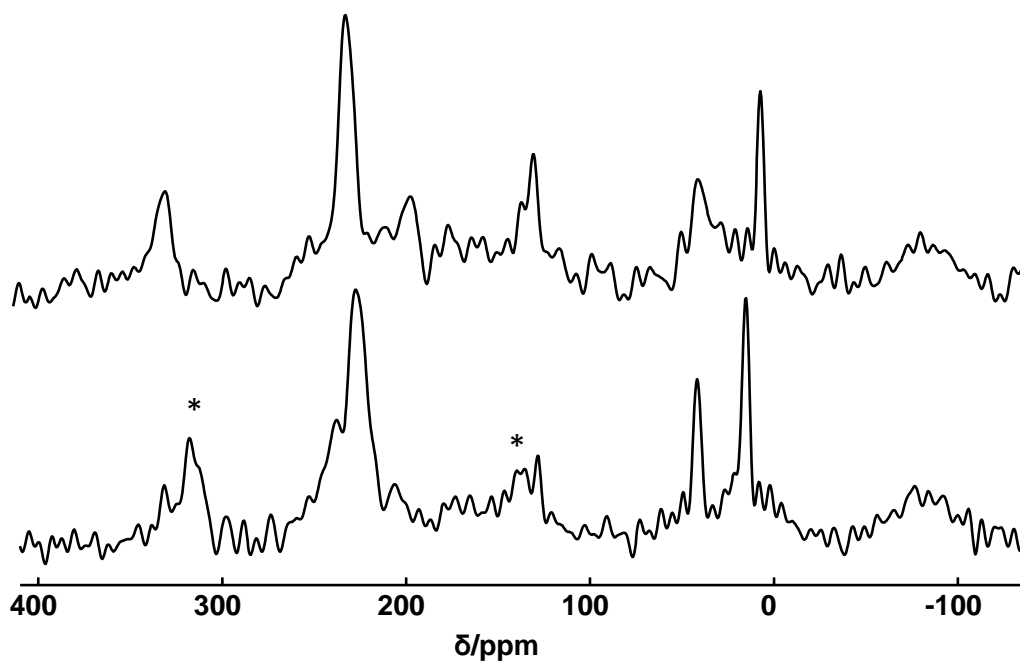


Figure S11: ^1H decoupled ^{13}C MAS spectra of activated UHM-37 (bottom) and 1.6 NO/NHEt-loaded UHM-37 (top). Asterisks mark spinning sidebands only in the bottom spectrum for clarity.

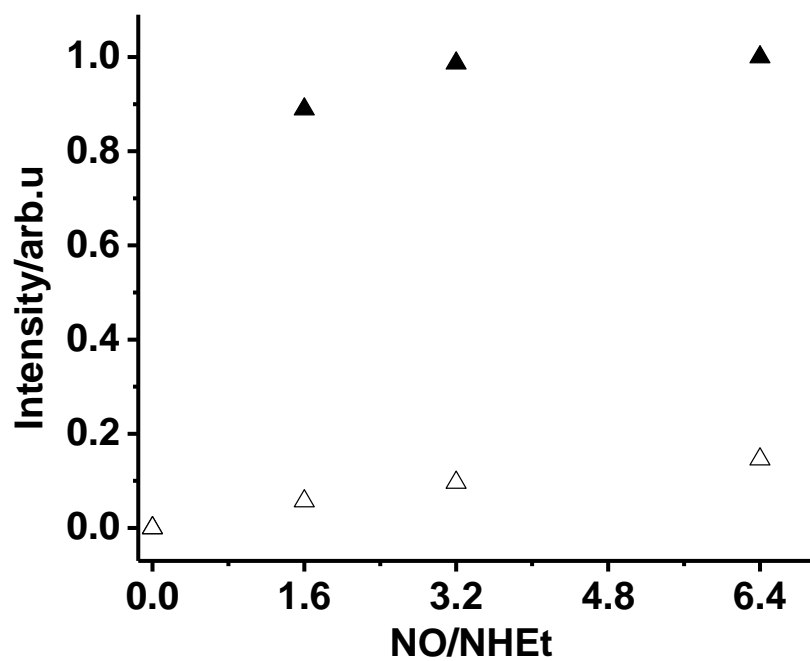


Figure S12: Normalized area intensity of ^{15}N signals at -82 ppm (solid triangles) and -72 ppm (open triangles).

Paper IV: Nitric oxide adsorption in the MOF MIL-100(Al) studied by solid-state NMR spectroscopy [*J. Phys. Chem. C*, 122 (24): 12723-12730, 2018.]

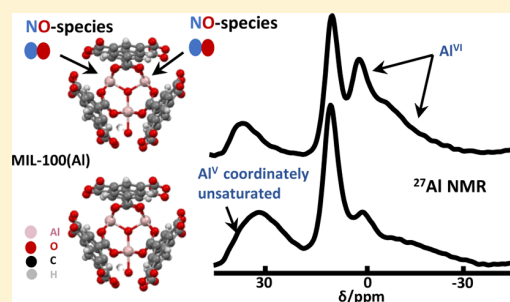
MAS NMR is ideally well-suited to characterize the interaction of NO in Cu_3btc_2 and its derivatives. NO interaction of another set of carboxylate MOFs, MIL-100(Al) is investigated by MAS NMR. The detailed characterization of MIL-100(Al) has been executed by ^1H , ^{13}C and ^{27}Al NMR. ^{27}Al NMR data show that half of all Al sites are free for gas adsorption. The presence of a extraframework $\text{Al}(\text{OH})_3$ inside the pores is well-documented by $^{27}\text{Al}\{^1\text{H}\}$ HETCOR spectra. The variation of ^1H relaxation with NO loading demonstrates NO interactions with MIL-100(Al) as well as uniform distribution of NO within the MOFs. Furthermore, ^{27}Al NMR studies represent that the intensity of five-coordinated aluminum site is decreasing with increasing NO loading, while the intensity of six-coordinated aluminum site is increasing upto 1 NO per Al trimer. This concludes rather weak NO adsorption. Moreover, FTIR is also performed on the same NMR samples for further understanding NO interactions with Al sites. The result of NO interaction with MIL-100(Al) is presented in paper IV.

Nitric Oxide Adsorption in MIL-100(Al) MOF Studied by Solid-State NMR

Arafat Hossain Khan,[†] Benjamin Barth,[‡] Martin Hartmann,[‡] Jürgen Haase,[†] and Marko Bertmer^{*,†}[†]Felix Bloch Institute for Solid State Physics, University of Leipzig, 04103 Leipzig, Germany[‡]Erlangen Catalysis Resource Centre (ECRC), Friedrich-Alexander-Universität Erlangen–Nürnberg, 91058 Erlangen, Germany

Supporting Information

ABSTRACT: Adsorption of nitric oxide (NO) in the metal–organic framework (MOF) MIL-100(Al) is studied by solid-state NMR. Owing to a modified synthesis, no extraframework benzenetricarboxylate is present on the cost of a small amount of extraframework Al(OH)₃ as evident from ²⁷Al, ¹H, as well as heteronuclear correlation spectra. Five-coordinated aluminum sites represent about 50% of the aluminum in a dehydrated sample, which remain open for adsorption. With increasing NO loading, a decrease of five-coordinated aluminum with a subsequent increase of six-coordinated aluminum site intensity is found. Additionally, ¹H spin–lattice relaxation time *T*₁ is decreasing with an increasing amount of NO, which also supports the NO interaction with the MOF because of the paramagnetism of NO. Fourier-transform infrared spectroscopy data further hint at Al–NO interactions.



INTRODUCTION

Gas-delivery technologies using metal–organic frameworks (MOFs) are of increasing importance in many areas of science with emerging applications that include storage of nitric oxide (NO). NO delivery from a storage material is attractive for many in vitro and in vivo antibacterial, antithrombotic, and wound healing applications.^{1–3} Currently, there is interest in developing medical devices such as stents and catheters using porous materials to deliver NO to prevent life-threatening complications associated with thrombosis formation.^{4,5} Porous materials—especially MOFs^{6–8}—are one of the best candidates for delivering NO.^{9–11} MOFs are materials with extremely high porosities, and some of them have coordinatively unsaturated metal sites (CUSs) that are available for binding and releasing of small molecules such as NO. The presence of CUSs in MOFs has a particularly pronounced effect on the NO adsorption and release characteristics.^{9,12–15}

We studied MIL-100(Al) prepared by a modified synthesis and its interaction with NO by multinuclear solid-state nuclear magnetic resonance (NMR). MIL-100(Al) is an aluminum trimesate MOF.¹⁶ The MIL-100 framework is constructed from oxo-centered metal trimers linked by benzenetricarboxylate (btc) ligands, forming tetrahedral cages, referred to as supertetrahedra. Corner-sharing of the supertetrahedral building blocks defines a highly porous structure of mesoporous cages. In supertetrahedral building blocks, each tetrahedron is built up from four μ_3 -oxo-centered trinuclear units connecting to the four btc ligands. Two water molecules and one hydroxide are bonded to the three aluminum atoms in the μ_3 -oxo trimer; the water molecules can be removed by heating and therefore generate CUSs. The rigid porous structure combined with the

accessibility of the activated metal sites upon dehydration has created interest for adsorption, separation, and catalysis applications.^{17–22} Haouas et al. identified the main adsorption sites of MIL-100(Al) by NMR studies and observed that open metal sites are the most favorable ones.²³ Furthermore, it was concluded that only one metal site is open for adsorption. Recently, Gallis et al. reported selective O₂ over N₂ sorption at ambient temperatures via node distortions in MIL-100(Sc) by Grand Canonical Monte Carlo simulation.²⁴ Eubank et al. reported that a significant amount of NO is chemisorbed at MIL-100(Fe) at 298 K with a loading capacity that depends on the nature of the Fe(II) cation and the Lewis acidity of this site.¹²

In this manuscript, solid-state NMR techniques are used to determine interactions between adsorbed NO and the MOF. Prior to this, the unloaded MOF is characterized in detail, as the MIL-100(Al) discussed here was prepared via a modified synthesis procedure,²⁵ and comparison to published NMR spectra of the original synthesis¹⁶ is performed. Characterization is done via ¹H and ²⁷Al spectra with the help of multiple-quantum magic-angle spinning (MQMAS) and ²⁷Al–¹H heteronuclear correlation (HETCOR) spectra. Afterward, differences to the unloaded case are discussed with different NO loading via ²⁷Al MAS and ¹³C CPMAS spectra, ¹H spin–lattice relaxation times, and Fourier-transform infrared spectroscopy (FTIR) data.

Received: February 21, 2018**Revised:** May 19, 2018**Published:** May 21, 2018

EXPERIMENTAL SECTION

Synthesis of MIL-100(Al)-Type MOFs. MIL-100(Al) was synthesized based on published procedures.^{16,25} At first, 1.363 g (3.633 mmol) $\text{Al}(\text{NO}_3)_3 \cdot 9\text{H}_2\text{O}$ and 0.614 g (2.434 mmol) trimethyl-1,3,5-benzenetricarboxylate were dissolved in 17.5 mL water and the mixture was transferred to a Teflon-lined stainless steel autoclave after adding 0.302 g (4.793 mmol) of nitric acid. The autoclave was placed in an oven at a temperature of 303 K, which was increased to 483 K at a rate of 3 K/min and subsequently held at this temperature for 3 days. After thermal treatment, a light-yellow solid was recovered by filtration and washed with 200 mL of water. For further purification, the obtained solid was extracted via soxhlet extraction with ethanol for 16 h. After activation, the Brunauer–Emmett–Teller area was determined to be 1480 m^2/g . The X-ray diffraction pattern is included in the Supporting Information (Figure S1).

Sample Preparation. MIL-100(Al) was dehydrated under high vacuum at a temperature of 443 K for 24 h to remove water molecules coordinated to aluminum. The color of the MIL-100(Al) samples turned from dark yellow to pale yellow after dehydration. Afterward, the dehydrated MOF was loaded in 4 mm zirconia NMR rotors under a nitrogen environment for NMR studies.

For the preparation of NO loading, samples were placed in 3 mm glass tubes (Wilmad Lab Glass Company, USA), which were perfectly fitting in 4 mm MAS rotors. Loading was carried out via the gas phase in a pressure-controlled vacuum apparatus under nitrogen cooling at 77 K. A defined amount of NO corresponding to 0.25, 0.5, 0.75, and 1 number of molecules (labeled b to e), with respect to one Al trimer was transferred to the MOF samples. Afterward, the glass tubes were sealed to prevent further modification of the samples. In addition to this, a sample of just the dehydrated MOF was also prepared in a glass tube and sealed. This sample is denoted as sample a. First, NMR measurements were conducted immediately after completion of the sealing process.

Solid-State NMR Measurements. ^1H and ^{13}C solid-state NMR experiments were conducted on a Bruker Avance 400 spectrometer (magnetic field 9.4 T). ^{27}Al measurements were performed on a Bruker AVANCE 750 spectrometer (magnetic field strength 17.6 T) unless specified otherwise. MAS probes (4 mm) were used at MAS rotation frequencies of 10–12 kHz.

^1H spectra were recorded using the DEPTH sequence²⁶ to suppress signals from the probe background. The recycle delay was 50 s, which is more than five times the longitudinal relaxation time (T_1). The 90° pulse length was 2.4 μs . ^1H spin–lattice relaxation times were obtained with the inversion–recovery sequence modified with DEPTH detection. As all ^1H s show the same T_1 , no differentiation with regard to different proton sites is done.

Single-pulse ^{27}Al MAS NMR spectra have been acquired with a pulse length of 0.5 μs ($<30^\circ$ flip angle) and a recycle delay of 1 s. ^{27}Al MQMAS spectra were obtained with the Z-filter method,²⁷ applying high-power pulses of 3 and 1 μs to excite triple quantum (3Q) coherence and reconvert back to zero quantum coherence with a radio frequency (rf) field of 120 kHz. After 2D Fourier transform, a shearing transformation was done to obtain a purely isotropic frequency component along the F1 axis. Z-filter time and t_1 increment were 20 and 10 μs , respectively. $^{27}\text{Al}\{^1\text{H}\}$ FSLG-HETCOR²⁸ spectra have been acquired with a range of contact times between 1 and 4 ms and

32 t_1 increments with 1680 scans and rf field strengths of 170 and 125 kHz for ^{27}Al and ^1H , respectively. $^{27}\text{Al}\{^1\text{H}\}$ CPMAS²⁹ spectra were recorded with variable contact times up to 6 ms. ^{13}C CPMAS spectra were acquired with a contact time of 1 ms, and a ramped pulse on the ^1H channel was employed. Spectrum deconvolution was done using the dmfit software.³⁰ ^1H and ^{13}C spectra were referenced to $\text{Si}(\text{CH}_3)_4$ (TMS) using polydimethylsiloxane and tyrosine hydrochloride as secondary references, respectively. ^{27}Al spectra are referenced to a 1 M solution of $\text{Al}(\text{NO}_3)_3$. All measurements were performed at room temperature.

IR Spectra of NO-Loaded MIL-100(Al). FTIR spectra were recorded for the sealed glass tube samples a to e and a sealed glass tube sample just containing NO in an IR microscope (Bruker Hyperion 3000) with the help of a Bruker VERTEX 80v spectrometer. At first, background and sample scans are recorded as interferograms from a polychromatic Mid-IR source, having a Michelson-interferometer in the optical path. Prior to the measurement, sealed glass tubes were introduced into the IR cell. All experiments were carried out at room temperature in the transmission mode. By measuring the empty glass tube as background, only the IR bands of the MOF and of the adsorbed NO molecules appear in the absorption spectra.

RESULTS AND DISCUSSION

^1H MAS NMR of MIL-100(Al). The isotropic region of the ^1H MAS spectrum of dehydrated MIL-100(Al) is shown in Figure 1. A major signal at 9.1 ppm assigned to framework

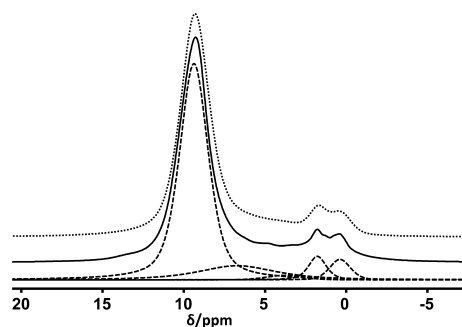


Figure 1. ^1H MAS spectrum of dehydrated MIL-100(Al) (full rotor). The experimental spectrum is shown as a solid line and the corresponding fit as a dotted line on top. Individual signals are given below the experimental spectrum as dashed lines.

aromatic protons of btc and two minor signals at 1.5 and 0.3 ppm for hydroxyl protons can be distinguished. For deconvolution, two additional signals at 6.8 and 4.5 ppm are necessary for a reasonable fit. These are assigned to protons from $\text{Al}(\text{OH})_3$ (see below) and remaining water adsorbed during packing of the sample into the MAS rotor, respectively. As can be seen in Figure S2, the signal at 4.5 ppm is practically absent in a sample prepared in a sealed glass tube (sample a), and a signal for aromatic protons appears at 9.4 ppm. The ^1H resonance of aromatic protons in the sealed glass tube (sample a) is shifted 0.3 ppm to a higher frequency in comparison to the ^1H resonance of the hydrated MOF as dehydration changed the coordination environment of MOF. A similar observation was also reported for $\text{Cu}_3(\text{btc})_2$, showing an increase of the ^1H chemical shift after removal of water.³¹

In comparison to the results from Haouas et al., similar shifts for btc and hydroxyl protons are reported.²³ However, because of the modified synthesis no extraframework btc is present on the cost of some Al(OH)₃. Furthermore, the hydroxyl proton signals are much better visible in our samples. It is also interesting why there are exactly two different hydroxyl proton signals present. This hints at the fact that not all Al₃(μ₃-O) trimers are identical in terms of hydroxyl group attachment to the aluminum.

Hunger et al. reported three different types of SiOH groups yielding ¹H MAS NMR signals of 1.2, 1.7, and 2.1 ppm in H-ZSM-5 because of hydrogen bonding of SiOH groups to neighboring framework oxygen atoms.³² Maybe this is also the case in MIL-100(Al). From the deconvolution of the ¹H spectrum, the area ratio between btc and hydroxyl protons is 6.5:1, which is close to the calculated value of 6:1 based on the chemical formula of MIL-100(Al) showing reasonable agreement.

²⁷Al MAS NMR of MIL-100(Al). Figure 2 shows the ²⁷Al MAS NMR spectrum of as-synthesized, hydrated MIL-100(Al).

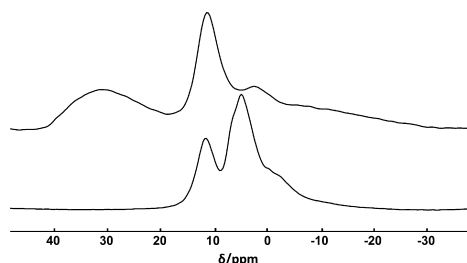


Figure 2. Central part of the ²⁷Al MAS NMR spectra of hydrated (bottom) and dehydrated (top) MIL-100(Al).

Two signals and a shoulder can be seen, all representing six-coordinated aluminum sites. The spectrum is similar to the one of Haouas et al.²³ apart from the signal at 12.1 ppm. We assign this to extraframework Al(OH)₃ present in the MOF (see also the Experiments below). There are several crystalline modifications of aluminum hydroxide existing, additional to amorphous ones whose NMR data have been investigated by several researchers.^{33–36} For instance, Ashbrook et al. reported similar shift values for bayerite (α-Al(OH)₃).³⁴ From both ¹H and ²⁷Al quantification, we conclude that the amount of Al(OH)₃ is about 15%.

Also included in Figure 2 is the ²⁷Al spectrum of dehydrated MIL-100(Al) showing an intense five-coordinated site around 35 ppm. The signal of extraframework Al(OH)₃ is still present. The other two six-coordinated sites are shifted to lower ppm values and significantly broadened. This is also observed in the dehydration of other aluminum-containing materials such as zeolites.³⁷

It can be clearly seen that the intensity of the two other six-coordinated sites is decreasing with respect to the Al(OH)₃ signal. Five- and six-coordinated sites have an approximate ratio of 1:1 based on only the isotropic signals. Haouas et al. reported that maximum 30% of the total aluminum is in a fivefold coordination.²³ This indicates that our material might offer more adsorption sites for guest molecules.

²⁷Al 3Q MAS NMR of MIL-100(Al). The MQMAS sheared spectrum of dehydrated MIL-100(Al) is shown in Figure 3. Two six-coordinated and one five-coordinated site can clearly be differentiated. The five-coordinated site shows a strong

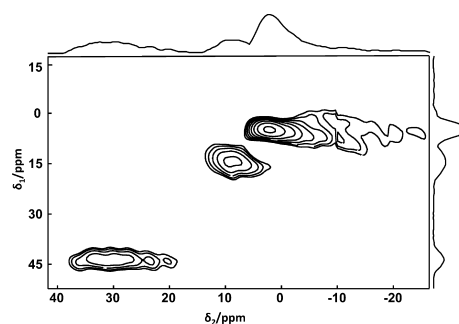


Figure 3. ²⁷Al MQMAS NMR spectrum of dehydrated MIL-100(Al).

quadrupolar coupling as expected for a strongly asymmetric geometry. However, one of the six-coordinated sites, the one from the MOF, shows a long tail to lower ppm values, indicating also a strong asymmetry. This is a consequence of the dehydration process as for the hydrated MOF a smaller width is present as can be seen in Figure S3. Because of the different multiple-quantum excitation efficiencies of the different sites, signals at the more negative shift values are not excited effectively.

The quadrupolar parameters for each site are determined with the help of the following equations³⁸

$$\text{SOQE}^2 = C_Q^2 \left(1 + \frac{\eta^2}{3} \right) = -\frac{(\delta_{G2} - \delta_{iso})\nu^2}{6000} \quad (1)$$

$$\delta_{iso} = \frac{(\xi(I, p)\delta_{G2} - |p|\delta_{G1})}{\xi(I, p) - |p|} \quad (2)$$

For the determination of the second-order quadrupolar effect containing the quadrupolar coupling constant C_Q and asymmetry parameter η , and the isotropic chemical shift δ_{iso} , input parameters are the centers of gravity in the F1 and F2 dimension δ_{G1} and δ_{G2} (in ppm), respectively, as well as the multiquantum coherence $p = 3$, and the relative induced quadrupolar shift, $\xi(I, p) = \frac{3}{4}$. The isotropic shift is determined with this equation from the nonsheared spectrum. The extracted values are summarized in Table 1.

Table 1. ²⁷Al MQMAS Analysis

	dehydrated		hydrated	
	C_Q (MHz)	δ_{iso} (ppm)	C_Q (MHz)	δ_{iso} (ppm)
Al ^V	5.3	35.5		
Al(OH) ₃	2.7	12.1	2.2	12.8
Al ^{VI} ₁	2.5	3	1.3	3.9

The extracted parameters show good agreement with those reported earlier.^{23,35,36} Dehydration increases the quadrupolar coupling for the octahedral sites because of increase of disorder by removal of coordinated water molecules in the local neighborhood.

The long tail of the octahedral sites is not well-represented in the MQMAS spectra as can be seen also in the fit of the 1D MAS spectra based on the values from Table 1 (see Figure S4). A better deconvolution can be achieved by assuming some disorder as, for instance, described by the Czjzek modeling.^{39,40} The Czjzek model (in the “Simple” package provided in dmfit³⁰) combines the quadrupolar coupling with a distribution

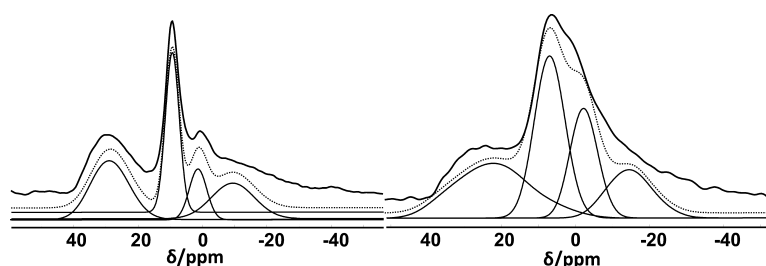


Figure 4. ^{27}Al deconvoluted spectra of dehydrated MIL-100(Al), measured at 195 MHz (left) and 104 MHz (right) using the Czjzek modeling. Parameters are summarized in Table 2.

of chemical shifts. We therefore also applied the Czjzek modeling for the deconvolution of the ^{27}Al MAS NMR spectra.

Figure 4 represents 1D MAS ^{27}Al spectra measured at magnetic fields of 9.4 and 17.6 T. Deconvolution of the spectra with identical parameters for both fields are summarized in Table 2. The Czjzek model was applied only for the octahedral sites of the MOF.

Table 2. ^{27}Al Parameters of the 1D MAS Spectra Recorded at Magnetic Fields of 9.4 and 17.6 T Including the Czjzek Model

	dehydrated			hydrated		
	C_Q (MHz)	δ_{iso} (ppm)	FWHMCS (ppm)	C_Q (MHz)	δ_{iso} (ppm)	FWHMCS (ppm)
Al^{V}	5.3	35.5				
$\text{Al}(\text{OH})_3$	2.7	12.1		2.2	12.8	
Al^{VI}_1	2.8	2.8	8	1.5	3.5	5
Al^{VI}_2	3.9	-5.2	20	3	-3.8	10

The agreement with the spectra is significantly improved with only small changes of the quadrupole coupling constant. Only small variations of isotropic shift are needed in the Czjzek modeling. Generally, in the hydrated MIL-100(Al), all quadrupole coupling constants are smaller than for the dehydrated MOF.

^1H - ^{27}Al Magnetization Transfer Experiments on MIL-100(Al). We recorded $^{27}\text{Al}\{^1\text{H}\}$ CPMAS spectra of dehydrated MIL-100(Al) for more insight into the proximity of proton and aluminum atoms. Figure 5 depicts spectra recorded with different contact times of dehydrated MIL-100(Al). The signal at 12 ppm assigned to $\text{Al}(\text{OH})_3$ shows a decreasing signal intensity with increasing contact time, finally disappearing at 2.5 ms. Because of the close proximity of aluminum to protons in $\text{Al}(\text{OH})_3$, this is expected and strengthens our assignment of the 12 ppm signal as $\text{Al}(\text{OH})_3$. The signal intensity of the six-coordinated MOF site(s) increases with the contact time, reaching maximum intensity at 2 ms. In addition, the intensity of the five-coordinated site increases steadily until it reaches maximum at a contact time of 5 ms, which indicates that these aluminum spins are more distant from proton spins compared to the six-coordinated sites. This also goes along with the structure in which the five-coordinated site is lacking the OH^- in opposition to the six-coordinated site; therefore, magnetization transfer comes from more distant btc protons, which requires a longer contact time for signal buildup.

A more quantitative comparison of the variable contact time experiments can be obtained by fitting the double-exponential behavior of CP kinetics for dehydrated MIL-100(Al) according to the following equation⁴¹ for the signal intensity

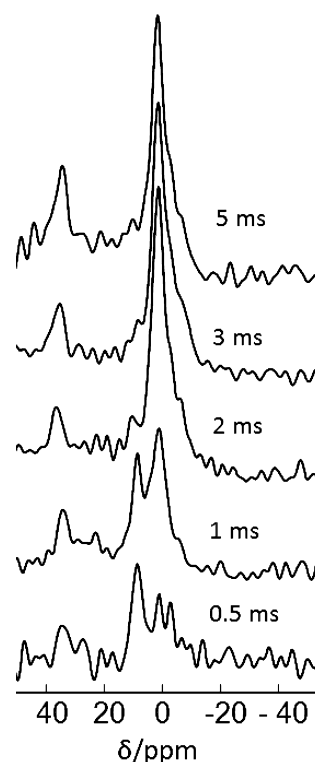


Figure 5. $^{27}\text{Al}\{^1\text{H}\}$ CPMAS NMR spectra of dehydrated MIL-100(Al) (full rotor). Contact times are given next to each spectrum.

$$I(t) = I_0 \left(1 - \frac{T_{\text{IS}}}{T_{1\rho}^I} \right)^{-1} [e^{-t/T_{1\rho}^I} - e^{-t/T_{\text{IS}}}] \quad (3)$$

Here, T_{IS} denotes the CP time constant between abundant spins I (^1H) and diluted spins S (^{27}Al). $T_{1\rho}^I$ indicates the spin-lattice relaxation of the dilute spin in the rotating frame. t is the contact time.

In Figure S5 the fitting of the variable-contact time experiment to the double-exponential function (eq 3) is shown for the three sites. The obtained values are summarized in Table 3.

T_{IS} for $\text{Al}(\text{OH})_3$ is very short, for both hydrated and dehydrated samples. Because ^{27}Al in $\text{Al}(\text{OH})_3$ is close to the ^1H species, this results in a strong I-S dipolar interaction and shortens T_{IS} . In the dehydrated sample, T_{IS} of the five-coordinated site is much longer than that of the six-coordinated site, as expected. Because of the larger distance to protons, the signal of the five-coordinated site requires a longer CP time for transfer. In the hydrated MOF, T_{IS} of the six-coordinated site

Table 3. T_{1S} and $T_{1\rho}^1$ Values for Dehydrated and Hydrated MIL-100(Al)

	dehydrated		hydrated	
	T_{1S} (ms)	$T_{1\rho}^1$ (ms)	T_{1S} (ms)	$T_{1\rho}^1$ (ms)
Al ^V	3.1	10.5 ^a		
Al(OH) ₃	0.2	2.2	0.2	2
Al ^{VI} ₁	1	7.5	0.7	6

^aApproximate value as experiments were run only until a contact time of 6 ms.

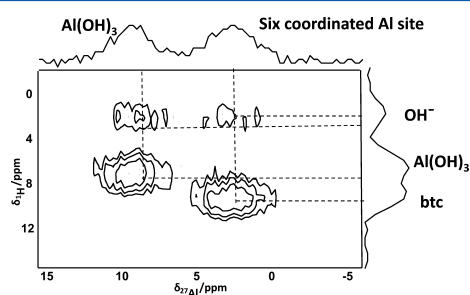
decreases as there are additional water molecules around that contribute to the magnetization transfer. $T_{1\rho}^1$ values also decrease in the hydrated form. A similar behavior was also observed in a ¹H–²⁹Si CP experiment for the Zeolite MAP.³⁷ The variation in $T_{1\rho}^1$ is indicative of the different proton mobilities in MIL-100(Al).

Additionally, T_{1S} can also be estimated from the following formula⁴²

$$\frac{1}{T_{1S}} = \frac{3}{2} \sqrt{\frac{2\pi}{5}} \frac{M_{2,IS}}{\sqrt{M_{2,II}}} \quad (4)$$

$M_{2,IS}$ and $M_{2,II}$ are the heteronuclear and homonuclear second moments, respectively, and were calculated from the atom positions in the crystal structure of MIL-100(Al). For that, the interatomic distances were included up to a distance of 10 Å. The surrounding of the aluminum trimer in the crystal structure is shown in Figure S6. The calculated values are 25 and 330 kHz², respectively. From that we determined T_{1S} to 0.5 ms, which is in good agreement with the experimental value of 0.6 ms for the hydrated form, as the crystal structure used for calculation is also given for the hydrated form.

Information about connectivities of protons and aluminum atoms is obtained from the 2D HETCOR spectrum shown in Figure 6. Only the six-coordinated aluminum sites are shown.

**Figure 6.** $^{27}\text{Al}\{^1\text{H}\}$ HETCOR spectrum of dehydrated MIL-100(Al) obtained with a contact time of 2 ms.

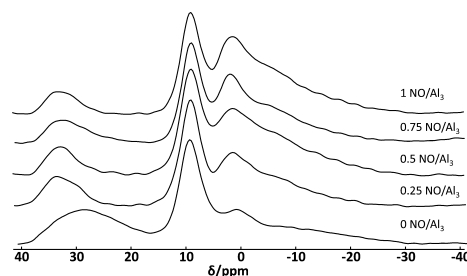
No five-coordinated ²⁷Al signal is observable in this correlation experiment because of signal-to-noise and the rather short contact time. Furthermore, the long tail because of the six coordinated sites is not resolved.

Despite the quite low resolution, interesting information can be obtained. Correlations between the Al site of the MOF at 2 ppm with hydroxide and btc proton signals are evident, as expected. The 12 ppm signal assigned as Al(OH)₃ shows a correlation peak with the ¹H signal around 7 ppm. This correlation between ¹H and ²⁷Al further supports our assignment to extraframework Al(OH)₃. The ¹H shift of Al(OH)₃ is reported as 6.7 ppm.³⁵ Interestingly, there is a

correlation peak for the Al(OH)₃ ²⁷Al signal with the hydroxide protons. This hints at the fact that the Al(OH)₃ resides within the pores.

Summarizing the different NMR experiments to characterize the MIL-100(Al) prepared by a different synthesis route, we can conclude that no extraframework btc is present, rather a small amount of Al(OH)₃ residing close to hydroxyl protons of the Al(3μ₃-O) trimer. Signals of the hydroxyl protons are more clearly visible compared to the first study by Haouas et al.²³ On this basis, we will now address the adsorption capacities of MIL-100(Al) with respect to NO studied by NMR.

Interaction of Nitric Oxide with MIL-100(Al). Because of the paramagnetic nature of NO, the direct detection of ¹⁵N NMR signals is not possible. Therefore, we base our analysis indirectly on the effects of NO on the NMR of other nuclei of the MOF. For understanding NO interaction with MIL-100(Al), at first ²⁷Al MAS spectra of sealed samples (a–e) were recorded. Figure 7 summarizes the results. The intensity of the

**Figure 7.** ^{27}Al NMR spectra of NO-loaded MIL100(Al) samples a–e (from bottom to top). Intensities are normalized with respect to the Al(OH)₃ signal.

five-coordinated site is decreasing with increasing NO loading, whereas the intensity of the six-coordinated site is increasing. This is an indication for NO adsorption at the unsaturated metal sites. Already at the lowest NO loading the width of the five-coordinated site is significantly reduced. This can be explained by a reduced asymmetry of this site. Alternatively—although not visible from the MQMAS experiment for the unloaded MOF—there are two five-coordinated sites present with one disappearing upon adsorption of NO (see also below).

From 1 NO/Al₃ upwards, the intensity of the five-coordinated site is not decreasing any further (data not shown), indicating that further adsorption of NO at the unsaturated metal sites is not possible. We assume that up to 1 NO/Al₃ is the maximum adsorption amount for NO in MIL-100(Al), though then there are still 50% unsaturated metal sites available. However, at room temperature adsorption of NO is supposedly rather weak in comparison to water,¹² with which all five-coordinated sites convert to six-coordinated sites.

Further information on NO interaction with the MOF is obtained from ¹H T_1 relaxation data, as shown in Figure 8. A quasi-linear decrease of T_1 with an increasing amount of NO is observed. NO is paramagnetic by nature because of the presence of an unpaired electron, which significantly influences the relaxation times. In a related study, we reported NO influence on ¹H T_1 of the MOF Cu₃btc₂ where unpaired electron density of antiferromagnetically coupled Cu²⁺ pairs is reduced by NO adsorption; thereby ¹H T_1 increased with increasing amount of NO.¹⁴ In case of diamagnetic MIL-100(Al), the close proximity of NO with the protons of the MOF (preferably at the unsaturated aluminum site or just

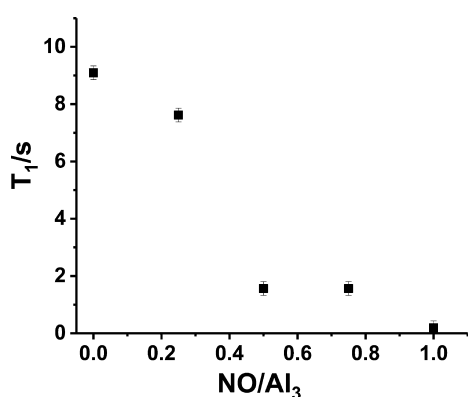


Figure 8. ^1H T_1 values of samples a–e.

within the pores) leads to a decrease of ^1H T_1 . The almost perfectly linear decrease of T_1 with the NO content and the fact that all samples show a monoexponential behavior indicates a uniform distribution of NO within the MOF. Further increasing NO loading up to 3 NO/Al₃ did not reduce T_1 anymore (data not shown). The reduction of T_1 by 1 NO/Al₃ is already very strong so that more NO might not have a significant effect on the spin–lattice relaxation time anymore.

In a related study, electron paramagnetic resonance (EPR) data have also been obtained in this system.²⁵ There, an Al–NO interaction was detected at low temperatures, showing a significant hyperfine interaction. This adsorption species is expected to also have a significant influence on the ^{27}Al spectrum and might lead to a strong line broadening that we might not detect. Furthermore, EPR data indicate desorption of NO at temperatures clearly below room temperature. Otherwise, EPR data only detect a small portion of the incorporated NO, so there might be NO species in a conformation that is not paramagnetic and therefore not detectable by EPR. It was postulated that dimerization of NO is happening which is EPR-insensitive. These dimers could also interact with aluminum, which we detect via the NMR measurements. However, dimer formation of NO is expected to be enhanced at lower temperatures only, as it was detected in MCM-41 below 70 K.⁴³ Another explanation could be the formation of NO⁺ (see FTIR data below).

The ^{13}C spectra of samples a to c together with the one from hydrated MIL-100(Al), as shown in Figure 9, also show interesting results. The two regions 170–175 ppm for carboxylate carbons and 130–140 ppm for aromatic carbons

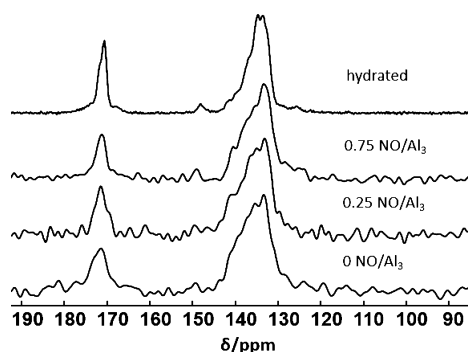


Figure 9. ^{13}C CPMAS spectra of samples a–c (from bottom), together with a hydrated MIL-100(Al) (top).

are clearly separated, without resolving each individual carbon site. After dehydration, the signals undergo some line broadening presumably because of chemical shift distributions as a result of changes of the local structural environment similar to the ^{27}Al spectra discussed above. The removal of water bound to the trimer probably causes a lowering of symmetry because of distortions. Interestingly, the carboxylate signal is getting narrower with an increasing NO content. Therefore, line broadening because of paramagnetic adsorption can be ruled out. In analogy to water adsorption, the change of aluminum coordination number seems to induce some stress release in the MOF structure, thereby increasing the local symmetry and with that reducing the ^{13}C linewidth. One may conclude that the direct interaction of NO with the carbon atoms is rather small and therefore the preferred interaction of NO-species with the aluminum sites exists.

We have also recorded FTIR spectra of the sealed glass tube samples which are prepared for NMR studies. The results are shown in Figure S7. Here bands appear at 2350 and 2230 cm^{-1} for the NO-loaded sample with increasing intensity with increasing NO loading. This falls within the typical range for NO⁺ (2390 cm^{-1} > $\tilde{\nu}$ > 2100 cm^{-1}).⁴⁴ Dehydrated MIL-100(Al) shows no bands in this region as expected. A neutral NO signal normally appears at 1876 cm^{-1} .⁴⁴ However, this could not be observed in our case, because the sealed glass tube absorbs all signals below 2100 cm^{-1} . Nevertheless, to measure exactly the same samples used for the NMR measurements, this glass tube could not be avoided.

Barth et al. reported bands of NO⁺ in the same spectral range for MIL-100(Fe) and MIL-100(Al).²⁵ As discussed there, the presence of an NO⁺ band derives from the interaction of Al with NO and would also explain our results of the ^{27}Al NMR spectra. Interaction of paramagnetic NO with aluminum would result in hyperfine couplings which we did not detect. This finding further strengthens NO interaction with the unsaturated metal site in MIL-100(Al). Quantification, however, is not easy and therefore it is not clear how intense this process is.

CONCLUSIONS

MIL-100(Al) prepared by a modified synthesis is studied by ^1H , ^{27}Al , and ^{13}C solid-state NMR. ^1H spectra have shown that there is no extraframework bdc ligand in the MOF. ^{27}Al NMR data show that half of all Al sites are free for gas adsorption and that additional Al(OH)₃ is present inside the pores, which is well-documented by $^{27}\text{Al}\{^1\text{H}\}$ HETCOR spectra. ^1H T_1 of NO-loaded MIL-100(Al) decreases with NO loading representing uniform distribution of NO in the MOF. In addition, MIL-100(Al) five-coordinated Al site intensity is decreasing with increasing NO loading, while six-coordinated site intensity is increasing and a maximum of 1 NO per Al trimer can be adsorbed. This indicates rather weak NO adsorption. Lewis acid Al³⁺ might lead to an attraction of the NO and transfer electron density to the aluminum. FTIR data show the presence of NO⁺ and goes along with the ^{27}Al NMR data. Quantification is not really possible and also paramagnetic NO interaction with aluminum might exist though undetectable for NMR. Related EPR data indicate that this interaction is only detectable at low temperatures. Most of the NO might be mobile within the pores and by interactions with the MOF walls lead to fast ^1H relaxation. Together with the previous EPR experiments, it seems that there are different possibilities for NO to interact with the MOF being detectable with either EPR or NMR.

■ ASSOCIATED CONTENT

S Supporting Information

The Supporting Information is available free of charge on the ACS Publications website at DOI: 10.1021/acs.jpcc.8b01725.

XRD pattern of MIL-100(Al), deconvolution of the ^1H spectrum, ^{27}Al MQMAS of hydrated MIL-100(Al), deconvolution of ^{27}Al spectra with MQMAS fitting parameters, fitting of variable contact time measurements, surrounding of aluminum trimer, and FTIR spectra of NO-loaded MIL-100(Al) (PDF)

■ AUTHOR INFORMATION

Corresponding Author

*E-mail: bertmer@physik.uni-leipzig.de.

ORCID

Marko Bertmer: 0000-0002-3208-7927

Notes

The authors declare no competing financial interest.

■ ACKNOWLEDGMENTS

We thank Dr. Christian Chmelik for the FTIR measurements and data analysis. Dr. Winfried Böhlmann is thanked for the NO loading of MIL-100(Al) samples. We thank the German Research Foundation (DFG) for financial support within the priority program “porous MOFs (SPP1362)”.

■ REFERENCES

- (1) Zhu, H.; Ka, B.; Murad, F. Nitric oxide accelerates the recovery from burn wounds. *World J. Surg.* **2007**, *31*, 624–631.
- (2) Moncada, S.; Higgs, E. A. The discovery of nitric oxide and its role in vascular biology. *Br. J. Pharmacol.* **2009**, *147*, S193–S201.
- (3) Hetrick, E. M.; Shin, J. H.; Stasko, N. A.; Johnson, C. B.; Wespe, D. A.; Holmuhamedov, E.; Schoenfisch, M. H. Bactericidal efficacy of nitric oxide-releasing silica nanoparticles. *ACS Nano* **2008**, *2*, 235–246.
- (4) Miller, M. R.; Megson, I. L. Recent developments in nitric oxide donor drugs. *Br. J. Pharmacol.* **2009**, *151*, 305–321.
- (5) Frost, M. C.; Reynolds, M. M.; Meyerhoff, M. E. Polymers incorporating nitric oxide releasing/generating substances for improved biocompatibility of blood-contacting medical devices. *Biomaterials* **2005**, *26*, 1685–1693.
- (6) Tranchemontagne, D. J.; Mendoza-Cortés, J. L.; O’Keeffe, M. Secondary building units, nets and bonding in the chemistry of metal-organic frameworks. *Chem. Soc. Rev.* **2009**, *38*, 1257.
- (7) Kitagawa, S.; Kitaura, R.; Noro, S.-i. Functional porous coordination polymers. *Angew. Chem., Int. Ed.* **2004**, *43*, 2334–2375.
- (8) Maurin, G.; Serre, C.; Cooper, A.; Férey, G. The new age of MOFs and of their porous-related solids. *Chem. Soc. Rev.* **2017**, *46*, 3104–3107.
- (9) McKinlay, A. C.; Xiao, B.; Wragg, D. S.; Wheatley, P. S.; Megson, I. L.; Morris, R. E. Exceptional behavior over the whole adsorption-storage-delivery cycle for NO in porous metal organic frameworks. *J. Am. Chem. Soc.* **2008**, *130*, 10440–10444.
- (10) Xiao, B.; Wheatley, P. S.; Zhao, X.; Fletcher, A. J.; Fox, S.; Rossi, A. G.; Megson, I. L.; Bordiga, S.; Regli, L.; Thomas, K. M.; et al. High-capacity hydrogen and nitric oxide adsorption and storage in a metal-organic framework. *J. Am. Chem. Soc.* **2007**, *129*, 1203–1209.
- (11) Zhang, H.; Annich, G. M.; Miskulin, J.; Stankiewicz, K.; Osterholzer, K.; Merz, S. I.; Bartlett, R. H.; Meyerhoff, M. E. Nitric oxide-releasing fumed silica particles: synthesis, characterization, and biomedical application. *J. Am. Chem. Soc.* **2003**, *125*, 5015–5024.
- (12) Eubank, J. F.; Wheatley, P. S.; Lebars, G.; McKinlay, C.; Leclerc, H.; Horcajada, P.; Daturi, M.; Vimont, A.; Morris, R. E.; Serre, C. Porous, rigid metal (III)-carboxylate metal-organic frameworks for the delivery of nitric oxide. *APL Mater.* **2014**, *2*, 124112.
- (13) Peikert, K.; McCormick, L. J.; Cattaneo, D.; Duncan, M. J.; Hoffmann, F.; Khan, A. H.; Bertmer, M.; Morris, R. E.; Fröba, M. Tuning the nitric oxide release behavior of amino functionalized HKUST-1. *Microporous Mesoporous Mater.* **2015**, *216*, 118–126.
- (14) Khan, A. H.; Peikert, K.; Fröba, M.; Bertmer, M. NO adsorption in amino-modified $\text{Cu}_3(\text{btc})_2$ -type MOFs studied by solid-state NMR. *Microporous Mesoporous Mater.* **2015**, *216*, 111–117.
- (15) McKinlay, A. C.; Morris, R. E.; Horcajada, P.; Férey, G.; Gref, R.; Couvreur, P.; Serre, C. BioMOFs: metal-organic frameworks for biological and medical applications. *Angew. Chem., Int. Ed.* **2010**, *49*, 6260–6266.
- (16) Volkringer, C.; Popov, D.; Loiseau, T.; Férey, G.; Burghammer, M.; Riekel, C.; Haouas, M.; Taulelle, F. Synthesis, single-crystal X-ray microdiffraction, and NMR characterizations of the giant pore metal-organic framework aluminum trimesate MIL-100. *Chem. Mater.* **2009**, *21*, 5695–5697.
- (17) Seo, Y.-K.; Yoon, J. W.; Lee, J. S.; Hwang, Y. K.; Jun, C.-H.; Chang, J.-S.; Wuttke, S.; Bazin, P.; Vimont, A.; Daturi, M.; et al. Energy-efficient dehumidification over hierarchically porous metal-organic frameworks as advanced water adsorbents. *Adv. Mater.* **2012**, *24*, 806–810.
- (18) Leclerc, H.; Vimont, A.; Lavalley, J.-C.; Daturi, M.; Wiersum, A. D.; Llwellyn, P. L.; Horcajada, P.; Férey, G.; Serre, C. Infrared study of the influence of reducible iron(III) metal sites on the adsorption of CO, CO₂, propane, propene and propyne in the mesoporous metal-organic framework MIL-100. *Phys. Chem. Chem. Phys.* **2011**, *13*, 11748.
- (19) Furukawa, H.; Cordova, K. E.; O’Keeffe, M.; Yaghi, O. M. The chemistry and applications of metal-organic frameworks. *Science* **2013**, *341*, 1230444.
- (20) Britt, D.; Furukawa, H.; Wang, B.; Glover, T. G.; Yaghi, O. M. Highly efficient separation of carbon dioxide by a metal-organic framework replete with open metal sites. *Proc. Natl. Acad. Sci. U.S.A.* **2009**, *106*, 20637–20640.
- (21) Yoon, M.; Srirambalaji, R.; Kim, K. Homochiral metal-organic frameworks for asymmetric heterogeneous catalysis. *Chem. Rev.* **2012**, *112*, 1196–1231.
- (22) Trickett, C. A.; Helal, A.; Al-Maythaly, B. A.; Yamani, Z. H.; Cordova, K. E.; Yaghi, O. M. The chemistry of metal-organic frameworks for CO₂ capture, regeneration and conversion. *Nat. Rev. Mater.* **2017**, *2*, 17045.
- (23) Haouas, M.; Volkringer, C.; Loiseau, T.; Férey, G.; Taulelle, F. Monitoring the activation process of the giant pore MIL-100(Al) by solid state NMR. *J. Phys. Chem. C* **2011**, *115*, 17934–17944.
- (24) Gallis, D. F. S.; Chapman, K. W.; Rodriguez, M. A.; Greathouse, J. A.; Parkes, M. V.; Nenoff, T. M. Selective O₂ Sorption at Ambient Temperatures via Node Distortions in Sc-MIL-100. *Chem. Mater.* **2016**, *28*, 3327–3336.
- (25) Barth, B.; Mendt, M.; Pöppel, A.; Hartmann, M. Adsorption of nitric oxide in metal-organic frameworks: Low temperature IR and EPR spectroscopic evaluation of the role of open metal sites. *Microporous Mesoporous Mater.* **2015**, *216*, 97–110.
- (26) Robin Bendall, M.; Gordon, R. E. Depth and refocusing pulses designed for multipulse NMR with surface coils. *J. Magn. Reson.* **1983**, *53*, 365–385.
- (27) Amoureux, J.-P.; Fernandez, C.; Steuernagel, S. Z-filtering in MQMAS NMR. *J. Magn. Reson.* **1996**, *123*, 116–118.
- (28) Van Rossum, B.-J.; Förster, H.; De Groot, H. J. M. High-field and high-speed CP-MAS ^{13}C NMR heteronuclear dipolar-correlation spectroscopy of solids with frequency-switched Lee-Goldburg homonuclear decoupling. *J. Magn. Reson.* **1997**, *124*, 516–519.
- (29) Stejskal, E. O.; Schaefer, J.; Waugh, J. S. Magic-angle spinning and polarization transfer in proton-enhanced NMR. *J. Magn. Reson.* **1977**, *28*, 105–112.
- (30) Massiot, D.; Fayon, F.; Capron, M.; King, I.; Le Calvé, S.; Alonso, B.; Durand, J.-O.; Bujoli, B.; Gan, Z.; Hoatson, G. Modelling one- and two-dimensional solid-state NMR spectra. *Magn. Reson. Chem.* **2002**, *40*, 70–76.
- (31) Gul-E-Noor, F.; Jee, B.; Pöppel, A.; Hartmann, M.; Hims, D.; Bertmer, M. Effects of varying water adsorption on a $\text{Cu}_3(\text{BTC})_2$

metal-organic framework (MOF) as studied by ^1H and ^{13}C solid-state NMR spectroscopy. *Phys. Chem. Chem. Phys.* **2011**, *13*, 7783–7788.

(32) Hunger, M.; Ernst, S.; Steuernagel, S.; Weitkamp, J. High-field ^1H MAS NMR investigations of acidic and non-acidic hydroxyl groups in zeolites H-Beta, H-ZSM-5, H-ZSM-58 and H-MCM-221. *Microporous Mater.* **1996**, *6*, 349–353.

(33) Isobe, T.; Watanabe, T.; d'Espinose de la Caillerie, J. B.; Legrand, A. P.; Massiot, D. Solid-state ^1H and ^{27}Al NMR studies of amorphous aluminum hydroxides. *J. Colloid Interface Sci.* **2003**, *261*, 320–324.

(34) Ashbrook, S. E.; Mackenzie, K. J. D.; Wimperis, S. ^{27}Al multiple-quantum MAS NMR of mechanically treated Bayerite (α - $\text{Al}(\text{OH})_3$) and silica mixtures. *Solid State Nucl. Magn. Reson.* **2001**, *20*, 87–99.

(35) Xue, X.; Kanzaki, M. High-pressure δ - $\text{Al}(\text{OH})_3$ and δ - AlOOH phases and isostructural hydroxides/oxyhydroxides: new structural insights from high-resolution ^1H and ^{27}Al NMR. *J. Phys. Chem. B* **2007**, *111*, 13156–13166.

(36) Vyalikh, A.; Zesewitz, K.; Scheler, U. Hydrogen bonds and local symmetry in the crystal structure of gibbsite. *Magn. Reson. Chem.* **2010**, *48*, 877–881.

(37) Carr, S. W.; Gore, B.; Anderson, M. W. ^{29}Si , ^{27}Al and ^1H solid-state NMR study of the surface of zeolite MAP. *Chem. Mater.* **1997**, *9*, 1927–1932.

(38) Fernandez, C.; Amoureux, J. P.; Chezeau, J. M.; Delmotte, L.; Kessler, H. ^{27}Al MAS NMR characterization of AlPO_4 -14 Enhanced resolution and information by MQMAS. *Microporous Mater.* **1996**, *6*, 331–340.

(39) Hoatson, G. L.; Zhou, D. H.; Fayon, F.; Massiot, D.; Vold, R. L. ^{93}Nb magic angle spinning NMR study of perovskite relaxor ferroelectrics $(1-x)\text{Pb}(\text{Mg}_{1/3}\text{Nb}_{2/3})\text{O}_3 - x\text{Pb}(\text{Sc}_{1/2}\text{Nb}_{1/2})\text{O}_3$. *Phys. Rev. B: Condens. Matter Mater. Phys.* **2002**, *66*, 224103.

(40) Czjzek, G.; Fink, J.; Götz, F.; Schmidt, H.; Coey, J. M. D.; Rebouillat, J.-P.; Liénard, A. Atomic coordination and the distribution of electric field gradients in amorphous solids. *Phys. Rev. B: Condens. Matter Mater. Phys.* **1981**, *23*, 2513–2530.

(41) Kolodziejewski, W.; Klinowski, J. Kinetics of cross-polarization in solid-state NMR: A guide for chemists. *Chem. Rev.* **2002**, *102*, 613–628.

(42) Pines, A.; Gibby, M. G.; Waugh, J. S. Proton-enhanced NMR of dilute spins in solids. *J. Chem. Phys.* **1973**, *59*, 569–590.

(43) Mito, M.; Tatano, T.; Komorida, Y.; Tajiri, T.; Deguchi, H.; Takagi, S.; Kohiki, S.; Ohba, M.; Matsuda, R.; Kitagawa, S. Magnetic properties of nitric oxide molecules physisorbed into nano-sized pores of MCM-41. *Microporous Mesoporous Mater.* **2010**, *132*, 464–469.

(44) Hadjiivanov, K. I. Identification of neutral and charged N_xO_y surface species by IR spectroscopy. *Catal. Rev.* **2000**, *42*, 71–144.

Supporting Information

**Nitric Oxide Adsorption in MIL-100(Al) MOF Studied
by Solid-State NMR**

Arafat H. Khan,[†] Benjamin Barth,[‡] Martin Hartmann,[‡] Jürgen Haase,[†] and
Marko Bertmer^{*,†}

*Felix Bloch Institute for Solid State Physics, University of Leipzig, Leipzig, Germany, and
Erlangen Catalysis Resource Centre (ECRC), Friedrich-Alexander-Universität
Erlangen-Nürnberg, Erlangen, Germany*

E-mail: bertmer@physik.uni-leipzig.de

^{*}To whom correspondence should be addressed

[†]Felix Bloch Institute for Solid State Physics, University of Leipzig, Leipzig, Germany

[‡]Erlangen Catalysis Resource Centre (ECRC), Friedrich-Alexander-Universität Erlangen-Nürnberg, Erlangen, Germany

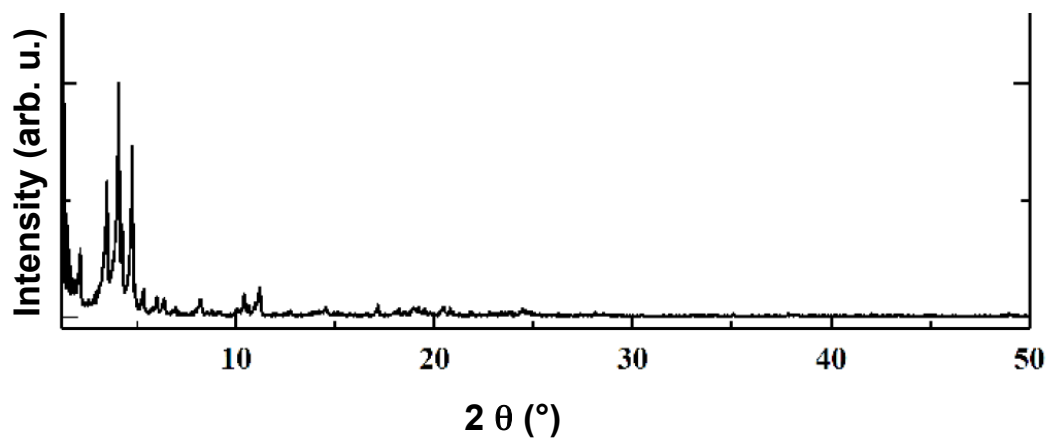


Figure S1: XRD powder pattern of MIL-100(Al).

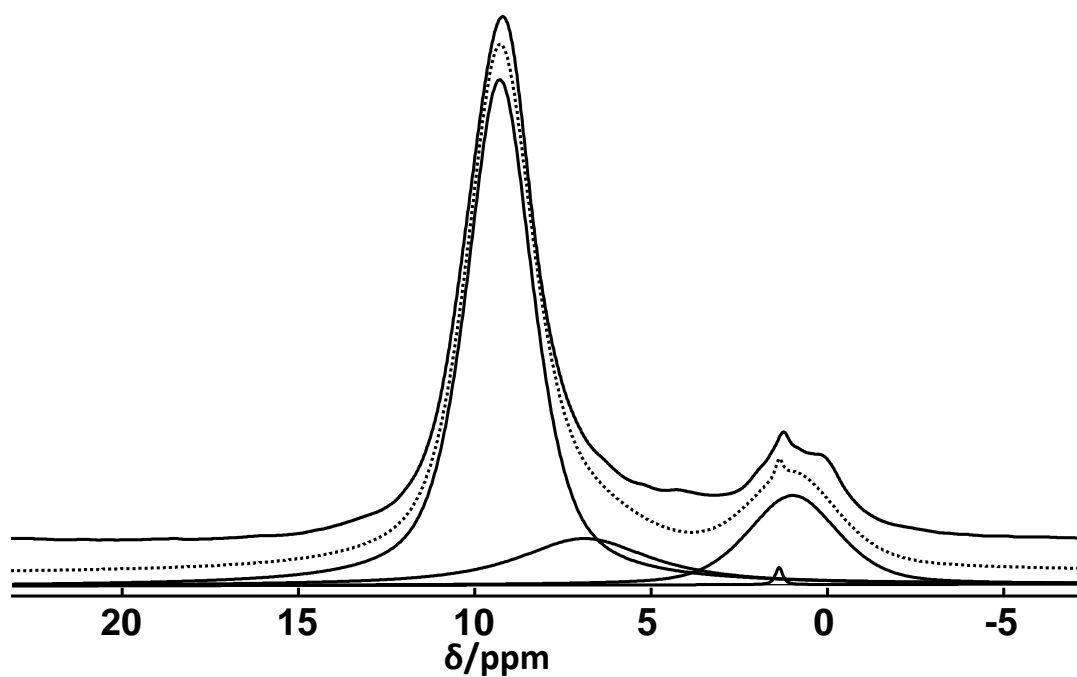


Figure S2: 1D deconvoluted ¹H spectrum of dehydrated MIL-100(Al) stored in glass tube (sample a). The experimental spectrum is shown as a solid line, the corresponding fit as dotted line below. Individual signals are given below the experimental spectrum.

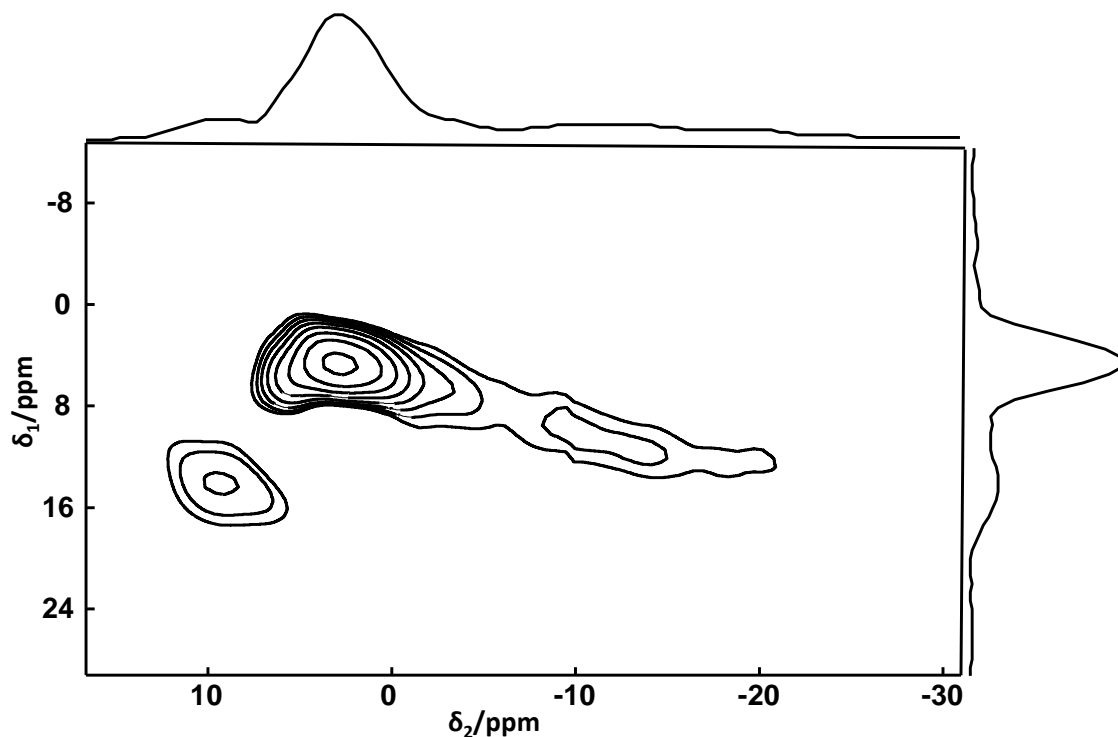


Figure S3: ^{27}Al MQMAS NMR spectrum of hydrated MIL-100(Al).

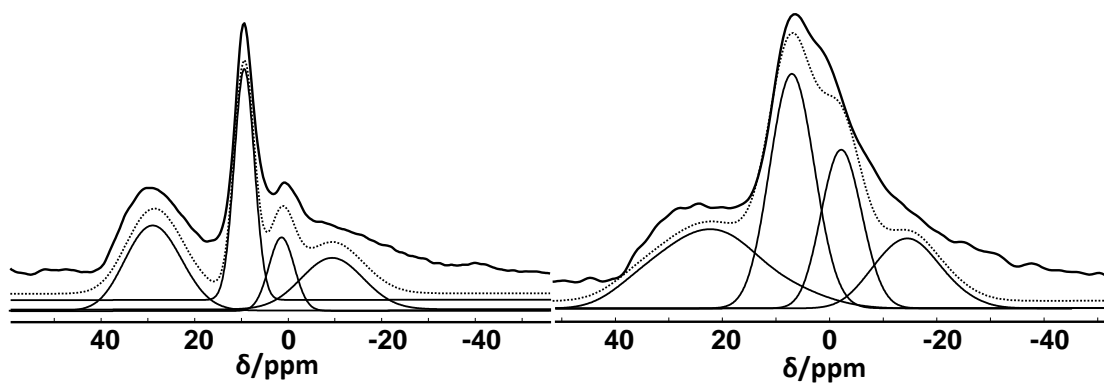


Figure S4: ^{27}Al deconvoluted spectra of dehydrated MIL-100(Al), measured at 195 MHz (left) and 104 MHz (right) using the MQMAS fitting parameters (Table 1). For better agreement a fourth line with parameters $\delta_{iso} = -5.2$ ppm and $C_Q = 4.2$ MHz was added that is not represented in the MQMAS spectrum..

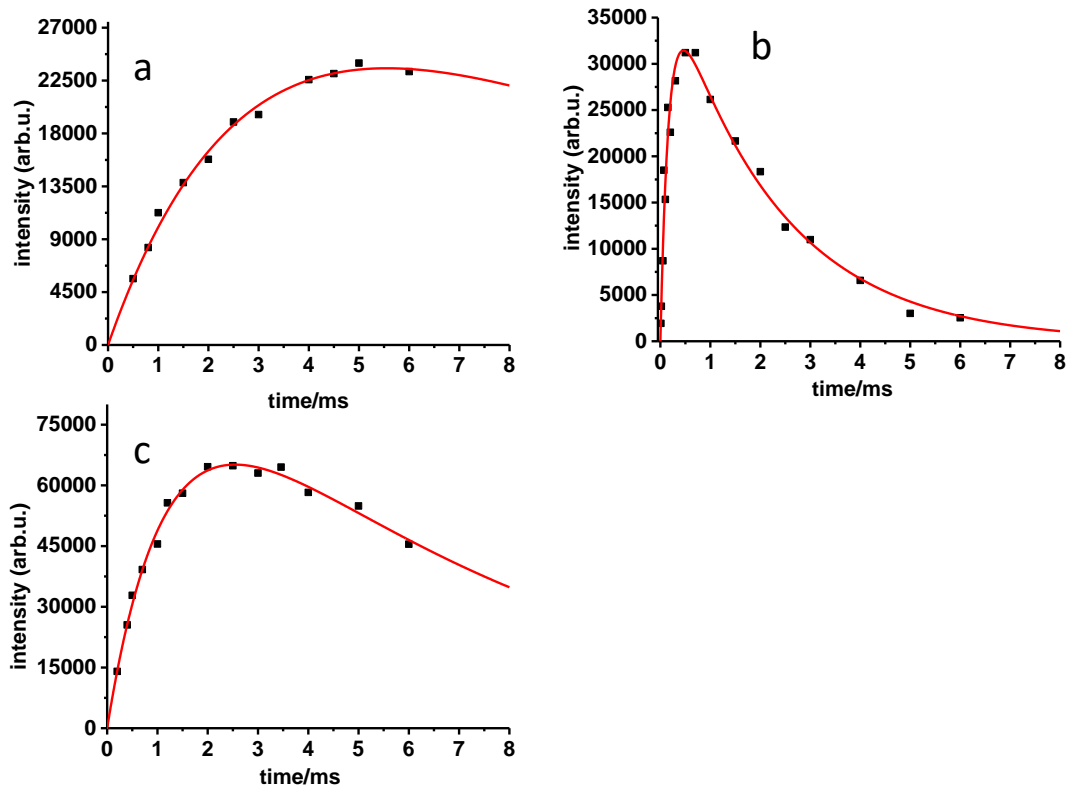


Figure S5: Intensities of the $^{27}\text{Al}\{^1\text{H}\}$ variable contact time measurement of dehydrated MIL-100(Al): (a) five-coordinated Al MOF site; (b) Al(OH)₃; (c) six-coordinated Al MOF site. The lines indicate fits according to equation 3.

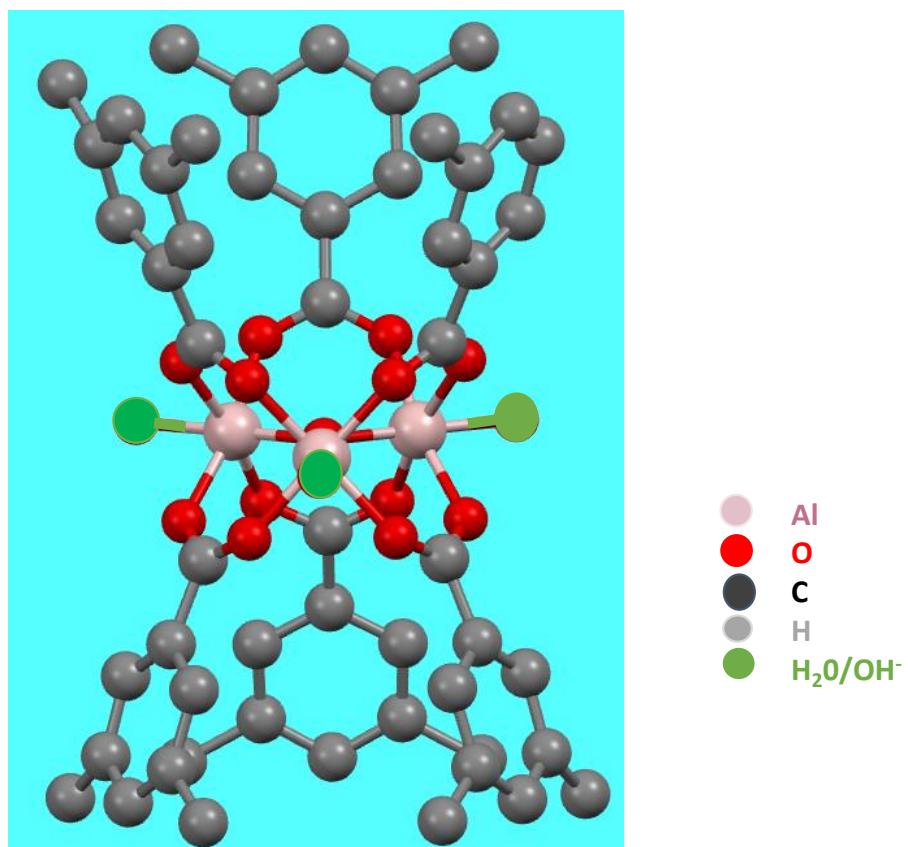


Figure S6: View at the crystal structure of MIL-100(Al), showing the surrounding of the aluminum trimer.

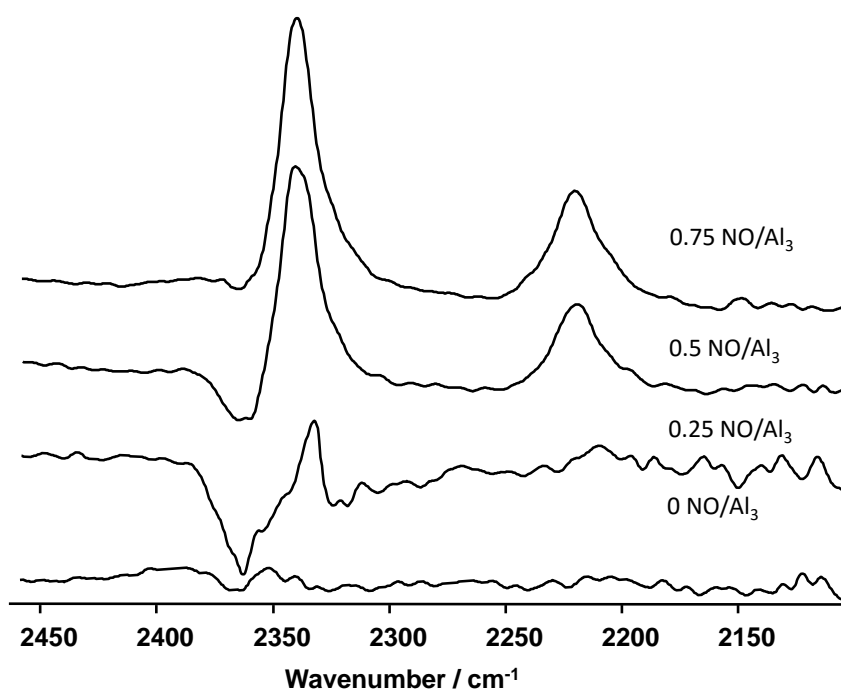


Figure S7: FTIR spectra of samples a to d (bottom to top). Only the relevant range for NO adsorption is shown.

Paper V : Temperature dependent ^{15}N NMR study of Nitric Oxide [*Solid State Nucl. Magn. Reson.*(accepted on 2nd May 2019)]

The magnetic properties of NO make it quite challenging for NMR measurements. In general, the presence of unpaired electron causes a strong electron-nuclear interaction that severely complicates the NMR measurements of NO. Being paramagnetic NO is studied routinely by EPR, however, the dimeric form of NO is EPR insensitive. On the other hand, NMR could contribute to the detection of diamagnetic $(\text{NO})_2$, therefore, an isotopically labeled ^{15}NO is investigated by NMR. The temperature dependence behavior of ^{15}N NMR spectra within the liquefaction temperature of NO is demonstrated in paper V. NMR studies of ^{15}NO unfold the first time ^{15}N spectra at variable temperature, and the influence of paramagnetic NO on the NMR parameters. A fast dynamic equilibrium of NO and $(\text{NO})_2$ is documented by the chemical shift as well as the spin-lattice relaxation time. $(\text{NO})_2$ signal at solid state is also measured. Additionally, SQUID measurements on the same sample supported the fact of NMR analysis.

Temperature dependent ^{15}N NMR study of Nitric Oxide

Arafat H. Khan, Dieter Michel, and Marko Bertmer*

Felix Bloch Institute for Solid State Physics, Leipzig University, Leipzig, Germany

E-mail: bertmer@physik.uni-leipzig.de

Abstract

For the first time, ^{15}N NMR data are obtained for a sample of nitric oxide at various temperatures. Spectra have been obtained in the liquid and solid state. In the former, the chemical shift as well as the spin-lattice relaxation time is characterized by the dynamic equilibrium of the dimerization reaction. Only the signal of the $(\text{NO})_2$ dimer is observed, while the paramagnetic NO has strong influences on the NMR parameter. From T_1 relaxation and linewidth analysis a range for the correlation time of the exchange between monomer and dimer is obtained. SQUID measurements corroborate the NMR analysis.

Introduction

Three decades ago nitric oxide (NO) was known primarily as an environmental pollutant because nitric oxide is readily transformed into nitrogen dioxide (NO_2) by reaction with oxygen. In the late 1990's the scenario has changed, and NO was found to be an important biological messenger molecule that mediates a variety of biological functions, including inhibition of platelet adhesion and aggregation, vasodilation and cell proliferation.¹⁻⁶ The

multiple role of NO in physiology and pathophysiology has triggered a great interest in the strategies to use exogenous NO for biomedical applications.⁷⁻¹¹

For the studies presented here, the magnetic properties of NO molecules are of particular interest. The NO molecule is a free radical that possesses one unpaired electron in an antibonding Π^* molecular orbital (MO).¹² The paramagnetic molecule NO follows Hund's coupling case A: the electronic orbital motion and spin are strongly coupled to the internuclear axis and weakly coupled to the nuclear rotation.¹² Therefore, the ${}^2\Pi_{1/2}$ ground state of free NO is diamagnetic since the components $\Sigma = 1/2$ and $\Lambda = 1$ of the electron spin momentum S and the orbital momentum L are antiparallel with respect to the internuclear axis and cancel each other.^{13,14} The lowest rotational level of the first excited ${}^2\Pi_{3/2}$ state of the NO gas is paramagnetic, since S and L are parallel in this case. Hence, in the temperature range where the state ${}^2\Pi_{3/2}$ is excited, strong changes in the magnetic properties of the NO molecules in the gas phase occur. It is very interesting that EPR is capable to reveal these particularities.¹⁵ There are differences in the magnetic properties between the NO in the gas phase and isolated NO within porous media as has been demonstrated by EPR measurements.¹⁶ For this reason, NO molecules in the gaseous state and after adsorption in porous materials has been extensively investigated by various analytical techniques like EPR, SQUID, FTIR .¹⁶⁻¹⁹

EPR spectroscopy is very sensitive to reveal the behavior of NO both in the gaseous state and after adsorption in porous materials. In the ${}^2\Pi_{3/2}$ state of NO (for NO gas at lower temperatures) the g -factor is given by an unusually small value of $g = 0.7776$. Due to the coupling between L and S and the interaction with the nuclear spin, nine EPR transitions can be observed.^{12,16} Upon adsorption of NO into porous materials, S and L are decoupled and the coupling scheme changes completely. This results in a paramagnetic complex with an $S = 1/2$ ground state, a g factor close to that of the free electron $g_e \approx 2$ and thus giving rise to quite conventional EPR spectra.^{16,20} Furthermore, it is known that EPR measurements only detect small portions of NO adsorbed in porous materials, because there might be NO

species in a conformation that is not paramagnetic and therefore not detectable by EPR.

It is known that nitric oxide can dimerize to form $(\text{NO})_2$. In particular, the process of dimerization of NO is EPR-insensitive.^{16,21} Earlier data from infrared absorption,²² susceptibility measurements,²¹ and pressure-volume-temperature relations^{23,24} have concluded that above its boiling point, predominantly ($> 99\%$) the monomer form exists. This is reversed in the liquid phase. Based on calculations from the experimental findings, the degree of dissociation in the liquid phase between 110 and 120 K should be on the order of 2 to 5 %. Computation on the DFT level has predicted that the dimerization by combining the two unpaired electrons of each NO molecule leads to a fairly weak bond similar to a van-der-Waals-bond.²⁵ This is also the reason why several isomer structures of $(\text{NO})_2$ result in similar energy. The crystal structure of the dimer has also been characterized with a long N-N bond of 238 pm.²⁶

NMR is widely used to probe the electronic and chemical properties of materials on an atomic scale. The dynamic exchange between monomer and dimer forms has also been well-studied by NMR.^{27,28} The presence of unpaired electrons means that, in addition to the interactions normally observed in NMR, typically electron-nuclear interactions dominate the spectra. Previously, we have used this principle to show that ^1H NMR can elucidate the NO adsorption behavior in metal-organic frameworks (MOFs) to get information on adsorption processes.^{29,30}

In this work, ^{15}N NMR studies are carried out on ^{15}N -labeled NO samples prepared under vacuum conditions and measured under variable temperature conditions in the liquid as well as solid state. Variations of chemical shift, spin-lattice relaxation time T_1 , and linewidth is used to deduce information about the dimerization equilibrium between paramagnetic NO and diamagnetic $(\text{NO})_2$.

Experimental

Preparation of glass container samples

For the NMR measurements a special glass container was constructed at first which is shown in Figure 1. The container is mounted with a special holder inside of a home built probe. The whole diameter of the container as well as its height are about 33 mm, i. e., height and diameter of the glass container are adapted for the NMR probe. The part with the larger diameter is outside of the NMR coil and serves as an NO reservoir, while the smaller one with a diameter of 4 mm fits well within the NMR coil. In general, before gas loading, the glass container shown in Figure 1 is connected to a vacuum line and evacuated for 24 h at 393 K to a final pressure of 10^{-6} bar in order to remove air and in particular water. Then a definite amount of NO, corresponding to a pressure of ca. 1 bar at room temperature, is loaded at 77 K under vacuum conditions into the empty glass container. The ^{15}NO gas is supplied by Icon Service Inc (USA) with a ^{15}N enrichment of 98 %. Immediately after the gas loading, the glass container is sealed by torch with sample cooling at 77 K prior to the NMR experiment. The relatively high amount of NO molecules (about 10^{21} spins) contained now in the glass container assists to detect the ^{15}N NMR signal, as the chemical shift range is unknown. With decreasing temperature accumulation of molecules within the small part of the container within the coil is expected, increasing signal-to-noise ratio. Disadvantage of this setup is that not all spins are detectable at all times, because the bigger part of the glass container is outside of the NMR coil. Even condensation at lower temperatures in the lower part lying within the NMR coil, does not guarantee that the total amount of NO is within the coil. After the successful use of this special sample container to find the signal and optimize the measuring conditions, for the subsequent measurements a small 4 mm quartz glass container was taken which completely fits within the NMR coil, containing ca. 10^{18} spins (loading pressure ca. 40 mbar at room temperature).

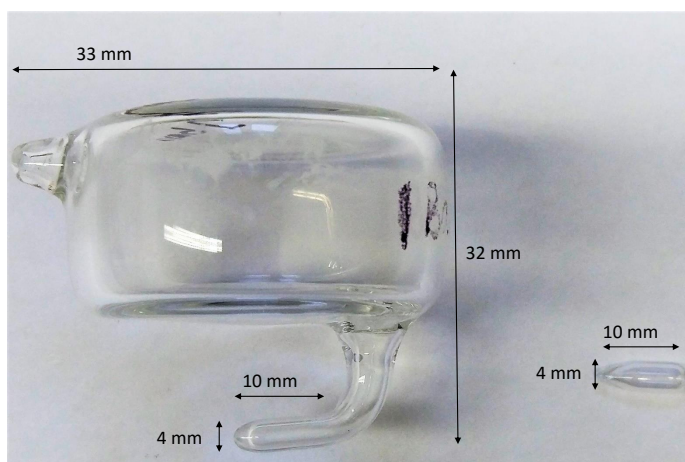


Figure 1: View of the large and small containers for the preparation of NMR samples with nitric oxide.

NMR measurements

NMR measurements were carried out with a Bruker Avance III spectrometer at a magnetic field of 11.6 T (^{15}N frequency 50.67 MHz) with a home-built probe in an Oxford cryostat. The NMR spectra were recorded by simple FID measurements. The length of the 90° pulse was $15 \mu\text{s}$. The repetition time was set to 10 ms which is more than five times the longitudinal relaxation time T_1 (see below). Variable temperature dependent ^{15}N NMR measurements of ^{15}NO were mainly run in the range from the liquefaction temperature until 94 K. The temperature was controlled by a Lakeshore temperature controller with an accuracy of ± 0.5 K. A typical waiting time for cooling was 20 minutes to reach a stable temperature of the desired value. ^{15}N NMR spin-lattice relaxation times were measured by the inversion recovery pulse sequence. Data analysis is carried out with dmfit.³¹ ^{15}N NMR spectra are referenced to nitromethane using glycine as secondary reference (-347 ppm).

SQUID measurements

Magnetic moments were measured with a SQUID magnetometer (Quantum Design MPMS-7) with a constant applied field of 1 T. The measurements were conducted in the temperature

range from 5 K to 200 K in cooling and heating mode. Both field cooling (FC) and zero field cooling (ZFC) procedures were used. For the SQUID measurements the same samples were used as mentioned already in connection with the NMR studies.

Results and discussion

Detection of ^{15}N NMR signal

In the gas phase, above 121.5 K, no ^{15}N NMR signal for nitric oxide could be detected. Several attempts have been carried out to detect NO above its boiling point, but were all unsuccessful. This is in agreement with conclusions from Wu *et al.*³² NO possesses an unpaired electron and therefore a strong electron magnetic moment, which can give rise both to strong paramagnetic shifts in the ^{15}N NMR spectra and to very short ^{15}N spin-lattice relaxation times (T_1) because of the strong local magnetic field originating from the unpaired electrons. To check whether strong resonance shifts occur, a systematic study with various offset frequencies over a broad frequency range has been carried out. However, we did not observe ^{15}N NMR signals in the gas phase and hence an interpretation in terms of a strong resonance shift is ruled out here. Hence, the most probable reason is the very short ^{15}N relaxation times T_1 .

In the following we mainly deal with ^{15}N NMR measurements in the temperature range where NO exists in the liquid state, i. e., in the temperature interval between about 122 K and 109 K. A typical ^{15}N NMR spectrum is shown in Figure S1 (temperature 117 K). The measurement was performed in this case using the large glass container. In addition to the single intense resonance line for nitric oxide, two weak ^{15}N NMR lines appear at -147 ppm and -220 ppm. The latter two weak lines are ascribed to N_2O as has been also reported by other authors.³²⁻³⁴ Moreover, Figure S2 shows that the shift of the ^{15}N NMR signals for the (diamagnetic) N_2O is practically independent of temperature. We also note the small linewidth as expected for diamagnetic signals in comparison to the much larger linewidths

shown below. The small amount of N_2O is an impurity in the original starting material and is of no further interest and importance for our analysis.

Temperature dependent ^{15}N NMR spectra

The ^{15}N NMR spectra measured in the liquid phase show a strong variation in shift with temperature. In Figure 2 the influence of temperature on the resonance line is shown for the small glass container. We observe a shift variation between 3035 ppm close to the boiling point and 2045 ppm at the melting point (109.5 K). We assign the detectable ^{15}N NMR signal in the liquid phase to the $(\text{NO})_2$ dimer. This is in agreement with the observation that the ^{15}N NMR resonance position near the melting point is close to that of solid $(\text{NO})_2$ (see below). Figure S3 represents ^{15}N NMR spectra measured for the large glass container. Here the resonance lines appear in the range between 2800 and 2000 ppm between melting and boiling point. The shift difference between the two glass containers is shown in Figure S4. The deviations between the two sample containers are probably due to the differences in the total number of NO spins. Especially in the larger container a certain amount of NO is in the gas phase which is outside of the coil but in contact with it. Therefore, more not dimerized NO spins are present even at low temperature that contribute to the shift deviation (see analysis below). For our further analysis this shift deviation between the two containers is not of general importance. Hence, for the following discussion it is sufficient to consider only the resonance shift analysis as has been studied by using the small glass container.

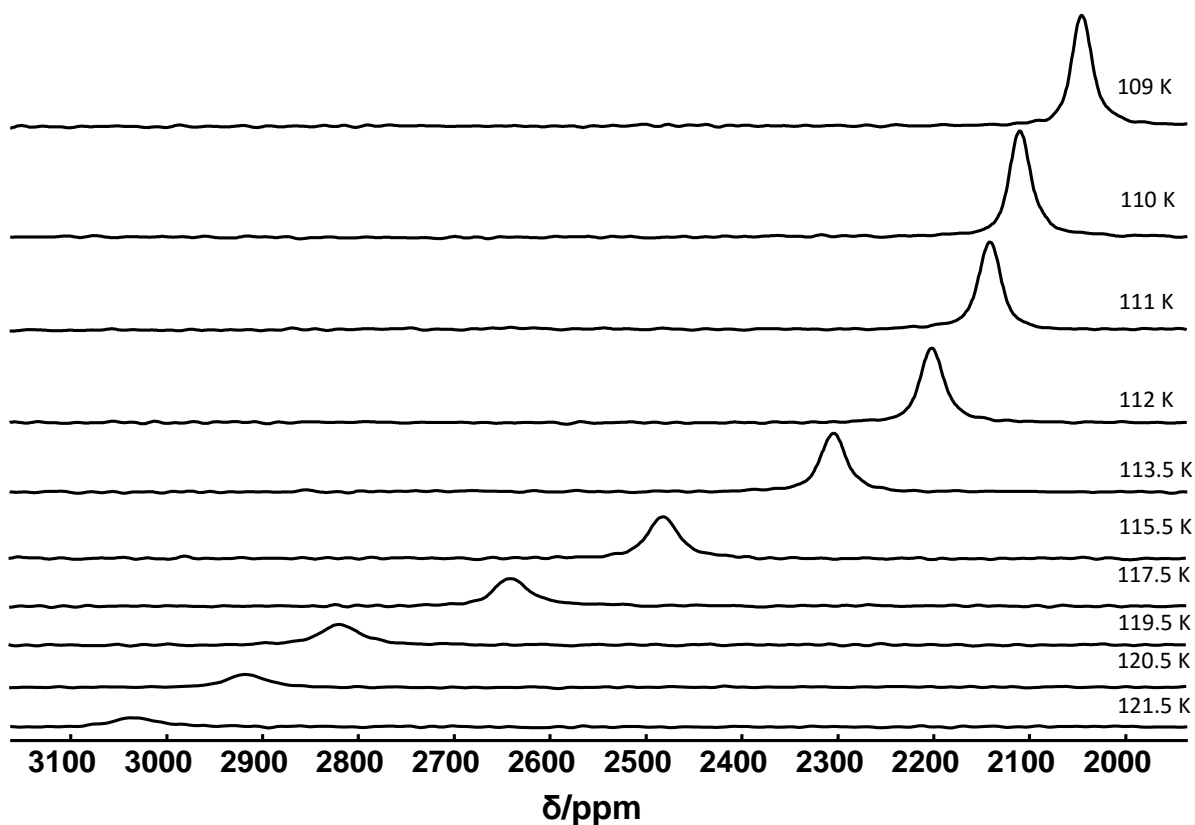


Figure 2: ^{15}N NMR spectra of the small glass container in the temperature range of the liquid state. All spectra were acquired with 8 K scans and plotted without normalization.

From extrapolation of the resonance shift towards the boiling point we could determine the chemical shift value of the NO monomer (see Figure S4). At 123 K a chemical shift of 3070 ppm is obtained from which we could approximately determine the resonance shift for the NO monomer. For the further discussion it is essential that with decreasing temperature a significant increase of signal intensity is observed until the melting point is reached, as shown in Figure 3. The relative fraction of the dimer is then estimated from the peak area of the ^{15}N NMR signal of $(\text{NO})_2$. Within this temperature range the signal increase with decreasing temperature based on Boltzmann population is negligible. Therefore, the intensity variation is a result of the equilibrium reaction for dimerization. The relative amount of the $(\text{NO})_2$ dimer decreases in favor of the increasing amount of NO monomer (which cannot be measured by means of ^{15}N NMR as already mentioned) if temperature increases. The temperature dependence of ^{15}N resonance shift and area intensity therefore

contains information on the dynamic equilibrium between NO monomer and $(\text{NO})_2$.

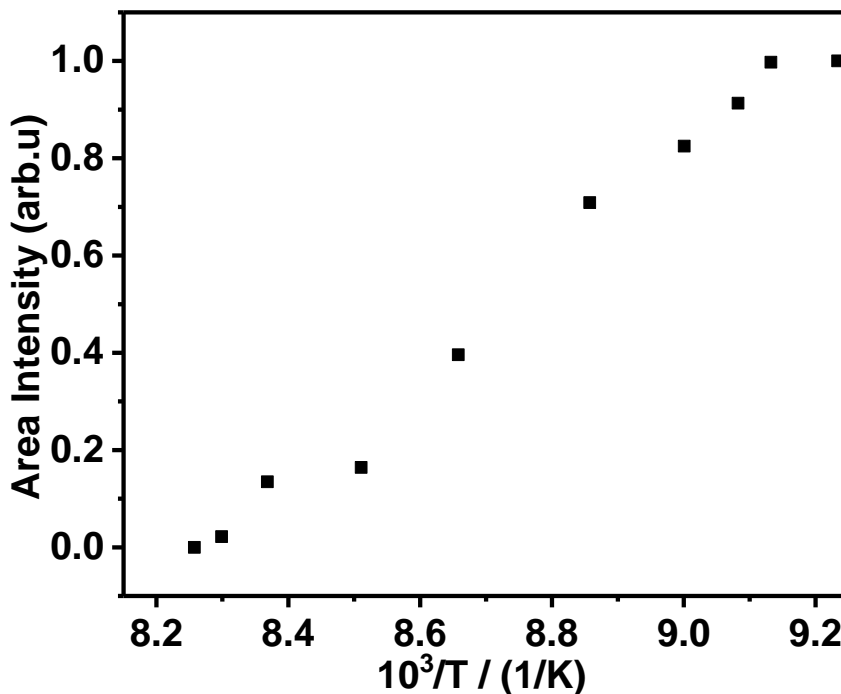


Figure 3: Intensity of the ^{15}N signal as a function of inverse temperature.

Analysis of ^{15}N shift in terms of dynamic equilibrium

The ^{15}N NMR spectra for nitric oxide measured between 121.5 K and 109 K (Figures 2 and S3) can be well understood if we consider a temperature dependent equilibrium between the non-detectable (paramagnetic) NO monomer and the diamagnetic $(\text{NO})_2$ dimer in the liquid state. The exchange process of the monomer - dimer dynamics will be examined in details by the analysis of the resonance shift, area intensities and the inspection of the longitudinal relaxation time T_1 of the dimer. The temperature dependence of the ^{15}N resonance shift can be understood on the basis of the following model: In the temperature range of the gas-liquid transition, a continuous variation of the ^{15}N resonance shifts for $(\text{NO})_2$ is occurring because of the fast exchange dynamics process between the two states with the fractions $p_{monomer}$

and p_{dimer} :

$$p_{monomer} + p_{dimer} = 1 \quad (1)$$

Although not detected by ^{15}N NMR, we may derive the monomer fraction from the NMR experiment. $p_{monomer} = 1 - p_{dimer}$ increases at the expense of the diamagnetic $(\text{NO})_2$ fraction p_{dimer} with increasing temperature. Therefore, the measured resonance shift is given as the weighted average of both species.

$$\delta_{exp} = p_{dimer} \cdot \delta_{dimer} + (1 - p_{dimer}) \cdot \delta_{monomer}. \quad (2)$$

where δ_{dimer} and $\delta_{monomer}$ are the corresponding chemical shifts of the dimer (2045 ppm) and the monomer (extrapolated shift at the boiling point, 3070 ppm).

As a consequence, we observe that the measured shift changes until the value $\delta_{exp} = \delta_{monomer}$ is approached, but the signal intensity (Figure 3) is moving towards 0. The reason is that the measurable fraction p_{dimer} disappears at the boiling point and the monomer is not observable. δ_{dimer} is the isotropic shift obtained at the melting point and assumed to be approximately independent of temperature. Based on this, the time scale of the exchange dynamics could be estimated by the difference in angular frequencies, $\Delta\omega = \omega_{monomer} - \omega_{dimer}$ of a nuclear spin in monomer and dimer state. The chemical shift difference in ppm scale is about 1000 ppm, resulting in $\Delta\omega \approx 3.18 \times 10^5 \text{rads}^{-1}$. From this, we may estimate the time scale for the temperature dependent dynamic equilibrium between NO and $(\text{NO})_2$. It is well-known that for a fast exchange process the exchange time, $\tau_{exchange}$ between the two states should be smaller than the inverse of the frequency difference³⁵, i. e., $\tau_{exchange} < \frac{1}{\Delta\omega}$. Thus, we may estimate an upper limit of $\tau_{exchange} \approx 3.2 \times 10^{-6}\text{s}$. A rough estimation of the lower limit for the exchange dynamics is possible by considering the temperature dependence of the spin lattice relaxation time T_1 discussed in the next section.

A slow exchange process³⁶ would be recognized easily by the presence of a temperature independent value for ω with decreasing signal intensity with increasing temperature. This

situation can be ruled out.

Analysis of the spin-lattice relaxation time T_1

Figure 4 shows the temperature variation of the ^{15}N spin-lattice relaxation time T_1 in the range 95 K to 122 K. The relaxation times T_1 are rather short (ca. 0.5 ms) at the melting point and decrease to a value of ≈ 0.23 ms at 122 K. It is interesting to note that the relaxation times at temperatures below 104 K (in the solid state) are about 10^3 times larger than the values measured in the liquid state. This indicates that no unpaired electrons are present anymore that with the electron-nucleus magnetic interaction are the primary source for relaxation. Together with the lower mobility, typically relaxation times for diamagnetic samples in the solid-state are observed. Furthermore, this finding also corroborates our assumption that we only detect the dimer signal above: in the solid phase there is only $(\text{NO})_2$ dimer present which is diamagnetic giving rise to long T_1 values.

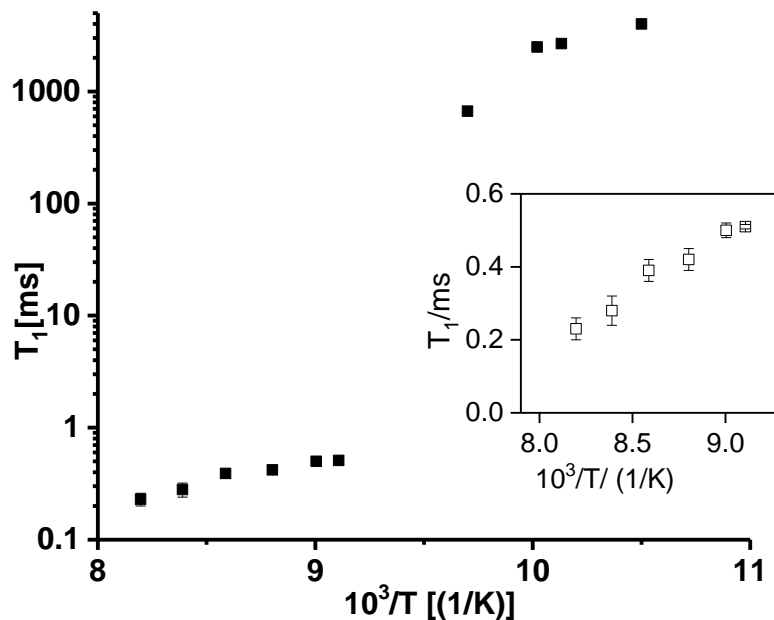


Figure 4: ^{15}N T_1 as a function of inverse temperature (95 to 122 K). The inset shows only the range 109 to 123 K (liquid state).

In the liquid phase, however, there is a rapid exchange between $(\text{NO})_2$ dimer and NO monomer. In fact, in agreement to the analysis of the resonance shifts, the measured relaxation rate $1/T_1$ should be given in the case of fast exchange as³⁷

$$\frac{1}{T_1} = \frac{p_{dimer}}{T_{1,dimer}} + \frac{(1 - p_{dimer})}{T_{1,monomer}}, \quad (3)$$

where the second contribution is strongly dominating. In accordance with the rather short relaxation times we observe a strong contribution to the longitudinal ^{15}N NMR relaxation rates $\frac{1}{T_1}$, due to the magnetic interaction between the ^{15}N spins in the dimer and the magnetic moments of the unpaired electrons in the NO monomer.

The short values for the ^{15}N NMR relaxation times T_1 of the NO molecules (above 104 K) are related to the scalar contact interaction $\hat{I} \overset{\leftrightarrow}{A} \hat{S}$ between the ^{15}N nuclear magnetic moment \hat{I} (angular frequency ω_I) and the magnetic moment of the electron spins \hat{S} (angular frequency ω_S), with $\overset{\leftrightarrow}{A}$ describing the hyperfine coupling tensor. In this context the measured relaxation rate would be given by the well-known relation³⁵

$$\frac{1}{T_1} \propto \frac{\tau_c}{1 + [(\omega_I - \omega_S)\tau_c]^2} \approx \frac{\tau_c}{1 + [\omega_S\tau_c]^2} \quad (4)$$

If we take into account that the relaxation time T_1 is decreasing in the temperature interval between 109 K and 122 K, we may assume that $\omega_S\tau_c \geq 1$.³⁵ This situation would allow for a fairly rough estimation of a lower limit for the correlation time to be $\tau_c \geq (\omega_S)^{-1} \approx (660 \times 2\pi \times \nu_{^{15}\text{N}})^{-1} \approx 5 \times 10^{-12}$ s. The correlation time τ_c in the temperature range of the liquid phase is related to the interaction between the ^{15}N nuclear spin and the local magnetic fields of the NO monomer. It is characterized by the statistical reorientation of $(\text{NO})_2$ superimposed by the exchange dynamics between NO and $(\text{NO})_2$ species. The long relaxation times in the solid phase, in contrast to the very short values in the liquid phase, clearly indicate that the interaction between ^{15}N spin and local magnetic fields does not play any role. The behavior of the longitudinal relaxation time nicely supports the

model of the exchange behavior between the magnetic monomer NO and the diamagnetic (NO)₂ dimer in the liquid phase. Combining the analysis of the resonance shifts and the spin-lattice relaxation time, we derive a time interval for the exchange dynamics: 10^{-6} s $\gg \tau_{exchange} \gg 5 \times 10^{-12}$ s. This time range is typical for a rapid stochastic reorientation and fast exchange behavior in liquids.

Variation of the ¹⁵N NMR linewidths for (NO)₂ with temperature

In Figure S5 the linewidth is shown as a function of temperature. An increase of linewidth with increasing temperature is observed resulting in a more than doubled linewidth near the boiling point compared to the melting point. The Lorentzian lineshape of the dimer signal yields a width at half height of $\Delta\omega_{1/2} = \frac{2}{T_2^*}$. Thus we can determine the (effective) transverse relaxation time T_2^* to compare with the longitudinal relaxation time T_1 . We obtain values for T_2^* between 0.26 ms and 0.13 ms at 109 K and 122 K, respectively. The T_2^* values are about half of the values for T_1 . This situation is not surprising because comparable values for T_1 and T_2^* are expected in the case of strong magnetic interactions and fast molecular motions. Usually, transverse relaxation times increase with increasing temperature and therefore linewidths decrease with increasing temperature. Here, the opposite effect is observed, the linewidth increases with increasing temperature. This could be related to an increasing paramagnetic susceptibility^{38,39} at higher temperatures. Another reason for the broadening could be the exchange between monomer and dimer and the increasing influence of the paramagnetic NO monomer. Ideally, the contribution to the linewidth or transverse relaxation rate from a chemical kinetic process depends critically on the exchange process in the NMR chemical shift time scale.³⁶ Although the present data do not allow to arrive at a more detailed inspection of the dynamics of the exchange process, we may conclude that the linewidths of (NO)₂ support the conclusions derived already from the analysis of the ¹⁵N NMR resonance shifts.

^{15}N NMR of solid $(\text{NO})_2$

Besides the gas - liquid transition temperature, some measurements were also run in the solid phase below 108 K. From the melting point down to about 94.7 K, NMR signals appear in the range between 1900 and 2600 ppm which we assign to signals from different solid $(\text{NO})_2$ crystallites. Figure 5 represents different ^{15}N NMR spectra of solid $(\text{NO})_2$ below the melting point. Down to 108.2 K signal for the liquid $(\text{NO})_2$ at 1980 ppm can still be found, the shift is not changing with temperature. This indicates the diamagnetic nature of the dimer.

During freezing, different crystallites are forming simultaneously with different orientations with respect to the external magnetic field, leading to different resonance shifts. Intensities increase with lowering temperature. Below 105 K, more and more crystallites are formed or crystallites grow in size so that the individual lines broaden (maybe due to homonuclear dipolar coupling) and finally a quasi powder pattern spectrum is obtained. Due to the long spin-lattice relaxation time (as discussed above), intensity does not increase further as full relaxation is not reached.

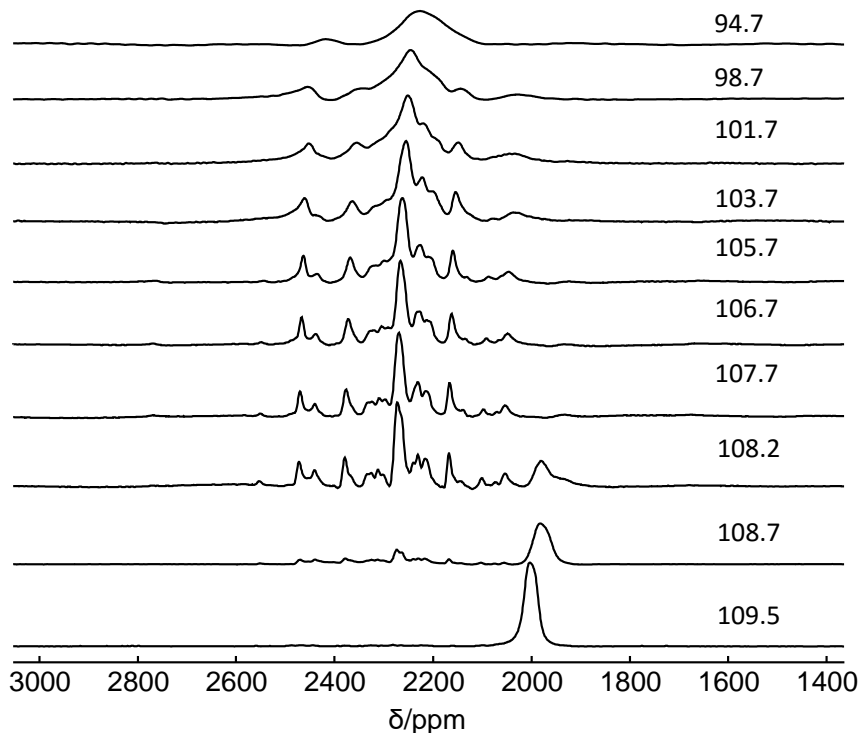


Figure 5: ^{15}N NMR spectra of solid $(\text{NO})_2$ close to and below the melting point.

SQUID measurements

The investigation of the magnetic moment of NO by means of SQUID measurements was done to support our analysis of the results obtained from NMR. Therefore, the same small glass container from the NMR measurements was also used for the SQUID measurements. Figure 6 summarizes the results in the temperature range between 5 and 200 K for the field cooling procedure with a constant applied field of 1 T. In the range above 108 K the magnetic moment is positive, which indicates the presence of paramagnetic species and is in agreement with NO being paramagnetic in the gas phase. In the temperature range between 108 to 102 K a fast transition from paramagnetic to diamagnetic behavior is observed. The decrease of magnetization basically follows the expected behavior for paramagnetic materials according to Curie's law.⁴⁰ The results are in good agreement to earlier works on NO adsorbed in MCM-41.^{18,21,41} Differences are that in MCM-41 the phase transition shows a slight deviation from

standard temperature and that the transition is slower because of multilayer adsorption of NO.^{18,41} Data can also be compared to early susceptibility measurements following the same trend.²¹ In summary, a positive magnetization arises from the presence of paramagnetic NO monomer which has a dynamic equilibrium with diamagnetic (NO)₂ species above the melting point and below this temperature only solid (NO)₂ is observable. This result strengthens our analysis based on the NMR parameters discussed above.

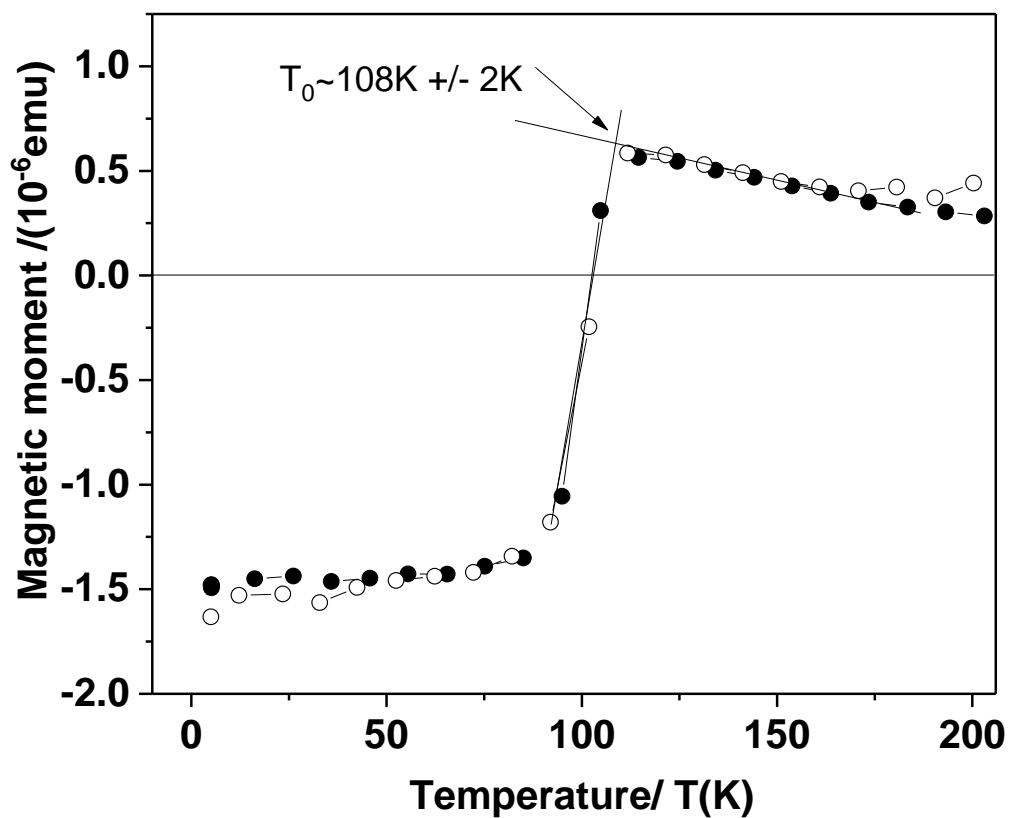


Figure 6: Temperature dependence of the magnetic moment at a magnetic field of 1 T. The arrow indicates the transition temperature. Closed and open symbols refer to cooling and heating in the SQUID experiment, respectively.

Conclusions

For the first time, ^{15}N NMR data were obtained on isotopically ^{15}N labeled nitric oxide. No signal is detected in the gas phase, but we studied the equilibrium between $(\text{NO})_2$ dimer and NO monomer in the liquid state. In the solid state, individual crystallites are observed with constant shift typical for diamagnetic samples. The presence of the NO monomer in equilibrium with $(\text{NO})_2$ has significant influence on the resonance shifts and the signal intensities in the liquid temperature range. Only the signal of $(\text{NO})_2$ can be measured. Similar information on the equilibrium between NO and $(\text{NO})_2$ is obtained from analysis of the ^{15}N NMR relaxation times and the variation of linewidth with temperature. The correlation time of exchange process is in the range 10^{-6} s and 5×10^{-12} s. SQUID data indicate the transition from the diamagnetic behavior to the paramagnetic properties in the liquid phase of nitric oxide that is in good agreement with the NMR data.

Acknowledgement

The authors thank the German Research Foundation (DFG) for financial support within the priority program “Porous Metal-Organic Frameworks (MOFs) (SPP1362)”, project Be 2434/4-2. We thank Dr. Jose Barzola Quiquia (Superconductivity and Magnetism Division, Leipzig University) for SQUID measurements and discussion.

References

- (1) Katsumi, H.; Nishikawa, M.; Yamashita, F.; Hashida, M. Development of Polyethylene Glycol-Conjugated Poly-S-Nitrosated Serum Albumin, a Novel S-Nitrosothiol for Prolonged Delivery of Nitric Oxide in the Blood Circulation in Vivo. *J. Pharmacol. Exp. Ther.* **2005**, *314*, 1117–1124.

- (2) Hirst, D.; Robson, T. Nitric Oxide in Cancer Therapeutics: Interaction with Cytotoxic Chemotherapy. *Curr. Pharm. Des.* **2001**, *16*, 411–420.
- (3) Carpenter, A. W.; Schoenfisch, M. H. Nitric oxide release: Part II. Therapeutic applications. *Chem. Soc. Rev* **2012**, *41*, 3742–3752.
- (4) Moncada, S.; Higgs, E. A. The discovery of nitric oxide and its role in vascular biology. *Br. J. Pharmacol.* **2006**, *147*, S193–S201.
- (5) Hetrick, E. M.; Shin, J. H.; Stasko, N. A.; Johnson, C. B.; Wespe, D. A.; Holmuhamedov, E.; Schoenfisch, M. H. Bactericidal Efficacy of Nitric Oxide-Releasing Silica Nanoparticles. *ACS Nano* **2008**, *2*, 235–246.
- (6) Miller, M. R.; Megson, I. L. Recent developments in nitric oxide donor drugs. *Br. J. Pharmacol.* **2007**, *151*, 305–321.
- (7) Frost, M. C.; Reynolds, M. M.; Meyerhoff, M. E. Polymers incorporating nitric oxide releasing/generating substances for improved biocompatibility of blood-contacting medical devices. *Biomaterials* **2005**, *26*, 1685–1693.
- (8) McKinlay, A. C.; Xiao, B.; Wragg, D. S.; Wheatley, P. S.; Megson, I. L.; Morris, R. E. Exceptional Behavior over the Whole Adsorption - Storage - Delivery Cycle for NO in Porous Metal Organic Frameworks. *J. Am. Chem. Soc.* **2008**, *130*, 10440–10444.
- (9) Xiao, B.; Wheatley, P. S.; Zhao, X.; Fletcher, A. J.; Fox, S.; Rossi, A. G.; Megson, I. L.; Bordiga, S.; Regli, L.; Thomas, K. M.; Morris, R. E. High-capacity hydrogen and nitric oxide adsorption and storage in a metal-organic framework. *J. Am. Chem. Soc.* **2007**, *129*, 1203–1209.
- (10) Zhang, H.; Annich, G. M.; Miskulin, J.; Stankiewicz, K.; Osterholzer, K.; Merz, S. I.; Bartlett, R. H.; Meyerhoff, M. E.; Uni, V.; Arbor, A.; Critical, M.; Consultants, C. Ni-

- tric Oxide-Releasing Fumed Silica Particles: Synthesis, Characterization, and Biomedical Application. *J. Am. Chem. Soc.* **2003**, *41*, 5015–5024.
- (11) Khan, A. H.; Barth, B.; Hartmann, M.; Haase, J.; Bertmer, M. Nitric Oxide Adsorption in MIL-100(Al) MOF Studied by Solid-State NMR. *J. Phys. Chem. C* **2018**, *122*, 12723–12730.
- (12) Beringer, R.; Castle Jr, J. Magnetic resonance absorption in nitric oxide. *Phys. Rev.* **1950**, *78*, 581.
- (13) Gerhard Herzberg, *Molecular Spectra and Molecular Structure: Spectra of Diatomic Molecules*, 2nd ed.; von Nostrand company: New York, 1953.
- (14) James, T. C.; Thibault, R. J. Spin—Orbit Coupling Constant of Nitric Oxide. Determination from Fundamental and Satellite Band Origins. *J. Chem. Phys.* **1964**, *41*, 2806–2813.
- (15) Rudolf, T.; Pöppel, A.; Brunner, W.; Michel, D. EPR study of NO adsorption–desorption behaviour on Lewis acid sites in NaA zeolites. *Magn. Reson. Chem* **1999**, *37*, 93–99.
- (16) Rudolf, T.; Böhlmann, W.; Pöppel, A. Adsorption and desorption behavior of NO on H-ZSM-5, Na-ZSM-5, and Na-A as studied by EPR. *J. Magn. Reson.* **2002**, *155*, 45–56.
- (17) Hetrick, E. M.; Schoenfish, M. H. Analytical Chemistry of Nitric Oxide. *Annu. Rev. Anal. Chem.* **2009**, *2*, 409–433.
- (18) Mito, M.; Tatano, T.; Komorida, Y.; Tajiri, T.; Deguchi, H.; Takagi, S.; Kohiki, S.; Ohba, M.; Matsuda, R.; Kitagawa, S. Magnetic properties of nitric oxide molecules physisorbed into nano-sized pores of MCM-41. *Microporous Mesoporous Mater.* **2010**, *132*, 464–469.
- (19) Bordiga, S.; Regli, L.; Bonino, F.; Groppo, E.; Lamberti, C.; Xiao, B.; Wheatley, P.;

- Morris, R.; Zecchina, A. Adsorption properties of HKUST-1 toward hydrogen and other small molecules monitored by IR. *Phys. Chem. Chem. Phys.* **2007**, *9*, 2676–2685.
- (20) Mendt, M.; Pöppel, A. The Line Width of the EPR Signal of Gaseous Nitric Oxide as Determined by Pressure and Temperature-Dependent X-band Continuous Wave Measurements. *Appl. Magn. Reson.* **2015**, *46*, 1249–1263.
- (21) Lee Smith, A.; Johnston, H. L. The Magnetic Susceptibility of Liquid Nitric Oxide and the Heat of Dissociation of (NO)₂. *J. Am. Chem. Soc.* **1952**, *74*, 4696–4698.
- (22) Dinerman, C. E.; Ewing, G. E. Infrared Spectrum, Structure, and Heat of Formation of Gaseous (NO)₂. *J. Chem. Phys.* **1970**, *53*, 626–631.
- (23) Johnston, H. L.; Wejmer, H. R. Low Pressure Data of State of Nitric Oxide and of Nitrous Oxide between their Boiling Points and Room Temperature. *J. Am. Chem. Phys.* **1934**, *56*, 625–630.
- (24) Guggenheim, E. Dimerization of gaseous nitric oxide. *Mol. Phys.* **1966**, *10*, 401–404.
- (25) Park, J. K.; Sun, H. Relative stabilities of (NO)₂. *Chem. Phys.* **2001**, *263*, 61–68.
- (26) Dulmage, W. J.; Meyers, E. A.; Lipscomb, W. N. The Molecular and Crystal Structure of Nitric Oxide Dimer. *J. Chem. Phys.* **1951**, *19*, 1432–1433.
- (27) Bloom, M.; Reeves, L. W.; Wells, E. J. Spin echoes and chemical exchange. *J. Chem. Phys.* **1965**, *42*, 1615–1624.
- (28) Gutowsky, H. S.; Saika, A. Dissociation, chemical exchange, and the proton magnetic resonance in some aqueous electrolytes. *J. Chem. Phys.* **1953**, *21*, 1688–1694.
- (29) Khan, A. H.; Peikert, K.; Fröba, M.; Bertmer, M. NO adsorption in amino-modified Cu₃(btc)₂-type MOFs studied by solid-state NMR. *Microporous Mesoporous Mater.* **2015**, *216*, 111–117.

- (30) Khan, A. H.; Peikert, K.; Hoffmann, F.; Fröba, M.; Bertmer, M. Nitric Oxide Adsorption in Cu₃btc₂-Type MOFs-Physisorption and Chemisorption as NONOates. *J. Phys. Chem. C* **2019**, doi:10.1021/acs.jpcc.8b11919.
- (31) Massiot, D.; Fayon, F.; Capron, M.; King, I.; Calvé, S. L.; Alonso, B.; Durand, J.-O.; Bujoli, B.; Gan, Z.; Hoatson, G. Modelling one- and two-dimensional solid-state NMR spectra. *Magn. Reson. Chem.* **2002**, *40*, 70–76.
- (32) Wu, J.; Larsen, S. C. ¹⁵N solid state NMR study of the reactions of propane or propene, ¹⁵NO and oxygen on Na-, H-, and CuZSM-5. *Catal. Lett.* **2000**, *70*, 43–50.
- (33) Bhattacharyya, P. K.; Dailey, B. P. ¹⁵N magnetic shielding anisotropies in ¹⁵N¹⁵NO. *J. Chem. Phys.* **1973**, *59*, 5820–5823.
- (34) Carravetta, M.; Levitt, M. H. Long-lived nuclear spin states in high-field solution NMR. *J. Am. Chem. Soc.* **2004**, *126*, 6228–6229.
- (35) Abragam, A. *The principles of nuclear magnetism*; Oxford University Press Inc: New York, 1961.
- (36) Cavanagh, J.; Fairbrother, W. J.; Palmer III, A. G.; Skelton, N. J. *Protein NMR spectroscopy: principles and practice*; Elsevier, 1995.
- (37) Zimmerman, J.; Brittin, W. E. Nuclear magnetic resonance studies in multiple phase systems: lifetime of a water molecule in an adsorbing phase on silica gel. *J. Phys. Chem.* **1957**, *61*, 1328–1333.
- (38) Van Vleck, J. *The theory of electric and magnetic susceptibilities*; Oxford Univ. Press, 1934; pp 90–280.
- (39) Van Vleck, J. H. The dipolar broadening of magnetic resonance lines in crystals. *Phys. Rev.* **1948**, *74*, 1168–1183.

- (40) Giauque, W. A thermodynamic treatment of certain magnetic effects. A proposed method of producing temperatures considerably below 1 absolute. *J. Am. Chem. Soc.* **1927**, *49*, 1864–1870.
- (41) Kachi-Terajima, C.; Akatsuka, T.; Kohbara, M.-a.; Takamizawa, S. Magnetic properties of nitric oxide adsorbed within channel crystals. *Polyhedron* **2007**, *26*, 1876–1880.

Supporting Information Available

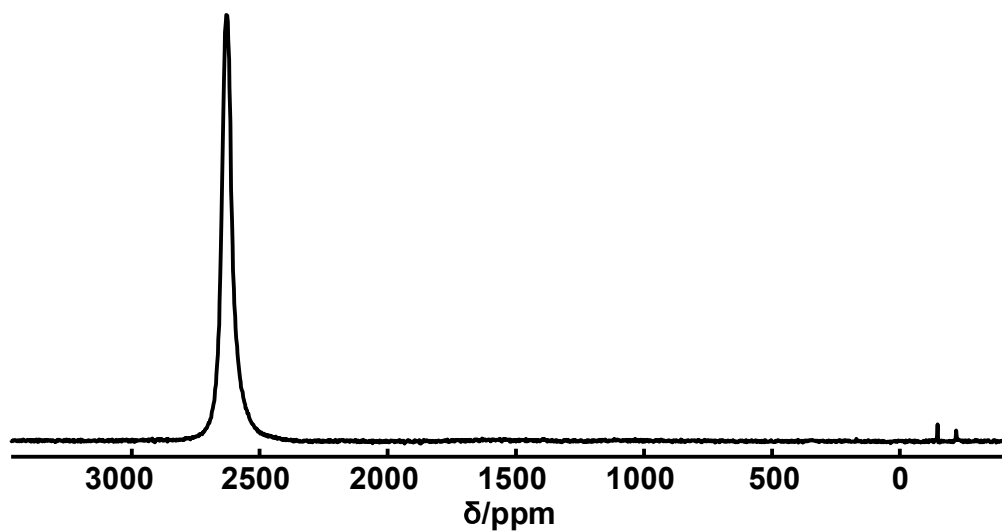


Figure S1: ^{15}N NMR spectrum at 117 K.

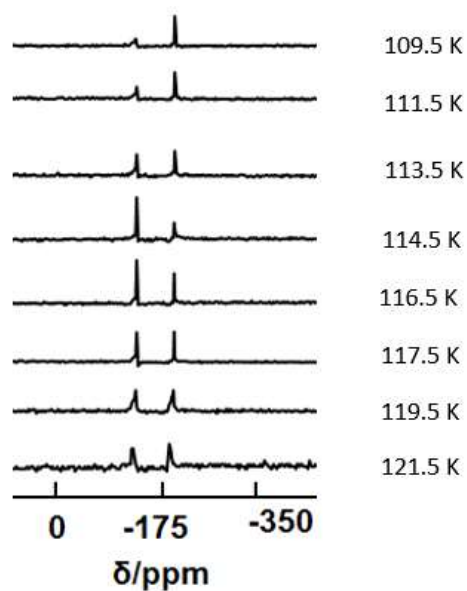


Figure S2: ^{15}N NMR spectra for the $^{15}\text{N}_2\text{O}$ signals at various temperatures. The variation of signal intensities is due to non-optimal excitation conditions for these signals.

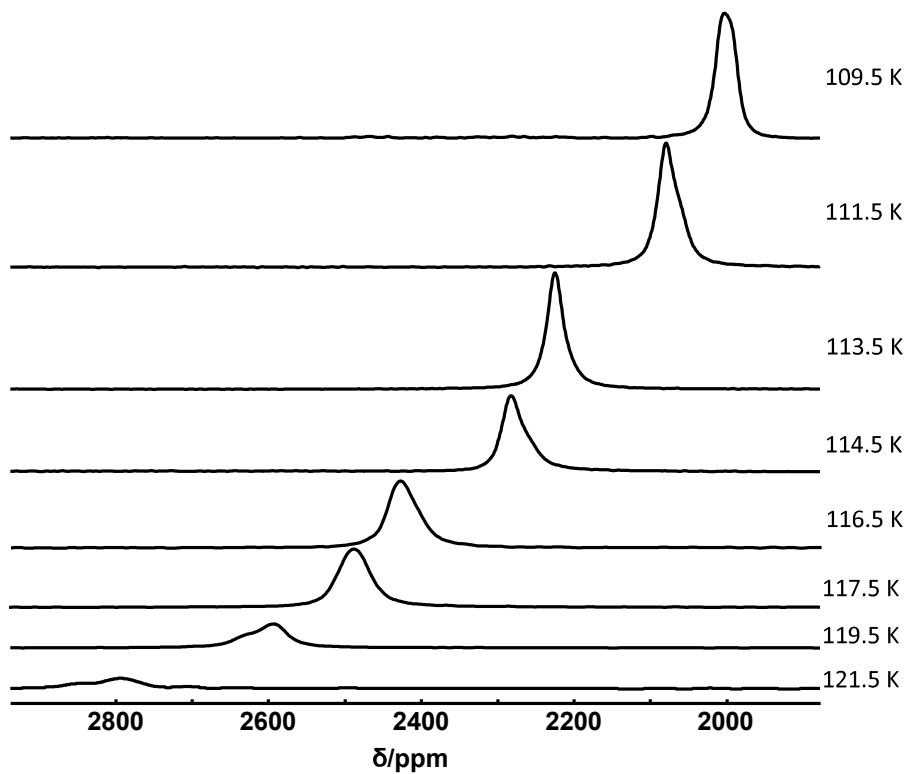


Figure S3: Temperature dependent ^{15}N NMR spectra of NO loaded into the big glass container, acquired with 1 K scans.

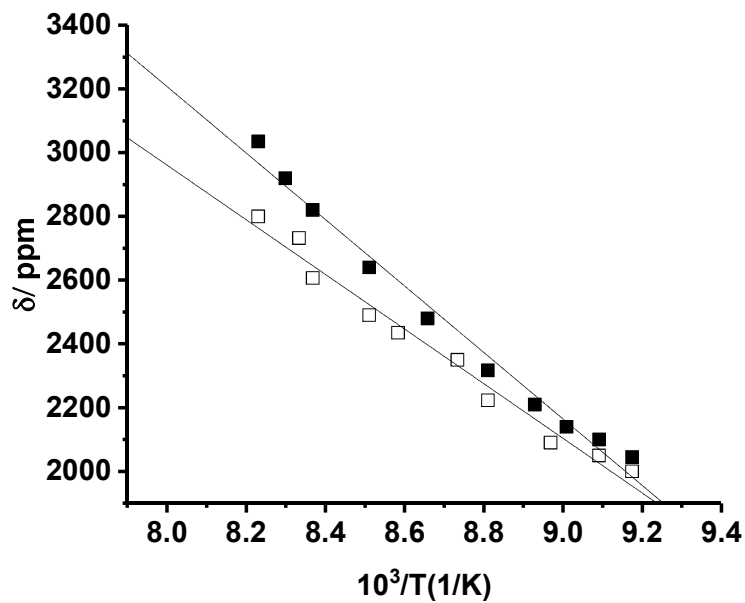


Figure S4: ^{15}N chemical shift as a function of inverse temperature for small (filled squares) and large glass container (open squares). Lines are linear fits of the data.

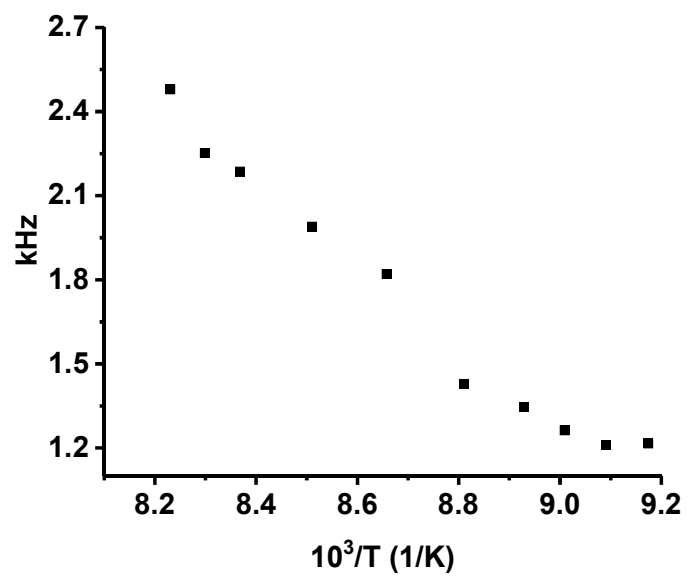


Figure S5: Variation of ^{15}N line width as a function of inverse temperature.

Paper VI: Spectroscopic Study of $[(\text{CH}_3)_2\text{NH}_2][\text{Zn}(\text{HCOO})_3]$ (DMAZn) Hybrid Perovskite Containing Different Nitrogen Isotopes [*J. Phys. Chem. C*, 122(18): 10284-10292, 2018.]

A highly attractive class of perovskite type formate framework, DMAZn has been studied by NMR, due to its structural phase transition at T_c and high temperatures. The ^{15}N isotope effect on the phase-transition properties at high-temperatures ($T > T_c$), due to the motion of the dimethylammonium (DMA^+) cation in ^{15}N leveled DMAZn. This is demonstrated by EPR, NMR, IR and DSC measurements by the work with Šimėnas *et.al.* We contributed ^{15}N NMR relaxation studies of DMAZn in paper VI. ^{15}N NMR measurements are carried out for the direct probing of the motion of DMA^+ in DMAZn. Variable temperature dependent $^{15}\text{N}T_1$ measurements corroborate the hopping motion of DMA^+ . The activation energy is calculated from the relaxation measurements via Arrhenius equation, which is in good agreement with the EPR analysis.

Spectroscopic Study of $[(\text{CH}_3)_2\text{NH}_2][\text{Zn}(\text{HCOO})_3]$ Hybrid Perovskite Containing Different Nitrogen Isotopes

Mantas Šimėnas,^{*,†,‡} Maciej Ptak,[‡] Arafat Hossain Khan,[§] Laurynas Dagys,[†] Vytautas Balevičius,^{†,§} Marko Bertmer,[§] Georg Völkel,[§] Mirosław Mączka,^{‡,§} Andreas Pöpl,[§] and Jūras Banys[†]

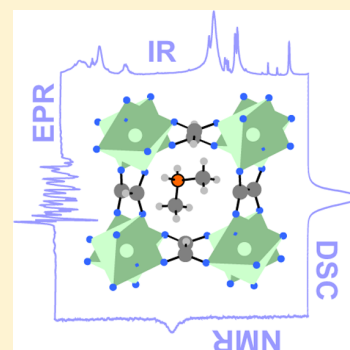
[†]Faculty of Physics, Vilnius University, Sauletekio Avenue 9, LT-10222 Vilnius, Lithuania

[‡]Institute of Low Temperature and Structure Research, Polish Academy of Sciences, P.O. Box 1410, PL-50-950 Wrocław 2, Poland

[§]Felix Bloch Institute for Solid State Physics, Leipzig University, Linnéstrasse 5, D-04103 Leipzig, Germany

Supporting Information

ABSTRACT: We present a combined differential scanning calorimetry (DSC) and infrared (IR), Raman, electron paramagnetic resonance (EPR), and NMR spectroscopy study of dimethylammonium zinc formate frameworks $[(\text{CH}_3)_2\text{NH}_2][\text{Zn}(\text{HCOO})_3]$ containing ^{14}N and ^{15}N nitrogen isotopes. The DSC reveals very small differences in the phase-transition temperatures for both compounds. The IR and Raman spectroscopies indicate different frequencies of the vibrational modes that involve a nitrogen atom. The temperature-dependent IR and Raman spectra also show a tiny isotope effect on the properties and temperature of the phase transition. The EPR measurements are performed for both compounds doped with small amount of paramagnetic Mn^{2+} ions. The obtained continuous-wave Mn^{2+} EPR spectra of the disordered phase are very similar for both frameworks, whereas the temperature dependence of the zero-field splitting parameter indicates a slightly different distortion of the MnO_6 octahedra in the low-temperature phase. The EPR line width analysis reveals that the activation energy of the $(\text{CH}_3)_2\text{NH}_2^+$ cation hopping in the disordered phase is 0.21 eV for both compounds. The ^{15}N NMR spectroscopy measurements of the framework containing the ^{15}N isotope are used to directly probe this motion. The obtained temperature dependence of the spin–lattice relaxation time is approximated using the same value of the activation energy as determined from the EPR spectroscopy. The negligible nitrogen isotope effect indicates an order–disorder nature of the phase transitions in the investigated compounds.



INTRODUCTION

Dimethylammonium metal formate frameworks $[(\text{CH}_3)_2\text{NH}_2][\text{M}(\text{HCOO})_3]$ (DMAM, where $\text{M} = \text{Mn}, \text{Fe}, \text{Co}, \text{Ni}, \text{Cu}, \text{Zn}$, or Mg) attract significant scientific attention due to the indications of the ferroelectric and multiferroic behavior.^{1–4} X-ray diffraction (XRD)-based methods revealed that these compounds consist of metal centers that are connected by HCOO^- (formate) linkers into frameworks with cuboid cavities.⁵ Each such cavity hosts a single $(\text{CH}_3)_2\text{NH}_2^+$ (dimethylammonium, DMA^+) cation, which forms H-bonds with the formate anions. The structure of these materials has a well-known AMX_3 perovskite topology, where A and X correspond to $(\text{CH}_3)_2\text{NH}_2^+$ and HCOO^- ions, respectively.²

These compounds exhibit a structural phase transition, which involves a cooperative ordering of the DMA^+ cations. Depending on a metal center, the phase-transition temperature is $T_0 = 160\text{--}180\text{ K}$,² with exception for the Mg compound ($T_0 = 270\text{ K}$).⁶ Above this temperature, the DMA^+ cations are dynamically disordered since nitrogen atoms easily hop between three energetically favorable positions, as depicted in Figure 1. The space group of the disordered (high temperature, $T > T_0$) phase is trigonal $R\bar{3}c$.⁵ In the low-temperature phase ($T < T_0$), the DMA^+ cations arrange in such a way that the long-

range order is established (Figure 1). The low-temperature structure reported for the DMAMn compound has a monoclinic noncentrosymmetric Cc space group, which permits a ferroelectric behavior.⁵ In addition, compounds containing paramagnetic transition-metal ions exhibit a long-range spin order below 40 K, making these materials potential single-phase multiferroics.^{2,7–11}

The type and mechanism of the structural phase transition in these hybrid materials were studied using various experimental techniques, such as XRD;^{1,2,5} differential scanning calorimetry (DSC);¹² specific heat,^{1,2} pyrocurrent,^{9,13} and electric polarization measurements;¹⁴ second-harmonic generation;³ and NMR,^{15–19} electron paramagnetic resonance (EPR),^{20–23} infrared (IR), Raman,^{8,24,25} and dielectric spectroscopies.^{14,26} Most of these studies revealed a strong first-order phase transition. An electric polarization hysteresis loop (evidence of the ferroelectric behavior) was only observed for the deuterated DMACo compound.¹⁴ Our recent single-crystal EPR study with simultaneously applied external electric field raised serious

Received: March 21, 2018

Revised: April 22, 2018

Published: April 23, 2018

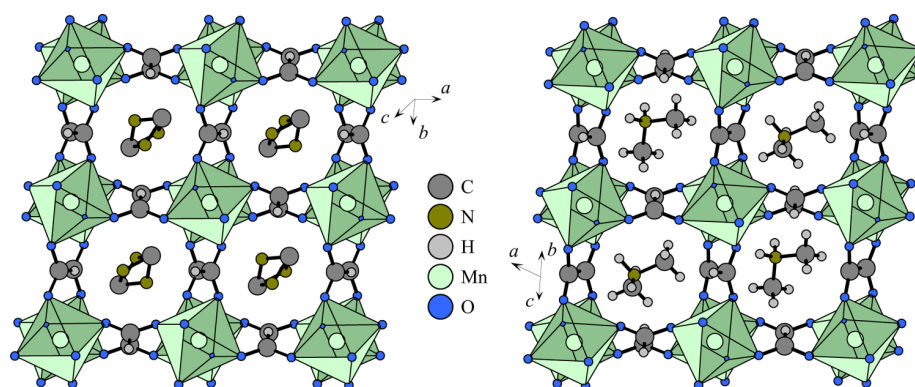


Figure 1. Crystal structure of the DMAMn framework at $T > T_0$ (left) and $T < T_0$ (right).⁵ The hydrogen atoms of the DMA⁺ cations are not shown in the high-temperature phase, while the nitrogen atoms can hop between the three indicated positions.

doubts about the ferroelectric origin of the DMAZn compound.²²

The presence of the polarization hysteresis loop in the deuterated DMACo is not the only manifestation of the isotope effect in these materials. The DMANi perovskite demonstrates a decrease of the phase-transition temperature by about 6 K upon deuteration,⁸ and the deuterated DMACo compound also exhibits an additional phase transition at about 319 K.¹⁴ These observations indicate that the isotope substitution may significantly alter the properties of DMAM frameworks, stimulating further attention to this topic.

The isotope effect can also provide important information about the properties of the structural phase transitions. For example, a substantial increase of the phase-transition temperature upon deuteration is frequently observed in classical H-bonded ferroelectrics, such as KH_2PO_4 .^{27,27} In contrast, the transitions occur at lower temperature as heavier isotopes are introduced in many displacive dielectric crystals like ferroelectric BaTiO_3 (transition temperature shifts by 21 K upon ^{46}Ti substitution by ^{50}Ti)²⁸ or antiferroelectric PbZrO_3 .²⁹ The pure order–disorder-type compounds, such as NaNO_2 , $(\text{NH}_4)_2\text{SO}_4$, or NH_4LiSO_4 , usually show a negligible isotope effect as ^{14}N is replaced by ^{15}N .^{29,30}

In this work, we investigate the nitrogen isotope effect on the phase-transition properties and motion of the DMA⁺ cations in DMAZn framework. The choice of nitrogen is motivated by its close relation to the ordering mechanism of the system. We use DSC and IR, Raman, as well as EPR spectroscopy techniques to investigate DMAZn samples prepared using ^{14}N and ^{15}N isotopes. The synthesis of the latter compound is reported for the first time. We observe a very small isotope effect, indicating an order–disorder nature of the DMAZn framework. In addition to the isotope effect, we also present the analysis of the temperature-dependent continuous-wave (CW) EPR line width, which was absent in our previous studies.^{21,22} The DMAZn framework containing ^{15}N isotope is for the first time investigated by ^{15}N NMR spectroscopy.

EXPERIMENTAL METHODS

Sample Preparation. $\text{Zn}(\text{ClO}_4)_2 \cdot 6\text{H}_2\text{O}$ (99%, Sigma-Aldrich), $\text{Mn}(\text{ClO}_4)_2 \cdot 6\text{H}_2\text{O}$ (99%, Sigma-Aldrich), a 2.0 M solution of $(\text{CH}_3)_2\text{NH}$ in methanol (Sigma-Aldrich), methanol (99.8%, Sigma-Aldrich), formic acid (98%, Fluka), and *N,N*-dimethylformamide (DMF, 99.8%, Sigma-Aldrich) were commercially available and used without further purification.

$[(\text{CH}_3)_2\text{NH}_2][\text{Zn}(\text{HCOO})_3] \cdot 0.1 \text{ Mn}^{2+} \text{ mol } \%$ (DMAZn- ^{14}N) was synthesized by a slow evaporation method. In a typical experiment, 2 mL of 2.0 M solution of $(\text{CH}_3)_2\text{NH}$ in methanol, 1 mL of formic acid, and 10 mL of DMF were added to 10 mL of methanol. After mixing these chemicals, 10 mL of methanol solution containing 0.999 mmol of $\text{Zn}(\text{ClO}_4)_2 \cdot 6\text{H}_2\text{O}$ and 0.001 mmol of $\text{Mn}(\text{ClO}_4)_2 \cdot 6\text{H}_2\text{O}$ was added, mixed, and left at room temperature in a glass beaker. The crystals grown at the bottom of the beaker were harvested after 5 days, washed three times with methanol, and dried at room temperature.

ZnCl_2 (99%, Fluka), MnCl_2 (99%, Sigma-Aldrich), methanol (99.8%, Sigma-Aldrich), formic acid (98%, Fluka), dimethylamine-15N hydrochloride (Sigma-Aldrich), and HCOONa (99%, Sigma-Aldrich) were commercially available and used without further purification. To obtain $[(\text{CH}_3)_{215}\text{NH}_2][\text{Zn}(\text{HCOO})_3] \cdot 0.1 \text{ Mn}^{2+} \text{ mol } \%$ (DMAZn- ^{15}N), 2 mmol of dimethylamine-15N hydrochloride (Sigma-Aldrich, 98 atom % ^{15}N) was dissolved in 5 mL of methanol and this solution was added to a methanol solution containing 2 mmol of HCOONa . The mixture was stirred for about 20 min, and then, a white precipitate was filtered. To the obtained clear and transparent solution, 0.2 mL of formic acid and 10 mL of methanol solution containing 0.999 mmol of ZnCl_2 and 0.001 mmol of MnCl_2 were added, mixed, and left at room temperature in a glass beaker. The precipitated white crystallites were harvested after 3 days, washed three times with methanol, and dried at room temperature.

Doping of the samples with small amount of paramagnetic Mn^{2+} ions was necessary for the EPR experiments.

DSC Measurements. DSC was measured using a Mettler Toledo DSC-1 calorimeter with a resolution of 0.4 μW . Nitrogen was used as a purging gas, and the heating and cooling rate was 5 K/min. The sample weights were 41.3 and 23.5 mg for DMAZn- ^{14}N and DMAZn- ^{15}N , respectively.

IR and Raman Spectroscopy. Room-temperature Raman spectra of DMAZn- ^{14}N and DMAZn- ^{15}N were measured using a Bruker FT 100/S spectrometer with YAG:Nd laser excitation (1064 nm). Temperature-dependent IR spectra were measured using a Nicolet iN10 stand-alone Infrared Microscope and a THMS600 Linkam cryostat cell equipped with ZnSe windows. The spectral resolution of Raman and IR spectra was 2 cm^{-1} .

EPR Spectroscopy. Continuous-wave (CW) EPR measurements were performed at X-band microwave frequency (~ 9.4 GHz) using a conventional Bruker ELEXSYS E580 EPR spectrometer. Most of the measurements were performed at 4 mW microwave power. The strength and frequency of the

modulating field were set to 6 G and 100 kHz, respectively. The sample temperature was determined using a T-type thermocouple placed next to the sample in the EPR tube. During the measurements, the temperature control was ± 0.1 K. Simulations of the CW EPR spectra were performed using EasySpin 5.1.9 software.³¹

NMR Spectroscopy. Spin–lattice relaxation time (T_1) measurements of ^{15}N isotope in **DMAZn- ^{15}N** were done at a magnetic field strength of 11.7 T using a Bruker Avance III HD spectrometer at a frequency of 50.676 MHz. A home-built static probe was used with a $\pi/2$ pulse length of 13.7 μs . The saturation recovery technique was used to measure T_1 . Temperature was controlled by an Oxford cryostat with a Lakeshore temperature controller with an accuracy of ± 1 K.

The ^{15}N NMR spectra of **DMAZn- ^{15}N** were measured at 9.4 T with a Bruker Avance III HD spectrometer with a 4 mm double-resonance magic-angle spinning (MAS) probe at a frequency of 41 MHz. The magic-angle spinning frequency was 2 kHz due to the reduced-size sample in the original 4 mm zircon rotor. Spectrum of the ^{15}N was obtained using CPMAS technique with a 3 ms ramped contact pulse at radio frequency field of 90 kHz. Recycle delay was set to 4 s for the full proton relaxation. A total of 128 scans were accumulated to ensure a fair signal-to-noise ratio.

RESULTS AND DISCUSSION

DSC. First, we used the DSC to investigate the influence of nitrogen isotopes on the phase-transition temperature (T_0) of **DMAZn- ^{14}N** and **DMAZn- ^{15}N** compounds. The obtained DSC curves are presented in Figure 2 revealing clear anomalies

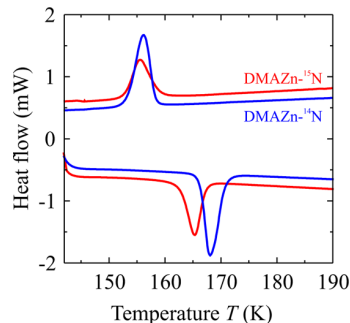


Figure 2. DSC curves on cooling (top) and heating (bottom) for **DMAZn- ^{14}N** (blue) and **DMAZn- ^{15}N** (red).

at the transition points. The temperatures of the heat flow maxima are 156.1 K (on cooling) and 168.0 K (on heating) for the compound with ^{14}N isotope. The corresponding temperatures of the framework containing ^{15}N are 155.5 and 165.3 K. The obtained data indicate that a substitution of the nitrogen isotope has a tiny effect on the phase-transition temperature, although the temperature hysteresis of **DMAZn- ^{15}N** seems to be narrower. This may indicate that the ordered phase is slightly more stable in **DMAZn- ^{14}N** .

IR and Raman Spectroscopy. The influence of different nitrogen isotopes on the vibrational modes of **DMAZn** is investigated using IR and Raman spectroscopy techniques. The observed modes can be subdivided into internal vibrations of the DMA^+ and formate ions (above 300 cm^{-1}) and lattice vibrations (below 300 cm^{-1}). As discussed in our previous studies,^{8,24,25} internal vibrations of the HCOO^- ion consist of C–H stretching (ν_1), symmetric C–O stretching (ν_2),

antisymmetric C–O stretching (ν_4), symmetric O–C–O bending (scissor, ν_3), C–H in-plane bending (ν_5), and C–H out-of-plane bending (ν_6) modes. Internal modes of the DMA^+ cation correspond to symmetric stretching ($\nu_s(\text{NH}_2)$), antisymmetric stretching ($\nu_{as}(\text{NH}_2)$), scissoring ($\delta(\text{NH}_2)$), rocking ($\rho(\text{NH}_2)$), wagging ($\omega(\text{NH}_2)$), and torsion or twisting ($\tau(\text{NH}_2)$) modes of the NH_2 group; symmetric stretching ($\nu_s(\text{CNC})$), antisymmetric stretching ($\nu_{as}(\text{CNC})$), and bending ($\delta(\text{CNC})$) modes of the CNC group; and stretching (ν), bending (δ), rocking (ρ), and torsion (τ) modes of the methyl groups.^{8,24,25} The lattice modes are vibrational modes of the formate and DMA^+ ions as well as translational modes of the HCOO^- , DMA^+ , and metal ions.

The room-temperature Raman and temperature-dependent IR spectra of **DMAZn- ^{14}N** and **DMAZn- ^{15}N** are presented in Figures 3 and S1 (Supporting Information). The observed IR and Raman frequencies (in cm^{-1}) are listed in Table S1. Since assignment of the modes for **DMAZn** containing ^{14}N was already reported, we recall it in Table S1 and focus here only on the differences between the two samples. In the Raman spectra, a clear shift toward lower wavenumbers when lighter ^{14}N is replaced by heavier ^{15}N is observed for the 1094, 1029, 898, and 412 cm^{-1} bands. A significant change of the three lower-wavenumber bands is consistent with their assignment to vibrations of the CNC groups ($\nu_{as}(\text{CNC})$, $\nu_s(\text{CNC})$, and $\delta(\text{CNC})$ modes). The 1094 cm^{-1} band was previously assigned to the $\rho(\text{CH}_3)$ mode.^{8,24} The present data show a significant isotopic effect for this band, and thus, it should be attributed to the coupled mode involving both $\rho(\text{CH}_3)$ and $\nu_{as}(\text{CNC})$ vibrations. IR spectra also reveal a shift of the 1092, 1028, and 898 cm^{-1} bands when ^{14}N is replaced by ^{15}N (Figure 3). A change by 8 cm^{-1} is also observed for the 1256 cm^{-1} band, indicating contribution of the nitrogen atom vibration to this mode.

The temperature-dependent IR spectra of both compounds show significant narrowing of many bands, especially those related to the NH_2^+ groups, and splitting of some bands in the low-temperature phase (see Figures 3 and S1). As discussed in our previous studies,^{8,24} this type of behavior indicates that the phase transition is associated with the ordering of the DMA^+ cations. This ordering is also related to a weak distortion of the zinc formate framework. To better visualize the observed changes at T_0 , we present plots of wavenumbers and full width at half-maximum (FWHM) for several selected modes (see Figure 4). The observed discontinuous jumps at T_0 are comparable for both frameworks. The changes of the FWHM of the corresponding modes are also very similar for both samples. In particular, the temperature dependence of FWHM for the $\rho(\text{NH}_2)$ mode is practically the same for both compounds. All of these observations show that the replacement of ^{14}N by ^{15}N has a weak effect on the phase-transition mechanism in **DMAZn**.

EPR Spectroscopy. We further employ CW EPR spectroscopy to investigate the local changes of the Mn^{2+} -ion environment in the manganese-doped **DMAZn- ^{14}N** and **DMAZn- ^{15}N** . The X-band EPR spectra recorded at 183 K are presented in Figure 5 revealing typical powder patterns of the Mn^{2+} ions in the $3d^5$ electronic configuration ($^6\text{S}_{5/2}$ electronic ground state). The total electron spin of this state is $S = 5/2$, which results in five fine-structure (fs) $\Delta m_s = \pm 1$ transitions, where m_s is the magnetic electron spin quantum number.³² In case of a nonzero zero-field splitting (zfs), the resonance fields of the fs transitions are different. The

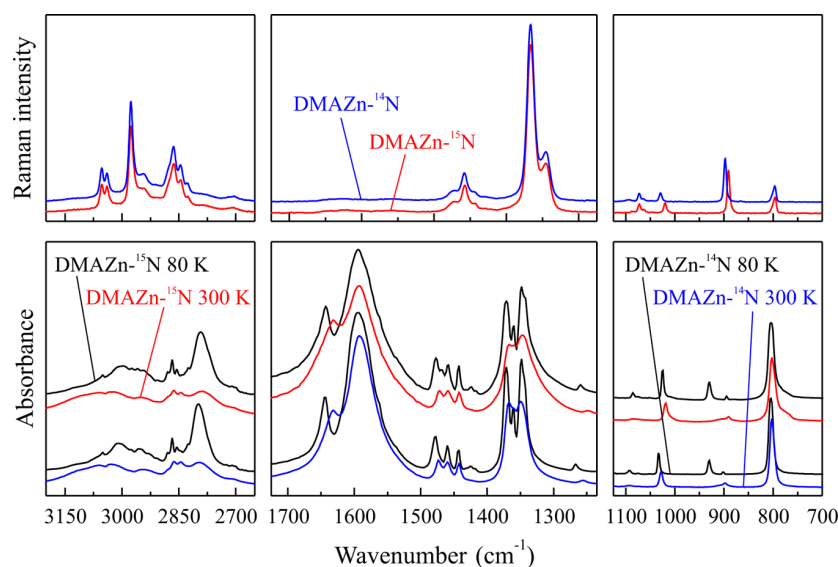


Figure 3. Raman spectra at 300 K (top panels) and IR spectra at 300 and 80 K (bottom panels) of DMAZn-¹⁴N and DMAZn-¹⁵N.

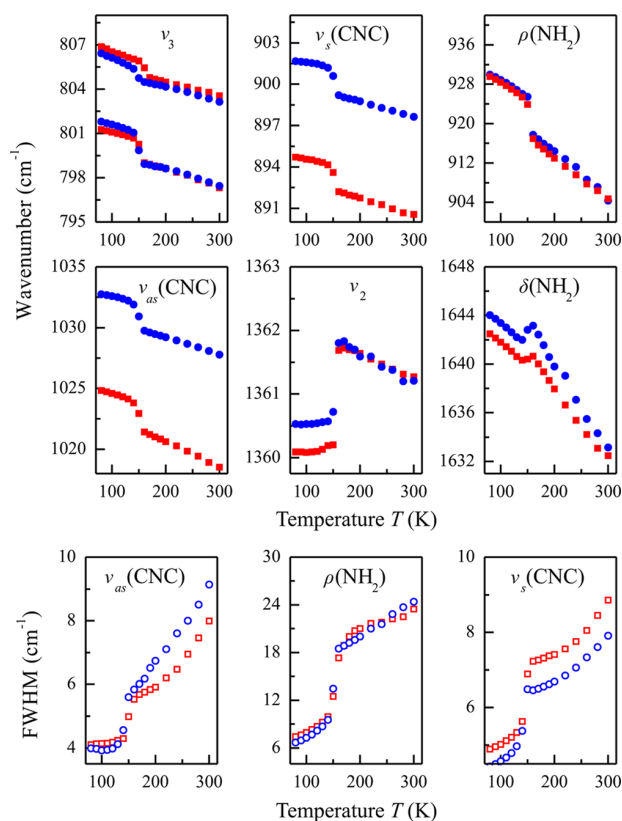


Figure 4. Temperature dependence of selected IR wavenumbers and FWHM of DMAZn-¹⁴N (blue circles) and DMAZn-¹⁵N (red squares).

interaction between the unpaired electrons and the nuclear spin (for ⁵⁵Mn, it is $I = 5/2$) causes further splitting of each fs transition into six hyperfine (hf) lines ($\Delta m_S = \pm 1$ and $\Delta m_I = 0$). The hf lines of the central fs transition ($m_S = -1/2 \leftrightarrow 1/2$) dominate the recorded spectra, whereas the outer transitions ($m_S = \pm 3/2 \leftrightarrow \pm 1/2$ and $\pm 5/2 \leftrightarrow \pm 3/2$) are unresolved. The spectra of DMAZn-¹⁴N and DMAZn-¹⁵N are almost identical, indicating that the fs and hf interactions are very similar in the

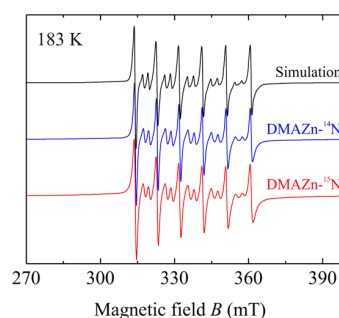


Figure 5. X-band CW EPR spectra of DMAZn-¹⁴N (blue) and DMAZn-¹⁵N (red) recorded at 183 K. The simulated spectrum is presented in black.

disordered phases of both compounds. In addition, both spectra are in agreement with the previously obtained spectrum of DMAZn: 0.05 Mn²⁺ mol % framework.^{21,22}

We used the same spin Hamiltonian as in our previous studies to simulate the recorded spectra^{21,22}

$$\mathcal{H} = \beta_e g \mathbf{B} \cdot \mathbf{S} + A_{\text{iso}} \mathbf{S} \cdot \mathbf{I} + \mathcal{H}_{\text{fs}} \quad (1)$$

where the first and second terms describe the electron Zeeman and hf interactions, respectively; g and A_{iso} denote the g -factor and the isotropic hf coupling constant of the Mn²⁺ center, respectively; β_e is the Bohr magneton; and \mathbf{B} is the external magnetic field. The fs of the spectrum is described by the last term, which is expressed using the extended Stevens operators $\hat{O}_k^q(\mathbf{S})$ ($k = 2, 4, 6$ and $q = +k, \dots, -k$)

$$\mathcal{H}_{\text{fs}} = \sum_k \sum_q B_k^q \hat{O}_k^q(\mathbf{S}) \quad (2)$$

The real coefficients B_k^q characterize the magnitude of the associated zfs. The analytical expressions for the Stevens operators can be found in ref 33. The ordinary axial and orthorhombic zfs parameters can be expressed as $D = 3B_2^0$ and $E = B_2^2$.

The simulation of the DMAZn-¹⁴N spectrum recorded at 183 K was performed with $g = 2.0013(1)$, $A_{\text{iso}} = -264(1)$ MHz,

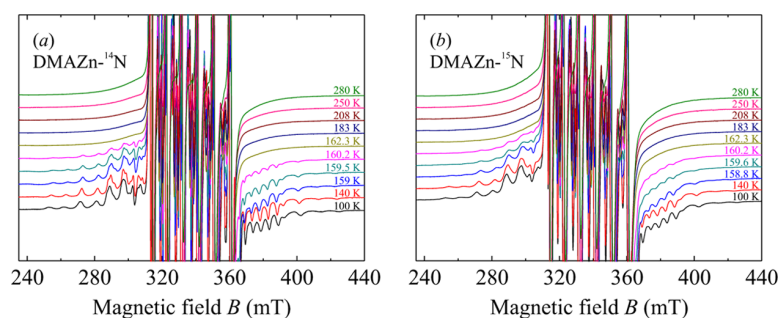


Figure 6. Temperature-dependent X-band CW EPR spectra of the Mn^{2+} ions in (a) $\text{DMAZn-}^{14}\text{N}$ and (b) $\text{DMAZn-}^{15}\text{N}$. Emphasis is on the outer fs transitions.

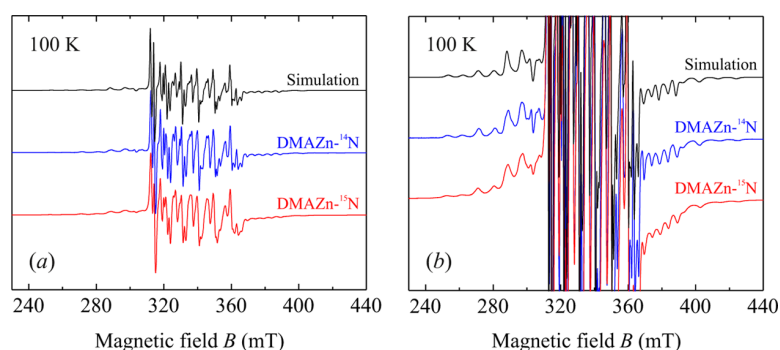


Figure 7. X-band CW EPR spectra of the Mn^{2+} ions in $\text{DMAZn-}^{14}\text{N}$ (blue) and $\text{DMAZn-}^{15}\text{N}$ (red) measured at 100 K. Emphasis is on the (a) central and (b) outer fs transitions. The simulated spectrum of $\text{DMAZn-}^{14}\text{N}$ is presented in black.

$D = 230(20)$ MHz, and $E \approx 0$. To account for the unresolved outer fs transitions, we used distribution $\Delta D = 300(50)$ MHz of the axial zfs parameter. The same set of parameters is used to describe the spectrum of $\text{DMAZn-}^{15}\text{N}$. This indicates that the MnO_6 octahedra are similarly distorted in the disordered phase of both compounds. We note that the spectrum of $\text{DMAZn: } 0.05 \text{ Mn}^{2+} \text{ mol } \%$ was simulated using somewhat smaller distribution of the D parameter.²¹

The temperature-dependent EPR spectra of $\text{DMAZn-}^{14}\text{N}$ and $\text{DMAZn-}^{15}\text{N}$ are presented in Figures 6 and S2. At the phase-transition points, the distribution widths of the zfs parameters become significantly smaller and thus the outer fs transitions are well resolved in the ordered phases. The transition points obtained by EPR in both compounds are $T_0 = 160.2(1)$ K. As described in our previous study, the high value of ΔD above T_0 originates from the differently distorted MnO_6 octahedra due to the hopping motion of the DMA^+ cations.²¹ The cations slow down and order at T_0 , causing uniform distortion of all octahedra (small distribution of D).

We simulated the spectrum of $\text{DMAZn-}^{14}\text{N}$ recorded at 100 K using the following spin Hamiltonian parameters: $g = 2.0013(1)$, $A_{\text{iso}} = -264(1)$ MHz, $D = 419$ MHz, $E = 58$ MHz, $B_2^{-2} = 25(1)$ MHz, $B_4^2 = 0.30(3)$ MHz, $B_4^0 = 0.27(3)$ MHz, and $B_4^4 = 0.83(4)$ MHz. The distributions of the axial and orthorhombic zfs parameters are $\Delta D = 25(3)$ MHz and $\Delta E = 17(3)$ MHz. The simulation is presented in Figure 7 together with the experimental spectra. The simulation is also in agreement with the spectrum of $\text{DMAZn-}^{15}\text{N}$, although it has a slightly larger width indicating higher value of D . A very similar set of spin Hamiltonian parameters was also used to simulate the low-temperature spectrum of $\text{DMAZn: } 0.05 \text{ Mn}^{2+} \text{ mol } \%$.^{21,22}

The temperature dependence of the axial zfs parameter D is presented in Figure 8 for both samples. The sudden jumps of D

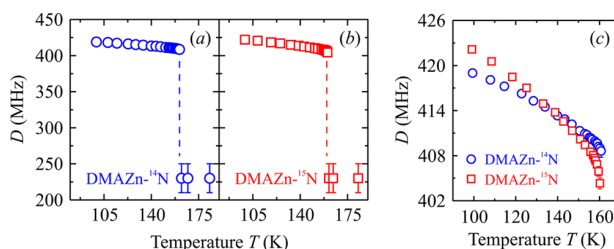


Figure 8. Temperature dependence of the axial zfs parameter D of the Mn^{2+} ions in (a) $\text{DMAZn-}^{14}\text{N}$ and (b) $\text{DMAZn-}^{15}\text{N}$. The dependence below T_0 is presented in (c).

are observed at phase-transition points indicating strong first-order phase transitions, which is in agreement with the majority of other studies.^{8,12,14,21} The observed temperature dependences resemble a behavior typical for a phase-transition order parameter η (see Figure 8c).³⁴ The dependences are slightly different for both samples, as a higher value of D is observed in $\text{DMAZn-}^{15}\text{N}$ below 130 K. This indicates that the distortions of the MnO_6 octahedra are more severe at low temperatures in this compound. This difference may originate from slightly different motion of the DMA^+ cations, as they form H-bonds with the metal–oxygen octahedra. However, we cannot completely rule out the possibility that the internal lattice strains (framework deformation) are different in both compounds due to possibly different Mn^{2+} doping level. The overall increase of D with decreasing temperature reveals a

further gradual deformation of the frameworks in the ordered phases.

We did not observe a splitting into two fs branches due to the positive and negative values of the order parameter η , and therefore, we assume that the axial zfs parameter is proportional to the square of the order parameter: $D = D_0 + C\eta^2$. Here, D_0 denotes the value of D just above T_0 .

The Landau theory provides the following temperature dependence of η^2 for a first-order phase transition³⁴

$$\eta^2 = -\frac{\beta}{2\gamma} \left[1 \pm \left(1 - \frac{4\alpha(T - T_c)\gamma}{\beta^2} \right)^{1/2} \right] \quad (3)$$

where $\beta < 0$ and $\alpha, \gamma > 0$ are constants. T_c determines the low-temperature limit at which the disordered phase can still exist. The maximum temperature hysteresis is $\beta^2/4\alpha\gamma$. We tried to fit the experimentally determined temperature dependence of D of DMAZn-¹⁴N using eq 3 and the fit provided $\beta^2/4\alpha\gamma = 200(20)$ K. This value is higher than the phase-transition temperature itself, indicating that the simple Landau model is not suitable to describe the ordering in DMAZn. There could be several reasons for this discrepancy. First of all, eq 3 characterizes the first-order phase transitions close to the second-order ones,³⁴ whereas DMAZn exhibits a strong first-order phase transition. Second, there is experimental evidence that the disorder of the DMA⁺ cations persists below T_0 , suggesting a more complex ordering mechanism, which is not accounted in this model.^{2,15} Finally, eq 3 provides two solutions of the order parameter that are equal in magnitude, but opposite in direction, whereas the order parameter in DMAZn system is expected to have a three-fold character. We note that in our previous study of DMAZn: 0.05 Mn²⁺ mol % we performed only a preliminary power-law fit of the temperature-dependent D parameter that led to an incomplete conclusion about the validity of the Landau model to describe this phase transition.²¹

The temperature dependence of the peak-to-peak EPR line width Γ_{pp} of the $m_I = 5/2$ hf line of the central fs transition is presented in Figure 9a for DMAZn-¹⁴N and DMAZn-¹⁵N. The lines of compound containing ¹⁵N isotope are broader by about 0.2 mT in the whole investigated temperature range. This may indicate a slightly higher amount of the incorporated Mn²⁺ ions because of the different synthesis procedures. The line width significantly narrows as the temperature is decreased in the

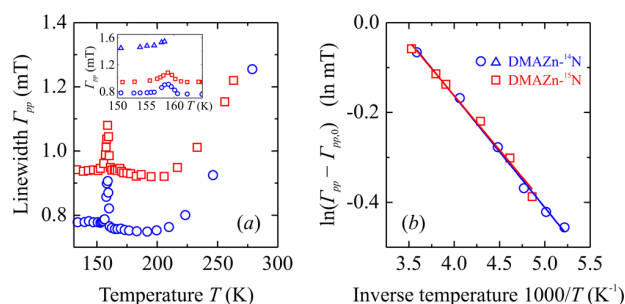


Figure 9. (a) Temperature dependence of the peak-to-peak CW EPR line width of Mn²⁺ centers in DMAZn-¹⁴N (blue) and DMAZn-¹⁵N (red). (b) Arrhenius-type analysis of the temperature-dependent Γ_{pp} in the disordered phase. The inset in (a) presents Γ_{pp} about the phase-transition point. The blue triangles mark the EPR line width of the hf line of the outer fs transition.

disordered phase, whereas a sharp anomaly of Γ_{pp} is observed at the phase transitions.

There could be two possible reasons for the observed maximum of Γ_{pp} . First, it could be related to the sudden change of the axial zfs parameter at T_0 , which causes the broadening of the hf lines of the central fs transition. On the other hand, such an anomalous behavior is frequently observed in many other ferroelectric and related materials, e.g., triglycine sulfate,³⁵ trissarcosine calcium chloride,^{36,37} SrTiO₃,³⁸ and others.³⁹ It is attributed to the critical slowing down of the order parameter fluctuations. To check which scenario is more feasible, we determined the line width of the outer fs transitions that should be much less affected by the change of the spin Hamiltonian parameters. However, the outer fs transitions are not resolved in the disordered phase and thus we were able to accurately obtain the line width only below T_0 (see inset in Figure 9a). A sudden decrease of Γ_{pp} with decreasing temperature below T_0 is also observed for the outer fs transitions, suggesting that the anomaly is related to the order parameter fluctuations. We note that we also observed a maximum of Γ_{pp} at the transition point in the manganese-doped [NH₃(CH₂)₄NH₃][Zn(HCOO)₃]₂ formate framework.⁴⁰ In addition, using pulse EPR spectroscopy, we measured an anomalous increase of the Mn²⁺-ion phase memory relaxation rate in DMAZn.²³

The decrease of Γ_{pp} with lowering of temperature in the disordered phase may originate from the gradual slowing down of the DMA⁺ cation motion. As indicated in Figure 9b, it can be well described by the Arrhenius law: $\Gamma_{pp} - \Gamma_{pp,0} = \Gamma_{pp,\infty} e^{-E_a/kT}$, where E_a is the activation energy of the motion, $\Gamma_{pp,\infty}$ is the EPR line width in the high-temperature limit, $\Gamma_{pp,0}$ is the residue line width unrelated to the motion, and k is the Boltzmann constant. The best fits provide $E_a = 0.21(2)$ eV for both compounds. The determined activation energies are close to the value obtained by NMR (0.24 eV) and dielectric spectroscopy (0.28 eV) for the hopping motion of the DMA⁺ cations in DMAZn,¹⁶ DMAMg,¹⁷ and DMACo.²⁶ Thus, we assign the observed temperature dependence of Γ_{pp} in the disordered phase to the deformation of the MnO₆ octahedra caused by this motional process. A negligible difference of the activation energies between the ¹⁴N and ¹⁵N compounds suggests that the motion of the DMA⁺ cations is very similar to that in the disordered phase. We note that the analysis of the temperature-dependent EPR line width was absent in our first study of DMAZn: 0.05 Mn²⁺ mol %.²¹

¹⁵N NMR Spectroscopy of DMAZn-¹⁵N. We also performed the ¹⁵N (nuclear spin $I = 1/2$) NMR measurements of the DMAZn-¹⁵N sample to directly probe the nitrogen motion. The obtained NMR spectrum and temperature-dependent spin–lattice relaxation time T_1 are presented in Figure 10. The spectrum consists of a single line. The temperature dependence of T_1 exhibits a maximum at 184 K and a minimum at 300 K. A minimum of the spin–lattice relaxation time can be usually related to a motional process.⁴¹ Asaji et al. detected two minima in the ¹H proton relaxation time of DMAZn framework, which were assigned to the hopping motion of the whole DMA⁺ cation and methyl group rotation.^{16,17}

We analyzed the observed temperature dependence of T_1 using the following equation (see Supporting Information and refs 42–44 for more details)

$$T_1^{-1} = \frac{C\tau}{1 + \omega_N^2\tau^2} \quad (4)$$

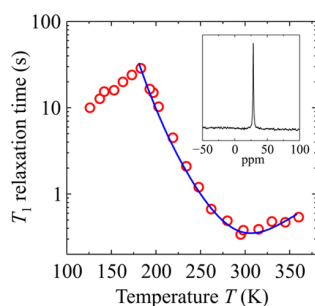


Figure 10. Temperature dependence of the spin–lattice relaxation time of ^{15}N in DMAZn- ^{15}N . The spectrum obtained using MAS at 300 K is presented in the inset. The blue curve marks the best fit to eq 4.

where C is a constant, ω_{N} is the Larmor frequency of ^{15}N , and τ denotes the correlation time of motion. We assume that τ follows the Arrhenius law as

$$\tau = \tau_{\infty} e^{E_a/kT} \quad (5)$$

where τ_{∞} is the correlation time at infinite temperature. The best fit of the minimum using eq 4 is also presented in Figure 10. The fit parameters are: $C = 1.8(3) \times 10^9 \text{ s}^{-2}$, $\tau_{\infty} = 1.5(3) \times 10^{-12} \text{ s}$, and $E_a = 0.20(1) \text{ eV}$. The obtained value of τ_{∞} is similar to the value reported in other NMR studies of DMAZn.^{15–17} The determined parameter C provides the N–H distance of 1.06(3) Å (see eq S5 in Supporting Information), which is in a very good agreement with previous ^1H NMR and XRD studies.^{5,16} The value of the activation energy agrees perfectly with the EPR analysis, indicating that both spectroscopies detect the same motional process, which is the hopping of the DMA⁺ cations.

The origin of the observed T_1 maximum at 184 K is not completely clear. This temperature is rather close to T_0 , but usually a minimum of T_1 is encountered at the phase-transition points in the majority of the ferroelectrics and related materials.^{27,45} Thus, we expect that the maximum occurs due to an additional minimum of T_1 at lower temperatures.

SUMMARY AND CONCLUSIONS

In this work we used several experimental techniques to study DMAZn hybrid perovskite frameworks containing ^{14}N and ^{15}N isotopes. The latter compound was investigated for the first time. In addition to the investigation of the nitrogen isotope effect, we also report new insights into the structural phase transition and the DMA⁺ cation dynamics in DMAZn.

The DSC measurements revealed almost the same phase-transition temperatures for DMAZn frameworks containing ^{14}N and ^{15}N isotopes, whereas the ordered phase of the former compound appeared to be slightly more stable.

IR and Raman spectroscopies were employed to investigate the vibrational modes in both compounds. We observed significant shifts of the mode frequencies that are related to the nitrogen motion. This proved a successful synthesis of DMAZn with the heavier ^{15}N isotope. The obtained data were also used to confirm and correct the mode assignment, which was previously reported only for the ^{14}N compound. We observed a very similar anomalous behavior of the mode frequencies and widths at the phase-transition points in both compounds.

CW EPR spectroscopy was used to investigate the differences of the local Mn^{2+} -ion environments in both compounds doped with small amount of manganese. We observed the same phase-

transition temperatures and very similar spectra for both compounds. The EPR results below the phase-transition temperature indicate a slightly different distortion of the MnO_6 octahedra for both frameworks. This effect may originate from the slightly different DMA⁺ cation motion, which directly influences the metal–oxygen octahedra via the H-bonds. However, we cannot rule out the possibility that the origin of this effect is slightly different from the Mn^{2+} -ion doping in both samples. We also found that the simplest case of the Landau theory cannot be used to properly describe the temperature dependence of the axial zfs parameter D , indicating a more complex ordering mechanism in DMAZn. In addition, the analysis of the CW EPR line width Γ_{pp} was performed for both compounds, which was absent in our previous studies of DMAZn: 0.05 Mn^{2+} mol %.^{21,22} We observed an anomalous behavior of Γ_{pp} at the phase-transition points, which was assigned to the critical slowing down of the order parameter fluctuations. The Arrhenius-type analysis of the temperature-dependent line width provided the activation energies E_a of the DMA⁺ cation motion in the disordered phase. For both compounds, we obtained $E_a = 0.21(2) \text{ eV}$, which is close to the values determined by other techniques.

We also performed ^{15}N NMR spectroscopy of DMAZn containing ^{15}N isotope. The obtained NMR spectrum consists of a single line, while the temperature-dependent spin–lattice relaxation time exhibits a minimum at 300 K. The analysis of the observed minimum provided the N–H distance of 1.06 Å. The determined activation energy is 0.20(1) eV, which is in a perfect agreement with the EPR results. This demonstrates that both techniques capture the same hopping cation motion, although in the EPR case, this process manifests itself indirectly via the deformation of the MnO_6 octahedra that are H-bonded with the DMA⁺ cations.

The DSC, IR, Raman, and EPR experiments indicate a negligible nitrogen isotope effect for the DMAZn framework despite a close relation between the nitrogen motion and phase transition in this material. The absence of this effect was also observed for several other ferroelectrics and related materials, such as NaNO_2 and sulfates like $(\text{NH}_4)_2\text{SO}_4$.^{29,30} The common feature of these compounds is that they exhibit pure order–disorder structural phase transitions. In contrast, the isotope effect is significant in materials that have phase transitions of the displacive type (e.g., Ti isotope effect in BaTiO_3).²⁸ Thus, the results of the current study likely indicate that the phase transitions in dimethylammonium metal formates are of the order–disorder nature. This result is in agreement with the dielectric spectroscopy study of DMACo framework, where order–disorder dynamics of DMA⁺ cations was observed.²⁶

ASSOCIATED CONTENT

Supporting Information

The Supporting Information is available free of charge on the ACS Publications website at DOI: 10.1021/acs.jpcc.8b02734.

Additional data of IR, Raman, and EPR spectroscopies (PDF)

AUTHOR INFORMATION

Corresponding Author

*E-mail: mantas.simenas@ff.vu.lt. Phone: +370 5 2234537. Fax: +370 5 2234537.

ORCID

Mantas Šimėnas: 0000-0002-2733-2270

Vytautas Balevičius: 0000-0002-3770-1471

Marko Bertmer: 0000-0002-3208-7927

Mirosław Mączka: 0000-0003-2978-1093

Notes

The authors declare no competing financial interest.

ACKNOWLEDGMENTS

This work was supported by the Research Council of Lithuania (Project No. TAP LLT-4/2017) and the DFG within the priority program SPP 1601. The authors sincerely thank the first reviewer for valuable comments on the NMR data analysis.

REFERENCES

- Jain, P.; Dalal, N. S.; Toby, B. H.; Kroto, H. W.; Cheetham, A. K. Order-Disorder Antiferroelectric Phase Transition in a Hybrid Inorganic-Organic Framework with the Perovskite Architecture. *J. Am. Chem. Soc.* **2008**, *130*, 10450–10451.
- Jain, P.; Ramachandran, V.; Clark, R. J.; Zhou, H. D.; Toby, B. H.; Dalal, N. S.; Kroto, H. W.; Cheetham, A. K. Multiferroic Behavior Associated with an Order-Disorder Hydrogen Bonding Transition in Metal-Organic Frameworks (MOFs) with the Perovskite ABX₃ Architecture. *J. Am. Chem. Soc.* **2009**, *131*, 13625–13627.
- Jain, P.; Stroppa, A.; Nabok, D.; Marino, A.; Rubano, A.; Paparo, D.; Matsubara, M.; Nakotte, H.; Fiebig, M.; Picozzi, S.; et al. Switchable Electric Polarization and Ferroelectric Domains in a Metal-Organic-Framework. *NPJ Quantum Mater.* **2016**, *1*, No. 16012.
- Asadi, K.; van der Veen, M. A. Ferroelectricity in Metal-Organic Frameworks: Characterization and Mechanisms. *Eur. J. Inorg. Chem.* **2016**, 4332.
- Sánchez-Andújar, M.; Presedo, S.; Yáñez-Vilar, S.; Castro-García, S.; Shamir, J.; Señaris-Rodríguez, M. A. Characterization of the Order-Disorder Dielectric Transition in the Hybrid Organic-Inorganic Perovskite-Like Formate Mn(HCOO)₃[(CH₃)₂NH₂]. *Inorg. Chem.* **2010**, *49*, 1510–1516.
- Pato-Doldán, B.; Sánchez-Andújar, M.; Gómez-Aguirre, L. C.; Yáñez-Vilar, S.; López-Beceiro, J.; Gracia-Fernández, C.; Haghghirad, A. A.; Ritter, F.; Castro-García, S.; Señaris-Rodríguez, M. A. Near Room Temperature Dielectric Transition in the Perovskite Formate Framework [(CH₃)₂NH₂][Mg(HCOO)₃]. *Phys. Chem. Chem. Phys.* **2012**, *14*, 8498–8501.
- Wang, X.-Y.; Gan, L.; Zhang, S.-W.; Gao, S. Perovskite-like Metal Formates with Weak Ferromagnetism and as Precursors to Amorphous Materials. *Inorg. Chem.* **2004**, *43*, 4615–4625.
- Mączka, M.; Gągor, A.; Macalik, B.; Pikul, A.; Ptak, M.; Hanuza, J. Order-Disorder Transition and Weak Ferromagnetism in the Perovskite Metal Formate Frameworks of [(CH₃)₂NH₂][M(HCOO)₃] and [(CH₃)₂ND₂][M(HCOO)₃] (M = Ni, Mn). *Inorg. Chem.* **2014**, *53*, 457–467.
- Tian, Y.; Stroppa, A.; Chai, Y.; Yan, L.; Wang, S.; Barone, P.; Picozzi, S.; Sun, Y. Cross Coupling between Electric and Magnetic Orders in a Multiferroic Metal-Organic Framework. *Sci. Rep.* **2014**, *4*, No. 6062.
- Clune, A. J.; Hughey, K. D.; Lee, C.; Abhyankar, N.; Ding, X.; Dalal, N. S.; Whangbo, M.-H.; Singleton, J.; Musfeldt, J. L. Magnetic Field-Temperature Phase Diagram of Multiferroic [(CH₃)₂NH₂][Mn(HCOO)₃]. *Phys. Rev. B* **2017**, *96*, No. 104424.
- Hughey, K. D.; Clune, A. J.; Yokosuk, M. O.; et al. Phonon Mode Links Ferroicities in Multiferroic [(CH₃)₂NH₂][Mn(HCOO)₃]. *Phys. Rev. B* **2017**, *96*, No. 180305.
- Sánchez-Andújar, M.; Gómez-Aguirre, L. C.; Doldán, B. P.; Yáñez-Vilar, S.; Artiaga, R.; Llamas-Saiz, A. L.; Manna, R. S.; Schnelle, F.; Lang, M.; Ritter, F.; et al. First-Order Structural Transition in the Multiferroic Perovskite-Like Formate [(CH₃)₂NH₂][Mn(HCOO)₃]. *CrystEngComm* **2014**, *16*, 3558–3566.
- Šimėnas, M.; Balciunas, S.; Mączka, M.; Banys, J.; Tornau, E. E. Structural Phase Transition in Perovskite Metal-Formate Frameworks:

a Potts-Type Model with Dipolar Interactions. *Phys. Chem. Chem. Phys.* **2016**, *18*, 18528–18535.

(14) Fu, D.-W.; Zhang, W.; Cai, H.-L.; Zhang, Y.; Ge, J.-Z.; Xiong, R.-G.; Huang, S. D.; Nakamura, T. A Multiferroic Perdeutero Metal-Organic Framework. *Angew. Chem., Int. Ed.* **2011**, *50*, 11947–11951.

(15) Besara, T.; Jain, P.; Dalal, N. S.; Kuhns, P. L.; Reyes, A. P.; Kroto, H. W.; Cheetham, A. K. Mechanism of the Order-Disorder Phase Transition, and Glassy Behavior in the Metal-Organic Framework [(CH₃)₂NH₂][Zn(HCOO)₃]. *Proc. Natl. Acad. Sci.* **2011**, *108*, 6828–6832.

(16) Asaji, T.; Ashitomi, K. Phase Transition and Cationic Motion in a Metal-Organic Perovskite, Dimethylammonium Zinc Formate [(CH₃)₂NH₂][Zn(HCOO)₃]. *J. Phys. Chem. C* **2013**, *117*, 10185–10190.

(17) Asaji, T.; Yoshitake, S.; Ito, Y.; Fujimori, H. Phase Transition and Cationic Motion in the Perovskite Formate Framework [(CH₃)₂NH₂][Mg(HCOO)₃]. *J. Mol. Struct.* **2014**, *1076*, 719–723.

(18) Abhyankar, N.; Kweon, J. J.; Orio, M.; Bertaina, S.; Lee, M.; Choi, E. S.; Fu, R.; Dalal, N. S. Understanding Ferroelectricity in the Pb-Free Perovskite-Like Metal-Organic Framework [(CH₃)₂NH₂][Zn(HCOO)₃]: Dielectric, 2D NMR, and Theoretical Studies. *J. Phys. Chem. C* **2017**, *121*, 6314–6322.

(19) Svane, K. L.; Forse, A. C.; Grey, C. P.; Kieslich, G.; Cheetham, A. K.; Walsh, A.; Butler, K. T. How Strong Is the Hydrogen Bond in Hybrid Perovskites? *J. Phys. Chem. Lett.* **2017**, *8*, 6154–6159.

(20) Abhyankar, N.; Bertaina, S.; Dalal, N. S. On Mn²⁺ EPR Probing of the Ferroelectric Transition and Absence of Magnetoelectric Coupling in Dimethylammonium Manganese Formate (CH₃)₂NH₂Mn(HCOO)₃, a Metal-Organic Complex with the Pb-Free Perovskite Framework. *J. Phys. Chem. C* **2015**, *119*, 28143–28147.

(21) Šimėnas, M.; Ciupa, A.; Mączka, M.; Pöppel, A.; Banys, J. EPR Study of Structural Phase Transition in Manganese-Doped [(CH₃)₂NH₂][Zn(HCOO)₃] Metal-Organic Framework. *J. Phys. Chem. C* **2015**, *119*, 24522–24528.

(22) Šimėnas, M.; Kultaeva, A.; Balciunas, S.; Trzebiatowska, M.; Klose, D.; Jeschke, G.; Mączka, M.; Banys, J.; Pöppel, A. Single Crystal Electron Paramagnetic Resonance of Dimethylammonium and Ammonium Hybrid Formate Frameworks: Influence of External Electric Field. *J. Phys. Chem. C* **2017**, *121*, 16533–16540.

(23) Šimėnas, M.; Macalik, L.; Aidas, K.; Kalendra, V.; Klose, D.; Jeschke, G.; Mączka, M.; Völkel, G.; Banys, J.; Pöppel, A. Pulse EPR and ENDOR Study of Manganese Doped [(CH₃)₂NH₂][Zn(HCOO)₃] Hybrid Perovskite Framework. *J. Phys. Chem. C* **2017**, *121*, 27225–27232.

(24) Mączka, M.; Ptak, M.; Macalik, L. Infrared and Raman Studies of Phase Transitions in Metal-Organic Frameworks of [(CH₃)₂NH₂]-[M(HCOO)₃] with M = Zn, Fe. *Vib. Spectrosc.* **2014**, *71*, 98–104.

(25) Mączka, M.; Zierkiewicz, W.; Michalska, D.; Hanuza, J. Vibrational Properties and DFT Calculations of the Perovskite Metal Formate Framework of [(CH₃)₂NH₂][Ni(HCOO)₃] System. *Spectrochim. Acta, Part B* **2014**, *128*, 674–680.

(26) Yadav, R.; Swain, D.; Bhat, H. L.; Elizabeth, S. Order-Disorder Phase Transition and Multiferroic Behaviour in a Metal Organic Framework Compound (CH₃)₂NH₂Co(HCOO)₃. *J. Appl. Phys.* **2016**, *119*, No. 064103.

(27) Blinc, R.; Žekš, B. *Soft Modes in Ferroelectrics and Antiferroelectrics*; North-Holland Publishing Company, 1974.

(28) Hidaka, T.; Oka, K. Isotope Effect on BaTiO₃ Ferroelectric Phase Transitions. *Phys. Rev. B* **1987**, *35*, 8502–8508.

(29) Hidaka, T.; Oka, K. Nonhydrogen Isotope Effects on Structural Phase Transitions in Dielectric Crystals. *Phys. Rev. B* **1990**, *42*, 8295–8304.

(30) Hidaka, T. Isotope Effects on Structural Phase Transitions in Several Sulfates. *Phys. Rev. B* **1992**, *45*, 440–443.

(31) Stoll, S.; Schweiger, A. EasySpin, a Comprehensive Software Package for Spectral Simulation and Analysis in EPR. *J. Magn. Reson.* **2006**, *178*, 42–55.

- (32) Abragam, A.; Bleaney, B. *Electron Paramagnetic Resonance of Transition Ions*; Clarendon Press: Oxford, 1970.
- (33) Ryabov, I. D. On the Generation of Operator Equivalents and the Calculation of Their Matrix Elements. *J. Magn. Reson.* **1999**, *140*, 141–145.
- (34) Strukov, B. A.; Levanyuk, A. P. *Ferroelectric Phenomena in Crystals: Physical Foundations*, 1st ed.; Springer-Verlag: Berlin, Heidelberg, 1998.
- (35) Nishimura, K.; Hashimoto, T. ESR Investigation of TGS Doped with Cr³⁺ Ions. *J. Phys. Soc. Jpn.* **1973**, *35*, 1699–1703.
- (36) Völkel, G.; Brunner, W.; Windsch, W. Critical Fluctuations in Trissarcosine Calcium Chloride (TSCC) Observed by the Electron Spin Echo (ESE) Method. *Solid State Commun.* **1975**, *17*, 345–348.
- (37) Windsch, W. Paramagnetic Resonance Studies in Ferroelectric Tris-Sarcosine Calcium Chloride. *Ferroelectrics* **1976**, *12*, 63–69.
- (38) von Waldkirch, T.; Müller, K. A.; Berlinger, W. Fluctuations in SrTiO₃ near the 105-K Phase Transition. *Phys. Rev. B* **1973**, *7*, 1052–1066.
- (39) Owens, F. J.; Poole, C. P.; Farach, H. A. *Magnetic Resonance of Phase Transitions*; Academic Press, 1979.
- (40) Šimėnas, M.; Ciupa, A.; Mączka, M.; Völkel, G.; Pöpl, A.; Banys, J. EPR of Structural Phase Transition in Manganese- and Copper-Doped Formate Framework of [NH₃(CH₂)₄NH₃][Zn(HCOO)₃]₂. *J. Phys. Chem. C* **2016**, *120*, 19751–19758.
- (41) Levitt, M. H. *Spin Dynamics: Basics of Nuclear Magnetic Resonance*, 2nd ed.; Wiley, 2008.
- (42) O'Reilly, D. E.; Peterson, E. M.; Tsang, T. Nuclear Magnetic Resonance and Nonexponential Spin-Lattice Relaxation in Ferroelectric Ammonium Fluoroberyllate. *Phys. Rev.* **1967**, *160*, 333–342.
- (43) Albert, S.; Gutowsky, H. S. Nuclear Relaxation and Spin Exchange in Ammonium Hexafluorophosphate (NH₄PF₆). *J. Chem. Phys.* **1973**, *59*, 3585–3594.
- (44) Idziak, S. N. M. R. Study of the Molecular Dynamics in Crystalline Trichloroacetic Acid. *Mol. Phys.* **1989**, *68*, 1335–1340.
- (45) Blinc, R.; Stepisnik, J.; Jamsek-Vilfan, M.; Zumer, S. Deuteron Magnetic Resonance and Relaxation in Ferroelectric KD₂PO₄, KD₂AsO₄, and CsD₂AsO₄. *J. Chem. Phys.* **1971**, *54*, 187–195.

References

- [1] Jeffrey R Long and Omar M Yaghi. The pervasive chemistry of metal–organic frameworks. *Chem. Soc. Rev.*, 38(5):1213–1214, 2009.
- [2] Gérard Férey. Hybrid porous solids: past, present, future. *Chem. Soc. Rev.*, 37(1):191–214, 2008.
- [3] David J. Tranchemontagne, José L. Mendoza-Cortés, Michael O’Keeffe, Omar M. Yaghi, I. Halow, S. M. Bailey, K. L. Churney, R. L. Nuttall, R. E. P. Winpenny, E. Rentschler, G. A. Timco, Q. Li, and W. E. Streib. Secondary building units, nets and bonding in the chemistry of Metal-Organic Frameworks. *Chem. Soc. Rev.*, 38(5):1257–1283, 2009.
- [4] Susumu Kitagawa, Ryo Kitaura, and Shin-ichiro Noro. Functional Porous Coordination Polymers. *Angew. Chemie Int. Ed.*, 43(18):2334–2375, 2004.
- [5] OM Yaghi, Charles E Davis, Guangming Li, and Hailian Li. Selective guest binding by tailored channels in a 3-D porous zinc (II)- benzenetricarboxylate network. *J. Am. Chem. Soc.*, 119(12):2861–2868, 1997.
- [6] Mircea Dincă, Anta F. Yu, and Jeffrey R. Long. Microporous Metal-Organic Frameworks Incorporating 1,4-Benzeneditetrazolate:- Syntheses, Structures, and Hydrogen Storage Properties. *J. Am. Chem. Soc.*, 128(27):8904–8913, 2006.
- [7] Paul S. Wheatley, Anthony R. Butler, Michael S. Crane, Sarah Fox, Bo Xiao, Adriano G Rossi, Ian L. Megson, and Russell E. Morris. NO-Releasing Zeolites and Their Antithrombotic Properties. *J. Am. Chem. Soc.*, 128(2):502–509, 2006. PMID: 16402837.
- [8] S Moncada and EA Higgs. The discovery of nitric oxide and its role in vascular biology. *Br. J. Pharmacol.*, 147(S1):S193–S201, 2006.

REFERENCES

- [9] Alexis W Carpenter and Mark H Schoenfisch. Nitric oxide release: Part II. Therapeutic applications. *Chem. Soc. Rev.*, 41(41):3742–3752, 2012.
- [10] M R Miller and I L Megson. Recent developments in nitric oxide donor drugs. *Br. J. Pharmacol.*, 151(3):305–321, 2007.
- [11] Megan C. Frost, Melissa M. Reynolds, and Mark E. Meyerhoff. Polymers incorporating nitric oxide releasing/generating substances for improved biocompatibility of blood-contacting medical devices. *Biomaterials*, 26(14):1685–1693, 2005.
- [12] Evan M. Hetrick, Jae Ho Shin, Nathan A. Stasko, C. Bryce Johnson, Daniel A. Wespe, Ekhsan Holmuhamedov, and Mark H. Schoenfisch. Bactericidal efficacy of nitric oxide-releasing Silica nanoparticles. *ACS Nano*, 2(2):235–246, 2008.
- [13] Daniel A Riccio and Mark H Schoenfisch. Nitric oxide release: Part I. Macromolecular scaffolds. *Chem. Soc. Rev.*, 41(41):3731–3741, 2012.
- [14] Alistair C McKinlay, Russell E Morris, Patricia Horcajada, Gérard Férey, Ruxandra Gref, Patrick Couvreur, and Christian Serre. BioMOFs: metal-organic frameworks for biological and medical applications. *Angew. Chem., Int. Ed*, 49(36):6260–6266, 2010.
- [15] Peng George Wang, Ming Xian, Xiaoping Tang, Xuejun Wu, Zhong Wen, Tingwei Cai, and Adam J. Janczuk. Nitric oxide donors: Chemical activities and biological applications. *Chem. Rev.*, 102(4):1091–1134, 2002.
- [16] Sergio Huerta, Sapna Chilka, and Benjamin Bonavida. Nitric oxide donors: Novel cancer therapeutics. *Int. J. Oncol.*, 33(5):909–927, 2008.
- [17] Joseph A. Hrabie, John R. Klose, David A. Wink, and Larry K. Keefer. New nitric oxide-releasing zwitterions derived from polyamines. *J. Org. Chem.*, 58(6):1472–1476, 1993.
- [18] Bo Xiao, Paul S. Wheatley, Xuebo Zhao, Ashleigh J. Fletcher, Sarah Fox, Adriano G. Rossi, Ian L. Megson, S. Bordiga, L. Regli, K. Mark Thomas, and Russell E. Morris. High-capacity hydrogen and nitric oxide adsorption and storage in a metal-organic framework. *J. Am. Chem. Soc.*, 129(5):1203–1209, 2007.
- [19] Paul Trescony, Ken Rohly, and Michael Dror. Polymeric material that releases nitric oxide, 1999. US Patent 5,994,444.
- [20] Evan M Hetrick and Mark H Schoenfisch. Analytical chemistry of nitric oxide. *Annu. Rev. Anal. Chem.*, 2(1):409–433, 2009.

-
- [21] Rachel C Huxford, Joseph Della Rocca, and Wenbin Lin. Metal-organic frameworks as potential drug carriers. *Curr. Opin. Chem. Biol.*, 14(2):262–268, 2010.
- [22] Alistair C Mckinlay, Bo Xiao, David S Wragg, Paul S Wheatley, Ian L Megson, and Russell E Morris. Exceptional Behavior over the Whole Adsorption - Storage - Delivery Cycle for NO in Porous Metal Organic Frameworks. *J. Am. Chem. Soc.*, 130(15):10440–10444, 2008.
- [23] Zhenbo Ma and Brian Moulton. Recent advances of discrete coordination complexes and coordination polymers in drug delivery. *Coord. Chem. Rev.*, 255(15-16):1623–1641, 2011.
- [24] Michael J Ingleson, Romain Heck, Jamie a Gould, and Matthew J Rosseinsky. Nitric oxide chemisorption in a postsynthetically modified metal-organic framework. *Inorg. Chem.*, 48(21):9986–9988, 2009.
- [25] Joseph A Hrabie and Larry K Keefer. Chemistry of the nitric oxide-releasing diazeniumdiolate (“nitrosohydroxylamine”) functional group and its oxygen-substituted derivatives. *Chem. Rev.*, 102(4):1135–1154, 2002.
- [26] Pawel G. Parzuchowski, Megan C. Frost, and Mark E. Meyerhoff. Synthesis and characterization of polymethacrylate-based nitric oxide donors. *J. Am. Chem. Soc.*, 124(41):12182–12191, 2002.
- [27] Joseph G. Nguyen, Kristine K. Tanabe, and Seth M. Cohen. Postsynthetic diazeniumdiolate formation and NO release from MOFs. *CrystEngComm.*, 12(8):2335–2338, 2010.
- [28] Kristine K Tanabe and Seth M Cohen. Postsynthetic modification of metal-organic frameworks-a progress report. *Chem. Soc. Rev.*, 40(2):498–519, 2011.
- [29] Benjamin Barth, Matthias Mendt, Andreas Pöppl, and Martin Hartmann. Adsorption of nitric oxide in metal-organic frameworks: Low temperature IR and EPR spectroscopic evaluation of the role of open metal sites. *Microporous Mesoporous Mater.*, 216:97–110, 2015.
- [30] Farhana Gul-E-Noor, Bettina Jee, Andreas Pöppl, Martin Hartmann, Dieter Himsl, and Marko Bertmer. Effects of varying water adsorption on a Cu₃btc₂ metal-organic framework (MOF) as studied by ¹H and ¹³C solid-state NMR spectroscopy. *Phys. Chem. Chem. Phys.*, 13(17):7783–7788, 2011.

REFERENCES

- [31] Farhana Gul-E-Noor, Bettina Jee, Matthias Mendt, Dieter Himsl, Andreas Pöppel, Martin Hartmann, Jürgen Haase, Harald Krautscheid, and Marko Bertmer. Formation of mixed Metal $\text{Cu}_{3-x}\text{Zn}_x\text{btc}_2$ frameworks with different Zinc Contents: Incorporation of Zn^{2+} into the Metal-Organic Framework structure as Studied by Solid-State NMR. *J. Phys. Chem. C*, 116(39):20866–20873, 2012.
- [32] Farhana Gul-E-Noor, Dieter Michel, Harald Krautscheid, Jürgen Haase, and Marko Bertmer. Investigation of the spin-lattice relaxation of ^{13}CO and $^{13}\text{CO}_2$ adsorbed in the metal-organic frameworks $\text{Cu}_3(\text{BTC})_2$ and $\text{Cu}_{(3-x)}\text{Zn}_{(x)}(\text{btc})_2$. *J. Chem. Phys.*, 139(3):034202, 2013.
- [33] William P Arnold, Chandra K Mittal, Shoji Katsuki, and Ferid Murad. Nitric oxide activates guanylate cyclase and increases guanosine 3-, 5-cyclic monophosphate levels in various tissue preparations. *Proc. Natl. Acad. Sci. U.S.A.*, 74(8):3203–3207, 1977.
- [34] Robert F Furchgott. Endothelium-derived relaxing factor: discovery, early studies, and identification as nitric oxide. *Biosci. Rep.*, 19(4):235–251, 1999.
- [35] Louis J Ignarro, Georgette M Buga, Keith S Wood, Russell E Byrns, and Gautam Chaudhuri. Endothelium-derived relaxing factor produced and released from artery and vein is nitric oxide. *Proc. Natl. Acad. Sci. U.S.A.*, 84(24):9265–9269, 1987.
- [36] Lei Yang, Xingzhi Wang, Dakota J. Suchyta, and Mark H. Schoenfisch. Antibacterial Activity of Nitric Oxide-Releasing Hyperbranched Polyamidoamines. *Bioconjug. Chem.*, 29(1):35–43, 2018.
- [37] Hidemasa Katsumi, Makiya Nishikawa, Hiroyuki Yasui, Fumiyoshi Yamashita, and Mitsuru Hashida. Prevention of ischemia/reperfusion injury by hepatic targeting of nitric oxide in mice. *J. Control. Release*, 140(1):12 – 17, 2009.
- [38] Burnett Arthur L. The Role of Nitric Oxide in Erectile Dysfunction: Implications for Medical Therapy. *J Clin Hypertens*, 8(s12):53–62, 2006.
- [39] Hidemasa Katsumi, Makiya Nishikawa, Fumiyoshi Yamashita, and Mitsuru Hashida. Development of Polyethylene Glycol-Conjugated Poly-S-Nitrosated Serum Albumin, a Novel S-Nitrosothiol for Prolonged Delivery of Nitric Oxide in the Blood Circulation in Vivo. *J. Pharmacol. Exp. Ther.*, 314(3):1117–1124, 2005.
- [40] David Hirst and Tracy Robson. Nitric Oxide in Cancer Therapeutics: Interaction with Cytotoxic Chemotherapy. *Curr. Pharm. Des.*, 16(4):411–420, 2001.

-
- [41] Majida Rizk, Maria B. Witte, and Adrian Barbul. Nitric Oxide and Wound Healing. *World J. Surg.*, 28(3):301–306, 2004.
- [42] Robert Beringer and J G Castle. Magnetic Resonance Absorption in Nitric Oxide. *Phys. Rev.*, 78(5):581–586, 1950.
- [43] Gerhard Herzberg. *Molecular Spectra and Molecular Structure: Spectra of Diatomic Molecules*. von Nostrand company, Toronto, Newyork, 2nd edition, 1953.
- [44] Thomas C. James and Robert J. Thibault. Spin-Orbit Coupling Constant of Nitric Oxide. Determination from Fundamental and Satellite Band Origins. *J. Chem. Phys.*, 41(9):2806–2813, 1964.
- [45] Thomas Rudolf, Winfried Böhlmann, and Andreas Pöpl. Adsorption and Desorption Behavior of NO on H-ZSM-5, Na-ZSM-5, and Na-A as Studied by EPR. *J. Magn. Reson.*, 155(1):45–56, 2002.
- [46] Carl E. Dinerman. Comment on “Structure of $(\text{NO})_2$ in the Molecular Crystal”. *J. Chem. Phys.*, 54(2):3660, 1971.
- [47] Stephen G. Kukolich. Structure and quadrupole coupling measurements on the NO dimer. *J. Mol. Spectrosc.*, 98(1):80–86, 1983.
- [48] A. Lee Smith and Herrick L. Johnston. The Magnetic Susceptibility of Liquid Nitric Oxide and the Heat of Dissociation of $(\text{NO})_2$. *J. Am. Chem. Soc.*, 74(18):4696–4698, 1952.
- [49] EA Guggenheim. Dimerization of gaseous nitric oxide. *Mol. Phys.*, 10(4):401–404, 1966.
- [50] JE Williams and JN Murrell. Structure and stability of the nitric oxide dimer. *J. Am. Chem. Soc.*, 93(26):7149–7152, 1971.
- [51] Stephen G. Kukolich. The structure of the nitric oxide dimer. *J. Am. Chem. Soc.*, 104(17):4715–4716, 1982.
- [52] Russell S. Drago and F. E. Paulik. The Reaction of Nitrogen(II) Oxide with Diethylamine. *J. Am. Chem. Soc.*, 82(1):96–98, 1960.
- [53] Hiroyasu Furukawa, Kyle E. Cordova, Michael O’Keeffe, and Omar M. Yaghi. The chemistry and applications of Metal-Organic Frameworks. *Science*, 341(6149):1230444–12, 2013.

REFERENCES

- [54] Russell E Morris and Paul S Wheatley. Gas storage in nanoporous materials. *Angew. Chem., Int. Ed.*, 47(27):4966–4981, 2008.
- [55] BF Hoskins and Richard Robson. Design and construction of a new class of scaffolding-like materials comprising infinite polymeric frameworks of 3D-linked molecular rods. *J. Am. Chem. Soc.*, 112(4):1546–1554, 1990.
- [56] F Albert Cotton, Evgeny V Dikarev, Marina A Petrukhina, Marion Schmitz, and Peter J Stang. Supramolecular assemblies of dimetal complexes with polydentate N-donor ligands: From a discrete pyramid to a 3D channel network. *Inorg. Chem.*, 41(11):2903–2908, 2002.
- [57] Sujing Wang, Shunshun Xiong, Zhiyong Wang, and Jiangfeng Du. Rational Design of Zinc–Organic Coordination Polymers Directed by N-Donor Co-ligands. *Chem.: Eur. J.*, 17(31):8630–8642, 2011.
- [58] O Shekhah, J Liu, RA Fischer, and Ch Wöll. MOF thin films: existing and future applications. *Chem. Soc. Rev.*, 40(2):1081–1106, 2011.
- [59] Stephen S.-Y. Chui, Samuel M.-F. Lo, Jonathan P H Charmant, A Guy Orpen, and Ian D Williams. A Chemically Functionalizable Nanoporous Material $[\text{Cu}_3(\text{TMA})_2\text{H}_2\text{O}]_n$. *Science*, 283(5405):1148–1150, 1999.
- [60] Matthias Mendt, Bettina Jee, Norbert Stock, Tim Ahnfeldt, Martin Hartmann, Dieter Himsl, and Andreas Pöpl. Structural phase transitions and thermal hysteresis in the metal-organic framework compound MIL-53 as studied by electron spin resonance spectroscopy. *J. Phys. Chem. C*, 114(45):19443–19451, 2010.
- [61] Thierry Loiseau, Christian Serre, Clarisse Huguenard, Gerhard Fink, Francis Taulelle, Marc Henry, Thierry Bataille, and Gérard Férey. A rationale for the large breathing of the porous aluminum terephthalate (MIL-53) upon hydration. *Chem. Eur. J.*, 10(6):1373–1382, 2004.
- [62] Herbert C Hoffmann, Bassem Assfour, Fanny Epperlein, Nicole Klein, Silvia Paasch, Irena Senkowska, Stefan Kaskel, Gotthard Seifert, and Eike Brunner. High-pressure in Situ ^{129}Xe NMR spectroscopy and computer simulations of breathing transitions in the metal–organic framework $\text{Ni}_2(2,6\text{-ndc})_2(\text{dabco})(\text{DUT-8 (Ni)})$. *J. Am. Chem. Soc.*, 133(22):8681–8690, 2011.

-
- [63] Omar M Yaghi, Michael O'keeffe, Nathan W Ockwig, Hee K Chae, Mohamed Eddaoudi, and Jaheon Kim. Reticular synthesis and the design of new materials. *Nature*, 423(6941):705–710, 2003.
- [64] Shuai Yuan, Lanfang Zou, Jun-Sheng Qin, Jialuo Li, Lan Huang, Liang Feng, Xuan Wang, Mathieu Bosch, Ali Alsalme, Tahir Cagin, et al. Construction of hierarchically porous metal–organic frameworks through linker labilization. *Nat. Commun.*, 8:15356–15361, 2017.
- [65] Nicole Klein, Irena Senkowska, Kristina Gedrich, Ulrich Stoeck, Antje Henschel, Uwe Mueller, and Stefan Kaskel. A mesoporous metal–organic framework. *Angew. Chem. Int. Ed.*, 48(52):9954–9957, 2009.
- [66] Jun Hu, Hongpei Cai, Huiqing Ren, Yongming Wei, Zhengliang Xu, Honglai Liu, and Ying Hu. Mixed-matrix membrane hollow fibers of Cu_3btc_2 MOF and polyimide for gas separation and adsorption. *Ind. Eng. Chem. Res.*, 49(24):12605–12612, 2010.
- [67] Hailian Li, Mohamed Eddaoudi, Michael O'Keeffe, and Omar M Yaghi. Design and synthesis of an exceptionally stable and highly porous metal-organic framework. *Nature*, 402(6759):276–280, 1999.
- [68] Alexander U Czaja, Natalia Trukhan, and Ulrich Müller. Industrial applications of metal–organic frameworks. *Chem. Soc. Rev.*, 38(5):1284–1293, 2009.
- [69] David Britt, Hiroyasu Furukawa, Bo Wang, T Grant Glover, and Omar M Yaghi. Highly efficient separation of carbon dioxide by a metal-organic framework replete with open metal sites. *Proc. Natl. Acad. Sci. U.S.A.*, 106(49):20637–20640, 2009.
- [70] Jian-Rong Li, Ryan J Kuppler, and Hong-Cai Zhou. Selective gas adsorption and separation in metal–organic frameworks. *Chem. Soc. Rev.*, 38(5):1477–1481, 2009.
- [71] Andrew R. Millward and Omar M. Yaghi. Metal-organic frameworks with exceptionally high capacity for storage of carbon dioxide at room temperature. *J. Am. Chem. Soc.*, 127(51):17998–17999, 2005.
- [72] Ulrich Mueller, Markus M. Schubert, Friedhelm Teich, Hermann Puetter, Kerstin Schierle-Arndt, and Joerg Pastre. Metal–organic frameworks—prospective industrial applications. *J. Mater. Chem.*, 16(7):626–636, 2006.
- [73] Zhonghua Xiang, Sanhua Leng, and Dapeng Cao. Functional group modification of metal–organic frameworks for CO_2 capture. *J. Phys. Chem. C*, 116(19):10573–10579, 2012.

REFERENCES

- [74] Fei-Yan Yi, Dongxiao Chen, Meng-Ke Wu, Lei Han, and Hai-Long Jiang. Chemical sensors based on metal–organic frameworks. *ChemPlusChem*, 81(8):675–690, 2016.
- [75] Erik D Spoerke, Leo J Small, Michael E Foster, Jill Wheeler, Andrew M Ullman, Vitalie Stavila, Mark Rodriguez, and Mark D Allendorf. MOF-sensitized solar cells enabled by a pillared porphyrin framework. *J. Phys. Chem. C*, 121(9):4816–4824, 2017.
- [76] Erik A Flügel, Annkathrin Ranft, Frederik Haase, and Bettina V Lotsch. Synthetic routes toward MOF nanomorphologies. *J. Mater. Chem.*, 22(20):10119–10133, 2012.
- [77] Jia Liu, Fuxing Sun, Feng Zhang, Zhu Wang, Rui Zhang, Ce Wang, and Shilun Qiu. In situ growth of continuous thin metal–organic framework film for capacitive humidity sensing. *J. Mater. Chem.*, 21(11):3775–3778, 2011.
- [78] Hiromitsu Uehara, Stéphane Diring, Shuhei Furukawa, Ziya Kalay, Manuel Tsotsalas, Masashi Nakahama, Kenji Hirai, Mio Kondo, Osami Sakata, and Susumu Kitagawa. Porous coordination polymer hybrid device with quartz oscillator: Effect of crystal size on sorption kinetics. *J. Am. Chem. Soc.*, 133(31):11932–11935, 2011.
- [79] F Gándara, A de Andres, B Gómez-Lor, E Gutiérrez-Puebla, M Iglesias, MA Monge, DM Proserpio, and N Snejko. A rare-earth MOF series: fascinating structure, efficient light emitters, and promising catalysts. *Cryst. Growth Des.*, 8(2):378–380, 2008.
- [80] Gong Cheng, Zhi Gang Wang, Sachira Denagamage, and Si Yang Zheng. Graphene-Templated Synthesis of Magnetic Metal Organic Framework Nanocomposites for Selective Enrichment of Biomolecules. *ACS Appl. Mater. Interfaces*, 8(16):10234–10242, 2016.
- [81] Shu-Hui Huo and Xiu-Ping Yan. Facile magnetization of metal–organic framework MIL-101 for magnetic solid-phase extraction of polycyclic aromatic hydrocarbons in environmental water samples. *Analyst*, 137(15):3445–3450, 2012.
- [82] Akbar Bagheri, Mohsen Taghizadeh, Mohammad Behbahani, Ali Akbar Asgharinezhad, Mani Salarian, Ali Dehghani, Homeira Ebrahimzadeh, and Mostafa M Amini. Synthesis and characterization of magnetic metal-organic framework as a novel sorbent, and its optimization by experimental design methodology for determination of palladium in environmental samples. *Talanta*, 99:132–139, 2012.
- [83] Yoji Kobayashi, Benjamin Jacobs, Mark D. Allendorf, and Jeffrey R. Long. Conductivity, doping, and redox chemistry of a microporous dithiolene-based metal-organic framework. *Chem. Mater.*, 22(14):4120–4122, 2010.

-
- [84] Adina Morozan and Frédéric Jaouen. Metal organic frameworks for electrochemical applications. *Energy Environ. Sci.*, 5(11):9269, 2012.
- [85] Sánchez-Andújar, M and Presedo, S and Yáñez-Vilar, S and Castro-García, S and Shamir, J and Señaris-Rodríguez, MA. Characterization of the Order- Disorder Dielectric Transition in the Hybrid Organic- Inorganic Perovskite-Like Formate $\text{Mn}(\text{HCOO})_3[(\text{CH}_3)_2\text{NH}_2]$. *Inorg. Chem.*, 49(4):1510–1516, 2010.
- [86] L Claudia Goémez-Aguirre, Breogaén Pato-Doldaén, J Mira, Socorro Castro-García, María Antonia Senearis-Rodríguez, Manuel Saénchez-Anduéjar, John Singleton, and Vivien S Zapf. Magnetic ordering-induced multiferroic behavior in $[\text{CH}_3\text{NH}_3][\text{Co}(\text{HCOO})_3]$ metal–organic framework. *J. Am. Chem. Soc.*, 138(4):1122–1125, 2016.
- [87] Annika Herbst, Anupam Khutia, and Christoph Janiak. Brønsted instead of lewis acidity in functionalized MIL-101 Cr MOFs for efficient heterogeneous (nano-MOF) catalysis in the condensation reaction of aldehydes with alcohols. *Inorg. Chem.*, 53(14):7319–7333, 2014.
- [88] Amanda W Stubbs, Luca Braglia, Elisa Borfecchia, Randall J Meyer, Yuriy Román-Leshkov, Carlo Lamberti, and Mircea Dincă. Selective Catalytic Olefin Epoxidation with MnII-Exchanged MOF-5. *ACS Catal.*, 8(1):596–601, 2018.
- [89] Tong Zhang, Xiongfú Zhang, Xinjuan Yan, Linying Kong, Guangcai Zhang, Haiou Liu, Jieshan Qiu, and King Lun Yeung. Synthesis of Fe_3O_4 @ZIF-8 magnetic core-shell microspheres and their potential application in a capillary microreactor. *Chem. Eng. J.*, 228:398–404, 2013.
- [90] Danil N Dybtsev, Alexey L Nuzhdin, Hyungphil Chun, Konstantin P Bryliakov, Evgeniy P Talsi, Vladimir P Fedin, and Kimoon Kim. A homochiral metal–organic material with permanent porosity, enantioselective sorption properties, and catalytic activity. *Angewandte Chemie*, 118(6):930–934, 2006.
- [91] Ilknur Erucar and Seda Keskin. Computational investigation of metal organic frameworks for storage and delivery of anticancer drugs. *J. Mater. Chem. B*, 5(5):7342–7351, 2017.
- [92] Kathryn M. L. Taylor, William J. Rieter, and Wenbin Lin. Manganese-based nanoscale metal-organic frameworks for magnetic resonance imaging. *J. Am. Chem. Soc.*, 130(44):14358–14359, 2008.

REFERENCES

- [93] Jongsik Kim, Allen G Oliver, Gregory T Neumann, and Jason C Hicks. Zn-MOFs Containing Pyridine and Bipyridine Carboxylate Organic Linkers and Open Zn^{2+} Sites. *Eur. J. Inorg. Chem.*, 2015(18):3011–3018, 2015.
- [94] Banglin Chen, Chengdu Liang, Jun Yang, Damacio S Contreras, Yvette L Clancy, Emil B Lobkovsky, Omar M Yaghi, and Sheng Dai. A Microporous Metal–Organic Framework for Gas-Chromatographic Separation of Alkanes. *Angew. Chem. Int. Ed.*, 45(9):1390–1393, 2006.
- [95] Zoey R Herm, Brian M Wiers, Jarad A Mason, Jasper M van Baten, Matthew R Hudson, Pawel Zajdel, Craig M Brown, Norberto Masciocchi, Rajamani Krishna, and Jeffrey R Long. Separation of Hexane Isomers in a Metal–Organic Framework with Triangular Channels. *Science*, 340(6135):960–964, 2013.
- [96] Somboon Chaemchuen, Nawasad Alam Kabir, Kui Zhou, and Francis Verpoort. Metal–organic frameworks for upgrading biogas via CO₂ adsorption to biogas green energy. *Chem. Soc. Rev.*, 42(24):9304, 2013.
- [97] Jarrod F. Eubank, Paul S. Wheatley, Gaëlle Lebars, Alistair C. McKinlay, Hervé Leclerc, Patricia Horcajada, Marco Daturi, Alexandre Vimont, Russell E. Morris, and Christian Serre. Porous, rigid metal(III)-carboxylate metal-organic frameworks for the delivery of nitric oxide. *APL Mater.*, 2(12):124112–124120, 2014.
- [98] Thomas Devic, Patricia Horcajada, Christian Serre, Fabrice Salles, Guillaume Maurin, Béatrice Moulin, Daniela Heurtaux, Guillaume Clet, Alexandre Vimont, Jean-Marc Grenèche, et al. Functionalization in flexible porous solids: Effects on the pore opening and the host- guest interactions. *J. Am. Chem. Soc.*, 132(3):1127–1136, 2009.
- [99] Andreas Pöpl, Sebastian Kunz, Dieter Himsl, and Martin Hartmann. CW and pulsed ESR spectroscopy of cupric ions in the metal-organic framework compound Cu_3btc_2 . *J. Phys. Chem. C*, 112(7):2678–2684, 2008.
- [100] Xi Xiang Zhang, Stephen S.-Y. Chui, and Ian D. Williams. Cooperative magnetic behavior in the coordination polymers $Cu_3(TMA)_2L_3]_n$ (L=water, pyridine). *J. Appl. Phys.*, 87(9):6007, 2000.
- [101] Kai Liu, Dan Ryan, Koji Nakanishi, and Ann McDermott. Solid state NMR studies of paramagnetic coordination complexes: A comparison of protons and deuterons in detection and decoupling. *J. Am. Chem. Soc.*, 117(26):6897–6906, 1995.

-
- [102] Yoshitaka Ishii, Nalinda P. Wickramasinghe, and Sandra Chimon. A New Approach in 1D and 2D ^{13}C High-Resolution Solid-State NMR Spectroscopy of Paramagnetic Organometallic Complexes by Very Fast Magic-Angle Spinning. *J. Am. Chem. Soc.*, 125(12):3438–3439, 2003.
- [103] Boris M. Slepchenko, James C. Schaff, John H. Carson, and Leslie M. Loew. Computational Cell Biology: Spatiotemporal Simulation of Cellular Events. *Annu. Rev. Biophys. Biomol. Struct.*, 31(1):423–441, 2002.
- [104] Carmelo Prestipino, Laura Regli, Jenny Grazia Vitillo, F Bonino, A Damin, Carlo Lamberti, Adriano Zecchina, PL Solari, KO Kongshaug, and Silvia Bordiga. Local Structure of Framework Cu(II) in HKUST-1 Metallorganic Framework: Spectroscopic Characterization upon Activation and Interaction with Adsorbates. *Chem. Mater.*, 18(5):1337–1346, 2006.
- [105] Bettina Jee, Konrad Eisinger, Farhana Gul-E-Noor, Marko Bertmer, Martin Hartmann, Dieter Himsl, and Andreas Pöpl. Continuous Wave and Pulsed Electron Spin Resonance Spectroscopy of Paramagnetic Framework Cupric Ions in the Zn(II) Doped Porous Coordination Polymer $\text{Cu}_{3-x}\text{Zn}_x\text{btc}_2$. *J. Phys. Chem. C*, 114(39):16630–16639, 2010.
- [106] Barbara Panella, Michael Hirscher, Hermann Pütter, and Ulrich Müller. Hydrogen Adsorption in Metal–Organic Frameworks: Cu-MOFs and Zn-MOFs Compared. *Adv. Funct. Mater.*, 16(4):520–524, 2005.
- [107] Martin Hartmann, Sebastian Kunz, Dieter Himsl, Oliver Tangermann, Stefan Ernst, and Alex Wagener. Adsorptive Separation of Isobutene and Isobutane on $\text{Cu}_3(\text{BTC})_2$. *Langmuir*, 24(16):8634–8642, 2008.
- [108] Alexander Sachse, Rob Ameloot, Bernard Coq, François Fajula, Benoit Coasne, Dirk De Vos, and Anne Galarneau. In situ synthesis of Cu–BTC (HKUST-1) in macro/mesoporous silica monoliths for continuous flow catalysis. *Chem. Commun.*, 48(39):4749–4752, 2012.
- [109] Gregory W Peterson, George W Wagner, Alex Balboa, John Mahle, Tara Sewell, and Christopher J Karwacki. Ammonia Vapor Removal by $\text{Cu}_3(\text{BTC})_2$ and Its Characterization by MAS NMR. *J. Phys. Chem. C*, 3(113):13906–13917, 2009.
- [110] Katharina Peikert, Frank Hoffmann, and Michael Fröba. Amino substituted $\text{Cu}_3(\text{btc})_2$: a new metal-organic framework with a versatile functionality. *ChemComm*, 48(91):11196–11198, 2012.

REFERENCES

- [111] Katharina Peikert, Laura J McCormick, Damiano Cattaneo, Morven J Duncan, Frank Hoffmann, Arafat H Khan, Marko Bertmer, Russell E Morris, and Michael Fröba. Tuning the nitric oxide release behavior of amino functionalized hkust-1. *Microporous Mesoporous Mater.*, 216:118–126, 2015.
- [112] Alysia Lowe, Punya Chittajallu, Qihan Gong, Jing Li, and Kenneth J. Balkus. Storage and delivery of nitric oxide via diazeniumdiolated metal organic framework. *Microporous and Mesoporous Mater.*, 181:17–22, 2013.
- [113] Patricia Horcajada, Christian Serre, Guillaume Maurin, Naseem A. Ramsahye, Francisco Balas, María Vallet-Regí, Muriel Sebban, Francis Taulelle, and Gérard Férey. Flexible Porous Metal-Organic Frameworks for a Controlled Drug Delivery. *J. Am. Chem. Soc.*, 130(21):6774–6780, 2008.
- [114] T Hidalgo, M Giménez-Marqués, E Bellido, J Avila, MC Asensio, F Salles, MV Lozano, M Guillevic, R Simón-Vázquez, A González-Fernández, et al. Chitosan-coated mesoporous MIL-100 (Fe) nanoparticles as improved bio-compatible oral nanocarriers. *Sci. Rep.*, 7:43099–43103, 2017.
- [115] Stuart R. Miller, Daniela Heurtaux, Tarek Baati, Patricia Horcajada, Jean-Marc Grenèche, and Christian Serre. Biodegradable therapeutic MOFs for the delivery of bioactive molecules. *Chem. Commun.*, 46:4526–4528, 2010.
- [116] Christophe Volkringer, Dimitry Popov, Thierry Loiseau, Gérard Férey, Manfred Burghammer, Christian Riekkel, Mohamed Haouas, and Francis Taulelle. Synthesis, Single-Crystal X-ray Microdiffraction, and NMR Characterizations of the Giant Pore Metal-Organic Framework Aluminum Trimesate MIL-100. *Chem. Mater.*, 21(24):5695–5697, 2009.
- [117] Makoto Fujita, Yoon Jung Kwon, Satoru Washizu, and Katsuyuki Ogura. Preparation, Clathration Ability, and Catalysis of a Two-Dimensional Square Network Material Composed of Cadmium(II) and 4,4'-Bipyridine. *J. Am. Chem. Soc.*, 116(3):1151–1152, 1994.
- [118] Stefan K Henninger, Felix Jeremias, Harry Kummer, and Christoph Janiak. MOFs for use in adsorption heat pump processes. *Eur. J. Inorg. Chem.*, 2012(16):2625–2634, 2012.
- [119] Christophe Volkringer, Hervé Leclerc, Jean-Claude Lavalley, Thierry Loiseau, Gérard Férey, Marco Daturi, and Alexandre Vimont. Infrared Spectroscopy Investigation of

- the Acid Sites in the Metal-Organic Framework Aluminum Trimesate MIL-100(Al). *J. Phys. Chem. C*, 116(9):5710–5719, 2012.
- [120] Stephan Hermes, Marie-Katrin Schröter, Rochus Schmid, Lamma Khodeir, Martin Muhler, Arno Tissler, Richard W Fischer, and Roland A Fischer. Metal@ MOF: Loading of highly porous coordination polymers host lattices by metal organic chemical vapor deposition. *Angew. Chem. Int. Ed.*, 44(38):6237–6241, 2005.
- [121] AC McKinlay, JF Eubank, S Wuttke, B Xiao, PS Wheatley, Philippe Bazin, J-C Lavalley, Marco Daturi, Alexandre Vimont, G De Weireld, et al. Nitric oxide adsorption and delivery in flexible MIL-88 (Fe) metal–organic frameworks. *Chem. Mater.*, 25(9):1592–1599, 2013.
- [122] Matthias Mendt, Benjamin Barth, Martin Hartmann, and Andreas Pöppel. Low-temperature binding of NO adsorbed on MIL-100(Al)— A case study for the application of high resolution pulsed EPR methods and DFT calculations. *J. Chem. Phys.*, 147(22):224701–224708, 2017.
- [123] Malcolm H. Levitt. *Spin dynamics: basics of nuclear magnetic resonance*. John Wiley & Sons, 2001.
- [124] Melinda J. Duer. *Introduction to solid-state NMR spectroscopy*. Wiley, Blackwell publishing Ltd, Oxford, 2004.
- [125] Paul Terence Callaghan. *Principles of Nuclear Magnetic Resonance microscopy*. Clarendon Press, Oxford University Press, New York, 1991.
- [126] Anatole Abragam. *The principles of nuclear magnetism*. Oxford University Press Inc, New York, 1961.
- [127] Charles Pence Slichter. *Principles of Magnetic Resonance*. Springer-Verlag, New York, 3rd ed. edition, 1989.
- [128] Hazime Saitô, Isao Ando, and Ayyalusamy Ramamoorthy. Chemical shift tensor—the heart of NMR: insights into biological aspects of proteins. *Prog. Nucl. Magn. Reson. Spectrosc.*, 57(2):181, 2010.
- [129] J. P. Jesson, G. N. La Mar, W. DeW. Horrocks, and R. H. Holm. *Introduction to solid-state NMR spectroscopy*. Academic Press, New York, 1973.
- [130] L. J. Berliner and J.Reuben. *Biological magnetic resonance: NMR of paramagnetic molecules*. Plenum Press, New York, 1993.

REFERENCES

- [131] Ivano Bertini, Paola Turano, and Alejandro J. Vila. Nuclear magnetic resonance of paramagnetic metalloproteins. *Chem. Rev.*, 93(8):2833–2932, 1993.
- [132] Ivano Bertini and Claudio Luchinat. NMR of paramagnetic substances. *Coord Chem. Rev.*, 150(1):29–75, 1996.
- [133] Marko Bertmer. Paramagnetic solid-state NMR of materials. *Solid State Nucl. Magn. Reson.*, 81:1–7, 2017.
- [134] Nalinda P. Wickramasinghe, Medhat A. Shaibat, Christopher R. Jones, Leah B. Casabianca, Angel C. de Dios, John S. Harwood, and Yoshitaka Ishii. Progress in ^{13}C and ^1H solid-state nuclear magnetic resonance for paramagnetic systems under very fast magic angle spinning. *J. Chem. Phys.*, 128(5):052210–052215, 2008.
- [135] ET Olejniczak, Simon Vega, and Robert G. Griffin. Multiple pulse NMR in rotating solids. *J. Chem. Phys.*, 81(11):4804–4817, 1984.
- [136] M Robin Bendall and Roy E Gordon. Depth and refocusing pulses designed for multiple pulse NMR with surface coils. *J. Magn. Reson.*, 53(3):365–385, 1983.
- [137] Jian Feng and Jeffrey A. Reimer. Suppression of probe background signals via B1 field inhomogeneity. *J. Magn. Reson.*, 209(2):300 – 305, 2011.
- [138] Geoffrey Bodenhausen, Ray Freeman, and David L Turner. Suppression of artifacts in two-dimensional j spectroscopy. *Journal of magnetic resonance*, 27(3):511–514, 1977.
- [139] D.G Cory and W.M Ritchey. Suppression of signals from the probe in bloch decay spectra. *J. Magn. Reson.*, 80(1):128 – 132, 1988.
- [140] H. Y. Carr and E. M. Purcell. Effects of Diffusion on Free Precession in Nuclear Magnetic Resonance Experiments. *Phys. Rev.*, 94:630–638, 1954.
- [141] RL Vold, JS Waugh, M Pv Klein, and DE Phelps. Measurement of spin relaxation in complex systems. *J. Chem. Phys.*, 48(8):3831–3832, 1968.
- [142] Arnold L. Bloom and James N. Shoolery. Effects of Perturbing Radiofrequency Fields on Nuclear Spin Coupling. *Phys. Rev.*, 97:1261–1265, 1955.
- [143] Andrew E. Bennett, Chad M. Rienstra, Michèle Auger, K. V. Lakshmi, and Robert G. Griffin. Heteronuclear decoupling in rotating solids. *J. Chem. Phys.*, 103(16):6951–6958, 1995.

-
- [144] Andreas Detken, Edme H. Hardy, Matthias Ernst, and Beat H. Meier. Simple and efficient decoupling in magic-angle spinning solid-state NMR: the XiX scheme. *Chem. Phys. Lett.*, 356(3):298 – 304, 2002.
- [145] B.M. Fung, A.K. Khitrin, and Konstantin Ermolaev. An Improved Broadband Decoupling Sequence for Liquid Crystals and Solids. *J. Magn. Reson.*, 142(1):97 – 101, 2000.
- [146] S. R. Hartmann and E. L. Hahn. Nuclear Double Resonance in the Rotating Frame. *Phys. Rev.*, 128:2042–2053, 1962.
- [147] Waclaw Kolodziejski and Jacek Klinowski. Kinetics of Cross-Polarization in Solid-State NMR : A Guide for Chemists. *Chem. Rev.*, 102(3):613–628, 2002.
- [148] Lucio Frydman and John S. Harwood. Isotropic Spectra of Half-Integer Quadrupolar Spins from Bidimensional Magic-Angle Spinning NMR. *J. Am. Chem. Soc.*, 117(19):5367–5368, 1995.
- [149] Laura Marinelli, Ales Medek, and Lucio Frydman. Composite Pulse Excitation Schemes for MQMAS NMR of Half-Integer Quadrupolar Spins. *J. Magn. Reson.*, 132(1):88 – 95, 1998.
- [150] D. Massiot, B. Touzo, D. Trumeau, J.P. Coutures, J. Virlet, P. Florian, and P.J. Grandinetti. Two-dimensional magic-angle spinning isotropic reconstruction sequences for quadrupolar nuclei. *Solid State Nucl. Magn. Reson.*, 6(1):73 – 83, 1996.
- [151] B.J. Van Rossum, H F Rster, and H J M De Groot. High Field and High-Speed CP-MAS ^{13}C NMR Heteronuclear Dipolar Correlation Spectroscopy of Solids with Frequency Switched Lee - Goldburg Homonuclear Decoupling. *J. Magn. Reson.*, 124:516–519, 1997.
- [152] Anne Lesage, Dimitris Sakellariou, Stefan Steuernagel, and Lyndon Emsley. Carbon-proton chemical shift correlation in solid-state NMR by through-bond multiple-quantum spectroscopy. *J. Am. Chem. Soc.*, 120(50):13194–13201, 1998.
- [153] Nalinda P Wickramasinghe and Yoshitaka Ishii. Sensitivity enhancement, assignment, and distance measurement in ^{13}C solid-state nmr spectroscopy for paramagnetic systems under fast magic angle spinning. *J. Magn. Reson.*, 181(2):233–243, 2006.
- [154] Gareth A Morris and Ray Freeman. Enhancement of nuclear magnetic resonance signals by polarization transfer. *J. Am. Chem. Soc.*, 101(3):760–762, 1979.

REFERENCES

Chapter 5

Contribution

In this thesis, three different types of MOFs have been investigated by SSNMR. At first, NMR studies were conducted on Cu_3btc_2 and its amine derivatives, which were supplied by the working group of professor Fröba at the University of Hamburg. At the beginning, I carried out the dehydration of the MOFs under high vacuum at high temperature. For all MOFs samples, I prepared the desired amount of NO loaded samples to perform NMR measurements. In general, I executed all NMR experiments for NO loaded samples by myself. Furthermore, NMR data analyses are performed by using topspin, dmfit and origin 7.5 software. In Pub. 1, I studied NO adsorption in Cu_3btc_2 and UHM-30 by MAS NMR. That enabled us to understand NO adsorption in Cu_3btc_2 and UHM-30, as well as the indirect detection of NONOate in UHM-30 by NMR. In Pub. 2, I contributed MAS NMR investigation of the four $\text{Cu}_3(\text{NHRbtc})_2$ MOFs, known as UHM-36, UHM-37, UHM-38 and UHM-39. The characterization of those MOFs has been accomplished by MAS NMR. Additionally, in the case of UHM-37, the means (physisorption or chemisorption) governing NO adsorption could be determined by NMR. In Pub. 3, I executed detailed multi-nuclear NMR research on NO loaded UHM-37. A detection of NONOate was possible by applying ^{15}N NMR studies on ^{15}N -isotopically NO loaded UHM-37. The combined ^1H and ^{13}C data with ^{15}N NMR studies showed the priority of chemisorption of NO over physisorption. A second type of MOF, MIL-100(Al) was received from professor Hartmann's group at the Friedrich–Alexander University of Erlangen–Nürnberg. In Pub. 4, I carried out evacuation, NO loading, as well as NMR studies on the NO adsorbed MIL-100(Al). A multi-nuclear NMR approach on MIL-100(Al) summarized the presence of extra framework site, $\text{Al}(\text{OH})_3$ and NO adsorption at OMS. One of our latest paper has been accepted for publication, and that focused on ^{15}N NMR study

of ^{15}N at variable temperatures. In Pub. 5, the first report on ^{15}N NMR measurements of NO at variable temperatures, and the dynamic exchange behavior between NO and $(\text{NO})_2$ are disclosed. A perovskite type MOF, DMAZn, well-known for phase transition behavior that has been provided by Dr. Mantas Šimėnas at the University of Vilnius. For that MOF, I performed ^{15}N T_1 relaxation NMR studies in Pub. 6. This studies revealed the phase transition of DMAZn, due to the mobility of ^{15}N leveled DMA^+ cation. Aside from my main contribution, which was accomplishing scientific writing and executing of NMR experiments to generate credible results, I was always involved in scientific discussions, decision making and implementation.

List of publications

- **1** “NO adsorption in amino-modified Cu_3btc_2 - type MOFs studied by solid-state NMR”
Arafat H. Khan, Katharina Peikert, Michael Fröba, Marko Bertmer. *Microporous Mesoporous Mater.*, 216: 111-117, 2015.
- **2** “Tuning the nitric oxide release behavior of amino functionalized HKUST-1”
Katharina Peikert, Laura J. McCormick, Damiano Cattaneo, Morven J. Duncan, Frank Hoffmann, Arafat H. Khan, Marko Bertmer, Russell E. Morris, and Michael Fröba. *Microporous Mesoporous Mater.*, 216: 118-126, 2015.
- **3** “Nitric oxide Adsorption in Cu_3btc_2 -type MOFs - Physisorption and Chemisorption as NONOates”
Arafat H. Khan, Katharina Peikert, Frank Hoffmann, Michael Fröba, and Marko Bertmer. *J. Phys. Chem. C*, 123(7): 4299-4307, 2019.
- **4** “Nitric oxide Adsorption in the MOF MIL-100(Al) studied by solid-state NMR spectroscopy”
Arafat H. Khan, Benjamin Barth, Martin Hartmann, Jürgen Haase, and Marko Bertmer. *J. Phys. Chem. C*, 122(24): 12723-12730, 2018.
- **5** “Temperature dependent ^{15}N NMR study of Nitric Oxide”
Arafat H. Khan, Dieter Michel, and Marko Bertmer. *SOLID STATE NUCL MAG.*(accepted)
- **6** “Spectroscopic Study of $[(\text{CH}_3)_2\text{NH}_2][\text{Zn}(\text{HCOO})_3]$ Hybrid Perovskite Containing Different Nitrogen Isotopes”

Mantas Šimėnas, Maciej Ptak, Arafat H. Khan, Laurynas Dagys, Vytautas Balevičius, Marko Bertmer, Georg Völkel, Mirosław Maćzka, Andreas Pöpl, and Juras Banys. *J. Phys. Chem. C*, 122(18): 10284-10292, 2018.

5. Contribution
